Lightweight Portable Life Support System (PLSS) Final Report

Department of Aerospace Engineering, University of Maryland, 2026 Capstone

Kit for Off-World Astronaut Life Aid

Team Members:
Chase Latyak, Anthony Regli, Eric Sibanda, Mahek Shah, Vijay Dayal,
Emma Perez, Kateryna Sukhina, Sidharth Garg, Maethili Pael Mihir Miller, Nandira de Andrade,
Sofia Asuncion, Ishan Dutta, Chris Witherspoon, Kassandra Perez-Rivera, Sara Carter, Yaseen Taha,
Ayush Iyer, Daniel Mehreteab, Lindsey Wright

PI: David Akin

Table of Contents

1 Introduction

The Kit for Off-World Astronaut Life Aid (KOALA) is an innovative Portable Life Support System (PLSS) developed for the NASA X-Hab program. NASA looks to send a manned mission to Mars, existing PLSS designs are too heavy to be supported by humans in Martian gravity. KOALA addresses this challenge with a target dry system mass under 60 kg, while providing the necessary life support functions.

The X-Hab program aims to connect NASA research with Universities, outsourcing technological development to get innovative ideas in the Aerospace Field. This opportunity allowed the KOALA team to learn from PLSS experts to better develop ideas that can hopefully be implemented in future NASA missions.

KOALA was developed by a team of 20 students across six sub teams, working with Dr. David Akin's Space Systems Laboratory at the University of Maryland. We would like to thank Dr. Akin, graduate students Romeo Perlstein, Nicolas Bolatto, and Daniil Gribok, and undergraduate students Avery Pierce and Meredith Embrey for their assistance in research, fabrication, and testing throughout this project.

1.1 Team Breakdown

Avionics

Chase Latyak

Anthony Regli

Mission Planning and Analysis

Eric Sibanda

Mahek Shah

Vijay Dayal

Loads, Structures, and Mechanisms

Emma Perez

Kateryna Sukhina

Sidharth Garg

Crew Systems

Maethili Patel

Mihir Miller

Nandira de Andrade

Sofia Asuncion

Ishan Dutta

Systems Engineering, Analysis, and Integration

Chris Witherspoon

Kassandra Perez-Rivera

Sara Carter

Yaseen Taha

Power, Propulsion, and Thermal

Ayush Iyer

Daniel Mehreteab

Lindsey Wright

1.2 Glossary of Acronyms

Term	Phrase	Description
AFSS	Avionics, Flight Software, and Simulation	
CAD	Computer-Aided Design	
CF	Carbon-Filled	Thermoplastic reinforced with carbon fibers
CFRP	Carbon-Fiber Reinforced Polymer	
CNT	Carbon Nanotube	
COPV	Composite Overwrapped Pressure Vessel	Multilayer tank that maintains same strength as metal tanks
CS	Crew Systems	
CWS	Caution and Warning System	
DCS	Decompression Sickness	
EMI	Electromagnetic Interference	
EMU	Extravehicular Mobility Unit	
EVA	Extravehicular Activity	
EVA Time	Extravehicular Activity Time	Time designation for EVA's is the time of outside activity plus a two hour margin (e.g. 8 hr EVA = 6 hrs + 2 hrs)
GF	Glass-Filled	Thermoplastic reinforced with glass fibers
GOX	Gaseous Oxygen	
HEPA	High-Efficiency Particulate Air	
HUT	Hard Upper Torso	Connection point between PLSS and Spacesuit
ISS	International Space Station	
JSC	Johnson Space Center	

LCVG	Liquid Cooling Ventilation Garment	The loop responsible for conducting metabolic heat from the astronaut
LiOH	Lithium Hydroxide	
LOX	Liquid Oxygen	
LSM	Loads, Structures, and Mechanisms	
MPA	Mission Planning and Analysis	
NASA	National Aeronautics and Space Administration	
NMSUS	NASA Modified System Usability Scale	
PEEK	Polyether Ether Ketone	High-performance thermoplastic
PGS	Pyrolytic Graphite Sheets	
PLSS	Portable Life Support System	
PPT	Power, Propulsion, and Thermal	
POR	Primary Oxygen Regulator	
PTFE	Polytetrafluoroethylene	Teflon material
RCA	Rapid Cycle Amine	
SOR	Secondary Oxygen Regulator	
SSER	Space-to-Space EMU Radio	
SSL	University of Maryland's Space Systems Laboratory	
SWME	Spacesuit Water Membrane Evaporator	Thermal loop component that removes heat from LCVG via evaporation and latent heat transfer
TCC (1)	Trace Contaminate Control	
TCC (2)	Thermo-Chromic Coating	

TRL	Technology Readiness Level	
UHF	Ultra High Frequency	
UMD	University of Maryland	
VSRS	Versatile Structural Radiation Shielding	PEEK + Tungsten layers for shielding
WLAN	Wide Local Area Network	

1.3 List of Figures

1.4 List of Tables

1.5 Mission Statement

To investigate the design space for Portable Life Support System architectures applicable to Lunar and Martian Extravehicular Activity, with a focus on minimizing mass and ensuring long-term mission functionality.

1.6 Requirements (Kassandra Perez-Rivera)

The KOALA requirements were developed through an iterative process based on NASA human spaceflights standards, feedback from NASA reviewers, and feedback from UMD faculty and graduate students throughout our design reviews. Requirements were repeatedly refined as our understanding of

the PLSS grew and subsystem designs evolved.

1.6.1 Mission Requirements

To start with the Mission Requirements, these are the operational goals KOALA must satisfy from the perspective of the overall mission. These reflect the NASA X-Hab guidelines for this project and were adjusted as our design matured. For example, an early question that arose was the EVA time required of our PLSS, as no requirement had been set by the NASA X-Hab guidelines. This was a variable that drove the sizing of all consumables and our overall system mass. This was eventually set at 8 hours to fulfill the goal set by the NASA X-Hab project description, consistent with the existing PLSS operational capabilities [1].

Req. ID	Requirement	Source
M-1	The PLSS shall support a continuous Mars surface EVA duration of 8 hours.	ENAE484 Team
M-2	Crew health and safety shall be maintained within acceptable limits throughout all phases of Mars surface EVA operations.	NASA X-Hab [1]
M-3	The PLSS total system mass shall be minimized and shall not exceed the mass limits imposed by Mars surface crew mobility.	NASA X-Hab [1]
M-4	The EVA mission shall remain safe for the crew following any single equipment failure.	NASA-HDBK-1002: Fault Management Handbook [2]
M-5	The PLSS design shall enable crew members to perform a defined task list with acceptable performance relative to	NASA X-Hab [1]

Req. ID	Requirement	Source
	shirt-sleeve conditions. (Task list is described in Appendix B of this document)	
M-6	The PLSS design shall be maintainable and repairable by the Mars surface crew using available tools and resources.	ENAE484 Team
M-7	The PLSS shall support a 2 hour reserve margin on all consumables.	ENAE484 Team

1.6.2 Top Level System Requirements

The top level requirements translate the mission requirements into specific, verifiable design constraints applicable to the whole PLSS. These requirements serve as the parent for all subsystem requirements which can be found in the following sections.

Req. ID	Requirement	Source
S-1	The PLSS shall have a total dry mass less than 60 kg.	M-3
S-2	Shall maintain suit pressure, ppO_2, $ppCO_2$, suit temperature, and relative humidity within the limits defined by NASA-STD-3001 Vol. 1 and Vol. 2.	M-2, NASA-STD-3001 [3],[4]
S-3	Shall not restrict crew mobility to a degree that prevents completion of pre-determined task list. (Task list is described in Appendix B of this document)	M-5
S-4	Shall be single-fault tolerant for all life-critical functions.	M-4
S-5	Shall continuously monitor life-critical parameters and provide the crew member with clear warnings upon detection of an out-of-limit condition.	M-2, M-4
S-6	Shall provide avionics functions consisting of telemetry, data logging, and two-way communication with the habitat.	M-2, M-4
S-7	Shall carry sufficient consumables to support an 8 hour EVA.	M-1, M-4, M-7
S-8	All life-critical field-replaceable parts shall be accessible and swappable using a defined tool kit that result in a	S-2, 5.1.2 in NASA-STD-3001 Vol.2 [4]

Req. ID	Requirement	Source
	satisfaction score of 85 or higher on the NASA Modified System Usability Scale (NMSUS).	
S-9	The system shall follow risk management methods defined by NASA-STD-6105.	ENAE484 PDR Feedback

1.6.3 Crew Systems Requirements

Req. ID	Requirement	Source
CS-1	Shall maintain the suit pressure to 4.3 psi and pressure fluctuations may not exceed 0.25 psi.	S-2, 11.1.4.2 in NASA-STD-3001 Vol. 2 [4]
CS-2	Shall maintain suit temperature to 22°C and shall remain within the allowable range of 18°C to 27°C.	S-2, 6.2.3.1 in NASA-STD-3001 Vol. 2 [4]
CS-3	Shall deliver O_2 at a partial pressure range of 2.8 psia - 3 psia.	S-2, Table 6.2-1 in NASA-STD-3001 Vol. 2 [4]
CS-4	Shall maintain CO_2 partial pressure below 0.06 psi.	S-2, 6.2.1.3 in NASA-STD-3001 Vol. 2 [4]
CS-5	Relative humidity shall be maintained at 45% and shall remain within the range of 25% to 75%.	S-2, Table 11.2-1 in NASA-STD-3001 Vol. 2 [4]
CS-6	During a purge event, the system shall provide an oxygen flow rate of 2540 g/hr (5.6 pph).	NASA PDR Feedback
CS-7	During a purge event, the system shall be capable of providing the increased flow rate for 54 minutes.	NASA PDR Feedback

1.6.4 Avionics Requirements

Req. ID	Requirement	Source
AV-1	The avionics system shall send and receive telemetry and voice communication to a base station.	S-6
AV-2	The avionics system shall interface with sensors in the PLSS to monitor astronaut vital signs and operating conditions of other systems.	S-5
AV-3	The avionics system shall monitor pumps, valves, and fans with trend logging.	S-6
AV-4	The avionics system shall utilize software that is effective, stable, and redundant.	S-4
AV-5	The avionics boxes shall be less than 3.5 kg total, or 50% of the mass of the xPLSS avionics boxes.	S-1
AV-6	Avionics boxes shall provide radiation and EMI shielding that is equivalent to or better than current xPLSS standards.	S-4
AV-7	Avionics boxes shall allow for sufficient thermal conduction to cool electronics.	TH-2, M-2
AV-8	Avionics boxes shall securely contain all necessary electronics and controllers.	S-5, S-6
AV-9	The avionics system shall have a caution & warning system that alters the astronaut when vitals such as ppO_2 and $ppCO_2$ are outside safe limits as set by NASA-STD-3001.	S-5, NASA-STD-3001 Vol. 2 [4]

1.6.5 Thermal Requirements

Req. ID	Requirement	Source
TH-1	The thermal loop shall accommodate a variable metabolic load up to 700W.	Based on NASA Feedback, M-2
TH-2	The thermal loop shall handle all heat loads from avionics and crew systems.	TH-1, AV-7, CS-2, M-2

Req. ID	Requirement	Source
TH-3	The thermal loop shall perform heat rejection throughout the temperate range of the Mars surface.	M-2
TH-4	The SWME feedwater supply shall be sufficient to support the full EVA duration plus a 2 hour reserve margin at maximum metabolic load.	S-7, M-7
TH-5	The thermal control system shall monitor feedwater tank level and present a warning when feedwater tank level is below 20% of the original capacity.	S-5, M-4
TH-6	The LCVG shall remain at a temperature between 21°C and 27°C.	CS-2, Figure 6.2-2 in NASA-STD-3001 Vol. 2 [4]
TH-7	The LCVG fluid shall be non-toxic to humans in case of exposure to the skin.	M-2, NASA-STD-3001 Vol. 2 [4]
TH-8	The thermal control system shall include a backup heat rejection mechanism capable of maintaining crew thermal safety during an emergency return.	S-4, M-4

1.6.6 Power Requirements

Req ID	Requirement	Source
PW-1	The primary power system shall supply power to avionics, pumps, fans, and control systems during nominal EVA operations.	M-1, S-7
PW-2	A backup power system shall supply power to life-critical loads upon detection of primary battery failure.	S-4, M-4
PW-3	The power system shall weigh less than 12.7 kg, or the current power system mass of the xPLSS.	S-1
PW-4	The state of charge of both the primary battery and backup battery shall be continuously monitored.	S-5, M-2
PW-5	The power system shall provide a warning when primary battery state of charge falls below 20%.	S-5

Req ID	Requirement	Source
PW-6	The batteries shall be rechargeable from habitat power systems between EVAs.	M-6, S-8
PW-7	The batteries shall be field replaceable using the defined tool kit.	M-6, S-8
PW-8	The primary battery shall provide sufficient energy to support all PLSS functions for an 8 hour EVA.	S-7, M-1, M-7
PW-9	The power system shall supply a continuous output energy level of 400 Wh under nominal operating conditions.	PW-1, S-4

1.6.7 Structural Requirements

Requirement ID	Requirement	Source
LSM-1	The PLSS structural components shall withstand all static and dynamic loads experienced during Mars surface EVA operations without permanent deformation or failure.	M-2, M-5
LSM-2	The PLSS structural components shall withstand a crew member fall load case.	M-2
LSM-3	The PLSS shall withstand worst-case launch load case (9g).	Falcon-9 Launch Vehicle Payload User Guide [5]
LSM-4	The PLSS shall attach to the Hard Upper Torso.	M-5, S-3
LSM-5	The PLSS to HUT connection shall remain secure under all expected load cases without requiring crew attention.	LSM-1, LSM-2, LSM-3, M-4
LSM-6	The PLSS structural components shall weigh less than 31.7 kg, or the current structural mass of the xPLSS.	S-1, M-3
LSM-7	All structural materials shall withstand the Mars surface temperature range of -125°C to +20°C.	M-2

Requirement ID	Requirement	Source
LSM-8	The PLSS cover shall protect all components from expected regolith particles.	M-2, M-4
LSM-9	All components shall survive all expected loads with appropriate factors of safety as described in NASA JSC-65828B, "Structural Design Requirements and Factors of Safety for Spaceflight Hardware For Human Spaceflight".	LSM-1, LSM-2, LSM-3

1.7 Requirements Verification (Kassandra Perez-Rivera)

The requirements verification matrix documents how each requirement was verified and confirms that the final design meets all requirements. Verification methods included analysis, inspection, demonstration, and test. Analysis is confirmation through calculations or simulations. Inspection is confirmation through visual examination. Demonstration is confirmation through operating the system. Test is confirmation through experimentation. As shown in the full requirements verification matrix below, most of KOALA requirements were verified through analysis, which reflects the scope of this project. In addition, several requirements could not be fully verified (neither fail or pass) due to the limitations of the hardware we could obtain for testing.

Requirements that were verified by demonstration (such as AV-1, AV-3, TH-5) could not be verified because a fully functional avionics prototype was not developed for our project. As many requirements are centered around safety, emergencies, and redundancy it is hard to verify these without flight representative hardware and software. Instead, the avionics system and sensors were designed with these requirements in mind, and the analysis supports their feasibility. However, physical demonstrations of the caution and warning system, data logging, and system monitoring remain a recommended test for future work.

In a similar vein, requirements verified by inspection were also unable to be verified. For example, "Shall not restrict crew mobility to a degree that prevents completion of pre-determined task list (S-3)" was unable to be tested as a fully wearable mockup of the KOALA design was not fabricated (with physical prototyping detailed in Section 9). These gaps in the requirements verification are only limitations to obtain flight hardware rather than issues in the KOALA design. The analysis conducted provides a strong confidence that all requirements would be met upon advanced physical prototyping, which is a recommended step in any future fabrication efforts.

Req. ID	Requirement	Verification Success Criteria	Verification Method	Verification Status	Subteam Responsible	Reference
S-1	The PLSS shall have a total dry mass less than 60 kg.	Total estimated dry mass of all PLSS components is less than 60 kg.	Analysis	Fail	Full Team	Table 2.3.1
S-2	Shall maintain suit pressure, ppO_2, $ppCO_2$, suit temperature, and relative humidity within the limits defined by NASA-STD-3001 Vol. 1 and Vol. 2.	Analysis confirms predicted life critical parameters are kept within the limits defined by NASA-STD-3001 Vol. 1 and Vol. 2 during both nominal and emergency operating conditions.	Analysis	Pass	CS, PPT	Sections 3, 5, and 6
S-3	Shall not restrict crew mobility to a degree that prevents completion of pre-determined task list. (Task list is described in Appendix B of this document)	Crew member successfully completes all tasks defined in Appendix B while wearing the PLSS without task performance being prevented by mobility restriction.	Test	Unverified - did not create a fully wearable mockup of the KOALA design. Recommended future test.	MPA	Appendix B
S-4	Shall be single-fault tolerant for all life-critical functions.	Risk analysis demonstrates that no single component failure results in loss of any life-critical function, with redundancy available for each.	Analysis	Pass	SEAI	Section 8
S-5	Shall continuously monitor life-critical parameters and provide the crew member with clear warnings upon detection of an out-of-limit condition.	There are sensors for life critical parameters throughout the PLSS, and a caution & warning system to alert the astronaut.	Analysis	Pass	AFSS, CS	Section 4

S-6	Shall provide avionics functions consisting of telemetry, data logging, and two-way communication with the habitat.	Demonstration confirms successful transmission and receipt of telemetry, data logging, and two-way communication with simulated habitat base station.	Demonstration	Unverified - did not prototype avionics system due to scope of project.	AFSS	Section 4
S-7	Shall carry sufficient consumables to support a 8 hour EVA.	Consumables budget confirms oxygen supply, CO2 scrubber capacity, feedwater supply, and battery energy each meet or exceed the 8 hour EVA duration requirement.	Analysis	Pass	CS, PPT	Sections 3, 5, and 6
S-8	All life-critical field-replaceable parts shall be accessible and swappable using a defined tool kit that result in a satisfaction score of 85 or higher on the NASA Modified System Usability Scale (NMSUS).	Maintainability test results are at least 85 or above on the NMSUS.	Test	Pass	MPA	Section 9.3 and Table 8.3.1
S-9	The system shall follow risk management methods defined by NASA-STD-6105.	Risk analysis is completed in accordance to NASA-STD-6105, including likelihood and consequence ratings for all identified risks.	Analysis	Pass	SEAI	Section 8.2
CS-1	Shall maintain the suit pressure to 4.3 psi and pressure fluctuations may not exceed 0.25 psi.	Pressure regulators are sized to maintain pressure within these bounds.	Analysis	Pass	CS	Section 3

CS-2	Shall maintain suit temperature to 22°C and shall remain within the allowable range of 18°C to 27°C.	Thermal system confirms suit temperature is maintained within the range of 18C to 27C under all expected metabolic load conditions.	Analysis	Pass	PPT, CS	Section 5.4
CS-3	Shall deliver O_2 at a partial pressure range of 2.8 psia - 3 psia.	Analysis confirms ppO2 is remain within the nominal range under all operating conditions.	Analysis	Pass	CS	Section 3.4
CS-4	Shall maintain CO_2 partial pressure below 0.06 psi.	Analysis of CO2 scrubber performance confirms CO2 partial pressure remains below 0.06 psia for the full EVA duration at the predicted metabolic load.	Analysis	Pass	CS	Section 3.5
CS-5	Relative humidity shall be maintained at 45% and shall remain within the range of 25% to 75%.	Analysis confirms humidity will remain within the nominal range under expected operating conditions.	Analysis	Pass	CS	Section 3.6
CS-6	During a purge event, the system shall provide an oxygen flow rate of 2540 g/hr (5.6 pph).	Analysis of oxygen supply confirms a flow rate of 5.6 pph is achievable during a purge event.	Analysis	Pass	CS	Section 3.4
CS-7	During a purge event, the system shall be capable of providing the increased flow rate for 54 minutes.	Analysis of oxygen consumables confirms sufficient supply to sustain a 54 min. long purge event at 5.6 pph.	Analysis	Pass	CS	Section 3.4

AV-1	The avionics system shall send and receive telemetry and voice communication to a base station.	Demonstration confirms telemetry data is successfully transmitted to and received from a base station, and two-way voice communication is established and maintained.	Demonstration	Unverified - did not prototype avionics system due to scope of project.	AFSS	Section 4
AV-2	The avionics system shall interface with sensors in the PLSS to monitor astronaut vital signs and operating conditions of other systems.	The avionics system is designed to interface with selected sensors for all life-critical parameters.	Analysis	Pass	AFSS, CS	Section 4
AV-3	The avionics system shall monitor pumps, valves, and fans with trend logging.	Demonstration confirms pumps, valves, and fans are monitored by the avionics system and data is logged.	Demonstration	Unverified - did not prototype avionics system due to scope of project.	AFSS	Section 4
AV-5	The avionics boxes shall be less than 3.5 kg total, or 50% of the mass of the xPLSS avionics boxes.	Total estimated avionic box mass is less than 3.5 kg.	Analysis	Pass	AFSS	Section 4.6
AV-6	Avionics boxes shall provide radiation and EMI shielding that is equivalent to or better than current xPLSS standards.	Analysis of avionics boxes confirm radiation and EMI shielding meets or exceeds xPLSS shielding specifications.	Analysis	Pass	AFSS	Section 4.5.3
AV-7	Avionics boxes shall allow for sufficient thermal conduction to cool electronics.	Thermal system can handle the expected avionics heat load to remain within manufacturer rated operating limits at peak heat load.	Analysis	Pass	PPT, AFSS	Section 4.5.5

AV-8	Avionics boxes shall securely contain all necessary electronics and controllers.	Inspection confirms all electronics and controllers are fully enclosed within avionics boxes throughout expected load cases.	Inspection	Unverified - did not prototype avionics system due to scope of project.	AFSS, LSM	Section 4.5
AV-9	The avionics system shall have a caution & warning system that alters the astronaut when vitals such as ppO_2 and $ppCO_2$ are outside safe limits as set by NASA-STD-3001.	Demonstration confirms that the caution & warning system generates an alert to the astronaut when ppO2, ppCO2, temperature, or humidity limits exceed nominal limits as set by NASA-STD-3001.	Demonstration	Unverified - did not prototype avionics system due to scope of project.	AFSS	Section 4.5
TH-1	The thermal loop shall accommodate a variable metabolic load up to 700W.	Analysis confirms the thermal loop dissipates astronaut metabolic loads and maintains the LCVG temperature to the range defined in CS-2.	Analysis	Pass	PPT	Section 5.2
TH-2	The thermal loop shall handle all heat loads from avionics and crew systems.	Analysis confirms the radiator thermal loop is capable of dissipating avionics and crew system heat loads under worst case operating conditions.	Analysis	Pass	PPT	Section 5.2

TH-3	The thermal loop shall perform heat rejection throughout the temperate range of the Mars surface.	Analysis confirms the thermal system maintains the LCVG temperature and electronic temperature nominal conditions even at maximum ambient temperature (20 C).	Analysis	Pass	PPT	Section 5
TH-4	The SWME feedwater supply shall be sufficient to support the full EVA duration plus a 2 hour reserve margin at maximum metabolic load.	Analysis of feedwater consumption at maximum expected metabolic load confirms feedwater supply is sufficient for 8 hour EVA.	Analysis	Pass	PPT	Section 5
TH-5	The thermal control system shall monitor feedwater tank level and present a warning when feedwater tank level is below 20% of the original capacity.	Demonstration confirms feedwater tank level is continuously monitored and a warning is generated when tank level falls below 20% of the original capacity.	Demonstration	Unverified - did not prototype avionics system due to scope of project.	PPT, AFSS	Section 4
TH-6	The LCVG shall remain at a temperature between 20°C and 27°C.	Analysis confirms LCVG water temperature remains within 20 C and 27 C under all metabolic load conditions throughout the full EVA duration.	Analysis	Pass	PPT	Section 5
TH-7	The LCVG fluid shall be non-toxic to humans in case of exposure to the skin.	The LCVG fluid used is non-toxic.	Analysis	Pass	PPT	Section 5

TH-8	The thermal control system shall include a backup heat rejection mechanism capable of maintaining crew thermal safety during an emergency return.	Analysis confirms the backup SWME is sized to provide sufficient heat rejection to keep the astronaut temperature within nominal limits (CS-2) for an emergency return following primary SWME failure.	Analysis	Pass	PPT	Section 5
PW-1	The primary power system shall supply power to avionics, pumps, fans, and control systems during nominal EVA operations.	The power system is designed to provide power to all identified loads such as avionics, fans, pumps, controllers.	Analysis	Pass	PPT	Section 6.1
PW-2	A backup power system shall supply power to life-critical loads upon detection of primary battery failure.	Demonstration confirms backup power activates upon primary battery failure or depletion.	Demonstration	Unverified - did not prototype avionics system due to scope of project.	PPT, AFSS	Section 6.4.1
PW-3	The power system shall weigh less than 12.7 kg, or the current power system mass of the xPLSS.	Total power system mass is or less than 12.7 kg.	Analysis	Pass	PPT	Section 6.5
PW-4	The state of charge of both the primary battery and backup battery shall be continuously monitored.	Demonstration confirms the avionics system is logging the charge of both batteries.	Demonstration	Unverified - did not prototype avionics system due to scope of project.	AFSS, PPT	Section 4
PW-5	The power system shall provide a warning when primary battery state of charge falls below 20%.	Demonstration confirms a warning is generated when primary battery state reaches 20% charge.	Demonstration	Unverified - did not prototype avionics system due to scope of project.	AFFS, PPT	Section 4

PW-6	The batteries shall be rechargeable from habitat power systems between EVAs.	Analysis confirms both batteries selected are rechargeable and can be recharged from the habitat power source.	Analysis	Pass	PPT	Section 6.4
PW-7	The batteries shall be field replaceable using the defined tool kit.	Maintainability test results show that the battery removal and replacement satisfies S-8.	Test	Pass	MPA	Section 9.3
PW-8	The primary battery shall provide sufficient energy to support all PLSS functions for an 8 hour EVA.	Analysis of battery capacity confirms sufficient energy to power all PLSS loads for an 8 hour EVA at maximum expected continuous power draw.	Analysis	Pass	PPT	Section 6
PW-9	The power system shall supply a continuous output energy level of 400 Wh under nominal operating conditions.	Analysis confirms estimated energy consumption across all PLSS components over an 8 hour EVA does not exceed 400 Wh under nominal operation conditions.	Analysis	Pass	PPT	Section 6
LSM-1	The PLSS structural components shall withstand all static and dynamic loads experienced during Mars surface EVA operations without permanent deformation or failure.	Analysis confirms all structural components maintain structural integrity under the worst case loads expected during Mars EVA operations.	Analysis	Pass	LSM	Section 7

LSM-2	The PLSS structural components shall withstand a crew member fall load case.	Analysis confirms all structural components maintain structural integrity under the worst case loads expected in the event that an astronaut falls from a standing height.	Analysis	Pass	LSM	Section 7
LSM-3	The PLSS shall withstand worst-case launch load case (9g).	Analysis confirms all structural components maintain structural integrity under the worst case loads of 9g expected during launch.	Analysis	Pass	LSM	Section 7
LSM-4	The PLSS shall attach to the Hard Upper Torso.	Inspection confirms the PLSS interfaces with the HUT with no gaps or misalignment.	Inspection	Unverified - did not create a fully wearable mockup of the KOALA design.	LSM	Section 7.3
LSM-5	The PLSS to HUT connection shall remain secure under all expected load cases without requiring crew attention.	Analysis confirms the HUT attachment remains secure under all expected load cases.	Analysis	Pass	LSM	Section 7.3
LSM-6	The PLSS structural components shall weigh less than 31.7 kg, or the current structural mass of the xPLSS.	Total measured mass of all structural components is less than 31.7 kg.	Analysis	Pass	LSM	Section 7.9
LSM-7	All structural materials shall withstand the Mars surface temperature range of -125°C to +20°C.	Analysis of material properties data confirms all structural materials maintain required mechanical properties across the expected temperature range.	Analysis	Pass	LSM	Section 7

LSM-8	The PLSS cover shall protect all components from expected regolith particles.	Analysis of cover design confirms all internal components are enclosed and protected from regolith particles.	Analysis	Pass	LSM	Section 7.5
LSM-9	All components shall survive all expected loads with appropriate factors of safety as described in NASA JSC-65828B, "Structural Design Requirements and Factors of Safety for Spaceflight Hardware For Human Spaceflight".	The structural analysis was conducted with safety factors that reference NASA JSC-65828B.	Analysis	Pass	LSM	Section 7

1.8 Concept of Operations (Sara Carter)

The KOALA design is made to work in Lunar or Martian environments for extended missions. The operational procedures follow NASA standards as created for the ISS, as those have been proven to ensure astronaut safety. The design was also made with maintainability in mind, as simpler systems result in lower errors.

An overall operations management for an extended mission would require an estimate of how many EVA's will be done to supplement resources used during an EVA, including water and oxygen. Additionally, the lifecycle of each component must be considered, and enough replacements and backups must be sent such that the astronaut's life won't be at risk. There is also the usage of the KOALA in launch and landing scenarios.

The NASA ISS EVA procedure is as follows [6]:

Figure 1.8.1 xEMU EVA ConOps [6]

Breaking these down into their details gives more details as to how the mission operates.

Step	**Breakdown**
EVA Prep	This involves determining the purpose of the EVA and preparing all the necessary procedures and tools for the EVA. Ideally, if after a launch/landing, this step includes a maintenance overview of the components of KOALA, tools, and the airlock
Pre EVA	This includes the KOALA Donning - Prebreathe with 100% Oxygen (out of suit) - Suit Purge - In suit Prebreathe
EVA	- Airlock Depress - Airlock Egress - Predetermined EVA tasks - Airlock ingress - Airlock repress
Post EVA	KOALA Doffing
Maintenance & Recharge	- O2 Tank Recharge - Battery Recharge - CO2 Scrubber Replacement - SWME Water Tank Refill - Suit Cleaning - Inspection for Damage

Table 1.8.1 EVA Concept of Operations General Procedure [7]

The prebreathe is important because it reduces the risk of Decompression Sickness for the astronauts.

2 System Overview and Breakdown

2.1 Initial System Architecture (Sara Carter)

The basis of this project came from the xEMU, which is the current standard life support system used on the ISS and other NASA missions. This gave a baseline mass for subsystems to work off, as well as a diagram for how to split up the components. The gauge of all components came from the PLSS 2.5, which provided a baseline structure for the interior of a PLSS system.

The initial mass breakdown is as such:

Component	xEMU (kg)
Backplate	21.2
Cover	10.5
Oxygen Supply	12.2
Ventilation Loop	11.9
Thermal Loop	6.5
Avionics	14.8
Sensor	5.2
Power	12.7
Total	95

Table 2.1.1: xEMU Mass Breakdown [8]

And the initial PLSS layout is as such:

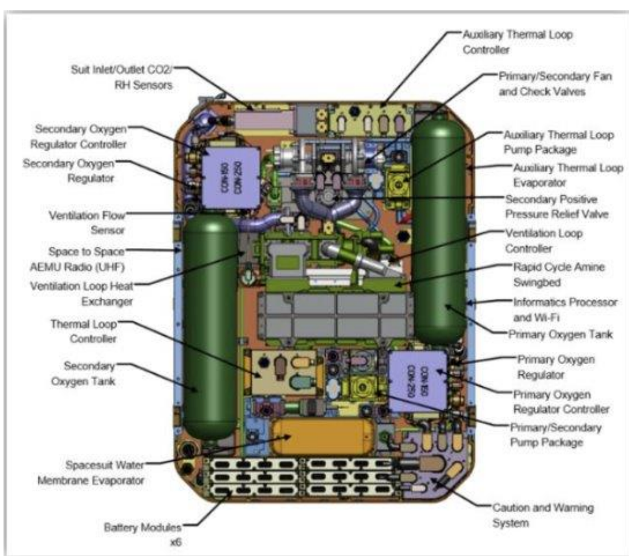

Figure 2.1.1: PLSS 2.5 Interior Layout [9]

These two metrics were used as a baseline as they gave thorough breakdowns to follow, and would allow the final results of this project to be displayed in a meaningful comparison.

2.2 System Block Diagram (Kassandra Perez-Rivera)

The KOALA internal system architecture can be broken down into four main subsystems: the oxygen supply, ventilation loop, thermal loops, and power and electronics. Figure 2.2.1 is the system block diagram which shows the physical flow paths between the various components and subsystems. The left side portion is an expanded view of the electronics system.

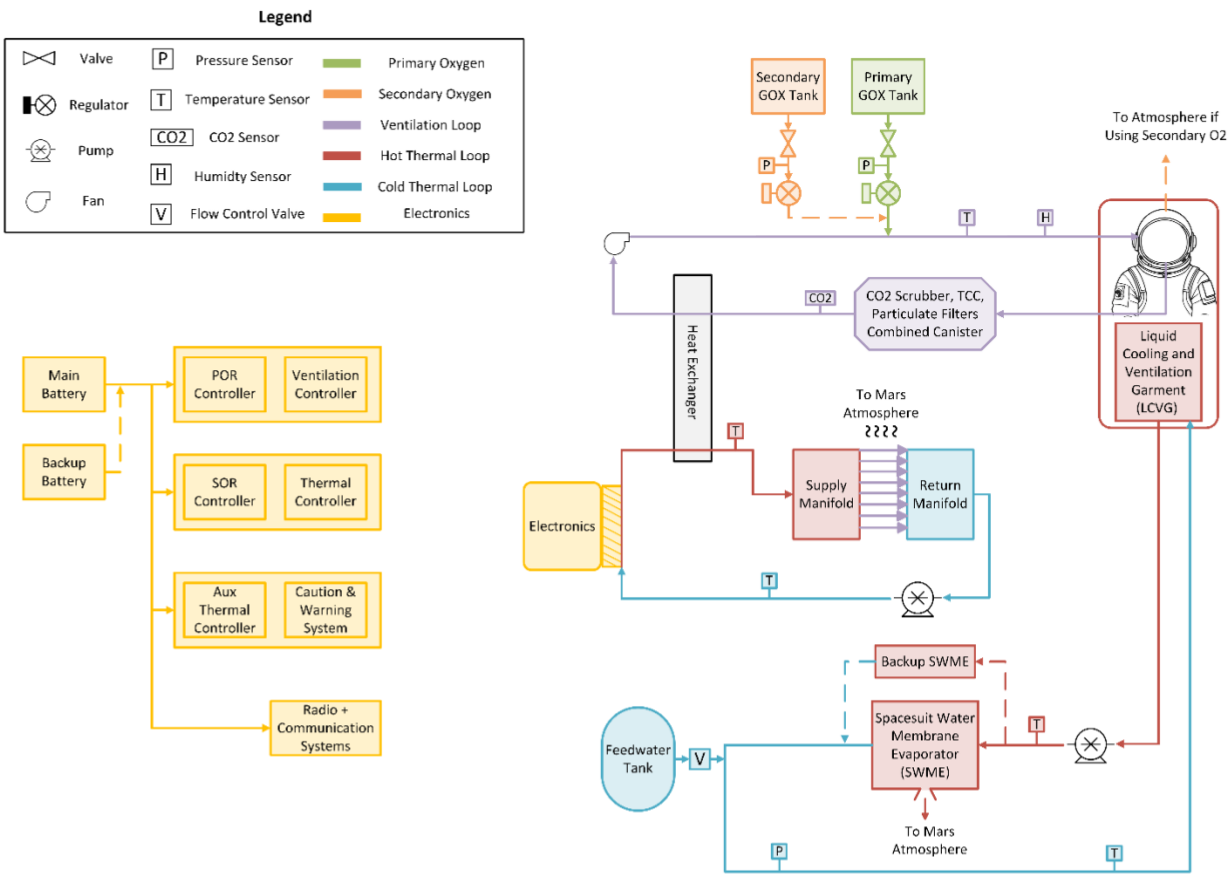

Figure 2.2.1: KOALA System Block Diagram

Starting with the oxygen supply, there are two oxygen tanks that are each equipped with a pressure sensor, regulator, and valve. Under nominal operating conditions, the primary tank supplies oxygen to the ventilation loop. The secondary tank provides a redundant oxygen source (S-4) in the event of primary tank failure or during a purge event, with its exhaust sent to the Mars atmosphere rather than recirculated.

Moving onto the ventilation loop, exhaled gas from the astronaut passes through a canister that contains the CO_2 scrubber, trace containment control (TCC), and particulate filters before being recirculated back to the astronaut. A fan drives air flow through the loop. Temperature, humidity, and CO_2 sensors monitor the conditions of the gas. The heat exchanger is used to cool the air that is being sent to the astronaut to keep it within the acceptable temperature limits.

The thermal management is done with two separate thermal loops. The first thermal loop regulates the temperature of the electronics and avionics boxes by running 50-50 propylene glycol-water coolant through a radiator. The second thermal loop dissipates heat from the Liquid Cooling Ventilation Garment (LCVG) by running water through the Spacesuit Water Membrane Evaporator (SWME). The SWME evaporates water vapor to the Mars atmosphere. A backup SWME provides redundant heat rejection capability (S-4). A feedwater tank is connected to the SWME thermal loop to maintain the water pressure as evaporation occurs.

Finally, the electronics system consists of a main battery and backup battery supplying the avionics system which is housed in four separate boxes. The avionics system consists of the primary oxygen regulator (POR), secondary oxygen regulator (SOR), ventilation controller, thermal controller, auxiliary thermal controller, a caution and warning system, and radio and communications. To point out the connection of design decisions with requirements, the backup battery can support the PLSS in the event of a main battery failure (S-4). The caution and warning system monitors inputs from all sensors across the PLSS and is responsible for altering the crew member to any out-of-limit condition (S-5).

2.3 System CAD (Sara Carter)

The full system CAD was assembled with maintainability in mind, such that systems would be placed together and be largely easily accessible. There is plenty of space present within the system to accommodate piping, wiring, and tubing as it is needed, and the paths that these will take are logical from component to component. There is extra space towards the top to support the transfer of resources and information between the PLSS and the Suit.

Many of the components are simplifications of their actual selves, so as to make it less complicated to manufacture through 3-D printing for testing.

Redacted due to Export Control/CUI requirements.

Figure 2.3.1 Simplified CAD Versions of (a) regulator, (b) fan, and (c) pump

Redacted due to Export Control/CUI requirements.

Figure 2.3.2 Full System CAD Model

2.4 System Mass Breakdown (Sara Carter, Kassandra Perez-Rivera)

The primary design objective of this project was to reduce the dry mass of the PLSS to 60 kg or less, as set by the NASA X-Hab program guidelines. Each subteam was designed to reduce mass relative to the xPLSS baseline. Table 2.3.1 presents the system mass breakdown. The current system mass of 75.9 kg exceeds the 60 kg dry mass requirement, reflecting the challenge of meeting the performance demands of an 8 hour Mars surface EVA. Additional mass reduction avenues to improve upon the KOALA design are presented in Section 10.

Component	xEMU (kg) [8]	KOALA (kg)	Difference (kg)
Backplate	21.2	7.84	-13.4
Cover	10.5	8.03	-2.47
Oxygen Supply	12.2	11.4	-0.8
Ventilation Loop	11.9	5.9	-6.0
Thermal Loop	6.5	6.6	+0.1
Avionics	14.8	10.6	-4.2
Sensor	5.2	4.5	-0.7
Power	12.7	11.1	-1.6
Total	95.0	66.0	**29.0**
Total + 15% Margin	95.0	75.9	**10.9**

Table 2.4.1: KOALA System Mass Breakdown with xEMU Comparison

2.5 System Interface Overview (Yaseen Taha)

The PLSS was developed as an integrated life support system rather than a collection of independent subsystem designs. Although each sub-team focused on a specific area, including structures, oxygen, ventilation, thermal, power, avionics, and crew systems, the success of the final design depended on how those subsystems connected and functioned together. For this reason, interface definition became a key part of the systems engineering process. The interface overview served as the link between the high-level system architecture and the detailed subsystem designs that follow in the report.

To manage this process, the team developed an Interface Tracker that identified the major connections between components, the type of interface, the method of connection, critical parameters, verification approach, criticality, and responsible sub-team. This allowed the team to clearly define where mechanical, pneumatic, fluid, electrical, thermal, and data connections occurred across the PLSS. More importantly, it helped reveal that many design risks existed at the boundaries between subsystems, such as oxygen regulation, breathing gas circulation, sensor feedback, power distribution, and thermal control.

ICD reference	Component	Component Connected To	Connected Via	Connection Type (Mechanical, Electrical, Pneumatic, Fluid, Thermal, Data/Signal)	Critical Parameters	Flow/Signal Direction	V&V method	Criticality	Subteam
ICD-001	Backplate/isogrid (7075 Aluminium)	GOX Tanks, Pressure Plate, all life support components	Mounting brackets (Inconel 718), bolts/fasteners, threaded inserts	Mechanical	Load Capacity (9g), Buckling resistance, Mass (5.70kg)	N/A	Test - Structural Analysis - FEA	Life-Critical	LSM
ICD-002	Pressure plate (CFRP)	Backplate/Isogrid, HUT	Threaded inserts to backplate, O-ring face seal (FFKM) to HUT, Bolts	Mechanical, Pneumatic (Pressure seal)	Pressure (4.3 psia), max deflection (0.063mm), Mass (~4.7kg)	N/A	Test - Pressure Test - Leak Analysis - FEA	Life-Critical	LSM
ICD-003	Cover (Al 6061 with ribs)	Backplate/Isogrid, Hinges, Latches, Radiator (Thermal Contact)	Hinge pins, latch points, thermal contact surface	Mechanical, Thermal	Load capacity (230kg fall) Thermal Conductivity (>=20W/mK), Mass (6.23kg)	N/A	Test - Structural Analysis - FEA	Mission-Critical	LSM

Table 2.5.1: Snippet of the interface tracker showing the different tracked categories.

Overall, the Interface Tracker helped turn the system block diagram into a more complete and verifiable design. It gave the team a shared reference for coordination, reduced ambiguity between sub-teams, and helped prioritize life-critical and mission-critical interfaces during design reviews. By documenting how each subsystem interacts with the rest of the PLSS, the interface overview ensured that integration was considered throughout the design process rather than left as a final assembly issue.

2.6 Full System Interface Document (Yaseen Taha)

ICD reference	Component	Component Connected To	Connected Via	Connection Type	Critical Parameters	Flow/ Signal Direction	V&V method	Criticality
ICD-001	Backplate/ isogrid (7075 Aluminium)	GOX Tanks, Pressure Plate, all life support components	Mounting brackets (Inconel 718), bolts/fasteners, threaded inserts	Mechanical	Load Capacity (9g), Buckling resistance, Mass (5.70kg)	N/A	Test - Structural Analysis - FEA	Life-Critical
ICD-002	Pressure plate (CFRP)	Backplate/Isogrid, HUT	Threaded insersts to backplate, O-ring face seal (FFKM) to HUT, Bolts	Mechanical, Pneumatic (Pressure seal)	Pressure (4.3 psia), max deflection (0.063mm), Mass (~4.7kg)	N/A	Test - Pressure Test - Leak Analysis - FEA	Life-Critical
ICD-003	Cover (Al 6061 with ribs)	Backplate/Isogrid, Hinges, Latches, Radiator (Thermal Contact)	Hinge pins, latch points, thermal contact surface	Mechanical, Thermal	Load capacity (230kg fall) Thermal Conductivity (>=20W/mK), Mass (6.23kg)	N/A	Test - Structural Analysis - FEA	Mission-Critical
ICD-004	Primary GOX Tank	Primary GOX Valve	High-pressure pipine (inconel 625)	Pneumatic	Max Pressure (4500psi/310bar), O2 capacity (4.7L), Leakage (<5%)	Tank → Valve	Test - Pressure Test - Leak Inspection - Visual	Life-Critical
ICD-005	Primary GOX Tank	Isogrid/Backplate	Bracket (Inconel 718), bolts	Mechanical	Tank Mass (3-5kg empty)	N/A	Test - Structural inspection - Dimensional	Life-Critical
ICD-006	Secondary GOX Tank	Secondary GOX Valve	High-pressure pipine (inconel 625)	Pneumatic	Max Pressure (4500psi/310bar), O2 capacity (4.7L), Leakage (<5%)	Tank → Valve	Test - Pressure Test - Leak Inspection - Visual	Life-Critical
ICD-007	Secondary GOX Tank	Isogrid/Backplate	Bracket (Inconel 718), bolts	Mechanical	Tank Mass (3-5kg empty)	N/A	Test - Structural	Life-Critical

							inspection - Dimensional	
ICD-008	Primary GOX Valve	Primary GOX Tank (inlet), Astronaut Helmet (outlet)	Piping (inconel 625) Manifolds (Monel 400) O2 Con-150/250	Pneumatic	Flow rate (up to 5.6 pph) Regulated Pressure (4.3psia) Max inlet (3750 psia)	Tank → helmet	Test - Functional Test- Performance Test - Pressure	Life-Critical
ICD-009	Primary GOX Valve	LIOH Canister	Piping (inconel 625) Manifolds (Monel 400)	Pneumatic	Flow rate (up to 5.6 pph for 54min) Pressure Regulation (4.3psia)	Valve → Canister	Test - Functional Test- Performance	Life-Critical
ICD-010	Secondary GOX Valve	Secondary GOX Tank (Inlet) Astronaut Helmet (outlet)	Piping (inconel 625) Manifolds (Monel 400) O2 Con-150/250	Pneumatic	Flow rate (up to 5.6 pph) Regulated Pressure (4.3psia) Max inlet (3750 psia)	Tank → Helmet	Test - Functional Test- Performance Test - Pressure	Life-Critical
ICD-011	Secondary GOX Valve	LIOH Canister	Piping (inconel 625) Manifolds (Monel 400)	Pneumatic	Flow Rate (Purge Capability) Pressure regulation (4.3 psia) Redundancy	Valve → Canister	Test - Functional Test- Performance	Life-Critical
ICD-012	TCCS	Vent Loop (Downstream of LiOH) Particulate filters	Polypropylene ducting/piping (SS 316 fittings)	Pneumatic	Contaminant removal efficiency Operating Life (150 EVA hr) Mass (0.9kg)	LiOH → TCCS → Helmet	Test - Performance Test - Functional Test - Endurance	Mission-Critical
ICD-013	LiOH (CO2 Scrubber)	Vent fans (upstream) TCCS (Downstream) Particulate filters GOX supply	Polypropylene ducting/piping (SS 316 fittings)	Pneumatic	CO2 removal efficiency Mass (2.95kg) Operating Pressure (4.3psia) Temperature Control	Fans → LiOH → TCCS	Test- Performance Test - Functional Test - Thermal	Life-Critical
ICD-014	Pressure Regulators (2 Units)	GOX tanks (inlet) Astronaut helmet & LiOH canister	High-pressure pipine (inconel 625) Manifolds	Pneumatic Electrical (Control)	Regulated Pressure (4.3psia) Flow rate (5.6 pph max)	GOX tanks → Distribution	Test - Performance Test - Functional	Life-Critical

		(outlets) Avionics (Control)	(Monel 400) Control Wiring		Max inlet (3750 psia)	Avionics ↔ Regulators	Test - Pressure	
ICD-015	Temperature Sensors (3 Units Total)	Avionics Box Thermal loop measurement points Vent Loop Avionics Cooling	Wiring Harness Sensor Probe Insertion Points	Electrical Data/Signal	Accuracy Range (-20C to 50C) Response time Power (negligible)	Sensors → Avionics	Test - Functional Test- Performance Test - Thermal-Vacuum	Mission-Critical
ICD-016	CO2 Sensors (2 - NDIR + Electrochemical)	Avionics Box Vent Loop (Sensing port at helmet return)	Wiring Harness Sensor probe/port into vent ducting	Electrical Data/Signal Pneumatic (Sensing Port)	Accuracy Response time Power (1.8W per M-PALSS array) Range	Sensors → Avionics	Test - Functional Test - Performance Test - Integrated System	Life-Critical
ICD-017	Pressure Sensors (8 Unit)	Avionics Box GOX Tanks (2) Regulators (2) Vent Loop, Thermal Loop, Helmet	Wiring harness Pressure tap fittings (SS 316)	Electrical Data/Signal Pneumatic (Pressure)	Accuracy Range (0-4500 psi for tanks, 0-10 psi for vent) Response time	Sensors → Avionics	Test - Functional Test - Performance Test - Pressure	Life-Critical
ICD-018	Vent Fans (2 Primary + 1 Auxilary)	Con350 (inlet from helmet) LiOH scrubber (outlet) Main Avionics (control)	Ducting (SS 316/PP) Power Wiring Control Wiring	Pneumatic Electrical	Flow Rate Power (12.1W each, 36.3W total) Reliability Mass (~1.5kg total)	Helmet → Fans → Scrubber Battery → Fans Avionics ↔Fans	Test - Performance Test - Endurance Test - Functional	Life-Critical
ICD-019	Drinking Bag (64 fl oz / 1,9kg)	Helmet Drinking port	Drinking tube/hose with bite valve	Fluid	Volume (1.9kg water max), Leak-proof, Flow rate, Biocompatibility	Bag → Helmet	Test - Leak Inspection - Visual Test- Functional	Operational
ICD-020	Particulate Filters (Mesh PP + Hepa Borosilicate/PP)	Vent Loop (between fans and LiOH, after TCCS)	Polypropylene ducting with integrated filter housing	Pneumatic	Filtration efficiency (HEPA), Pressure drop, Mass, Filter life	Bidirectiona l (Vent loop flow)	Test - Performance Test - Functional Inspection - Visual	Mission-Critical

ICD-021	Humidity Sensor (2)	Avionics box Vent Loop (Helmet return section)	Wiring harness, sensing port into ducting	Electrical Data/Signal Pneumatic (Sensing)	Accuracy, Range (0-100% RH), Response time, Power	Sensors → Avionics	Test - Functional Test- Performance Test - Thermal-Vacuum	Mission-Critical
ICD-023	O2 con-150/250	Pressure regulators (PLSS side) Helmet (suit side)	Quick disconnect fitting (High Pressure rated)	Pneumatic	Max pressure (3750 psi capable) leak rate (<1×10⁻⁶ sccs He) Disconnect force	PLSS → Helmet	Test - Leak Test - Pressure Test - Functional	Life-Critical
ICD-024	con350 vent loop	Helmet exhaust port (suit side) Vent fans (PLSS side)	Quick disconnect coupling (Low-pressue ducting interface)	Pneumatic	Flow rate, Leak rate, Disconnect force, Pressure drop	Helmet → PLSS	Test - Leak Test - Performance Test - Functional	Life-Critical
ICD-025	con450 thermal	LCVG (suit side), Water tank/thermal loop (PLSS side)	Quick Disconnect coupling with check valves	Fluid	Flow rate, leak rate, temperature range (18C-27C nominal, Disconnect force	Bidirectiona l (Cooling loop)	Test - Leak Test - Functional Test - Thermal	Life-Critical
ICD-026	con-550 aux thermal	Auxiliary thermal components, Backup thermal system	Quick disconnect coupling	Fluid	Flow rate, Leak rate, Compatibility, Redundancy	Bidirectiona l	Test - Leak Test - Functional	Mission-Critical
ICD-027	con-650 cws	LCVG (suit side) Water tank/SWME (PLSS side)	Quick disconnect coupling with flow control	Fluid	Flow rate, Leak rate, Temperature control, Heat removal capacity	PLSS → LCVG → PLSS (Loop)	Test - Leak Test - Performance Test Thermal	Life-Critical
ICD-028	Wifi (WLAN 2.4/5 GHz)	Avionics box (Internal radio module)	Antenna (Wireless RF), RF wiring/traces to avionics	Data/Signal Electrical (Power)	Range (100m), Data rate (10Mb/s), Power (0.5W), Signal Strength	Bidirectiona l	Test - Functional Test - Performance Demonstratio n - Operational	Operational
ICD-029	Radio (UHF duplex)	Avionics box, External antenna, Main battery	RF Cable, antenna mount,	Electrical Data/signal	Range (75-80m), Data rate (693kbps), Power	Bidirectiona l (duplex)	Test - Functional Test -	Life-Critical

			power wiring harness		(0.11W transmit), Mass (4.31kg)		Performance Demonstration - Operational	
ICD-030	Radiator (w/ AZ-93 coating, 1m^2)	SWME, Water Tank Cover (Thermal contact), Thermal loop	Tubing (Thermal loop), thermal conductive contact with cover interior	Thermal Fluid	Emissivity (0.9) heat rejection (250-300W nominal) Area (~1m^2), Mass	Heat out to environment Water bidirectional	Test - Thermal Analysis - Thermal Test - Thermal-Vacuum	Life-Critical
ICD-031	Water tank/bag	SWME LCVG (via con-650) Pumps (2) Radiator Loop	Tubing with fittings	Fluid	Volume (1kg tank + feedwater) Leak-proof Pressure rating, Mass	Bidirectional (Thermal loop circulation)	Test - Leak Test - Pressure Inspection - Visual	Life-Critical
ICD-032	SWME (Spacesuit Water Membrane Evaporator)	Water Tank, Radiator, Pumps (2), Thermal Loop	Tubing (Closed thermal loop), Backup SWME in parallel	Fluid Thermal	Cooling capacity (300W avg), Mass (2kg + 0.5kg backup), Water consumption rate, ΔP	Bidirectional (water flow), Heat rejection out	Test - Performance Test - Thermal Test - Endurance	Life-Critical
ICD-033	LCVG (Liquid Cooling Ventilation Garment)	Water tank (PLSS side via Con-450 & Con-650) Astronaut (Worn)	Quucj disconnect couplings (Con-450 & Con-650)	Fluid Thermal	Flow rate, Temperature regulation (18C-27C), Heat removal, Leak rate	Bidirectional (cooling water loop)	Test - Perfomance Test - Leak Test - Thermal	Life-Critical
ICD-034	Main Solid-State Battery	Avionics Box, Vent fans (3), Pumps (2), Sensors, Radio, WiFi, Loop heat pipe	Power wiring harness/power distribution bus from avionics	Electrical	Capacity (664 W-hr for 8hr EVA) Voltage, Mass (0.9kg) Cycle life (5000 EVA's), Temperature range (-40C to 120C)	Battery → All powered components	Test - Performance Test - Endurance Test - Thermal-Vacuum	Life-Critical
ICD-035	Backup Solid-State Battery	Avionics box, Critical life support systems (O2 Regulators,	Power wiring harness with automatic switching circuit	Electrical	Capacity (emergency reserve), Voltage, Reliability (no	Battery → Critical systems (when activated)	Test - Functional Test - Performance Demonstratio	Life-Critical

		vent fans, sensors, radio)			recharge), Auto-switchover		n - Operational	

Table 2.6.1 Interface Table

3 Crew Systems

3.1 Subsystem Overview

One of the most important subsystems of the PLSS is crew systems. Crew systems serve as the primary interaction between the astronaut and the life support system architecture. This subsystem focuses on maintaining crew health and safety by actively managing the air the astronaut breathes. Our systems include the oxygen tanks, ventilation loop, CO_2 scrubber, trace contaminant control system (TCC), particulate filters, and sensors.

Each of these elements plays a distinct role in the ventilation loop. The oxygen tanks provide the suit pressurization and breathable air, and the ventilation loop circulates this air to remove exhaled gases and contaminants. The CO_2 scrubber and TCC are stored in the same canister, and they remove toxic byproducts from the air which would otherwise accumulate and be dangerous for the astronaut.

The total mass of this subsystem is 17.3 This is 6.8 kg less than the mass of the crew systems architecture on the current PLSS.

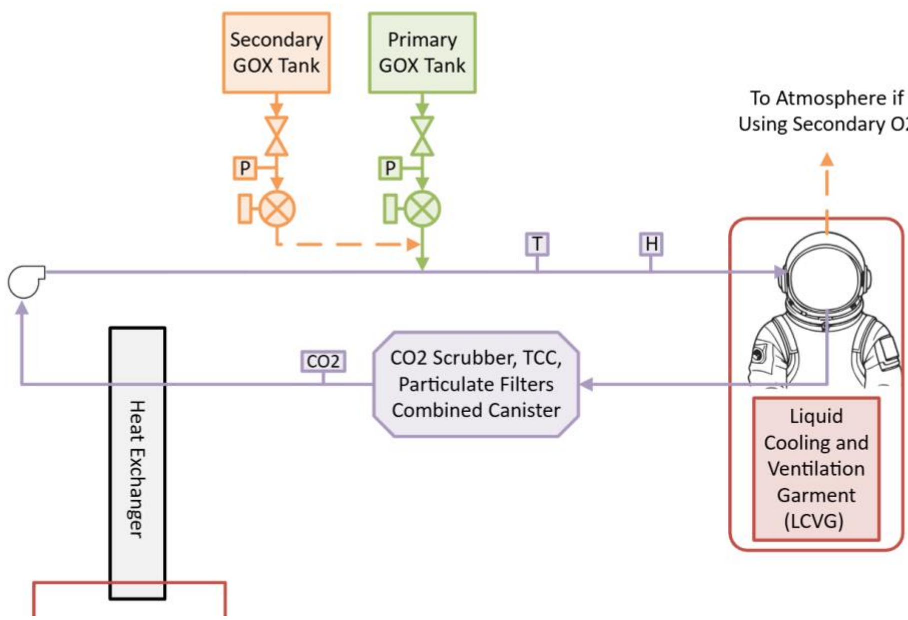

Figure 3.1.1: Crew Systems System Block Diagram

3.2 Oxygen Consumption and Storage System (Maethili Patel)

3.2.1 GOX vs. LOX

Earlier in the design process, one of our largest trade studies involved comparing GOX storage against LOX storage. Since oxygen storage was a major part of PLSS consumables and mass, evaluating both storage options was an important consideration.

The main advantage of LOX storage is higher oxygen density. Compared to high pressure GOX systems, LOX can store the same oxygen mass in much smaller tank volumes. However, LOX systems introduce complexities. LOX requires cryogenic storage, thermal insulation, and vaporization hardware [11]. Maintaining cryogenic temperatures during EVA operation introduces thermal management challenges that would increase overall system complexity and potentially operating risk.

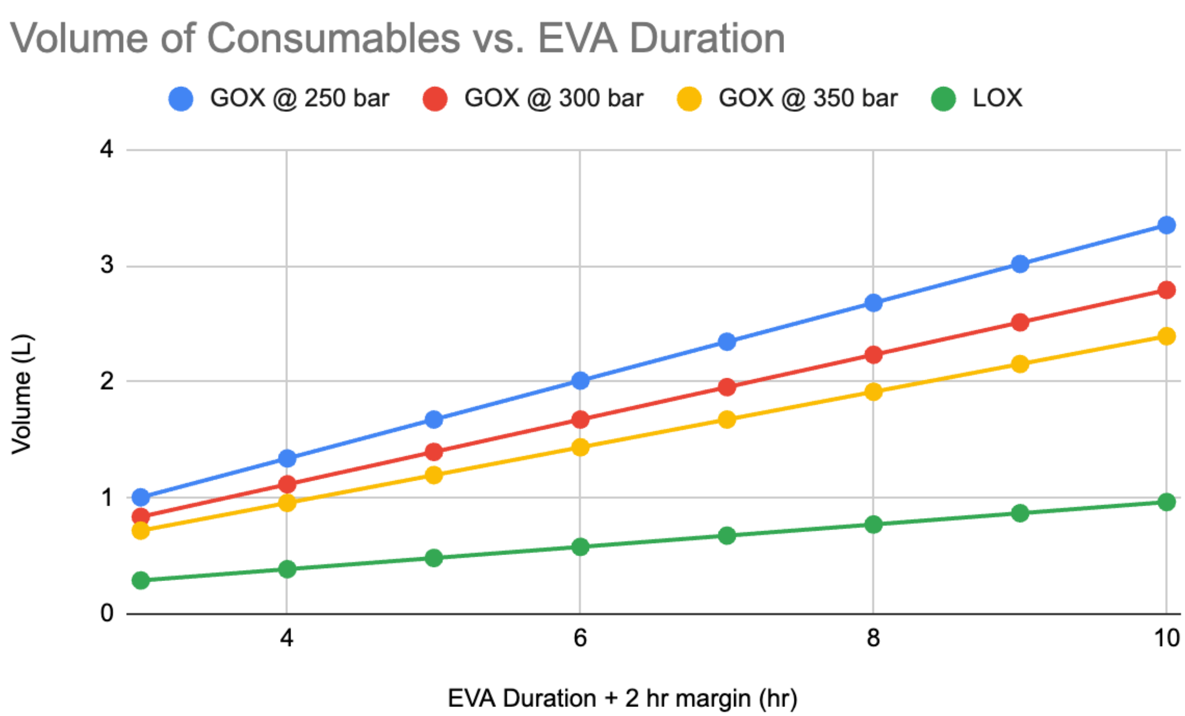

Figure 3.2.1: LOX and GOX Relationship with Volume vs. EVA Duration

GOX storage, while less volumetrically efficient, has several operational advantages. They are mechanically simpler, easier to regulate, and more compatible with many existing PLSS ventilation loop technologies (CO2 scrubber, TCC) [11]. GOX systems also eliminate the need for cryogenic insulation and additional thermal management. Based on this, the final design favored high pressure GOX storage.

3.2.2 Primary and Secondary Oxygen System

The next step was determining how the oxygen consumables would be stored and split. One trade study evaluated whether the emergency reserve should be integrated into the primary tank system or kept completely isolated. While a single tank system would slightly reduce hardware mass and complexity, we chose to keep separate tanks to reduce the risk of accidentally depleting the reserve oxygen. This two-tank system also aligns with existing NASA PLSS design philosophy.

The final design used two separate oxygen tanks. A primary tank was allocated for nominal EVA and a secondary emergency reserve tank. Separating the tanks prevented accidental depletion of the emergency reserve during normal operation.

The primary oxygen tank operates as a partially closed loop system. The secondary tank was designed for emergency purge and abort scenarios. It operates as an open loop configuration. Because emergencies typically cause elevated stress and physical activity for astronauts, the secondary reserve was sized using the peak metabolic rate rather than baseline.

3.2.3 Oxygen Consumption Model

The first step in designing the oxygen system was to determine total oxygen consumption during an EVA. We built a model in Excel to estimate oxygen consumption across different EVA durations and metabolic conditions.

Several assumptions were made to guide the design of this model. The baseline EVA duration was eight hours with an additional two-hour margin on top for pre-breathing and oxygen lost due to leakage. The system also had to support physically demanding tasks like climbing or lifting.

Based on guidance from the NASA review team and xPLSS references, the baseline metabolic rate of the astronaut was modeled at 350 W, with peak activity at 880 W [11]. This metabolic rate was kept consistent throughout all oxygen consumption and tank sizing calculations. Two separate 10-minute periods of peak activity were also included in the calculations for each EVA to better represent realistic astronaut workload conditions.

Oxygen consumption was estimated using the approximation that 1 L $O_2 \approx 20$ kJ metabolic energy [12]. Throughout the model, standard liters (SL) refer to oxygen volume referenced to 1 atm and 20°C.

During an abort scenario, oxygen is supplied directly to the astronaut at peak metabolic rate and at a purge flow rate of approximately 2540 g/hr for a 54-minute return-to-habitat duration [13].

Additional margins were also included in the model. NASA Constellation Space Suit PLSS showed suit leakage between 2-4 g/hr [14]. NASA showed leakage at about 6 g/hr [15]. Taking the higher value of 6 g/hr, we calculated an approximate leakage of about 5% and added that as an additional oxygen consumption margin. See Table 3.2.1 for a list of all variables used in the model.

Variables	**Values**	**Units**	**Notes**
Avg metabolic rate	350.0	W	Given from NASA Team
Peak metabolic rate	880.0	W	Given from NASA Team
EVA duration	10.0	hr	Primary tank covers this full EVA supply (8 hr + 2 hr margin)
Peak metabolic event duration	0.33	hr	2 x 10 min durations = 20 min = 0.3333 hr
Primary leakage fraction	5.0%		Applied to primary EVA supply
Emergency purge flow requirement (CS-6)	5.6	pph O2	From xEMU regulator paper
Emergency purge duration requirement (CS-7)	54.0	min	Time to return to vehicle with purge
O2 energy equivalence	20.0	kJ/SL	1 standard liter O2 ≈ 20 kJ
O2 molar mass	32.0	g/mol	Used for pph → SL conversion
Standard molar volume @ 20°C, 1 atm	24.1	L/mol	Reference volume for standard liters
Grams per pound	453.6	g/lb	Unit conversion constant
O2 mass per standard liter	0.00133	kg/SL	At 20°C and 1 atm

Table 3.2.1: Oxygen Consumption and Tank Sizing Model Variables and Inputs

The oxygen consumables model was created using a set of governing equations that related astronaut metabolic activity to oxygen consumption and gas mass. The equations below summarize the methodology used.

To convert oxygen volume into oxygen mass, the mass of oxygen contained in one standard liter was first determined using the molar mass of oxygen and the standard molar volume at 1 atm and 20°C. This conversion factor was then applied to all oxygen consumables calculations.

$$m_{SL} = \frac{M_{O2}}{V_m} \tag{3.1}$$

Where:

- m_{SL}= oxygen mass per standard liter $\left(\frac{kg}{SL}\right)$
- M_{O2} = molar mass of oxygen$\left(\frac{kg}{mol}\right)$
- V_m = standard molar volume $\left(\frac{SL}{mol}\right)$

Astronaut oxygen consumption was estimated from metabolic power using an energy equivalence relationship between oxygen consumption and metabolic energy. This allowed metabolic rates given in watts to be converted into oxygen flow rates in standard liters per hour.

$$V_{O2} = \frac{Q\cdot_{met}}{E_{O2}} \tag{3.2}$$

Expanded form:

$$V_{O2} = \frac{Q_{met}(W)\ \times 3600}{E_{O2} \times 1000} \tag{3.3}$$

Where:

- $\dot{V}_{O2}$ = oxygen consumption rate$\left(\frac{SL}{hr}\right)$
- Q_{met} = metabolic power $\left(\frac{kJ}{hr}\right)$?
- E_{O2} = oxygen energy equivalence $\left(\frac{kJ}{SL}\right)$

The total primary oxygen demand during EVA operation was modeled as the sum of baseline oxygen consumption and short-duration peak metabolic activity.

$$V_{primary} = \dot{V}_{base} \cdot t_{base} + \dot{V}_{peak} \cdot t_{peak} \tag{3.4}$$

Where:

- $V_{primary}$ = total primary oxygen volume (SL)
- $\dot{V}_{base}$ = baseline oxygen flow rate $\left(\frac{SL}{hr}\right)$
- t_{base} = baseline EVA duration (hr)
- $\dot{V}_{peak}$ = peak oxygen flow rate $\left(\frac{SL}{hr}\right)$
- t_{peak} = cumulative peak activity duration (hr)

An additional oxygen margin was included to account for suit leakage. The required primary oxygen volume was therefore increased by a fixed leakage fraction.

$$V_{req} = V_{primary}(1 + f_{leak}) \tag{3.5}$$

Where:

- V_{req} = required oxygen volume including leakage margin (SL)
- f_{leak} = leakage fraction

Once the total required oxygen volume was determined, the primary oxygen gas mass was calculated using the standard liter mass conversion factor.

$$m_{gas,\,primary} = V_{req} \cdot m_{SL} \tag{3.6}$$

Where:

- $m_{gas,\,primary}$ = primary oxygen gas mass (kg)

The secondary oxygen tank was sized separately because it operates in an open-loop configuration. The purge oxygen demand was calculated using the required purge mass flow rate and purge duration

$$V_{purge} = \frac{\dot{m_{purge}}\, t_{purge}}{m_{SL}} \tag{3.7}$$

Where:

- V_{purge} = oxygen required for purge (SL)
- $\dot{m_{purge}}$ = purge mass flow rate $\left(\frac{SL}{hr}\right)$
- t_{purge} = purge duration (hr)

After determining the required secondary oxygen volume, the corresponding oxygen gas mass was calculated using the same standard liter conversion applied to the primary oxygen system.

$$m_{gas,\,sec} = V_{purge}\, m_{SL} \tag{3.8}$$

Where:

- $m_{gas,\,sec}$ = secondary oxygen gas mass (kg)

Using the inputs provided in Table 3.2.1 and the formulas above, we were able to calculate the oxygen demand for both the primary and secondary tank, as shown in Table 3.2.2 below.

Metric	**Value**	**Units**
Baseline O2 rate	63.0	SL/hr
Peak O2 rate	158.4	SL/hr
Primary tank supply before leakage	682.8	SL
Primary leakage amount	34.1	SL
Primary tank requirement	716.9	SL

Metric	Value	Units
Secondary abort-return demand	158.4	SL
Purge flow in standard liters per hour	1909.5	SL/hr
Secondary purge demand over required duration	1718.6	SL
Secondary tank requirement	1718.6	SL
Total PLSS O2 requirement	2435.5	SL
Primary O2 gas mass	0.954	kg
Secondary O2 gas mass	2.286	kg
Total O2 gas mass	3.240	kg

Table 3.2.2: Oxygen Demand Calculations

The oxygen consumables model became one of the primary design tools used throughout the project and allowed for rapid iteration between different assumptions and variables.

3.3 Oxygen Storage and Inflow Delivery Architecture

3.3.1 Oxygen Tank Sizing (Maethili Patel)

Once oxygen demand was established, the next step was to determine oxygen tank size and mass. Once again, tank sizing calculations were done using standard liters at 1 atm and 20°C combined with scaling relationships derived from 18 existing Luxfer L6X carbon composite type 3 COPVs that are available on the market.

Tank	Pressure (bar)	Diameter (mm)	Length (mm)	Mass (kg)	Water Volume (L)	Air Capacity (SL)
T15A	207	102	371	1.3	2.0	396
T41A	207	155	470	2.9	5.9	1161
T45K	341	137	467	2.9	4.7	1416
T62A	210	173	526	4.1	8.5	1671
T71A	341	175	465	4.4	6.8	2067
T71R	341	175	465	4.4	6.8	2067
T72A	207	198	505	5.3	10.4	2039

Tank	Pressure (bar)	Diameter (mm)	Length (mm)	Mass (kg)	Water Volume (L)	Air Capacity (SL)
T79A	207	196	531	5.6	11.1	2180
T84A	310	150	810	5.7	9.0	2492
T90A	341	150	810	5.7	9.0	2718
T95A	241	198	617	6.9	13.1	2917
T144A	248	201	838	8.6	18.0	4134
T170A	310	206	795	10.3	18.1	5040
T188C	340	206	795	10.2	18.1	5465
T200A	227	257	744	11.4	26.8	5663
T307A	214	239	1295	19.5	43.3	8693
T340A	241	239	1295	19.5	43.3	9656
L930A	345	356	1440	74.8	88.8	27071

Table 3.3.1: Luxfer Tank Dataset

To estimate empty tank mass, the publicly available Luxfer data, as shown in Table 3.3.1, was used as a baseline reference [16]. The tanks used in the dataset covered operating pressures from 200-345 bar, and with it, a power-law regression model that related tank mass to oxygen storage capacity could be developed. The resulting regression relationship is shown in Eq. (3.9).

$$m_{tank} = a \cdot C^b \tag{3.9}$$

Where:

- m_{tank} = empty tank mass (kg)
- $C =$ oxygen storage capacity (SL)
- $a,\ b =$ regression constants derived from Luxfer dataset

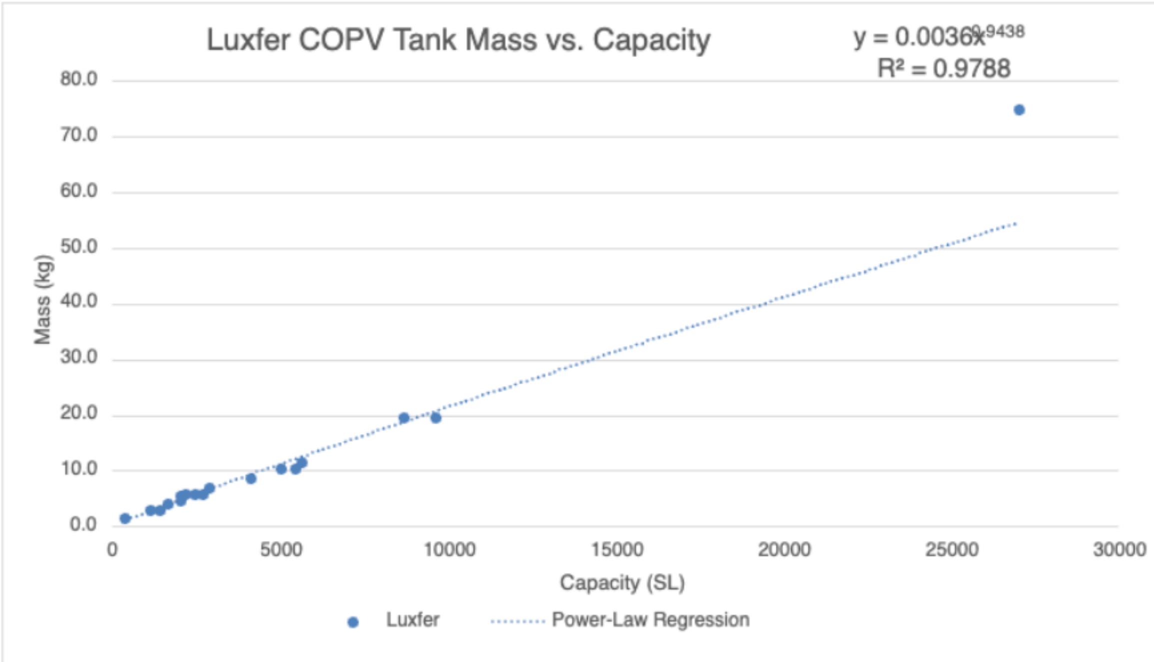

Figure 3.3.1: Power-law fit of tank mass vs. capacity

The regression produced y = $0.0036x^{0.9438}$ and a R^2 value of 0.979, showing strong agreement with the Luxfer dataset.

The model generated two outputs. One was the theoretical tank masses, representing an idealized minimum-mass design. The other was commercial tank masses, based on the closest available Luxfer tank matches. The theoretical output was useful for estimating lower bound system mass, while the commercial output better represented real aerospace hardware constraints like tank geometries and structural safety requirements.

The total oxygen system mass was calculated by combining both oxygen consumables mass and structural tank mass from the primary and secondary systems.

$$m_{total} = m_{gas,\,prim} + m_{gas,sec} + m_{\tan k,\,prim} + m_{\tan k,sec} \tag{3.10}$$

For an 8-hour EVA with a 2-hour margin, the following configuration is shown in the tables below.

Item	Formula / Logic	Value	Units
Primary required capacity	O2 model	716.9	SL
Secondary required capacity	O2 model	1718.6	SL
Primary O2 gas mass	Required primary SL * kg/SL	0.95	kg
Secondary O2 gas mass	Required secondary SL * kg/SL	2.3	kg

Item	Formula / Logic	Value	Units
Total O2 gas mass	Primary + secondary gas	3.2	kg

Table 3.3.2: Total Oxygen Consumables and Gas Mass

The total system oxygen gas mass, as shown in Table 3.3.2, is 3.2 kg which is split between primary and secondary tanks. The secondary tank contains more O_2 because it is sized for emergency use at peak metabolic rate in an open-loop configuration, resulting in faster consumption.

Item	Formula / Logic	Value	Units
Theoretical primary empty tank mass	Power-law regression estimate	1.8	kg
Theoretical secondary empty tank mass	Power-law regression estimate	4.1	kg
Theoretical combined empty tank mass	Primary + secondary regression estimate	5.8	kg
Theoretical primary total mass	Regression empty tank + primary gas	2.7	kg
Theoretical secondary total mass	Regression empty tank + secondary gas	6.3	kg
Theoretical combined total mass	Primary + secondary total	9.1	kg

Table 3.3.3: Theoretical Oxygen Tank and System Masses

Item	Formula / Logic	Value	Units
LUXFER matched primary tank	Part number: T41A Pressure: 207 bar	2.9	kg
LUXFER matched secondary tank	Part number: T72A Pressure: 207 bar	5.3	kg
Commercial combined empty tank mass	LUXFER matched primary tank + matched secondary tank	8.2	kg
Commercial primary total mass	Matched empty tank + primary gas	3.9	kg
Commercial secondary total mass	Matched empty tank + secondary gas	7.6	kg
Commercial combined total mass	Commercial primary + commercial secondary	11.4	kg

Table 3.3.4: Commercial Oxygen Tank and System Masses

Using the regression model, the theoretical primary empty tank mass is 1.8 kg, while the secondary empty tank mass is 4.1 kg. The closest matched Luxfer primary empty tank mass is

2.9 kg. The closest Luxfer secondary empty tank mass is 5.3 kg. Both these tanks store oxygen at a pressure of 207 bar.

The total theoretical oxygen system mass comes out to 9.1 kg, while the total commercial oxygen system mass comes out to 11.4 kg. The difference between the theoretical and commercial values comes from the real-world structural and manufacturing penalties tied to commercial COPVs.

The commercial design compared well with existing NASA PLSS systems. For reference, NASA reports the xPLSS oxygen system mass at approximately 12.2 kg, which is about 7% higher than the commercial estimate of 11.4 kg calculated by our model [8]. Additionally, NASA xEMU oxygen tanks operate near 3000 psi (approximately 207 bar), which matches exactly the storage pressure of 207 bar for our final commercial tanks [16].

Early in the design process, higher pressure tanks near 4500 psi (310 bar) were considered. While increasing storage pressure reduced the tank volume, it increased the tank mass and introduced risks such as fire and explosion. With those risks taken into consideration, the team selected lower operating pressures closer to existing NASA PLSS systems.

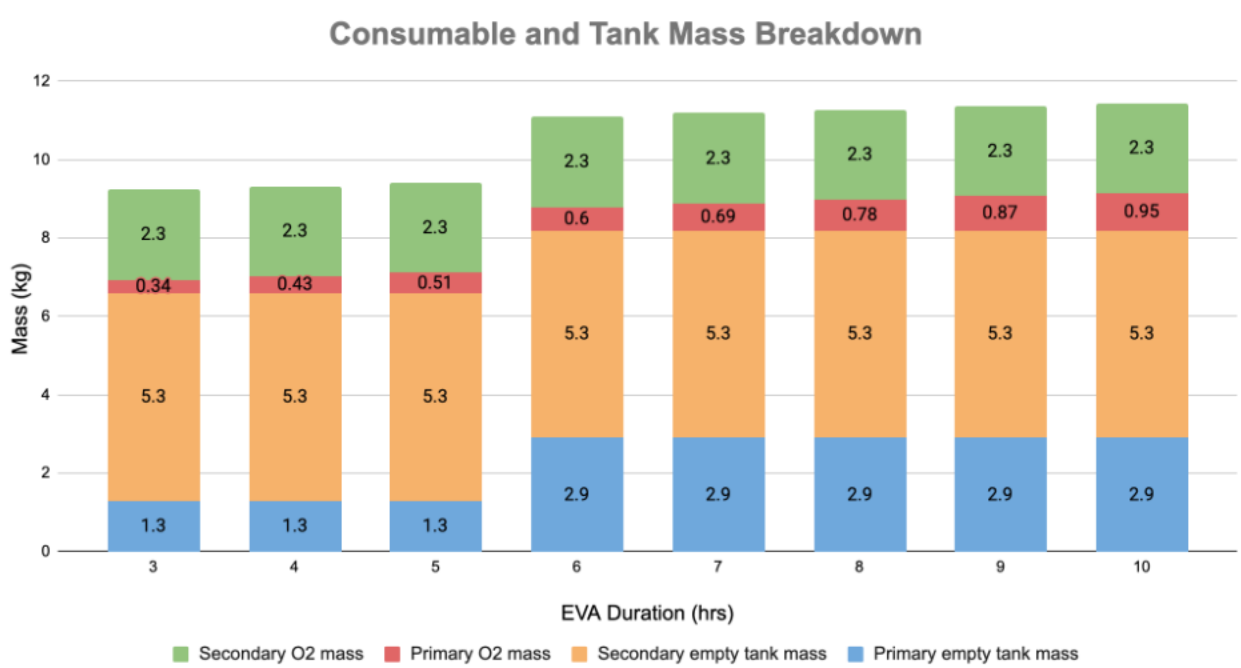

Figure 3.3.2: Oxygen Consumables and Tank Mass Breakdown vs. EVA Duration

Figure 3.3.2 shows the consumable and commercial tank mass breakdown. The model evaluated EVA durations ranging from 1 to 10 hours. Results showed that oxygen consumables mass scaled approximately linearly with EVA duration. This is because the model assumed a constant metabolic rate, so the oxygen consumption scales linearly with time. As the PLSS mass increases, the metabolic rate of the astronaut would also increase. This would introduce nonlinear growth in oxygen demand. Due to limited available data, we could not model this coupling. However, it represents an area for future refinement.

3.3.2 Oxygen Dynamic and Static Component Materials (Sofia Asuncion)

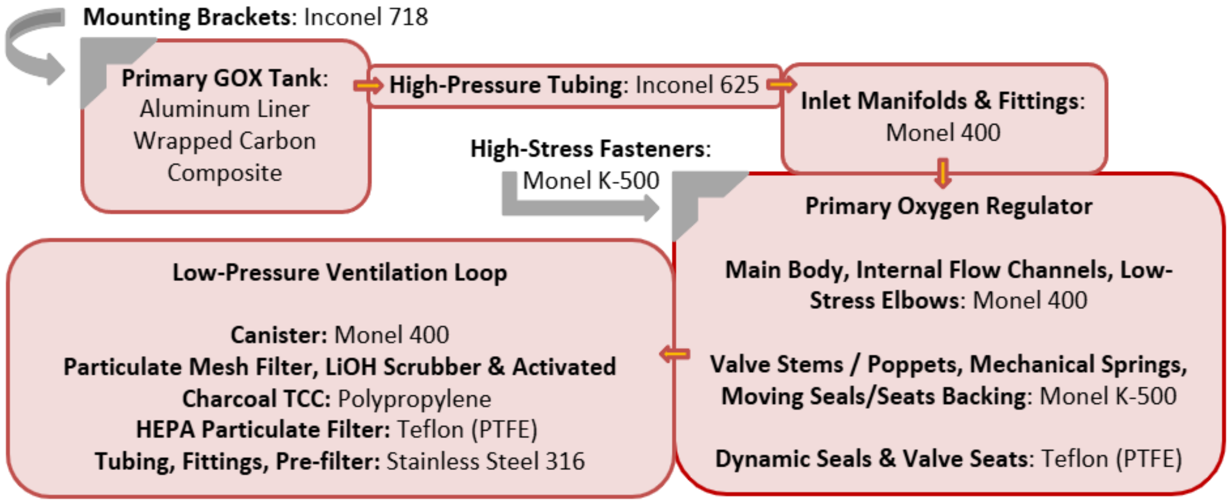

Figure 3.3.3: O_2 Dynamic and Static Component Materials Diagram

Before the high-pressure GOX stored within the primary COPV can safely enter the breathing loop or be utilized by the astronaut, it must transition through a definitive, heavily regulated pressure boundary. This section details the material selection, routing mechanics, and safety architectures governing the upstream tubing, manifolds, and regulation hardware that supply the ventilation loop. The overarching material selection strategy divides the architecture into two distinct safety regimes—a high-pressure superalloy boundary optimized for oxygen-fire and toxic-vapor mitigation, and a low-pressure polymer/steel boundary optimized for astronaut mass reduction and biological compatibility. The primary material candidates evaluated for these upstream loops are summarized below in Table 3.3.5, detailing their raw mechanical properties, thermal behaviors, and relative economic factors.

Material	Density (lb/in^3)	Yield Strength (MPa)	Ultimate Tensile Strength (ksi)	Temperature Range	Dynamic GOX Compatibility	Primary PLSS Use
Aluminum 7075-T73	0.101	73	68	-200°C to 100°C	Poor (High Ignition Risk)	Static Environment (GOX Tank)

Material	Density (lb/in^3)	Yield Strength (MPa)	Ultimate Tensile Strength (ksi)	Temperature Range	Dynamic GOX Compatibility	Primary PLSS Use
Monel 400	0.318	30	75	-150°C to 400°C	Excellent	Bulk, Static Components
Monel K-500	0.305	115	90	-250°C to 538°C	Excellent	Valve Stems, Springs
Inconel 625	0.305	60	119	-196°C to 982°C	Excellent	Tubing and Bellows
Inconel 718	0.297	150	180	-250°C to 700°C	Excellent	Structural Mounting Components
Stainless Steel 316	0.286	290	73	-150°C to 870°C	Moderate (Best for Low-Pressure)	Manifolds, Springs, Tube Fittings
PTFE (Teflon)	0.0795	23	3.5	-200°C to 260°C	Excellent	Seals, Gaskets, O-rings

Table 3.3.5: O_2 Dynamic and Static Component Materials

At high nominal storage pressures, pure oxygen drastically drops the ignition thresholds of surrounding mechanical hardware. A major hazard to the astronaut during surface operations is particle-impact ignition. The kinetic impact of microscopic debris traveling at a high velocity against a tube wall can spark a localized metal fire capable of breaching the backpack garment in fractions of a second.

Choosing materials with exceptionally high yield strengths and fire resistance like Inconel and Monel for these high-velocity segments is a fundamental life-safety decision. With a yield strength range of 60 to 150 ksi, Inconel 718 and 625 are utilized for the rigid high-pressure lines leading away from the COPV tanks. This massive mechanical threshold ensures an extreme safety factor against catastrophic structural burst failures, protecting the astronaut's back from high-energy pressure releases. Monel 400 and Monel K-500, with a yield strength up to 60 ksi, are applied to the primary manifolds, regulator body blocks, and internal spring elements. Monel is virtually non-ignitable in a 100% pure gaseous oxygen environment. Its high thermal conductivity helps rapidly dissipate any localized friction heat or impact energy throughout the metal bulk, preventing localized hot spots from ever reaching ignition temperatures.

The Primary Oxygen Regulator serves as the mechanical gatekeeper to the low-pressure ventilation environment. It steps down the intense, volatile tank storage pressure to a humantolerable breathing regime. The internal dynamic seats and sealing interfaces of this regulator rely on Polytetrafluoroethylene (Teflon) components paired with Monel K-500 poppets. Teflon features a low yield strength of 23 ksi and a tensile strength of 3.5 ksi, offering the mechanical flexibility required to deform slightly under load. This creates a gas-tight seat that avoids slow high-pressure leaking, which would otherwise cause dangerous over-pressurization of the suit helmet.

Once the primary oxygen passes successfully through the regulator, the constraints change entirely. Because the gas is now flowing through a low-pressure regime, the kinetic energy drops and the risk of particle ignition is minimized. This allows the system to shift its design focus toward mass optimization and durability to prevent astronaut fatigue during long-duration EVAs. The tubing routing the freshly regulated oxygen from the regulator outlet down into the main ventilation loop is fabricated from thin-walled Stainless Steel 316. Stainless Steel 316 gives the plumbing lines immense geometric stiffness, ensuring the delivery lines will not bend, crimp, or pinch closed when the astronaut performs dynamic upper-body movements or experiences severe vibrations during surface travel.

3.3.3 Carbon Dioxide Removal (Nandira De Andrade)

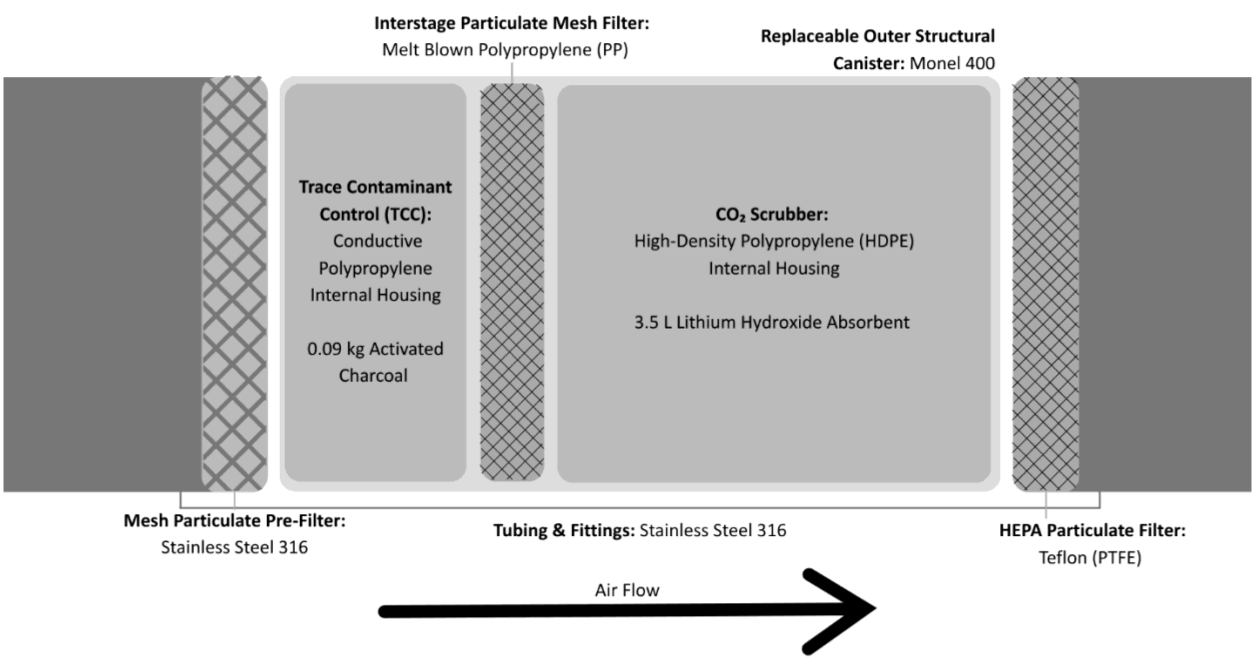

Figure 3.3.4: Diagram of carbon dioxide removal filtration system.

It is vital that the air an astronaut breathes is kept clear of metabolic CO_2, Martian regolith particles, and other trace contaminants. To maintain a safe, recyclable oxygen supply, the ventilation loop utilizes a multi-stage removal system consisting of three distinct particulate filters, a TCC bed, and a primary CO_2 scrubber. To facilitate quick servicing between missions, the TCC, the interstage particulate mesh filter, and the CO_2 scrubber are housed together in a replaceable Monel 400 structural canister that is swapped out after every 8-hour EVA. Meanwhile, the primary mesh particulate pre-filter and the final HEPA particulate filter remain permanently integrated into KOALA's main ventilation loop tubing.

3.3.4 Carbon Dioxide Scrubber (Nandira De Andrade)

Our chosen Carbon Dioxide (CO_2) Removal system is the Lithium Hydroxide (LiOH) CO_2 Scrubber. LiOH, with an average mass of 1.42 kg, removes CO_2 through a chemical reaction between lithium hydroxide and carbon dioxide in the PLSS ventilation loop [120]. The LiOH is housed in a combined canister with our chosen Trace Contaminant Control system and must be replaced after every EVA. Although it is consumable, LiOH is a simple, powerless, and lightweight option that fits the best with our goal of reducing mass [120].

LiOH was selected not only because it is the lowest PLSS mass option, but also because it provides reliable CO_2 removal without requiring additional pumps, valves, or electrical power for regeneration since the scrubber operates passively through chemical absorption. This is especially beneficial for a Mars EVA system where the Mars atmosphere, mass, complexity, and reliability are major design concerns.

	Rapid Cycle Amine	**Lithium Hydroxide**
Avg. Hardware Mass (kg)	7.12	1.42
Volume	9.59 m^3	0.005 m^3
Power	2 W 12 (Peak) W	0 W
Notes	Regenerable, includes humidity	Not regenerable but high efficiency
Needs	Vacuum -> Needs pump/sweep gas, vent flow	Vent flow, minor thermal control, consumables

Table 3.3.6: Table comparing the Rapid Cycle Amine scrubber with the Lithium Hydroxide scrubber

Originally, four different systems were compared: Metal Oxide (MetOx), cryogenic scrubbers, Rapid Cycle Amine (RCA), and Lithium Hydroxide. Since MetOx is the heaviest CO_2 scrubber and our goal is to decrease weight, we did not research this method further [123]. Cryogenic scrubbers work well with liquid oxygen [122]. Since our design uses gaseous oxygen, cryogenic CO_2 scrubbers would not be efficient for the KOALA design. RCA, weighing 7.12 kg, was a feasible choice [120], [121]. Table 3.4.1 shows the comparison between RCA and LiOH.

RCA is regenerable and would not require added scrubber mass per EVA, but as shown in the "Needs" section, a vacuum is ideal for regeneration, which Mars does provide. Without a vacuum, RCA requires either sweep gas or a pump, both of which add mass and make the system less feasible [121].

Originally, RCA with an added pump was selected because its regenerability offered the greatest mass savings over the overall mission. However, further research showed that identifying a lightweight pump capable of reaching below 1 Torr, which is the pressure needed for efficient CO_2 desorption from the swing beds [121], [124]. Without a definitive pump option that satisfied both mass and performance requirements, the design focus shifted from total mission mass reduction to minimizing the mass carried in the PLSS during a single EVA. An RCA system using oxygen sweep gas was also briefly considered, but this approach remains under development and would introduce additional consumable and tubing requirements. Being the lighter consumable system, LiOH becomes a desirable option since it provides the lowest mass carried on the PLSS [120]. Thus, although LiOH is not regenerable, it is less than half the mass of RCA and requires no power, making it the ideal choice.

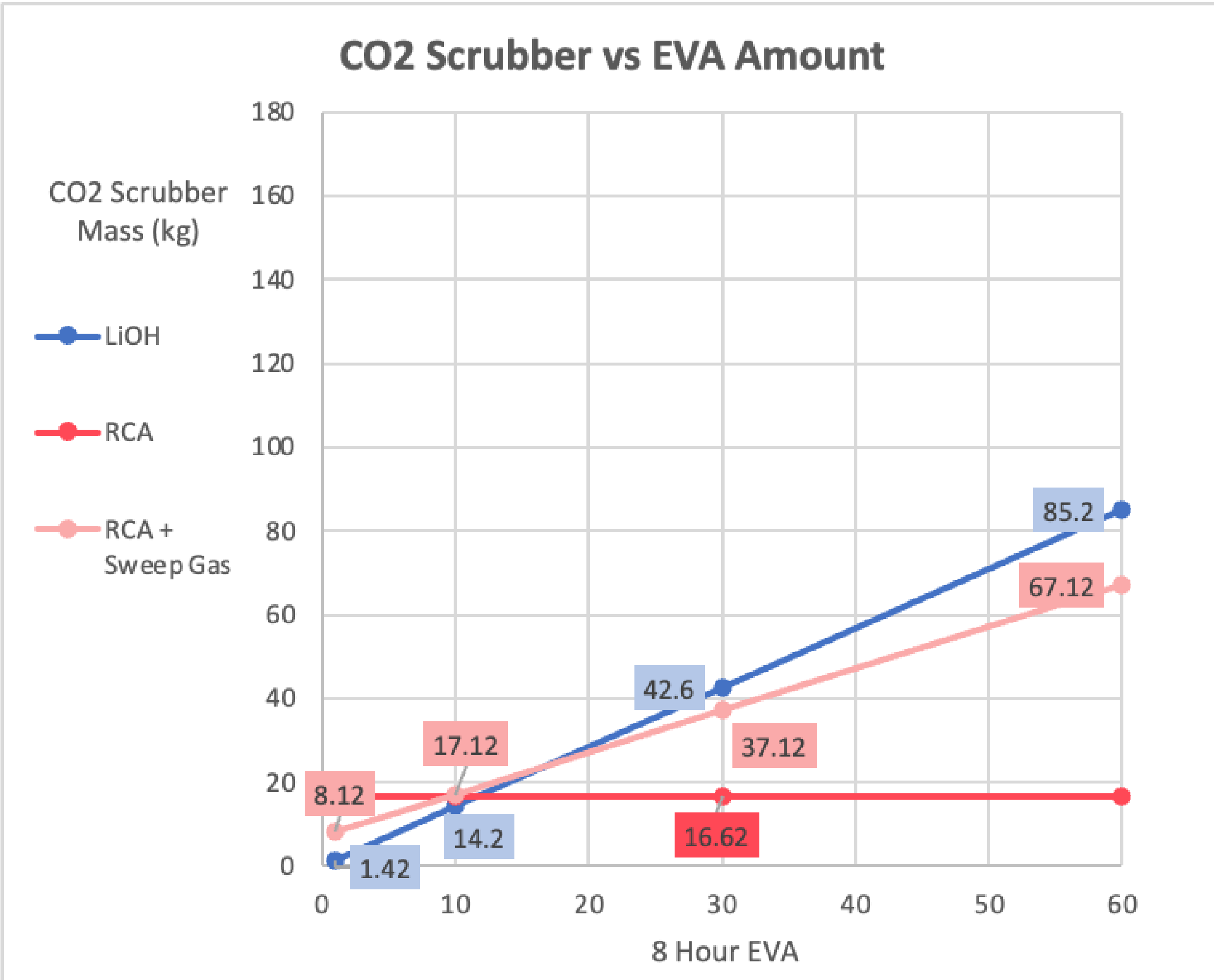

Figure 3.3.5: Graph comparing LiOH, RCA with pump, and RCA with sweep gas over 60, 8-hour EVAs

Figure 3.4.2 compares LiOH at 1.42 kg per EVA, RCA with a 9.5 kg Varian TriScroll pump at a constant 16.62, and RCA with oxygen sweep gas at 1 kg per EVA across 60, 8-hour EVAs [120], [124]. LiOH passes the RCA with the pump at about 12 EVAs and RCA with sweep gas at about 18 EVAs. Given that our priority is low mass for a single EVA, LiOH is the ideal choice for our PLSS.

3.3.5 Trace Contaminant Control (Mihir Miller)

Our chosen TCC system is activated charcoal, also known as Ammonasorb II. We are using it in a combined canister with our CO2 scrubber (Lithium Hydroxide). The TCC is necessary to filter out byproducts, mostly ammonia from perspiration. It is extremely important to regulate the concentration of these byproducts. If ammonia is not filtered out, it can lead to eye and lung irritation.

Our original design choice was using a newer advanced system called Microlith which utilizes small screens coated in sorbents which soak up ammonia from the air. These small screens are packed tightly together and create a turbulent flow which causes the air to come into contact with the screens and thus the sorbent. Additionally, the small meshes stacked on top of each other have a very short length which prevents a boundary layer from forming [9].

The Microlith system is regenerable and piggybacks off the RCA swing bed. Every two minutes a vacuum valve swaps one bed from being exposed to a vacuum to a bed that is being exposed to the air inside of the suit. This system allows for the combined RCA and Microlith system to be regenerable over the course of an 8-hour EVA. When a bed is exposed to the vacuum of space, the pressure difference between the suit (4.3 PSI) and space sucks out the ammonia and other contaminants from the Microlith. This process allows the system to be regenerated [18].

While regenerable systems are ideal, our goal for this project is to reduce the mass of the PLSS as much as possible. As a result, we switched to Lithium Hydroxide as our chosen CO2 scrubber since it is consumable and is much lighter than the RCA. Because of the CO2 scrubber design change, our TCC design was also affected. Without the RCA, the Microlith system would require its own heavy vacuum valves to swap beds every 2-5 minutes [18]. As a result, we switched to activated charcoal as our chosen TCC. Activated charcoal is not regenerable, but when you compare its mass to the standalone Microlith system, it saves the PLSS around 2.3kg. Since activated charcoal is a passive system, it doesn’t require any complex valves which means it carries less risk as a system. The Microlith relies on moving mechanical parts and valves which actuate hundreds of times each EVA. If dust or any contaminants get into these valves, it would ruin the TCC. Activated charcoal (Ammonasorb II) is treated with phosphoric acid so that when the ammonia contacts the pellets, a chemical reaction occurs which binds the ammonia to the pellets and makes sure it isn't released back into the suit [19].

Metrics	**Activated Charcoal**	**Microlith**
Sorbent Mass [kg]	0.09 [10]	0.4 [9]
Hardware/Valve Mass [kg]	0.0	~2.0
Total System Weight [kg]	0.09	~2.4 (requires heavy vacuum valves)
Volume [mL]	150 [10]	787 [9]
Operating Life (EVA hr)	8 [10]	>220 [9]

Metrics	Activated Charcoal	Microlith
Regenerative	Consumable	Regenerable

Table 3.3.7: Table comparing activated charcoal vs Microlith [9],[10]

Table 3.4.2 shows a comparison between activated charcoal and Microlith as a standalone system. Activated charcoal only needs 0.09kg of sorbent for a single 8-hour EVA [19]. In contrast, the Microlith only needs 0.4kg of sorbent mass, but to function independently of the RCA it needs ~2kg of added valve mass due to it needing the swing beds with a vacuum pump. [1]. The activated charcoal also only requires 150 mL [10] of volume compared to the 787mL needed by the Microlith [18].

Since we are putting the activated charcoal in the same canister as the Lithium Hydroxide, there is no added hardware mass for the activated charcoal either. After each 8-hour EVA, the astronaut must replace the LiOH canister. Storing the activated charcoal in the same canister as the LiOH simplifies the maintenance of the suit for the astronauts. If we had the TCC in a separate canister, the astronauts would have to remove and replace multiple different cartridges after each EVA.

Something else to note, however, is that the actual sorbent mass of activated charcoal needed for an 8-hour EVA is only 0.03kg. If we put 0.03kg of sorbent into the canister, the bed depth would not be large enough for all the air to come into contact with the pellets. The air would move through the bed too quickly, and the ammonia molecules would not react with the pellets. As a result, 0.09kg of activated charcoal is necessary to have a dense bed of pellets. This forces the air to come into contact with the activated charcoal long enough to react with the ammonia [19].

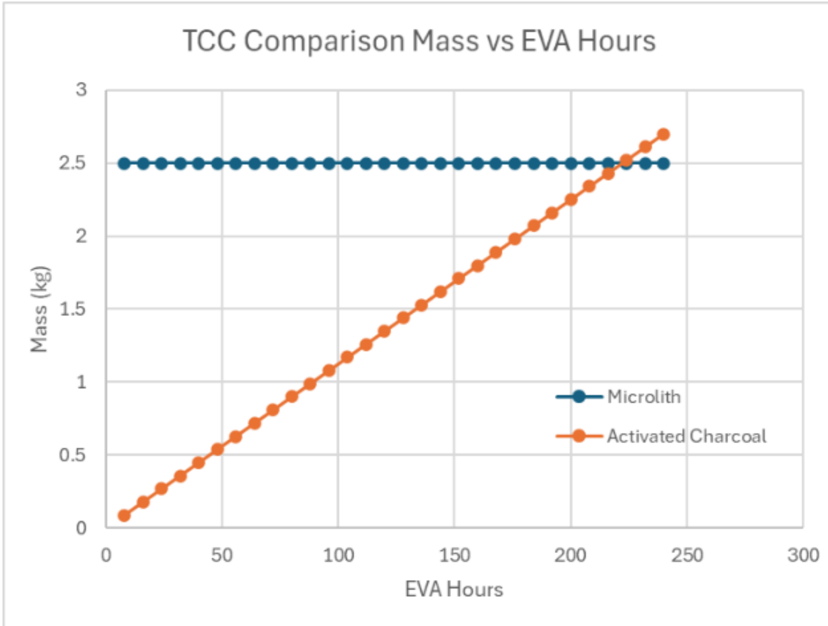

Figure 3.3.6: Graph comparing the mass of Microlith and activated charcoal over the course of 250 EVA Hours

Above is a graph comparing the mass between Microlith and activated charcoal from a mission perspective. We can see that the mass of activated charcoal increases linearly with each 8-hour EVA, whereas the Microlith stays constant (since it is regenerable). Our mission goal is hitting 60 8-hour EVAs every month, and we can see that we get a mass crossover at around ~240 EVA hours, which is 30 8-hour EVAs. Since each 8-hour EVA needs 0.09kg of activated charcoal, that leaves us with an additional mass cost of 2.7kg per month compared to the Microlith.

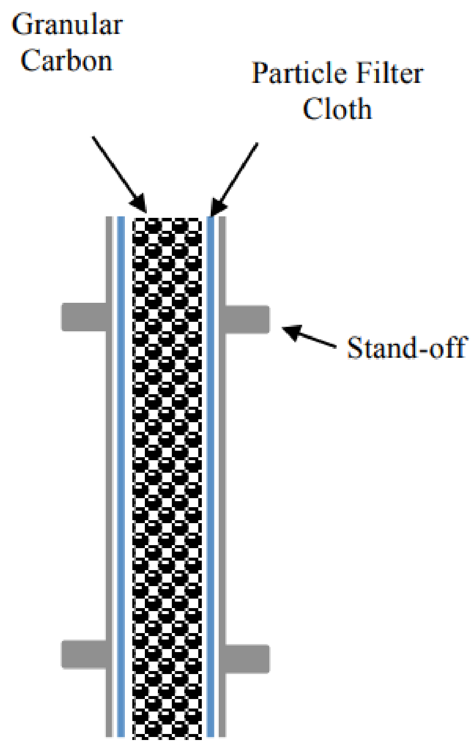

Figure 3.3.7: Cross section of activated charcoal inside the TCC canister [19]

The above image shows a cross section of a TCC canister with activated charcoal. We can see the housing on the outer edge in gray and then there is a particle filter cloth that separates the granular carbon from the wall of the canister. The pellets are packed tightly together and during high vibration loads, the pellets can rub against the canister walls and break down into dust. The particle filter cloth acts as a physical barrier between the pellets and the canister wall so that dust is minimized.

As stated earlier, our goal is to reduce the PLSS mass as much as possible, and by using activated charcoal we are reducing the PLSS mass by 2.3kg compared to a regenerable system such as the Microlith.

3.3.6 Particulate Filters (Sofia Asuncion)

The containment and elimination of particulate matter within the KOALA ventilation loop ensure both astronaut health and system-wide operational longevity. In a closed-loop spacesuit environment, particulates originate from both internal metabolic actions and external environmental infiltration. To systematically manage these risks, the filtration architecture incorporates a multi-stage approach featuring three distinct particulate filters strategically positioned around the chemical beds. Each filter is uniquely fitted for its local thermal, chemical, and mechanical environment, as summarized in the system material trade-study (Table 3.5.3).

	PTFE (Teflon)	**Stainless Steel 316**	**Polypropylene (PP)**
Density [kg/m³]	2200	8000	900
Max Temperature [°C]	260	870	80
Assembly Method	Bolted		Fusion Welded
Additional Material Needed	Requires fasteners made of Monel K-500 (8.44 g/cm³) = 0.045 kg to 0.065kg per filter assembly		None
Notes	High chemical stability in the presence of LiOH and oxidative Martian perchlorates; Hydrophobic	Highest Young's Modulus; Greatest strength against Martian temperature swing	Enables a fully-welded, leak-proof assembly, eliminating leak paths and mass of traditional mechanical fasteners

Table 3.3.8: Table comparing materials (Teflon, stainless steel, polypropylene) for particulate filters.

As depicted in Figure 3.4.1, the polluted air returning from the suit cabin first passes through the primary mesh particulate pre-filter. This component serves as the first line of defense and is designed to capture macro-sized debris discarded during an EVA, such as human hair, skin flakes, loose fibers from the LCVG, and ambient environmental regolith dust that may have infiltrated during suit ingress or egress operations.

Because this filter directly interfaces with the high-velocity return flow from the suit, it experiences constant aerodynamic drag and cyclic pressure fluctuations. Consequently, the mesh must maintain its structural shape without bowing or tearing over the entire operational lifespan of the KOALA system. To satisfy these structural constraints, Stainless Steel 316 was selected for the pre-filter screen. Stainless Steel 316 exhibits the highest Young's Modulus among the candidate materials, providing maximum geometric stiffness and tensile strength. This high modulus prevents micro-yielding or wire displacement under structural loads. Additionally, its maximum temperature rating of 870°C ensures total structural immunity to the intense, localized thermal swings characteristic of the Martian environment. The pre-filter is integrated into the permanent PLSS ventilation loop via a bolted assembly method. To mitigate the risk of galvanic corrosion between the steel mesh and the surrounding metallic plumbing, high-strength Monel K-500 fasteners (with a density of 8.44 g/cm^3) are utilized. This adds a nominal, predictable mass penalty of 0.045 kg to 0.065 kg per filter assembly, which is a justified trade-off for a permanent, high-reliability structural fixture.

Following the TCC bed, the gas stream encounters the interstage particulate mesh filter. The primary functional objective of this layer is to trap migrating charcoal dust generated by the physical attrition and vibration of the upstream activated charcoal granules.

Without this intermediate layer of filtration, carbon fines would escape the TCC and directly penetrate the downstream CO_2 scrubber bed. If fine charcoal dust were allowed to combine with the LiOH absorbent matrix, it would coat the active chemical surfaces, rapidly reducing the available surface area for gas-solid absorption. This poisoning of the bed would induce premature CO_2 breakthrough, endangering the astronaut well before the nominal 8-hour window. Furthermore, interstitial charcoal dust aggregation would compromise the gas flow paths, causing a severe pressure drop across the bed that would overload the ventilation fan.

Because this interstage filter is embedded directly inside the consumable Monel 400 canister, it is discarded and replaced after every 8-hour EVA. This specific operational lifecycle allows engineers to bypass long-term material fatigue constraints and utilize melt-blown polypropylene (PP). Polypropylene features a light density of only 900 kg/m^3, significantly minimizing the mass of the deployable canister.

Thermal management is a critical factor for this stage. The downstream exothermic absorption of CO_2 by the LiOH bed generates substantial heat, raising the local ventilation air temperature to a peak of approximately 51.67°C as it leaves the scrubber. While polypropylene possesses a relatively low maximum temperature threshold of 80°C, it retains sufficient structural margin against the 51.67°C reaction heat. As a thermoplastic polymer, polypropylene is inherently susceptible to structural deformation if exposed to prolonged load cycles over a long span of time. However, because it is safely enclosed within the short-duration, single-use consumable canister, the risk of long-term creep deformation is entirely neutralized.

A major manufacturing advantage of choosing polypropylene is its compatibility with fusion welding. The interstage filter can be thermally welded directly to the internal conductive polypropylene TCC housing structure. This process requires zero additional materials or fasteners, yielding a completely seamless, leak-proof assembly that eliminates both physical bypass leak paths and the parasitic mass associated with traditional mechanical fastening hardware.

The final stage of the particulate filtration stack is the HEPA filter, positioned immediately downstream of the CO_2 scrubber. The chemical neutralization of carbon dioxide within the scrubber relies on the following exothermic reaction:

$$2\ LiOH\ (s) + CO_2\ (g) \rightarrow Li_2CO_3\ (s) + H_2O\ (g)$$

As an inherent byproduct of this chemical reaction, a significant volume of moisture (H_2O vapor) is generated and swept into the exiting gas stream alongside highly caustic, microscopic LiOH and lithium carbonate chemical dust. If an astronaut were to inhale these, it would result in acute chemical burns to the respiratory tract.

The HEPA filter is specifically rated to capture 99.97% of these microscopic particulates down to 0.3 microns. PTFE, commercially known as Teflon, was selected as the substrate membrane for this critical application. Teflon possesses extreme chemical stability and inertness, allowing it to withstand prolonged contact with highly basic LiOH particulates without polymer degradation. It is immune to the oxidative effects of ambient Martian perchlorates that may enter the system loop. A defining characteristic of Teflon is its exceptional hydrophobicity. Because the air stream leaving the scrubber is saturated with warm reaction moisture, a standard hydrophilic filter material would act as a condensation site. This condensation would lead to water accumulation within the filter matrix, causing a restriction of airflow, choking the ventilation loop. Teflon's hydrophobic nature prevents liquid water retention, forcing moisture to remain in the vapor phase until it safely reaches the downstream moisture separator.

Teflon exhibits a robust density of 2200 kg/m³ and a high thermal threshold of 260°C, ensuring that it remains completely unaffected by the 51.67°C scrubber discharge air. Similar to the primary pre-filter, the HEPA filter is a permanent fixture attached directly to the main ventilation tubing loop and is integrated via a bolted flange. This interface utilizes Monel K-500 fasteners, adding a mass of 0.045 kg to 0.065 kg to guarantee gas-tight sealing and structural integrity across dozens of mission cycles. With the air stripped of macro-particles, chemical dust, organic volatiles, and toxic CO_2, the recycled oxygen stream is fully conditioned and safe to be consumed by the astronaut once again.

3.4 Sensing (Ishan Dutta)

3.4.1 Sensor Requirements

A PLSS has variety of different sensors to monitor the state of the system and provide feedback to the astronaut. The astronaut's metabolism deems it necessary for certain requirements for optimal working conditions for long periods of time. Thus, it is important to establish sensor requirements based on both the astronaut's metabolic needs and system requirements.

As stated in section 2.3.1, our requirements include maintaining suit pressure to 4.3 psia, maintaining suit temperature to a range of 18°C–27°C, delivering oxygen at a partial pressure range of 2.8–3.0 psia, maintaining the CO_2 partial pressure to below 0.06 psia, and maintaining a relative humidity within the range of 25%–75%. Each of these system requirements are compliant with NASA's Spaceflight Human-Standard System which details rationales for each of them [20].

NASA-STD-3001 identifies normoxic oxygen partial pressures near 2.8–3.0 psia, comparable to Earth-normal physiological conditions. However, NASA operates their EMU at 4.3 psia for a balance of suit maneuverability and safe ppO_2. Due to this design decision pressure and thus partial pressure for oxygen will be held at a nominal value of 4.3 psia at 100% O_2. For oxygen partial pressures, the standard details that exceeding beyond 15.30 psia for 6–9 hours can lead to health effects from hyperoxia. The limit gives enough room to allow DCS treatment. On the other hand, below 2.46 psia can lead to effects from hypoxia.

The average relative humidity exposure limits and temperature limits for the oxygen loop are designed according to an indefinite EVA time. Due to perspiration and exhalation, humidity levels can be dynamic. Oxygen environments that are too dry lead to dysfunctional mucous membranes and static electricity buildup and environments that are too humid affect evaporation of perspiration and can allow for increased formation of condensation. Formation of condensation can cause issues with sensors within the oxygen loop such as the CO_2 sensor in the ISS EMU [21]. The temperature must be conserved at these ranges simply to prevent thermal discomfort from hyperthermia (overheating) or hypothermia.

Exhalation by the astronaut also increases CO_2 levels in the breathing loop. Excessive amounts will lead to hypercapnia which can lead to various health issues including shortness of breath, drowsiness, headaches, and extreme amounts can cause death [22].

Additionally, the thermal loops will require a wet application temperature sensor to keep track of temperature alterations. The temperature range requirement within this thermal loop will be from 1.7°C–38°C [23].

With these metabolic ranges and their effects on the astronaut in mind, it establishes the importance of monitoring these quantities and allows us to choose sensors based on metabolic requirements. As such, the sensors required for this design will include O_2 sensors, humidity sensors, CO_2 sensors, dry and wet application temperature sensors, and pressure sensors.

3.4.2 Sensor Array

Due to the variety of different sensors required particularly for the ventilation loop, scattered locations for each sensor can make them difficult to wire and maintain. A sensor array is a condensed solution that can fulfill all the sensing requirements while simultaneously being easier to manage. Additionally, on the xEMU (Extravehicular Mobility Unit), a single Nondispersive Infrared (NDIR) sensor which encompasses a large volume (2.3 in. x 2.2 in. x 6.1 in) and consumes 2 W on its own. The proposed M-PALSS (Multi-Parameter Astronaut Life Support Sensor) design incorporates all the required sensors excluding the temperature sensors while encompassing a smaller volume and being more power efficient.

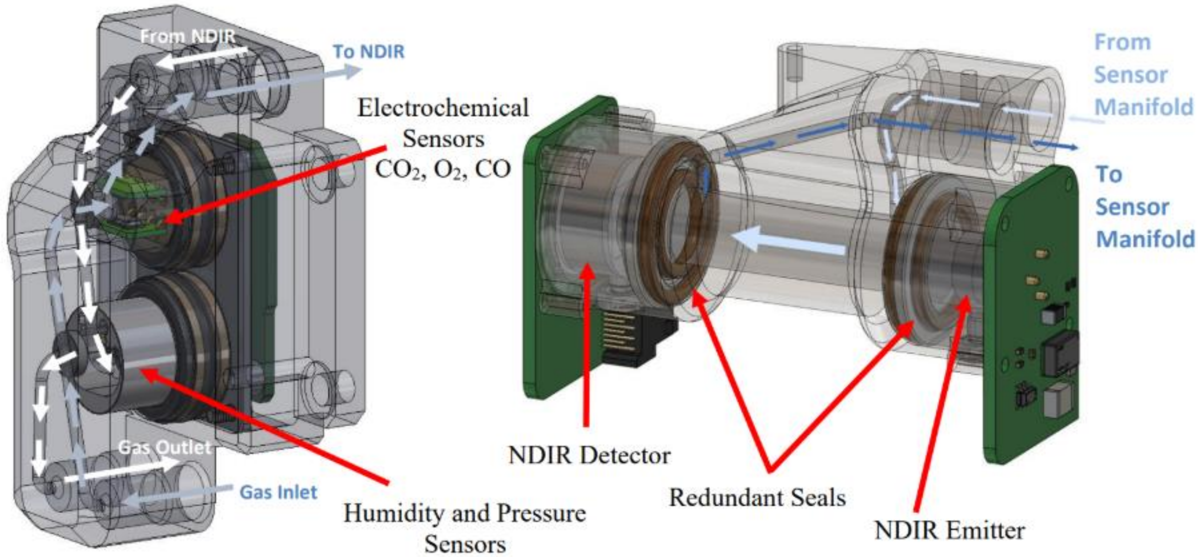

Figure 3.4.1: On the left is displayed the gas inlet and outlet of M-PALSS to demonstrate how it will be mounted on the system. Both images display the locations of the various sensors on the module. [24]

The M-PALSS is composed of electrochemical microsensors for O_2, CO_2, and CO, a capacitive humidity sensor, and piezoresistive pressure sensor, and an NDIR CO_2 sensor. The NDIR sensors emit infrared wavelengths across air with a receptacle on the other side. CO_2 absorbs the beams, so the more there is, the more are absorbed. These sensors are long lasting, efficient due to their ability to isolate CO_2 readings, drift less than electrochemical (measures signal via chemical reaction) and Metal Oxide Semiconductor (MOS) sensors (measure changes in resistance across a reactive semiconductor) [24]. Piezoresistive sensors analyze the change in resistance in a material because of mechanical stress/strain [25]. They are compact and sensitive making them a suitable option for pressure sensing in this use case. Finally, humidity sensors primarily come in the forms of capacitive, resistive, and thermally conductive [26]. Thermally conductive humidity sensors commonly use dry nitrogen for their applications which adds a layer of complexity to the system. Resistive humidity sensors are sensitive to contaminants leaving capacitive humidity sensors which can detect a wide measurement range of relative humidity (RH), provide stable results over a long usage period, and can measure RH from 0–100%. The M-PALSS sensor array uses optimal sensors that meet the sensor requirements.

The operating range for the O_2 sensor was 0-100% with a ±1% uncertainty, 0–30 mmHg (0–0.58 psia) with a ±0.3 mmHg (~0.006 psia) uncertainty for the NDIR sensor, 0-95% for the RH sensor, and 3.5 to 25 psia range for the pressure sensor. Thus, all of the sensors meet the sensing range requirements.

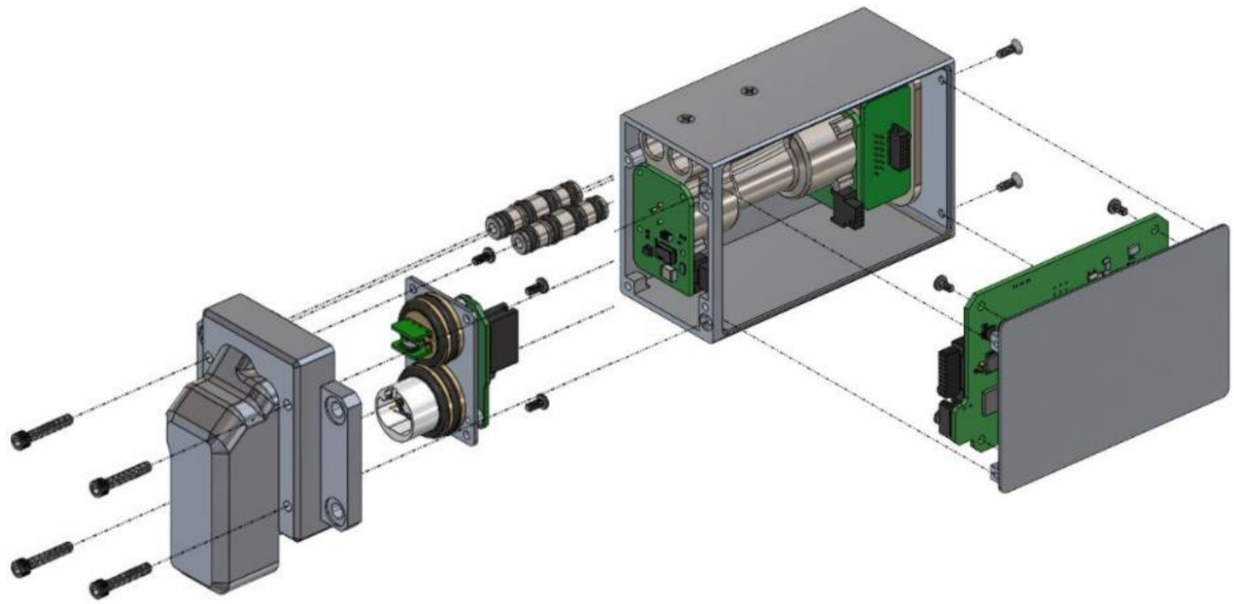

Figure 3.4.2: Exploded view of M-PALSS. [24]

The M-PALSS in total as a system occupied 1.5 in x 2.2 in x 4.6 in (3.8 cm x 5.6 cm x 11.7 cm) which is 15.2 in^3 (250 cm^3). This is ~51% reduction in volume from the original NDIR CO_2 design in the xEMU. It also achieves <2.5W of power, which although is larger than the 2W NDIR CO_2 design in the xEMU, that design does not account for all the additional sensors which fulfill the sensor requirements. Initially we believed that we required this sensor array for the primary and auxiliary oxygen loops, however the main sensing capabilities can be handled in the ventilation loop, meaning only 1 unit of this system will be required to fulfill the requirements of the full system.

Redacted due to Export Control/CUI requirements.

Figure 3.4.3: PLSS 1.0 System Schematic. [27]

According to the PLSS 1.0 system schematic, 4 additional pressure sensors will be required for both the primary and auxiliary oxygen loops, so 8 additional piezoresistive pressure sensors will be required in addition to the required amount for the M-PALSS [27].

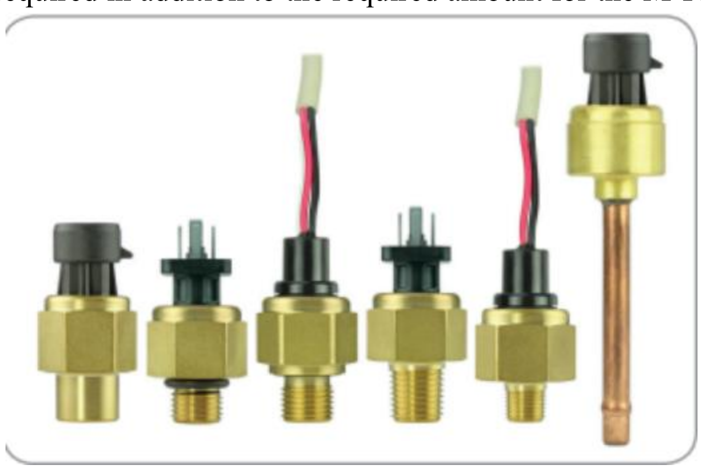

Figure 3.4.4: Honeywell PX3 piezoresistive wet applications sensor. [28]

In addition to the dry application pressure sensors, we will require 3 additional wet application piezoresistive sensors for the supply and return radiator manifold as well as a local pressure sensor in the SWME [27]. To meet that requirement, we use Honeywell's PX3 which is a piezoresistive as an example sensor with a pressure range of 15–700 psia for analysis [28].

3.4.3 Temperature Sensors

The temperature sensing requirements require both wet and dry capabilities for the gaseous oxygen/ventilation and liquid thermal loops. Types of temperature sensors include Resistance Temperature Detectors (RTDs), Thermistors, Thermocouples, and Semiconductor-based sensors [29]. RTDs change the resistance of the RTD element with temperature. Platinum RTDs tend to be the most accurate temperature sensors at the sacrifice of cost and tend to come in the 100Ω and 1000Ω variations. As implied in the name, the resistance is synonymous with the precision of the sensor, meaning 1000Ω PRTDs are 10x more precise than 100Ω variations. They come in 2, 3, and 4 wire configurations with 4-wire being the most accurate. Thermistors also have resistance that vary with temperature, but they require correction for accurate data and are less accurate. Thermocouples joint two dissimilar metal wires, and the voltage change between the two metals are proportional to change in temperature. Unlike PRTDs, they have a quick response time and a wider operating temperature range, however they lack accuracy. Semiconductor-based sensors use identical temperature-sensitive diodes and monitor temperature changes via voltage change. Although they have a linear relationship, they are the most inaccurate.

For the applications of the PLSS, higher accuracy is more desirable to response time for both the gaseous and liquid loops, so a 4-wire 1000Ω PRTD would be the best possible option. Industrial grade PRTDs are very accessible and options for dry and wet applications are shown in Figures 3.4.5 and 3.4.6. In total, 3 dry PRTDs are required for the primary, auxiliary, and ventilation loops and 2 wet PRTDs are required for the thermal control loop and Spacesuit Water Membrane Evaporator (SWME) [27].

Figure or Table containing sensitive information, or possible unauthorized copyright information has been removed.

Figure 3.4.5: Example of 4-wire 1000Ω PRTD for dry applications [30]

Figure or Table containing sensitive information, or possible unauthorized copyright information has been removed.

Figure 3.4.6: Example of 4-wire 1000Ω PRTD for dry applications [31]

3.5 Fans (Ishan Dutta)

In order to generate the flow rate within the ventilation loop, our design must incorporate fans. The setpoint of the flow rate must be 6 ACFM (Actual Cubic Feet per Minute) which is a figure generated through studies that evaluated the necessary volumetric flow rate required for CO_2 washout as well as to prevent moisture condensation on the helmet's faceplate[32]. Additionally, the air must be kept at 4.3 psia according to the pressure requirements.

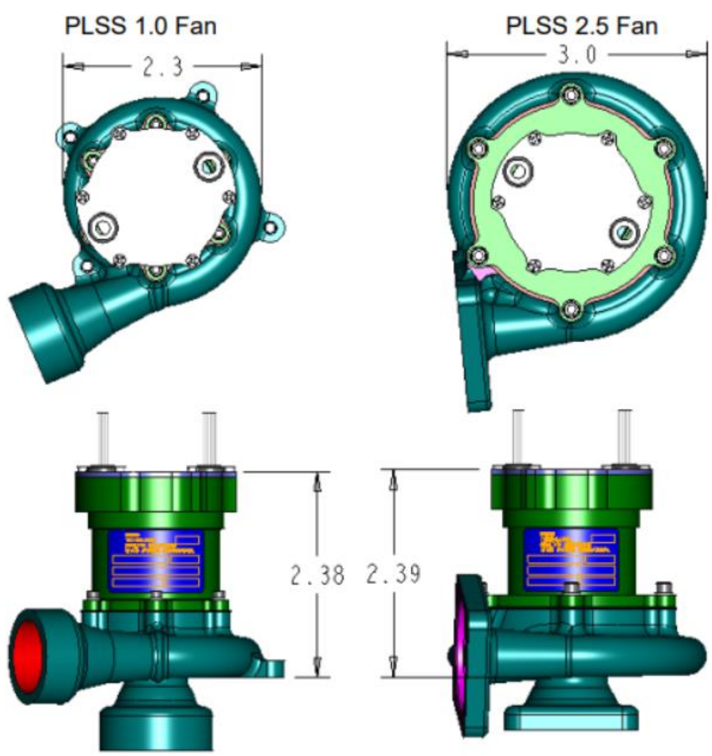

Figure 3.5.1: Comparison between original fan and revised fan for PLSS 2.5 [28]

The PLSS 1.0 fan had a nominal design point of 4.7 ACFM at 4.3 psia which would not meet the current fan requirements. NASA and Hamilton Sundstrand Space Systems as a result developed a more finalized fan design for the PLSS 2.5 [28]. Two designs were developed, one being an open impeller design (blades with no sidewalls) and the other being a shrouded impeller design. The open impeller design was 6% more efficient than the shrouded impeller design, so the open impeller design is the design we will implement. The power draw ended up being 13.3W at the operating speed of 36,690 rpm for 6 ACFM at 4.3 psia. Our design will incorporate 2 units with 1 serving as a backup.

3.6 Pumps (Ishan Dutta)

To create flow within the thermal control loop, the PLSS also requires pumps. According to NASA's Crew and Thermal Systems Division, the desired nominal flow rate is 200±10 lbm/hr (91±4.5 kg/hr) with an expected pressure drop of 6 psid [34]. It is also expected to have a range of 65–225 lbm/hr.

Figure 3.6.1: Original PLSS pump prototype of which the new prototype was based on. [34]

A prototype was designed by Hamilton Sundstrand, Cascon, and NASA for the Advanced Portable Life Support System APLSS [34]. Based on this, a new prototype was developed to improve upon the initial design. Both the original and the new design were able to meet the requirements as well as operate in various other conditions. It was tested at 2000, 3000, and 4000 rpm at a pressure differential range of 0–20 psid and was able to keep a relatively constant mass flow rate (~100, ~160, and ~225 lbm/hr). This also exhibits the pump's ability to function at the desired operating range. Our design will incorporate 2 pumps with an additional one for redundancy with each being 13cm x 4.5cm x 1.7cm with a power consumption of 15W.

3.7 Pressure Regulator (POR & SOR) (Ishan Dutta)

The ability to regulate the oxygen that the astronaut breathes not only keeps the pressure at a nominal 4.3 psia but also gives the astronaut the ability to perform prebreathing, post EVA airlock operations, and decompression sickness (DC) treatment [13]. These pressure regulators would be in the primary oxygen loop as the Primary Oxygen Regulator (POR) and the auxiliary oxygen loop as the Secondary Oxygen Regulator (SOR). Only recently has there been a redesign of this system undergoing iterations up until the xEMU which includes two stages, digital actuation, and pressure sensing.

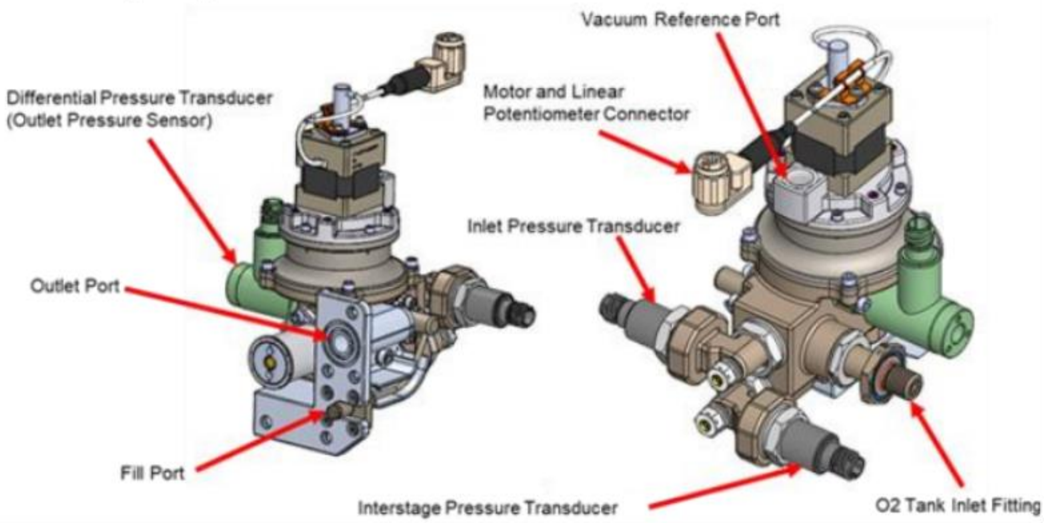

Figure 3.7.1: Pressure Regulator labelled diagram [13]

The two stages are essentially two regulators where the first one feeds the second regulator. If the first one fails, the second one can take over since they can both meet the performance requirements. If the second one were to fail, then the first stage can still prevent over-pressurization. The first stage also reduces the pressure in the range of 250–3,750 psia down to 200±40 psia and the second stage regulates it even further to 0-8.2 psid. As such, this two-stage design adds redundancy, safety, and additional efficiency. The design features for the xEMU pressure regulators include a Maximum Expected Operating Pressure (MEOP) of 3,750 psia, a flowrate of up to 5.6 lbm/hr, and additional features including filtration and position feedback between 0–8.2 psid via the linear actuator operated by the stepper. It also contains pressure sensors which are rated to 6000 psia which are above the rated pressure range in case of failure.

3.8 Temperature Control Valve (TCV) (Ishan Dutta)

The Thermal Control Valve (TCV) is another critical instrument in the PLSS. The main functionality is to control the flow of coolant to the Liquid Cooling and Ventilation Garment which is what the astronaut wears to cool themselves down from the buildup of metabolic heat within the suit. The design requirements for this device include minimizing leakage rate to 4 cm^3/min since astronauts only began to notice a difference beyond this rate [8]. The design requirements also revolved around the shortcomings of linear valve designs which were used in previous PLSS designs. Linear designs use an actuator to open and shut to create a metal-on-metal seal. This design led to issues including valve sticking due to stalling the linear actuator to keep the seal shut and non-linear flow control.

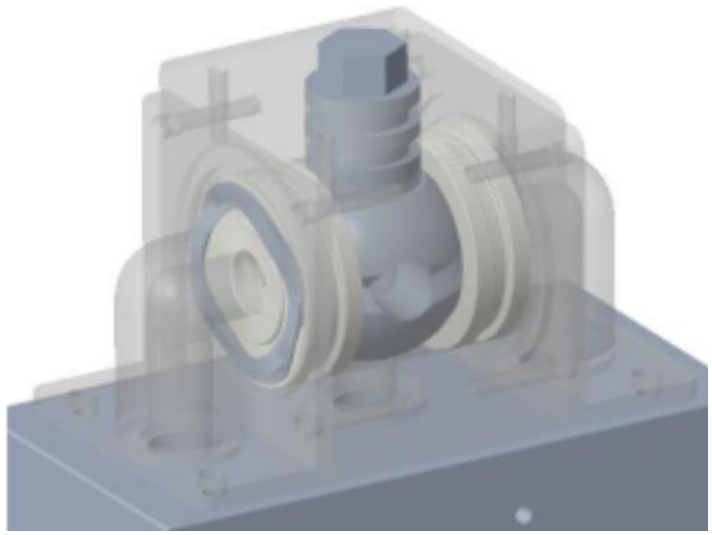

Figure 3.8.1: Transparent view of ball valve assembly [13]

Rotational valve designs a potential solution which can mitigate these issues. The proposed design is a ball valve design which does not stall its actuator but rotates it to control the flow rate. Due to the hole going through the center, the more it rotates, the volume is exposed for the liquid to pour through, thus allowing the valve to control flow rate. Due to this, it avoids stalling the motor by pressing it into anything causing stalling. This design also includes a Teflon ball on a metal seal. Due to Teflon's hydrophobic qualities, this allows the design to minimize leakage rate allowing it to stay below 4 cm^3/min. Additionally, due to the orifice geometry around the orifice of the Teflon ball, the flow rate was much more linear than that of the standard linear actuating design.

3.9 Analysis and Discussion of PLSS Instrumentation (Ishan Dutta)

Information on the specifics for most of the instrumentation (sensors, actuators, valves, regulators, etc.) is limited including the information required for a cost analysis. From studies gathered, preliminary power, mass, and volume analyses can be conducted with all of the discussed instrumentation. Future work will include more comprehensive designs for each instrument as well as further research into gauges and valve designs including check, solenoid, and release valves.

Sensor/Actuator	Power (W)	Mass (kg)	Dimensions (cm x cm x cm)	#	Total Power (W)	Total Mass (kg)	Total Volume (cm^3)
M-PALSS Sensor array: • O_2 • NDIR CO_2 • Electrochemical CO_2 • Humidity • Pressure	1.8	0.55	3.8 x 5.6 x 11.7	1	1.8	0.55	~250
Pressure sensor (Dry)	-	-	-	8	-	-	-
Pressure sensor (Wet)	0.02	~0.05	Diameter: 1.7 Length: 5.0	3	0.06	~0.15	~34
Temperature (Dry)	-	~0.03	2.5 x 1.9 x 0.03	3	-	~0.09	~0.43
Temperature (Wet)	-	~0.03	-	2	-	~0.06	~0.015
Fans	12.1	~0.5	6.6 x 7.6 x 8.9	2	24.2	~1.0	~900
Pumps	15	~0.5	13 x 4.5 x 5.8	2	30	~1.0	~680
Pressure Regulators**	~2	~0.5	-	3	~4	~1.0	~1050
Thermal Control Valve**	~2	~0.5	-	1	~2	0.5	~100
Total Estimations:					**~62**	**~4.5**	**~2660**

Table 3.9.1: Mass, Power, and Volume analysis of the sensors and instrumentation discussed

* -: Negligible

**: No figures were provided for power, mass, or volume, approximates were made

4 Avionics

4.1 Subsystem Overview (Chase Latyak)

In this Portable Life Support System (PLSS) design, there are two main purposes for avionics: control and communication. The control aspect of avionics makes up a majority of the system's mass and volume, as the PLSS contains a variety of complex moving parts that must be effectively controlled, with redundancy in place in case of emergency. The communications aspect of avionics consists of components like the radio, Wi-Fi module, and informatics processor. For the purposes of mass and volume estimation throughout this report, the avionics subsystem mass consists of the aforementioned control and communication electronics, their associated wiring, and the physical housings for these electronics.

When it comes to determining a baseline PLSS system for mass and volumetric comparisons, there can be some ambiguity as there are numerous next-generation PLSS configurations. The PLSS, Exploration Portable Life Support System (xPLSS), and Martian Exploration Portable Life Support System (mxPLSS) are all unique configurations of the system that have variations in components, mass, and volume. For the purposes of this section, comparisons for mass change or percentage mass change are drawn relative to the PLSS schematic outlined by Ogilvie, Miller, and Hetherington [8].

In this baseline configuration, the total mass of the avionics subsystem is 14.8 kg. This mass can be further broken up into electronics mass versus housing mass as follows: 7.81 kg of electronics and wiring, and 6.99 kg of avionics housings. Moving forward, it will be shown that the main avenue for mass reduction in the avionics subsystem is achieved via the avionics housings, or boxes.

4.2 Subsystem Architecture (Chase Latyak)

The avionics subsystem architecture, as outlined in the overall system block diagram, consists of the same two major components mentioned in section 4.1: controllers and communication components, each explained in more detail in sections 4.3 and 4.4 respectively. From a broader system-level perspective, the avionics subsystem has to interface with the power and thermal subsystems, as well as the crew systems subsystems. For power, the batteries within the PLSS provide power to electronics during an EVA. The thermal loop interacts directly with a liquid cooling loop that removes heat from the electronics, detailed further in section 4.5.4. Furthermore, the avionics subsystem interacts with the crew systems components both by controlling components such as fans and pumps, as well as reading and processing data obtained by the numerous sensors throughout the PLSS.

4.3 Controllers (Chase Latyak)

There are a total of six controllers considered in the avionics subsystem for this PLSS architecture. Each controller has a functional name as well as a NASA standard designation for reference and consistency [8, 35]. The primary oxygen regulator controller (CON-150) regulates oxygen flow for spacesuit pressurization and astronaut breathing within the primary oxygen loop. Similarly, the secondary oxygen regulator controller (CON-250) also regulates oxygen flow, but only if there is a failure with the primary oxygen tank, valve, or other component that requires the backup oxygen tank to be utilized. The oxygen ventilation loop controller (CON-350) manages flow within the ventilation loop by controlling the fans, which delivers oxygen to the astronaut and removes carbon dioxide. The thermal loop controller (CON-450) regulates the thermal loop for the PLSS, including pumps, valves, and the Spacesuit Water Membrane Evaporator (SWME). Closely related is the auxiliary thermal loop controller (CON-550), which serves as a backup or emergency controller in case of issues with the thermal loop to ensure sufficient cooling for the astronaut and PLSS components. Finally, the last component is the Caution and Warning System (CWS), referred to as CWS-650 or CON-650, which monitors PLSS operation and alerts the astronaut or spacecraft/habitat in case of an out-of-range condition or emergency.

4.4 Communication (Tony Regli)

One of the major requirements of the PLSS avionics subsystem is providing reliable communication between the astronaut and a ground station, such as a rover or a habitation module. The Space-to-Space EMU Radio (SSER) currently in use on the International Space Station provided baseline requirements of transmitting reliable duplex voice communications, along with telemetry data at 693kB/s at a range of 80 meters [8]. Modernizations in radio electronics since the development of the SSER meant that this was a possible avenue for reducing mass while improving data bandwidth.

4.4.1 Radio (Tony Regli)

Along with the protocol in use on the SSER, two other radio transmission protocols were considered: IEEE802.11 Wide Local Area Network (WLAN) and Bluetooth. Table 4.4.1 provides a list of technologies considered, along with the protocol specifications that were compared to decide which protocol to use.

Technology	Frequency Band	Transmission Power (W)	Range (m)	System Mass (estimated) (kg)	Maximum Data Transmission Rate
Wifi6/802.11WLAN	2.4/5 Ghz	0.5[37]	100	2.5[46]	10Mb/s[37]
SSER VHF/UHF	UHF Band[36]	0.11[36]	75/80[37]	4.31[37]	693 Kbp/s[36]
Bluetooth	2.4Ghz[38]	0.100[38]	100[41]	6[40]	3Mb/s[39]

Table 4.4.1: Radio Protocol Capability Comparison

The system mass of the WLAN and Bluetooth transmitters are merely estimates, as there is no available information on the mass of space-rated WLAN and Bluetooth components. By comparing the mass of the SSER with that of a consumer-grade handheld radio with similar specifications, we found an estimation ratio between consumer-grade and space grade hardware. The handheld radio used was a Yaesu VX-3R, with a mass of 70g without its battery [42, 43]. Dividing the mass of the SSER by this mass gives us 4100g /70g = 62.6. Then multiplying the mass of consumer-grade WLAN and Bluetooth devices gave us the masses in the table above [40, 46]. Based on this technique, using WLAN could reduce radio mass, but due to the intricacies of spaceflight hardware development, it is impossible to say whether the reduction in mass would be as large as the 1.81kg decrease seen here.

While Bluetooth's absolute maximum range is 250 meters, in practice most Bluetooth systems operate at a much shorter range. Bluetooth devices come in several classes; class 2 devices are the most common and transmit at 2.5mW with a maximum range of 10m, only an eighth of the required range of the SSER [44]. Class 1 Bluetooth devices can transmit at 0.1W and reach a max range of 100m. However, even Class 1 Bluetooth provides less than a third of the maximum data transmission rate of WLAN, while providing the same maximum range, thus Bluetooth is not the optimal choice for the PLSS radio system.

WLAN provides a 100m maximum range, 1.2 times the maximum range of the SSER radio. WLAN has a maximum transmission rate of 10Mb/s, more than 10 times the data transmission rate of the SSER. The downside of WLAN is additional system complexity and less signal reliability at a long range. WLAN at 2.4Ghz is considered "quasi-line-of-sight"; testing done by NASA of a chest-mounted WLAN antenna shows subject orientation has a significant impact on the received signal strength [37]. At 20m, the received signal strength when a subject is facing away from the receiver (thus blocking the antenna with their body) is 23dBm weaker than the received strength of an unobstructed signal at the same distance. At 100m, the difference is 31dBm. Additionally, the drop in signal strength due to distance is exacerbated by antenna obstruction: when facing the receiver, signal strength at 100m is 6dBm weaker than at 20m. When facing away from the receiver, signal strength drops by 14dBm between 20m and 100m [37]. The SSER does not have this problem, as a single omnidirectional antenna transmitting between 410 and 420MHz provides coverage in all directions [37]. This drawback could be remedied with multiple WLAN antennas for full coverage, but that is at the expense of additional mass.

The increased data rate of WLAN also introduces challenges. When transmitting at 5Mb/s, turning away from the receiver causes transmission rate to drop to 1.79Mb/s. At 10Mb/s, turning away from the receiver caused a complete loss of connection [37]. Signal reflections from lunar regolith can also lead to interference and packet loss for WLAN signals: at ranges of under 100m, UHF radio like the SSER shows over 20dBm less path loss when compared to S-band signals like WLAN [45]. The combination of these challenges makes WLAN alone likely not a viable protocol for PLSS communication. The ideal radio system would thus use a combination of UHF radio and WLAN, with UHF being used similarly to the SSER, providing high reliability transmission for low data rates signals like voice and astronaut vitals telemetry. WLAN could then be used in addition to UHF to provide transmission for lower-priority signals like live video that would require higher data transmission speeds but are not critical for astronaut safety. Ultimately, the lack of accessible mass information for modern space-rated radio systems means that it is impossible to say whether this would decrease total radio system mass, but the improvement of radio capability would be a useful benefit of a modernized PLSS.

4.5 Avionics Boxes

4.5.1 Box Configuration (Chase Latyak)

In previous PLSS iterations, the controllers were each packaged separately, but there is potential to save both mass and volume by consolidating these controllers into fewer, larger avionics boxes. In particular, the KOALA design features four avionics boxes, with controllers that serve in a primary/backup role always in separate boxes for increased redundancy. The diagrams below show the original separated design and the new configuration for these controller housings.

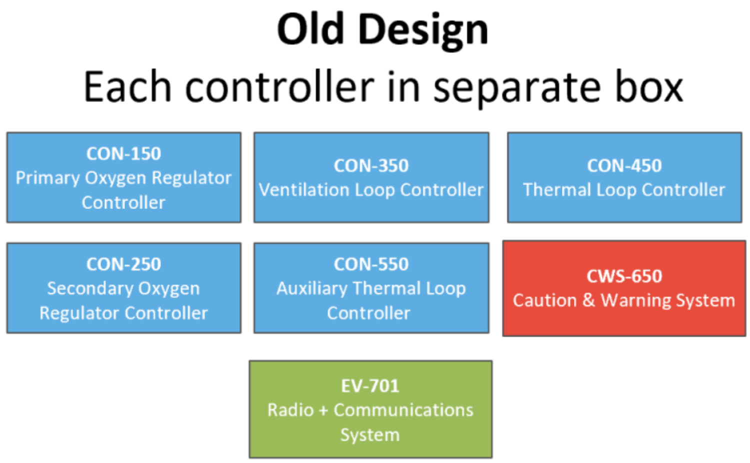

Figure 4.5.1: Diagram of old configuration with individual controller housings

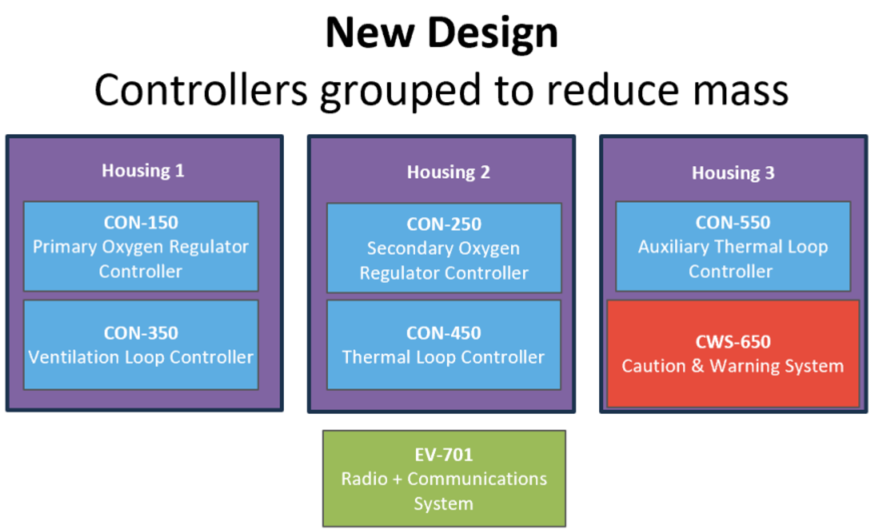

Figure 4.5.2: Diagram of new configuration with consolidated controller housings.

4.5.2 Material Selection (Chase Latyak)

The avionics boxes themselves take up 6.99 kg out of 14.8 kg total in the current PLSS design, or about 47% of the entire mass of the avionics subsystem [8]. Therefore, designing new lightweight avionics boxes can be a way to reduce overall PLSS mass significantly, which motivates the material trade studies that were conducted. Current avionics boxes are made from aluminum 6061, which is a solid, reliable option that has been utilized for decades, but the main drawback is its relatively high density of 2700 kg/m^3 [47].

There were a number of material properties that were considered and compared in this trade study. First and foremost, a low density material was desired to decrease mass with consistent volume and dimensions relative to previous designs. High strength is not of critical importance for avionics boxes in the PLSS, at least not to the level that a full aluminum 6061 box provides. Because of this, tensile strength and specific strength were considered for materials but did not need to outright exceed or match the performance of aluminum. See section 1.4.5 for more structural details. Another major factor considered is thermal conductivity, as higher values allow the box to conduct waste heat from the electronics better and prevent overheating. Finally, water absorption of any replacement material must be low, defined as <1%, in order to limit outgassing and prevent potential damage to avionics components.

From these constraints, a total of six potential materials were identified for this trade study: aluminum 6061 [47], polyether ether ketone 30% glass filled (PEEK 30% GF) [48], polyether ether ketone 30% carbon filled (PEEK 30% CF) [49], Ultem 1000 [50], T300 carbon fiber [51, 52], and LAR-TOPS-370 carbon fiber [53]. Table X below details the specific material properties of the first five materials. The last material, identified as LAR-TOPS-370, is a developmental carbon fiber composite that incorporates both pyrolytic graphite sheets (PGS) and carbon nanotubes (CNTs) in the epoxy to effectively increase thermal conductivity. However, due to limited testing, lack of data on all material properties, and a low technology readiness level (TRL) of 4, this material was not considered further in the trade study. A TRL 4 means there was component or breadboard validation in a lab setting, but not in a space environment or as part of a full system. In the future, as more studies are conducted and new innovations are made, the potential will increase for thermally conductive carbon fiber composites to be used in aerospace applications like the PLSS.

Material	**Density [kg/m^3]**	**Tensile Strength [MPa]**	**Specific Strength [MPa×m^3/kg]**	**Thermal Conductivity [W/(m×K)]**	**Water Absorption [% in 24h]**
Aluminum 6061	2700	310	0.115	166	~0
PEEK 30% GF	1540	103.4	0.0671	0.430	0.10
PEEK 30% CF	1410	120.6	0.0855	0.918	0.06
Ultem 1000	1280	113.8	0.0889	0.132	0.25
T300 Carbon Fiber	1760	1820	1.034	0.14 (out-of-plane) 10.5 (in-plane)	0.21

Table 4.5.1: Avionics box material trade study

In addition, the total masses of all avionics boxes were compared based on material selection, shown in Figure 4.5.3. Note that this bar chart considers total mass assuming volume and dimensions of all boxes are held constant. The numbers for total mass are therefore not final but serve as a first pass estimate to help determine the ideal material selection and move forward with a more detailed design. As previously mentioned, the mass of all avionics boxes using aluminum 6061 is 6.99 kg, and based on material choice alone, there is potential to save up to 3.68 kg.

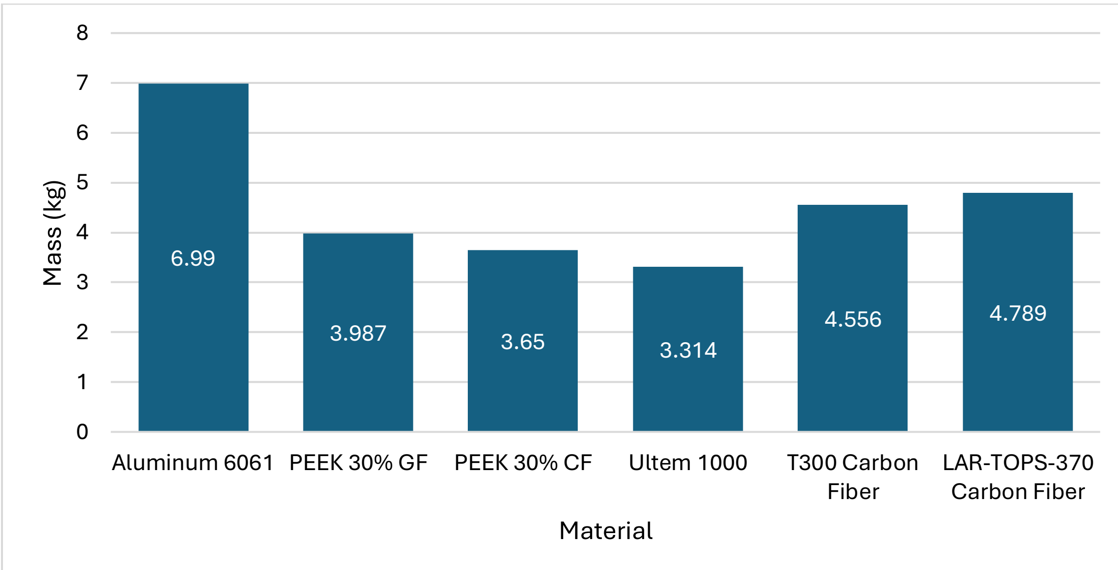

Figure 4.5.3: Avionics box material mass comparison.

Ultimately, PEEK 30% CF was selected as the best alternative material for the PLSS avionics boxes. Its low density of 1410 kg/m^3 makes it just 52% as dense as aluminum 6061, allowing for mass savings of 3.34 kg purely through material selection with size and volume held constant. Additionally, the carbon reinforcement makes this particular type of PEEK even stronger than others, also improving its specific strength. The two largest advantages of PEEK 30% CF over the other two thermoplastics, PEEK 30% GF and Ultem 1000, are its thermal conductivity of 0.918 W/(m×K) and water absorption of 0.06% in 24 hours.

On the other hand, there are two major drawbacks that come with the material selection of PEEK 30% CF over aluminum 6061 for avionics boxes: shielding and thermal conductivity. While PEEK 30% CF does have the highest thermal conductivity of the thermoplastics, this value is still miniscule compared to that of aluminum, which has a thermal conductivity that is over 180 times larger. Because of this, there must be some additional components within the boxes to help conduct and remove waste heat generated by the electronics other than the structure of the box itself. Also, PEEK 30% CF on its own does not provide enough shielding when it comes to either ionizing radiation or non-ionizing electromagnetic interference (EMI).

4.5.3 Shielding (Tony Regli)

One critical task of avionics boxes is shielding electronics from the harsh radiation environment of space. Without Earth's atmosphere and magnetic field to protect them, electronics components are exposed to a high rate of radiation from both ionizing and non-ionizing radiation. PEEK and aluminum have different radiation shielding characteristics, and for this design to be acceptable it must provide equivalent shielding to current avionics boxes, if not better. When compared to aluminum, PEEK provides better shielding against protons at the same given areal density (g/cm^2) [54]. Materials with low atomic numbers (Z) are best for shielding against protons, thus PEEK, being composed entirely of hydrogen, carbon, and oxygen, provides better proton shielding than aluminum [54, 57]. Electron radiation, on the other hand, is best blocked by high-Z elements like tungsten and aluminum [57]. PEEK is only 31% as effective as aluminum when shielding against electrons at the same mass thickness [54]. Thus, PEEK alone is not enough to provide sufficient shielding against radiation, but there is a significant amount of research focusing on how to improve the shielding capability of PEEK via various additives like tungsten.

One such technique uses direct inclusion of tungsten (W) and boron carbide into a PEEK superstructure via additive manufacturing. These composites provide better neutron and proton shielding by areal mass than stainless steel, at the expense of tensile strength dropping to 40-55MPa, only 45% of pure PEEK 30% CF [55]. The largest issue with this technique, however, is that it is still a relatively new technology. There are currently no commercially available PEEK-W composite 3D printing filaments. Additionally, most research into these composites focuses on significantly thicker sections of material than would be required for the PLSS, with most samples being thicker than 1cm [55]. Shielding effectiveness varies greatly with shield thickness, thus this data is useless without information about shielding capability within the range of thicknesses that are actually feasible for a PLSS avionics box (1-3mm).

Another, more feasible technique, for radiation shielding is that of graded-Z shielding, which uses alternating layers of a low-Z material like PEEK and a high-Z material like tungsten to provide shielding against a wide variety of radiation [56]. First, an external layer of EMI shielding provides protection against electromagnetic interference. Then, an outer layer of PEEK provides protection against protons and other forms of radiation blocked by low-Z materials. A thin inner layer of tungsten protects against electrons, and then an interior layer of PEEK provides additional protection against proton radiation, along with blocking secondary radiation caused by particle impacts [57]. Together, these layers are referred to as versatile structural radiation shielding (VSRS). Layered shielding such as this can achieve equivalent shielding capability to aluminum against electrons at a lower areal density [57]. To achieve equivalent shielding to the 0.349g/cm^2 of aluminum that is currently in use, an areal density of 0.2g/cm^2 is required; a drop to 57% of the current areal density [57]. The specific layer thicknesses used to achieve this shielding performance are not available publicly. The total thickness of the material required would be less than 1.5mm, which is the thickness of 0.2g/cm^2 of pure PEEK. As tungsten is denser than PEEK, any blend of the two materials must be denser than PEEK on its own; thus, layered shielding would be thinner than 1.5mm, which is already thinner than the 2mm of PEEK in use for the avionics boxes. Ultimately, graded-Z shielding promises mass reductions without loss in shielding performance, but additional research is required to verify the precise layer thicknesses required to achieve the desired shielding performance.

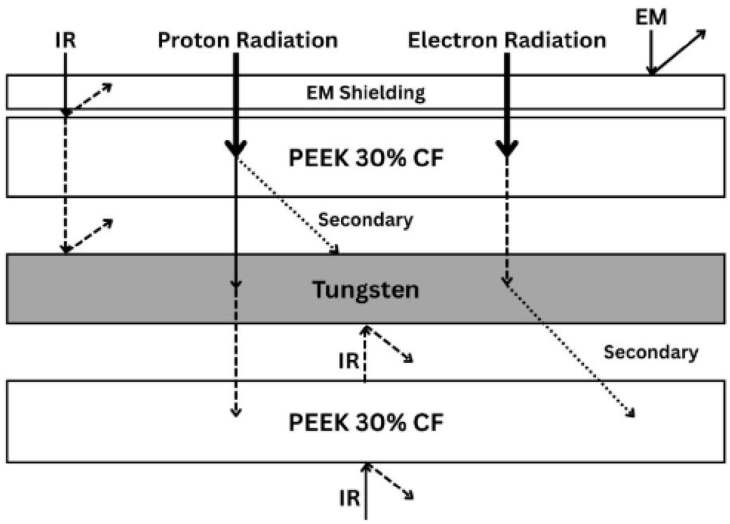

Figure 4.5.4: Graded-Z shielding diagram.

4.5.4 Thermal (Chase Latyak)

As previously mentioned, one of the biggest drawbacks for a PEEK 30% CF avionics box is the low thermal conductivity of just 0.918 W/(m×K), so an aluminum 6061 cold plate was included in the design to still provide sufficient thermal conduction. The controllers within the avionics box will be in contact with the cold plate, with a thin thermal pad in between, to conduct out waste heat. This cold plate will contain liquid cooling with embedded heat pipes; for more detail on heat pipes and associated heat transfer calculations, see section 5.3.3. The outer radius of the heat pipes used for avionics cooling is 3mm, and the required contact length was at least 160mm. The thickness of the plate itself is 4mm. Full renders of the cold plate, excluding heat pipes, and engineering drawings of the design are provided below in figures 4.5.5 and 4.5.6. The engraved S-shaped line on the top of the plate shows the internal path of the embedded heat pipe. The only differences between the cold plates in each of the avionics boxes are the outer rectangular plate dimensions, which correspond to the length and width of the box minus the wall thickness.

Redacted due to Export Control/CUI requirements.

Figure 4.5.5: Avionics box cold plate CAD model.

Redacted due to Export Control/CUI requirements.

Figure 4.5.6: Avionics box cold plate engineering drawing, dimensions in mm.

4.5.5 Design and CAD (Chase Latyak)

Sizing the avionics boxes proved difficult due mostly to the lack of specific information relating to the sizing and dimensions of the electronics mentioned in sections 4.3 and 4.4. This means that the numbers and designs presented here are not completely accurate to what a real, working PLSS would look like, but rather serve as an approximation to validate the mass reduction techniques that are proposed. In order to get baseline volumetric estimates to work with, older PLSS models were considered, specifically those used in the space shuttle era. In previous PLSS iterations, the avionics subsystem took up roughly 20% of the total PLSS volume. Using the total volume of 32,960 cm^3 from the shuttle PLSS [58], this puts the total avionics volume at 6592 cm^3. The mass proportions [8] of each controller can be used to approximate the volumetric proportions. Table 4.5.2 summarizes the volumetric contribution of the avionics components.

Component	Volume [cm^3]
CON-150	705
CON-250	705
CON-350	628
CON-450	610
CON-550	1174
CWS-650	1291
Radio	904
Wi-Fi/Informatics	575
Total	6592

Table 4.5.2: Volume of avionics components

Table 4.5.3 below details which controllers and components are contained within each box, the total volume of each box, and the dimensions (height, length, width) of each box.

Box Number	Components Within	Volume [cm^3]	Dimensions [cm]
1	CON-150, CON-350	1333	7.00, 13.00, 14.65
2	CON-250, CON-450	1315	7.00, 13.00, 14.45
3	CON-550, CWS-650	2465	7.00, 19.00, 18.53
4	Radio, Wi-Fi, Informatics	1497	7.00, 13.00, 16.45

Table 4.5.3: Avionics box configurations

The general design for each avionics box consists of the PEEK 30% CF and tungsten layered material for the main, lightweight structure of the box. Inside, two controllers will be mounted to the top and bottom of the box, potentially with standoffs to ensure the correct distance between the top of the electronics and the cold plate. Without detailed information on dimensions of electronics, it is not possible to give exact values for this standoff height, so models and diagrams moving forward contain a low-fidelity Arduino Uno as a stand-in for the actual PLSS controllers. The standoffs in the computer-aided design (CAD) model are sized to ensure contact between the cold plate and controller but would be differently sized based on the true dimensions of NASA controllers. Finally, there is an aluminum 6061 cold plate with embedded aluminum heat pipes to remove heat generated by the electronics within the box, as described in section 4.5.4.

The box itself is connected to the isogrid backplate via mounting holes included in the isogrid pattern. The box contains four 4 brackets sized for M4 screws to connect the box to the backplate. The box itself is split into two halves, each with a controller, connected similarly with M4 bolts to clamp the two halves of the box together. There are eight bolt holes to connect the halves of the box together, which will help distribute the clamping force and ensure good contact between the controllers, thermal pads, and cold plate. Three additional holes are present on the side of the box: the two symmetrical holes above and below the centerline are arbitrarily sized for wires to go through, while the third hole directly on the centerline is where the heat pipe will go. The box thickness throughout is 2 mm, slightly thicker than typical NASA aluminum 6061 avionics boxes [59], partially for extra structural support and partially for better shielding performance. The exterior of the box and engineering drawings can be seen below in figures 4.5.7 and 4.5.8. The dimensions for the box in the figures come from box 1, but the overall design is the same for each box, with the only major changes being the overall length and width based on required volume.

Redacted due to Export Control/CUI requirements.

Figure 4.5.7: Avionics box 1 exterior CAD model.

Redacted due to Export Control/CUI requirements.

Figure 4.5.8: Avionics box 1 engineering drawing, dimensions in mm.

The inside of the box is essentially identical on the top and bottom, as seen in figures 4.5.9 and 4.5.10. The external PEEK structure was made transparent for viewing purposes, but remains the same material and dimensions as shown before.

Redacted due to Export Control/CUI requirements.

Figure 4.5.9: Avionics box 1 assembly side view.

Redacted due to Export Control/CUI requirements.

Figure 4.5.10: Avionics box 1 assembly isometric view.

4.6 Final Results and Conclusions (Chase Latyak)

Ultimately, the mass savings in the KOALA avionics subsystem came from the new lightweight avionics box design and controller consolidation. Table 4.6.1 below details a full mass breakdown of the avionics subsystem, excluding heat pipe and cooling loop mass that is allocated to the thermal subsystem instead. The masses provided for the table are for all four boxes combined.

Component	Mass (kg)
PEEK boxes	1.658
Aluminum cold plates	0.970
Bolts, nuts, standoffs	0.133
Controllers and wiring	7.810
Total	10.57

Table 4.6.1: Full avionics subsystem mass breakdown.

The mass of the PEEK boxes was determined via the areal density determined for proper shielding discussed in section 4.5.3, and then by multiplying by the factor of 2/0.87 to account for the additional thickness of the box walls relative to the ideal minimum of 0.87 mm calculated purely from shielding performance metrics. The first two boxes, since the required volumes of 1333 and 1315 cm^3 respectively are so close, were assumed to be the same dimensions and mass. Having two identical boxes also can improve maintainability and reduce overall complexity, which is an added benefit of this assumption. Based on the dimensions and volumes of the four boxes provided in table 4.5.3, the PEEK box masses come out to: 353.1 g for box 1, 353.1 g for box 2, 565.3 g for box 3, and 386.2 g for box 4.

The mass of the aluminum plates was simply found by taking the volume of each plate multiplied by the density of standard aluminum 6061, which is 2.7 g/cm^3. This calculation yields a mass of 193.9 g for boxes 1 and 2, 364.2 g for box 3, and 218.4 g for box 4. Similarly, the mass of the aluminum standoffs was estimated to be the volume based on the rough approximation shown in the CAD in section 4.5.5 multiplied by that same density of 2.7 g/cm^3. With a total of eight per box, or four per box half, with height equal to 1.6 cm and a radius of 0.25 cm, the mass of the standoffs for each box is just 6.8 g. The mass of the M4 bolts and nuts is twelve times the individual bolt mass of 1.5 g and nut mass of 0.7 g, for a mass of 26.4 g per box. The last addition in the total mass breakdown comes from the electronics themselves, which cannot be defined or split up as detailed as the other components, but between the four boxes make up an additional 7.81 kg. The electronics and wiring mass is a majority of the avionics system mass, especially with the new lightweight boxes in place.

The final mass of the new avionics boxes comes out to only 2.76 kg, a reduction of 4.23 kg compared to the previous PLSS avionics box mass of 6.99 kg [8]. Adding on the unchanged controller mass, the avionics system as a whole is now just 10.57 kg, which is a -28.6% change in avionics mass. The bar chart in figure 4.6.1 visualizes these comparisons for both avionics box mass and total avionics mass. As all of the mass reduction for the avionics system was achieved through reducing the mass of the boxes, the percentage of the total avionics mass that these boxes make up dropped from 47.2% down to just 26.1%.

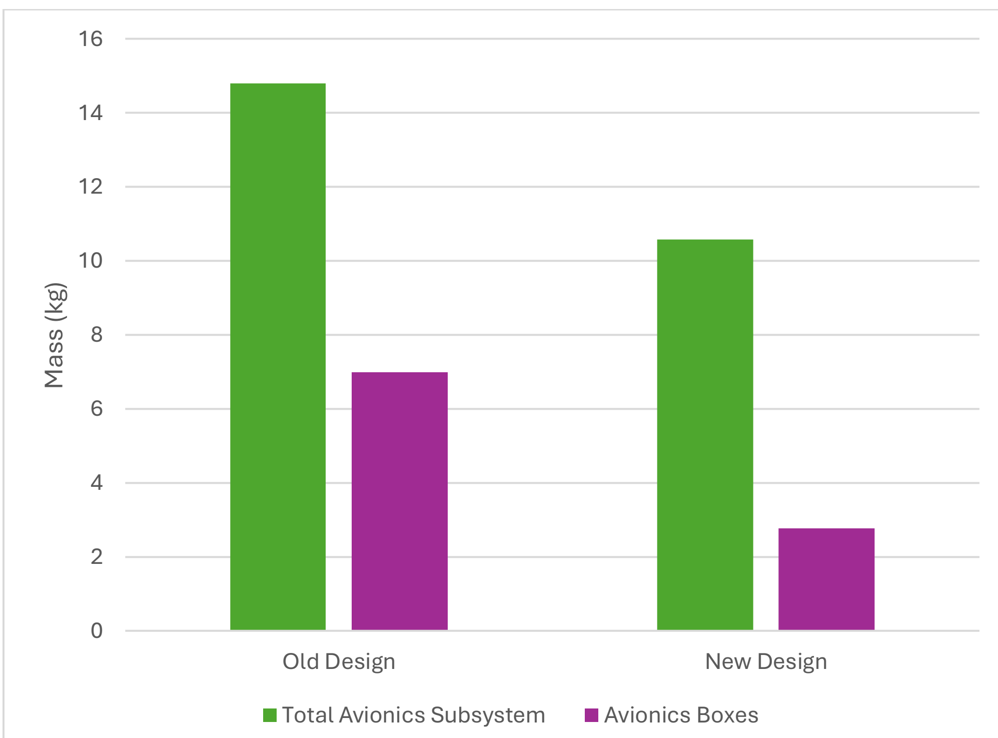

Figure 4.6.1: Final avionics mass comparison chart.

It is evident that there is room to save on mass in future PLSS designs by reconsidering material choices and design of components like the avionics boxes discussed here. While the analysis is partially limited, especially regarding specifics about electronics and their exact dimensions, the conceptual improvements proposed stand as potential avenues to enable a lightweight PLSS suitable for Martian EVAs. The major takeaways from the avionics subsystem include the material changes from aluminum to a thermoplastic, as well as the associated improvements to counteract the poorer shielding and thermal performance of thermoplastics like PEEK. Lightweight shielding technologies like VSRS allow for a much lighter box that can provide comparable protection to typical aluminum boxes. The inclusion of aluminum components in certain areas where needed allows for sufficient thermal conduction without the mass of a full aluminum casing. As with a lot of the new, innovative technologies proposed as ways of saving mass, one of the biggest challenges is a low TRL, which leads to a discussion of additional alternatives or future areas of research.

5 Thermal

5.1 Subsystem Overview

The thermal control system regulates both the astronaut's and internal PLSS component's temperatures during an EVA to ensure no overheating or freezing. While lunar missions operate around 250W steady-state heat load, our system must manage twice as much heat due to increased metabolic rate and other design choices. The liquid cooling ventilation garment (LCVG) is the ~80-meter-long water-cooling tube that loops around the astronaut's body to keep them cool by conducting body heat. This warms the water in the loop, requiring a reverse process to cool it down before recirculating. The spacesuit water membrane evaporator (SWME) is a component that cools the LCVG water by using a pressure difference across a hydrophobic microporous membrane, causing a small portion of the water to continuously evaporate into the low-pressure environment and remove heat through latent heat transfer [60]. However, the SWME was designed for lunar vacuum environments, reducing its efficiency on Mars due to its atmospheric pressure, requiring an upsized design to maintain performance. Another drawback is the open loop system the SWME relies on, venting several kilograms of water into the atmosphere per EVA, shown in Figure 5.1.1.

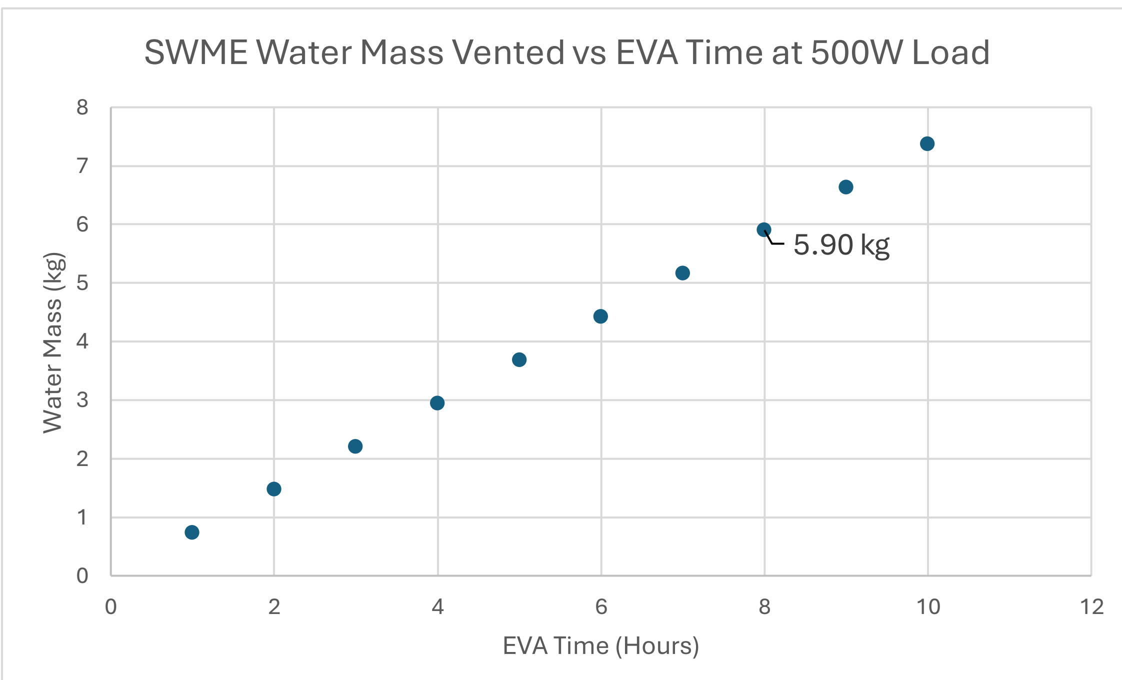

Figure 5.1.1: Mass of water lost through SWME over 10-hour EVA

Values come from using the latent heat of vaporization of water, h_{fg}, and the heat rejection rate, $\dot{Q}$.

$$\dot{m} = \frac{\dot{Q}}{h_{fg}} \frac{kg}{s} \tag{5.1}$$

$$\frac{500}{2.45 \cdot 10^6} \frac{kg}{s} \cdot 120 \frac{s}{hr} = 0.74 \frac{kg}{hr} \tag{5.2}$$

Over 10 hours, 7.4kg of water are vented and lost, meaning about 9kg of water must be carried to supplement the loss. The extra supply must account for peak metabolic rates which expedite the amount of water vented and a safety factor. This is a heavy mass penalty for both an EVA and the total mission, requiring hundreds of kilograms of water to be carried to Mars that will be lost to the environment. Freezing is another concern, since the Mars temperature is typically below the freezing point of water, for which is the only coolant the SWME is designed. This introduces another mass penalty from more hardware required to prevent freezing. From our analysis, we were unable to eliminate reliance on the SWME completely due to variable Mars temperatures and metabolic rate. Instead, our design focuses on reducing stored water mass by combining the SWME with a closed-loop radiative design.

5.2 Heat Requirements (Lindsey)

The production of the new thermal loop was directly affected by design choices in other systems, such as crew systems, avionics, and structures, making it vital to stay up to date with our peers. The most notable changes came from crew systems with their estimated average metabolic rate and LiOH cannister heat production. For lunar missions, the average metabolic rate is cited to be between 200-250W and maximum rates reaching around 450W [2]. Our crew systems team estimated the steady-state metabolic rate of an astronaut on Mars to be around 350W. The LiOH canister produces another extra ~50W from the chemical reaction. These, alongside an estimated 60W from avionics and 40W from pumps, fans, and other components, we determined our steady-state heat load to be about 500W. We broke down the baseline SWME mass and created an adjusted baseline mass in Table 6.3.1. This was done to provide a fair comparison of the mass reductions while accounting for the 30% decrease in SWME efficiency under Martian conditions, the increased metabolic rate, and the LiOH canister reaction, which led to higher water and tank mass.

	SWME Baseline	SWME Adjusted (500W)
SWME Mass (kg)	1.6	2.4
Water Mass (kg)	6	9.4
Tank Mass (kg)	0.56	1.3
Total Wet Mass (kg)	8.16	13.04

Table 5.2.1: Breakdown of baseline thermal system to adjusted system for increased heat load

This table clearly outlines water as the main mass driver in the thermal system, suggesting that a closed loop design such as a radiator should be investigated, as opposed to other designs initially considered.

5.3 Subsystem Architecture

5.3.1 Radiator (Lindsey)

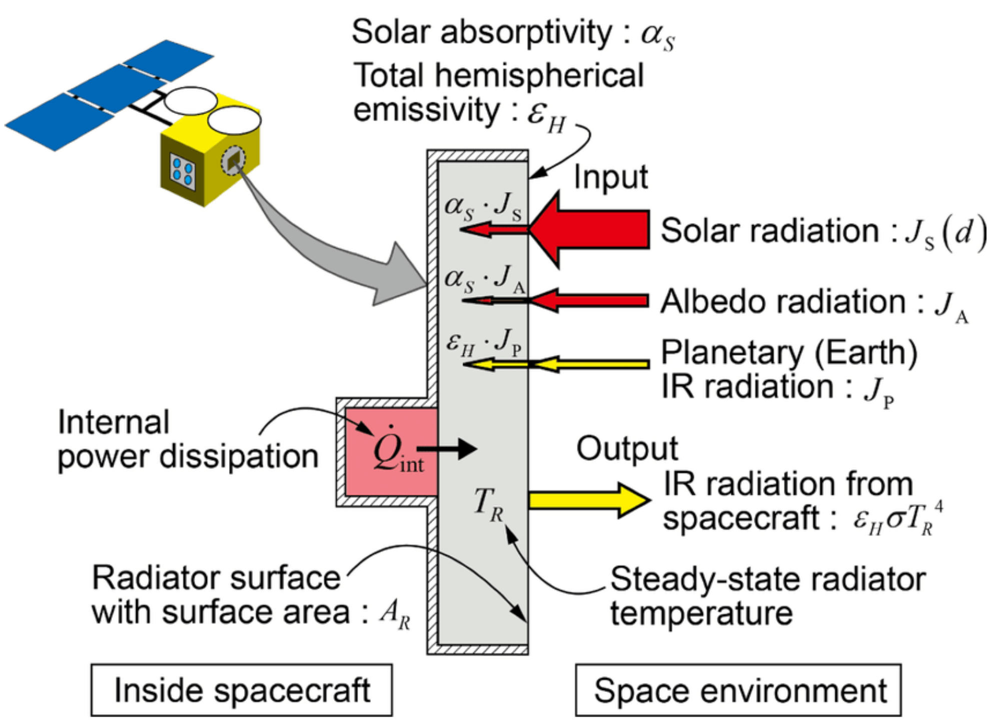

Figure 5.3.1: Spacecraft radiator diagram [3]

A radiator is a device used to dissipate thermal energy into a surrounding environment by conduction from a heated surface, in this case, coolant tubes. Figure 5.3.1 illustrates $\dot{Q}_{int}$ entering the under the radiator to heat the panel. The yellow arrow shows the IR radiative output, characterized by Stefan-Boltzmann Law which scales radiative output to the fourth power of the difference between the radiator's temperature and environmental temperature where ε is the emissivity, σ is the Stefan-Boltzmann constant, and A is the surface area of the radiator. A radiator has been considered by NASA for a Mars PLSS, though many challenges face the design. First, the surface temperature of Mars falls within -153 ^{o}C – 20 ^{o}C, introducing both freezing and power penalties on either extreme. The hot water temperature was estimated to be about 27 ^{o}C, meaning that on the hottest day on Mars, only 33W of power can be removed, assuming an emissivity of 0.9 and surface area of 1m^2.

To determine the radiative power, we used the formula below, assuming T_H is 300 K and T_M 293 K under worst-case conditions.

$$\dot{Q}_{out} = \varepsilon \sigma A (T_H - T_M)^4 = 33.5\ W \tag{5.3}$$

Figure 5.3.2 displays the radiative power output vs a range of Mars temperatures in Kelvin (-150 ^{o}C – 30 ^{o}C) with the nominal temperature (-20 ^{o}C) marked at 204W.

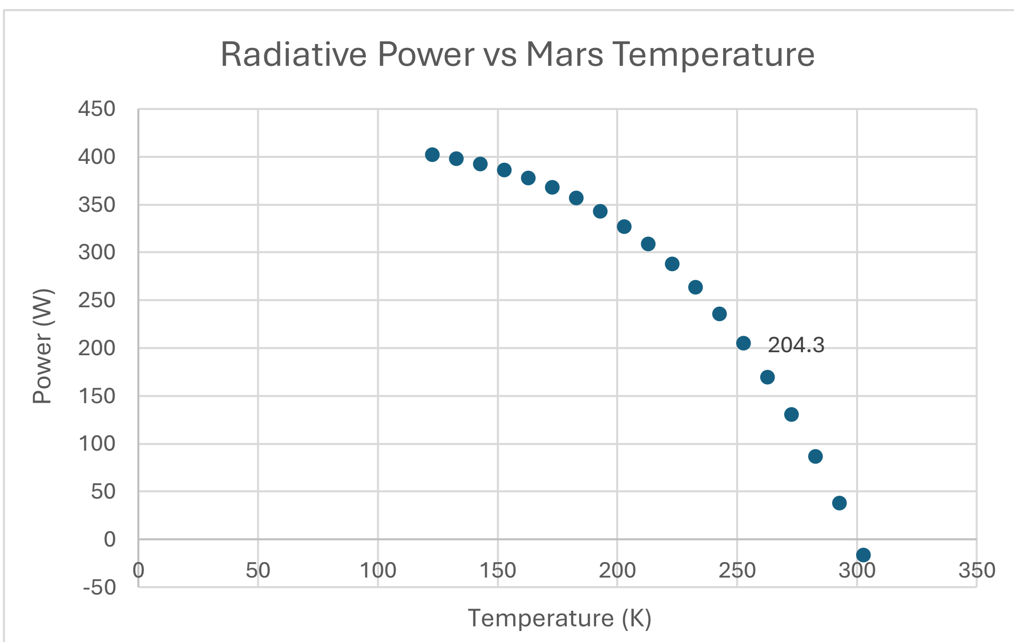

Figure 5.3.2: Radiative power output over range of Mars temperatures

This design alone would violate the requirement that the PLSS can function at any given environmental condition. Initially, a radiator-SWME hybrid design was considered to supplement insufficient power output, varying LCVG flow paths depending on Mars' temperature. However, this requires water to be the coolant, which would likely freeze under the radiator and burst the tubing.

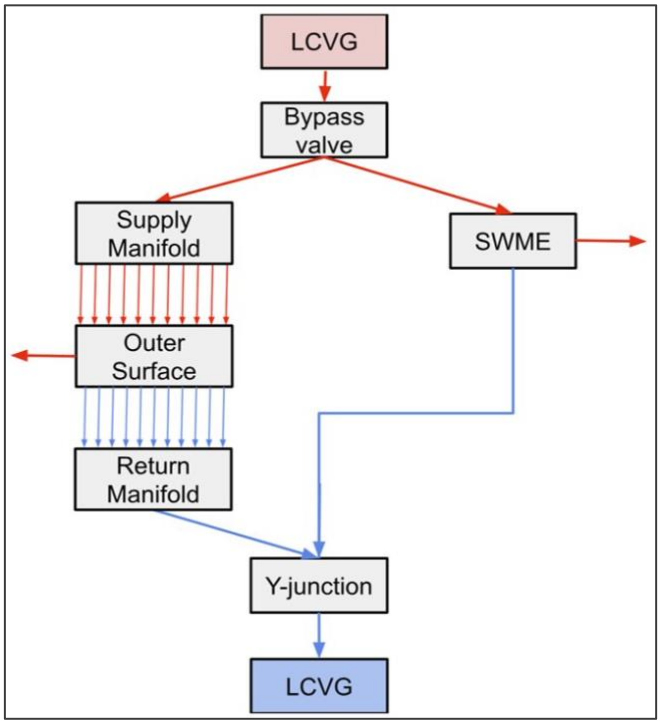

Figure 5.3.3: Initial thermal loop design

Because of this, we determined a thermal system that could handle all thermal requirements under the largest temperature range would require two separate loops; one water LCVG loop that cools via SWME (connected to a feedwater tank) and a second internal backpack loop that only cools avionics boxes and electronics using 50-50 propylene glycol-water coolant through a radiator. Propylene glycol–water was selected because it maintains strong heat-transfer performance and freeze protection while avoiding the toxicity, corrosion concerns, and electrical conductivity associated with the other coolants considered.

Coolant	Approx. freeze tolerance	Heat capacity kJ/kg·K	Toxicity	Corrosion and Degradation Concerns
50/50 ethylene glycol-water [4]	−37°C	3.4	Toxic	Non-corrosive to aluminum with inhibitors
50/50 propylene glycol-water [5]	-32°C	3.5–3.7	Low to Non-Toxic	Non-corrosive to aluminum with inhibitors
Potassium formate-water coolant [6]	−50°C	3.2–3.6	Non-Toxic	High electrical conductivity

Table 5.3.1: Coolant properties comparison

Because of this, we determined a thermal system that could handle all thermal requirements under the largest temperature range would require two separate loops; one water LCVG loop that cools via SWME (connected to a feedwater tank) and a second internal backpack loop that only cools avionics boxes and electronics using 50-50 propylene glycol-water coolant through a radiator. Propylene glycol–water was selected because it maintains strong heat-transfer performance and freeze protection while avoiding the toxicity, corrosion concerns, and electrical conductivity associated with the other coolants considered.

The radiator system consists of a cooling loop that removes heat from backpack components and splits into several parallel serpentine flow paths beneath the backpack cover. Heat is conducted from the coolant tubes into an aluminum plate coated with a high-emissivity material, described in section 5.3.6, which functions as the radiator surface. The coolant then recirculates, continuously picking up and radiating heat without any losses.

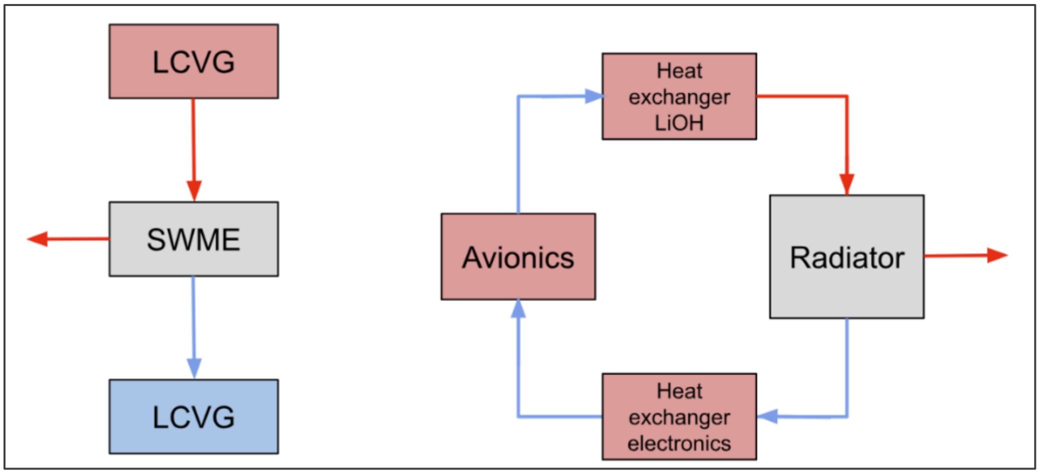

Figure 5.3.4: LCVG and radiator final design

5.3.2 Heat Pipes (Ayush Iyer)

Heat piping was originally the method through which heat would be transported from the avionics boxes and the crew systems pumps/fans/LiOH Canister to the radiator, but prolonged area of contact was required for conduction. For this reason, heat piping was used in conjunction with a cooling loop that would distribute coolant through the previously mentioned systems. We chose to use copper as the pipe material with a water working fluid to avoid the use of toxic working fluids and material combinations that could harm the system when used together (such as aluminum tubing with water working fluid).

Figure or Table containing sensitive information, or possible unauthorized copyright information has been removed.

Figure 5.3.5: Schematic drawing of a heat pipe and its components [66]

5.3.3 Avionics Heat Transfer (Ayush Iyer)

The primary goal of the avionics heat transfer system is to transfer an estimated 60 W of energy from the avionics boxes to the radiator (estimated through past NASA documentation), while maintaining an operating temperature of about 26°C for the components. Given the use of PEEK 30% CF as the outside of the boxes, the method of heat transfer for this system would need to involve directly interfacing with the interior of the box.

The method through which cooling was achieved was by running the coolant tube through the box directly, using an aluminum heat sink placed within the box to contain the tube. The tube would run 20°C 50/50 propylene/water coolant at a rate of 0.006 kg/s through a tube with an inner diameter of 1.5 mm and an outer diameter of 3 mm. To serve as an interface between the electronics and the aluminum heat sink, Laird Tgard 500 [8] will be used as a thermal pad to prevent electrical interference with the tube while allowing heat to pass through. With this information, we can mathematically determine an estimate of how long the tube needs to run through each plate.

First, to find the worst-case thermal resistance needed for the system to properly cool.

$$R_{total} = (T_{elec} - T_{coolant})/Q = 0.4°C/W \tag{5.4}$$

This determines the highest thermal resistance that needs to be designed for based on the electronic and fluid temperatures. From there, using the Laird Tgard 500 specifications from the manufacturer's website, and the contact area of the electronics on the pad, we estimate the pad resistance to be

$$R_{pad} = \frac{R_{pad,spec}}{A_{pad}} = 0.08℃/W \tag{5.5}$$

From there, we determine the tube's allowable resistance with

$$R_{tube} = R_{total} - R_{pad} = .32℃/W \tag{5.6}$$

From here, we determine the Reynold's number, which is used to determine Nusselt number, and convective heat transfer coefficient, which is used to determine final length.

$$Re = \frac{\rho * v * d}{\mu} = 1486 \tag{5.7}$$

This is laminar flow, which means that in developed pipe flow, we can assume the Nusselt number to be 3.66. The thermal conductivity k for 50/50 Propylene glycol/water is ~.42. Using these values as well as inner diameter of the tube, we find h to be:

$$h = \frac{(Nu \cdot k)}{d} = 1025\, W/m^2K \tag{5.8}$$

With this value, we can finally use the convective heat transfer coefficient with the tube's allowable resistance and contact area of the inner diameter of the tube to determine the maximum necessary length.

$$L = \frac{1}{R_{tube} \cdot h \cdot \pi \cdot d} = 0.65\, m \tag{5.9}$$

This length was determined to be 650 mm, which will be serpentine through each heat sink.

Temperature Goal	Maintain 26°C
Heat Transfer Goal	60 W across all boxes
Interface Length with Tube	650 mm per box
Interface method	Heat pads

Table 5.3.2: Summary of Avionics Heat Transport System

Redacted due to Export Control/CUI requirements.

Figure 5.3.6: CAD Model of Aluminum Tube Through Avionics Heat Sink

5.3.4 Electronics and LiOH Canister Heat Transfer (Ayush Iyer)

The crew systems team adopted the use of three fans and two pumps for their system that require cooling for proper function. These fans and pumps are very small, and the technique of running tubing through a heat sink that was used for the avionics boxes cannot be used in this application. Instead, we employed the previously mentioned copper-water heat pipes to transport excess heat from each fan/pump to the cooling tube, where the heat will be sent to the radiator.

To estimate the heat that would need to be transported from each component, we used an estimate for an inefficient pump and fan. Assuming a 50% efficient pump or fan, we calculated the heat emitted from each using the formula

$$Q = P_{in} * (1 - \eta) \tag{5.10}$$

This formula estimates about 6 W of heat per fan and 8 W of heat per pump. The heat pipes implemented for these would be capable of delivering up to 12 W of cooling while maintaining a 23°C temperature for the components.

Figure or Table containing sensitive information, or possible unauthorized copyright information has been removed.

Figure 5.3.7: Graph from Boyd Corporation, Heat Pipe Calculator [68]

However, a chief concern here was the interaction between the copper heat pipe and the aluminum cooling tube. Direct contact between the two would cause galvanic corrosion, which necessitates the use of an epoxy to allow safe contact between the two. We have chosen Master Bond EP48TC for ours [69]. Additionally, an aluminum saddle was used to add additional surface area of connection between the pipes, serving to increase conduction rate per unit length and reduce the length of contact. This saddle is essentially a small aluminum block with grooves on either side to house the pipe lengths needed for contact.

The size of the pipe depends on how much length of contact would be needed between the heat pipe and the coolant tube. We used a set of formulas to determine this necessary length. First, we determine the total maximum thermal resistance of the contact interface and the thermal resistance of the individual components as a function of length. Here, we size the saddle as a 6mm tall and 10 mm wide block of aluminum with 3mm grooves for each pipe and 1.5 mm between the pipes. Δx is the center-to-center distance of the pipes, 4.5 mm. K represents the thermal conductivity constant of Aluminum 6061, 200 W/(m* K). R''_c is the thermal contact resistance per unit area of the epoxy, estimated conservatively as $2 * 10^{-5}\ m^2K/W$

$$R_{total} = \frac{\Delta T_{contacts}}{Q} = \frac{2.5K}{8W} = .3125K/W \tag{5.11}$$

$$A_c = \pi \cdot d \cdot L = .003 \cdot \pi \cdot L \tag{5.12}$$

$$A_{saddle} = .006 \cdot L \tag{5.13}$$

$$\begin{aligned} R_{total} = R_{contacts,total} + R_{saddle} &= \frac{2 \cdot R''_c}{A_c} + \frac{\Delta x}{k \cdot A_{saddle}} \\ &= \frac{.008}{L} K \cdot m/W \end{aligned} \tag{5.14}$$

$$L = \frac{.008\, K \cdot m/W}{.3125\, K/W} = .026\, m = 26\, mm \tag{5.15}$$

We find L to be 26 mm of contact, which we round up to 3 for redundancy. This determines the length of the saddle.

Temperature Goal	Maintain 23°C
Heat Transfer Goal	8 W (per component)
Heat Pipe Diameter	3 mm
Heat Pipe Length	35 mm

Interface Length with Tube	30 mm
Interface method	Aluminum Saddle + epoxy

Table 5.3.3: Summary of Pipe/Fan Heat Transport System

A similar approach is taken to cool the LiOH Cannister. The main differences to be considered are the different copper heat pipe diameter and the increase in heat that needs to be moved. The LiOH cannister emits a predicted 50 W of heat that needs to be transported. Another heat pipe was added here to transport the heat to the cooling tube.

Figure or Table containing sensitive information, or possible unauthorized copyright information has been removed.

Figure 5.3.8: Graph from Boyd Corporation, Heat Pipe Calculator, [62]

Here, the heat pipe has a diameter of 1.27 cm, to allow for a low length of contact needed, and aims to maintain a temperature of 30°C for the cannister. Using a similar set of calculations for the contact length needed, we can determine how long the heat pipe needs to be. There is a 2 mm gap between the two pipes in the saddle, leaving the center-to-center distance between the two pipes, Δx, to be 9.85 mm.

First, the contact resistance of the two pipes needs to be calculated and added to the saddle conduction to determine total thermal resistance.

$$A_{c,copper} = \pi * d_{copper} * L = .040 * L \tag{5.16}$$

$$A_{c,aluminum} = \pi * d_{aluminum} * L = 0.0094 * L \quad (5.17)$$

$$R_{c,copper} = \frac{R_c''}{.040*L} = 5 * 10^{-4}/L \text{ K/W} \quad (5.18)$$

$$R_{c,aluminum} = \frac{R_c''}{.0094 * L} = 2.12 * \frac{10^{-3}}{L} K/W \quad (5.19)$$

$$R_{saddle} = \frac{\Delta x}{k*(h*L)} = .0033/L \text{ K/W} \quad (5.20)$$

$$R_{total} = R_{c,aluminum} + R_{c,copper} + R_{saddle} = \frac{0.0059}{L} K/W \quad (5.21)$$

Next, we estimate the required total resistance. This is determined by first finding the difference between canister and coolant temperature and subtracting the difference in temperature between the inner tube wall and coolant. That difference is divided by the heat emitted to determine required resistance.

$$\Delta T = T_{canister} - T_{coolant} - T_{convection} = 8\ K \quad (5.22)$$

$$R_{total} = \frac{8K}{50W} = .16\ K/W \quad (5.23)$$

Finally, we equate the R_{total} equations to each other to determine the length of contact required to transport the necessary amount of heat.

$$L = \frac{.0059}{.16} m = .0369\ m \quad (5.24)$$

We estimate about 4 cm of contact required between the two pipes, and we size our saddle accordingly.

Temperature Goal	Maintain 30°C
Heat Transfer Goal	50 W

Heat Pipe Diameter	1.27 cm
Heat Pipe Length	10 cm
Interface Length with Tube	4 cm
Interface method	Aluminum Saddle + epoxy

Table 5.3.4: Summary of LiOH Canister Heat Transport System

Using these estimates, we can determine the mass of the system for the section of the loop that flows from the avionics boxes, pumps and fans, and LiOH canister to the radiator. We estimate a total of 257.67 grams for this section of the system.

Component	Mass per unit	Quantity	Total Mass
Pump/Fan Pipe	.80	5	4 g
Pump/Fan Saddle	5 g	5	25 g
LiOH Canister Pipe	33 g	1	33 g
LiOH Canister Saddle	30 g	1	30 g
Avionics tubing per plate	9.31 g	4	37.2 g
Tubing between systems ~ 5m	43 g	1	71.6 g
Fluid Mass	1.84 g/m	7.6 m	14 g
Total +20% margin			257.76 g

Table 5.3.5: Mass Table of Heat Transport System to Radiator

5.3.5 Radiator Tubing Estimates (Lindsey)

The cooling loop was designed to conduct as much heat as possible without overheating the components to maximize radiative output. A mass flow rate of 0.006 kg/s achieves an outlet temperature of 27°C, (ΔT= 7°C), using tubes with an inner diameter of 3mm and thickness of 1mm.

$$\dot{Q} = \dot{m} C_p \Delta T \tag{5.25}$$

$$\dot{m} = \frac{150}{3500 \cdot 7} = 0.006 \, \frac{kg}{s} \tag{5.26}$$

Where C_p is the specific heat capacity of 50-50 propylene glycol-water in $\frac{kJ}{kg \cdot K}$

A supply and return manifold are required to split and merge the cooling loop as it enters and leaves the radiator. By analyzing the flow properties using 4, 6, 8, or 10 parallel paths, we determined that distributing the total mass flow rate across 8 parallel paths was ideal for reducing per-path velocity and pressure drop while maintaining heat capacity. Using 8 paths, the spacing between tubes is about 7cm which produces a temperature difference between tubes that is less than 1K, ensuring even heating. The pressure drop and velocity for N number of paths can be calculated as follows [70]:

Mass flow rate per path:

$$\dot{m}_{path} = \frac{\dot{m}}{N} \tag{5.27}$$

Where ṁ is the total mass flow rate

Using N=8:

$$\dot{m}_{path} = \frac{0.006}{8} = 0.0007 \, \frac{kg}{s} \tag{5.28}$$

Volumetric flow rate:

$$\dot{Q} = \frac{\dot{m}}{\rho} \tag{5.29}$$

$\rho = 1030 \, \frac{kg}{m^3}$

$$\dot{Q} = \frac{0.006}{1030} = 7.28 \cdot 10^{-7} \, \frac{m^3}{s} \tag{5.30}$$

Where ρ is the density of 50-50 propylene glycol-water

Velocity:

$$v = \frac{\dot{Q}}{A} \tag{5.31}$$

Where A is the cross-section area of the coolant tube

A = $7.07 \cdot 10^{-6}$

$$v = \frac{7.28 \cdot 10^{-7}}{7.07 \cdot 10^{-6}} = 0.103\ \frac{m}{s} \tag{5.32}$$

Reynolds number

$$R_e = \frac{\rho v D}{\mu} \tag{5.33}$$

D= 0.0015 m

$$R_e = \frac{1030 \cdot 0.103 \cdot 0.003}{0.004} = 80 \tag{5.34}$$

Pressure drop per meter for laminar flow:

$$\frac{\Delta P}{L} = \frac{32\mu v}{D^2} \tag{5.35}$$

$$\frac{\Delta P}{L} = \frac{32 \cdot 0.004 \cdot 0.103}{0.003^2} = 1460\ \frac{Pa}{m} \tag{5.36}$$

Paths	Length per Path (m)	Total Length (m)	Tube Mass (kg)	Fluid Mass (kg)	Velocity (m/s)	ΔP (kPa/m)
4	2.5	9.6	0.14	0.018	0.206	2.93
6	1.6	9.6	0.14	0.018	0.137	1.95
8	1.2	9.6	0.14	0.018	0.103	1.46
10	0.96	9.6	0.14	0.018	0.082	1.17

Table 5.3.6: Path number comparison

Mass estimates were determined using aluminum tubing with an outer diameter of 3mm and thickness of 1mm. The chosen coolant, 50-50 propylene glycol-water, is noncorrosive with inhibitors and because they are not in contact with different metals, galvanic corrosion is not a concern. However, for the PLSS to open and close in compliance with the structure design, an area of flexible tubing must also be integrated. We determined that PTFE-lined braided hoses, which are designed for flexibility in tight spaces, could be implemented to allow for internal access to the PLSS [71] These are commonly used in coolant loops and function within -70° - 250° C (203 -523K), well within our operating temperature, and are resistant to chemical corrosion, including our chosen coolant. We designed the length of the hoses assuming that PLSS would be opened 180° on the hinge side and 40° on the latch side. Because the cooling loop is connected to the avionics boxes, a disconnect is required to open the PLSS all the way.

Component	**Length (m)**	**Comments**
PTFE bend radius	0.0375	1.5 times the minimum bend radius
Bend arc (πR)	0.118	180 degrees
Total hose length (bend side)	0.368	Length of side, radius, plus slack
Latch side	0.161	40 degree opening large enough for disconnect
Component	**Mass (kg)**	**Comments**
PTFE hose estimate	0.02	Stats from "US hose" [13]
PTFE hose with hardware	0.15	Added 0.1kg for QD and fittings
Degree of bend/failure	12.5	Safety factor is greater than 4*OD, considered very safe [14]

Table 5.3.7: PTFE-lined braided hose sizing estimates

Along with the flexible hose, a quick disconnect is required to fully open the PLSS. A quick disconnect would isolate both flow sides, preventing dust from contaminating the loop. Designs such as the QD, Dry Break -3 AN JIC Aluminum are specifically designed for coolant systems with seals compatible with glycol-water coolants. Able to withstand extreme temperatures, they are also light and compatible with aluminum [15].

Figure 5.3.9: Picture of QD, Dry Break -4 AN JIC Aluminum [15]

The total PTFE hose mass, including the quick disconnect, is estimated to be 0.14kg. The degree of bend safety factor for the hoses is 3 times higher than the standard (4 times the outer diameter). Finally, additional sensors and hardware are required to operate and signal any defects in the cooling system. These include two temperature and pressure sensors at both manifolds and small pump to drive the coolant through the loop. The pump was sized for about 20 kPa, accounting for a combined 14 kPa across all paths and assuming 30% efficiency and other frictional losses. All together, these components make up the tubing under the radiator surface that allow for effective heat transfer and safe, reliable, internal access to the PLSS.

Components	**Mass (kg)**
Pressure Sensors x2	0.08
Temperature Sensors x2	0.02
Manifolds x2	0.4
Pump	0.25
Aluminum Radiator Tubing	0.14
PTFE Hose and Quick Disconnect	0.15
Total	**1.04**

Table 5.3.8: Mass breakdown of radiator system

5.3.6 Radiator Coatings (Lindsey)

High emissivity materials are a broad category of coatings that increase the emissivity, and thus the radiative power, of a system. There are a variety of types of high emissivity materials, of which we investigated thermochromic, electrochromic, and standard coatings for this design. Thermochromic and electrochromic are categorized as variable emittance materials, meaning they change their emissive states depending on external stimulus, typically environmental conditions or an external control signal [75]. This transition in emissivity is accomplished through changes in physical conditions, such as optical or phase changes. The difference between thermochromic and electrochromic materials is determined by the stimulus that determines the change in emissivity [76]. These designs come with drawbacks, such as technological readiness and complexity. Thermochromic coatings are optical stacks that are designed to respond to environmental temperature changes, depicted in Figure 5.3.10 [77]. Although these layers can be tailored to different environments, no stack is able to adjust meaningfully in a relatively small temperature range such as that of Mars.

Figure or Table containing sensitive information, or possible unauthorized copyright information has been removed.

Figure 5.3.10: Thermochromic coating stack including the base, spacer, active, and protective layers, listed from bottom to top [18]

Electrochromic coatings have more versatility in tight temperature ranges. This design would require full electrical insulation, complicating the cooling loop that is connected to electronics and other conductive materials. This, and the added electrical complexity required to signal an emissive response, influenced our decision to select a standard emissivity coating. AZ-93 was chosen as our coating due to its simplicity, previous uses in space, and optimal properties in Mars conditions [78].

Figure or Table containing sensitive information, or possible unauthorized copyright information has been removed.

Figure 5.3.11: AZ-93 properties [78]

According to Wien's Law, a radiator operating around 290–300 K on Mars will emit most strongly in the infrared region around 10 μm [79]. With an emissivity of 0.91, AZ-93 allows efficient thermal radiation in this infrared band while maintaining a low solar absorptance of about 0.15, reducing UV degradation over time. While slightly higher than optimal, the solar absorbance can be reduced using protective overcoats. AZ-93 has proficient spacecraft use, is non-toxic once cured, adds negligible mass, and is scratch and dust resistant, according to the manufacturing company AZ-technologies. Additionally, it can be bonded to a wide variety of materials, including aluminum. However, drawbacks such as blunt force impact must be considered since it could cause the coating to fail, though the data on this is limited.

5.4 Thermal Conclusions and Mass Breakdown (Lindsey)

In conclusion, the final thermal control loop balances minimizing consumable water loss for mass savings with maintaining operation and astronaut safety across a wide range of EVA conditions. Analysis showed that a purely SWME-based system creates a severe logistical penalty for Mars missions. At an average steady-state heat load of 500 W, approximately 9 kg of water would be lost during a single EVA, resulting in hundreds of kilograms of consumable water mass over the duration of a mission. In addition to the water loss, the SWME introduces the risk of freezing, which could cause total system failure due to Mars surface temperatures frequently falling well below the freezing point of water. Preventing coolant freezing would require additional insulation, heaters, sensors, and control hardware, further increasing total system mass and complexity. Although eliminating the SWME entirely was initially considered, the highly variable Martian environment and changing astronaut metabolic loads made a fully radiative system impossible under worst-case thermal conditions.

Because of this, the final design adopts a hybrid system that combines the SWME's versatility for peak heat loads with a radiator system designed to significantly reduce water consumption. Separating the thermal system into two loops enabled the design to avoid the freezing and coolant-compatibility limitations associated with routing water directly through a Mars radiator and the SWME. The water-based LCVG loop remains connected to the Mars-adjusted SWME and feedwater tank for direct astronaut cooling, while the second glycol-water loop continuously removes heat emitted from the avionics boxes, pumps, fans, and the LiOH cannister through a radiator system without any consumable losses. This configuration lowers the mass of the thermal system through water storage and low-weight heat pipes for heat transfer, while handling increased heat loads from various design changes throughout the system. This design is able to function in hotter environmental conditions, up to 270K, and periods of increased metabolic rate.

The radiator subsystem was designed around thermal and structural constraints. By distributing coolant through eight parallel serpentine paths beneath the backpack shell, the design achieves low pressure drop, nearly uniform panel temperatures, and effective heat spreading across the radiator surface, while using thin, lightweight aluminum tubing. The selected 50-50 propylene glycol-water coolant provides freeze protection while maintaining thermal conduction performance with only a slightly reduced specific heat capacity relative to pure water and compatibility with aluminum tubing when inhibitors are used. Additional integration challenges, including mitigating galvanic corrosion between copper heat pipes and aluminum cooling tubes, flexible access requirements for the hinged PLSS design, and contamination concerns during maintenance operations, were addressed through the use of epoxy isolation layers, PTFE-lined braided hoses, and quick-disconnect fittings. These additions meet PLSS accessibility requirements without jeopardizing the integrity of the coolant loop and adds minimal mass.

Emissivity coating selection was critical in determining the feasibility of a radiator design. Variable emittance technologies such as electrochromic and thermochromic coatings were investigated because of their ability to adapt to changing thermal conditions. However, limitations in technological readiness, added electrical complexity, and insufficient emissivity variation over the expected Mars temperature range made them less practical for this application. Instead, AZ-93 was selected as the final radiator coating due to its high emissivity and strong protective properties, which are critical for long-duration Mars missions.

Overall, the final design demonstrates that a hybrid thermal control system can substantially reduce consumable water mass carried during an EVA while maintaining reliable thermal control in the Martian environment. Future work includes developing a SWME design capable of operating with coolants other than water, which would allow the LCVG to be routed through the radiator and rely on the SWME during warmer temperatures and increased metabolic loads. The final mass breakdown in Table 5.3.9 demonstrates our savings.

Component Mass	SWME Baseline (kg)	SWME Adjusted (kg)	Final Design (+30% dry and total mass)
SWME	1.6	2.4	2.4
Tank	0.56	1.3	1.0
Water	6.0	9.4	7.4
Radiator components	-	-	1.03
Heat Pipes, Avionics, and crew systems heat transfer	-	-	0.26
*Other	4.34	4.34	2.5
Dry Mass	6.5	8.0	6.6
Total Mass	12.5	17.4	14.0

Table 5.3.9 Final thermal system mass breakdown

** "Other" includes the unidentified mass from the xPLSS breakdown that totals 6.5kg, including heat exchangers, sensors, backup systems, LCVG and other small hardware masses. This value was carried over for the adjusted breakdown. For the final design, the 2.5kg consists of the LCVG mass and SWME mass since other components are accounted for.*

.

6 Power (Daniel Mehreteab)

6.1 Overview

The power subsystem is responsible for storing and delivering electrical energy to all PLSS components throughout the duration of an EVA. Given the mass-constrained nature of the system, the power subsystem was designed with two primary goals: maximizing energy density to minimize battery mass and ensuring astronaut safety through redundant power architecture. This section covers the battery trade study, final technology selection, and the dual-battery system design.

6.2 Battery Trade Study

Four battery technologies were evaluated as candidates for the PLSS power system: lithium-ion (LIB), solid-state (SSB), lithium-sulfur (Li-S), and sodium-ion (SIB). Each was assessed across key metrics including energy density, cycle life, safety, cost, and technology readiness level (TRL).

Lithium-Ion (LIB): The current industry standard for space applications. LIBs are fully flight-proven and perform reliably across most metrics. Their primary limitations are a lower energy density ceiling compared to emerging technologies and inherent safety risks stemming from the use of a flammable liquid electrolyte. The optimal operating temperature range is 20–40°C, which is a design constraint in the extreme thermal environment of Mars.

Lithium-Sulfur (Li-S): Li-S batteries offer an exceptionally high theoretical energy density of up to 2,567 Wh/kg. However, the tested energy density of 350–609 Wh/kg, while impressive, is undermined by a critically short cycle life. Current Li-S pouch cells retain less than 80% capacity after approximately 100 cycles, compared to over 500 cycles for LIBs. This makes Li-S unsuitable for a system intended to support repeated mission EVAs.

Sodium-Ion (SIB): SIBs offer cost-effectiveness and safety advantages, and benefit from the abundance of sodium resources. Their gravimetric energy density of 100–160 Wh/kg and volumetric energy density of 100–200 Wh/L are significantly lower than the alternatives, making them poorly suited for a system where every kilogram matters.

Solid-State (SSB): Solid-state batteries replace the liquid electrolyte with a solid ceramic electrolyte. This eliminates the risk of thermal runaway, as the solid electrolyte is non-flammable and mechanically rigid. SSBs achieve high energy density through the use of lithium-metal anodes. While manufacturing complexity and cost remain challenges, SSBs have reached a TRL of 4–6 and have been successfully tested in relevant space environments.

Battery Type	Energy Density (Wh/kg)	Cycle Life	Safety	Cost	Technology Maturity
Lithium-Ion (Li-ion)	100–265	500–1,000	Moderate	$100 to $150 per kWh	TRL 9 Fully flight-proven
Solid State	400-500	1,000–5,000	Very High	$400 to $800 per kWh	TRL 5-6 Tested in space applications
Sulfur-Lithium	350–609 (tested)	50–100	Moderate	$115 to $151 per kWh	TRL 3-4 Mostly lab + early prototypes
Sodium Ion	100–160	800–1,500	High	$30 to $70 per kWh	TRL 3-4 Mostly lab + early prototypes

Table 6.2.1: Battery Trade Study for PLSS Power System

Based on this trade study, solid-state batteries were selected as the optimal technology for the PLSS power subsystem, offering the strongest balance of energy density, safety, and demonstrated space heritage.

6.3 Solid-State Battery Technology

6.3.1 Operating Principles

Solid-state batteries transport lithium ions between anode and cathode using a solid electrolyte rather than a liquid solution. This architecture has two major advantages. First, the solid electrolyte is non-flammable, eliminating the thermal runaway failure mode that poses a hazard in conventional lithium-ion cells. Second, the use of lithium-metal anodes in place of graphite anodes substantially increases the battery's energy density.

The primary drawbacks of solid-state technology are limited flight heritage compared to lithium-ion systems, manufacturing complexity, and higher cost. These tradeoffs were accepted given the safety-critical nature of astronaut life support and the demonstrated space testing results described below.

6.3.2 Space Heritage and Performance Testing

Solid-state batteries have been successfully demonstrated aboard the International Space Station, where they completed hundreds of charge and discharge cycles in microgravity and showed strong safety, stability, and long operational life. This represents a critical validation for a life support application.

Figure or Table containing sensitive information, or possible unauthorized copyright information has been removed.

Figure 6.3.1: Capacity retention [83]

Thermal performance testing showed an operational discharge range of −40°C to +120°C, with less than 5% capacity variation across the 25°C to 120°C range. At the high end of discharge rates (1C), the battery retains approximately 83% of rated capacity. This wide thermal operating envelope is a significant advantage over conventional LIBs, which are limited to approximately −20°C to 60°C — a constraint that could be problematic given Mars surface temperature extremes.

Rate performance is equally important for a system that may need to deliver peak power during high-activity EVA phases. Figure 6.3.2 shows the discharge capacity at four C-rates: 0.1C, 0.2C, 0.5C, and 1C. At the lowest rate of 0.1C, the battery delivers its full rated capacity of approximately 145 mAh. As the discharge rate increases to 1C — meaning the full battery capacity is drawn in one hour — the battery retains approximately 83% of that capacity, delivering around 120 mAh. This relatively modest capacity loss across a tenfold increase in discharge rate demonstrates strong rate tolerance. For the PLSS, nominal operation will draw at rates well below 1C given the 8-hour EVA duration, meaning the battery will operate near its peak capacity for the vast majority of the mission. The 1C performance also provides confidence that short-duration peak loads, such as fan startup or sensor bursts, will not meaningfully deplete the available energy budget.

Figure or Table containing sensitive information, or possible unauthorized copyright information has been removed.

Figure 6.3.2: Temperature dependence and rate dependence of discharge current [84]

6.3.3 Charging and Cycle Life Comparison

Two additional metrics distinguish solid-state from lithium-ion batteries in a mission context: charging speed and cycle lifetime.

For charging speed, lithium-ion batteries in EV applications reach 80% charge in 23–27 minutes. Solid-state batteries meet the USABC fast-charge requirement, achieving 80% charge in approximately 15 minutes. For a Mars surface mission conducting frequent EVAs, this faster recharge time directly reduces turnaround time between sorties.

For cycle lifetime, lithium-ion batteries show significant degradation after approximately 1,000 cycles. Solid-state batteries retain approximately 90% of original capacity after 5,000 cycles due to reduced mechanical strain on the electrodes. Some designs have demonstrated retention of 80% capacity after 6,000 cycles. This substantially longer operational lifespan improves mission reliability and reduces the logistical burden of battery replacement over an extended mission.

6.4 Power System Architecture

6.4.1 Dual-Battery Configuration

The PLSS power system uses a dual-battery configuration consisting of a main battery and a dedicated backup battery. This architecture mirrors NASA's approach to redundancy in astronaut power systems, ensuring that a single point failure cannot deprive the astronaut of power during an EVA.

The **main battery** is a rechargeable solid-state cell that provides all baseline PLSS power during nominal EVA operations. It is sized to cover the full 8-hour EVA duration with a 2-hour margin at the expected system power draw.

The **backup battery** is a separate rechargeable solid-state cell reserved strictly for emergency use. It is not drawn upon during nominal operations, ensuring that it remains fully charged and available in the event of a main battery failure. This isolation of emergency power directly supports crew safety.

6.4.2 Battery Integration and Servicing

The solid-state batteries are designed as sealed units within the PLSS structure. Charging is performed through an external interface on the backpack, either at the habitat or via a rover charging system, and does not require the astronaut to remove or handle the battery cells. The sealed design minimizes contamination risk and eliminates the need for in-field battery swaps during an EVA.

Battery health monitoring — including voltage, temperature, and cycle count — is managed by the avionics subsystem. Physical replacement of battery cells would be performed during ground servicing or scheduled refurbishment, not by the suited astronaut in the field.

6.5 Power Subsystem Mass Summary

Component	Mass (kg)	Volume (m^3)
Main Solid State Battery	1.25	0.00071
Backup Solid State Battery	0.25	0.00014
Total	1.50	0.00085

Table 6.5.1: Power subsystem mass and volume summary.

7 Structures

7.1 Subsystem Overview (Emma Perez)

This subsystem contains some of the heaviest components of the PLSS, including backplate, cover, hatch, and various smaller hardware such as bolts and mounting brackets. Because these components are responsible for protecting the internal components of the PLSS, structural integrity cannot be compromised, which in turn can increases the mass. This section walks through each of these components and the design approach taken to minimize mass while maintaining the protection of all components housed within the PLSS.

7.2 Subsystem Architecture (Kateryna Sukhina)

As stated previously, the main structural components described in this section, and heavily worked on during the project period, were backplate, cover and hatch. Mass breakdown for these components is shown in the table below.

Backplate	7.84 kg
Cover	8.03
Hatch	< 5kg

Table 7.2.1: Structural components mass breakdown

The hatch is attached to the isogrid backplate via 8 M6 bolts, as shown in the figure below. The cover is bolted to the isogrid on the opposite side, protecting PLSS components that mount to the isogrid.

(A)	(B)
	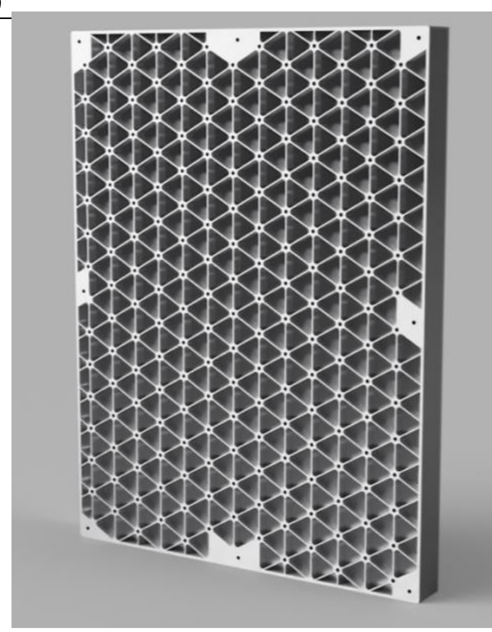

Figure 7.2.1: Assembly of pressurizing hatch and structural backplate. (A) Hatch side facing the suit; (B) Isogrid side facing PLSS components

7.3 Hatch (Kateryna Sukhina)

The hatch is an important component of the EVA suit with a back-entry design. It acts as a boundary between the pressurized conditions of the suit and PLSS components exposed to the environment of the EVA mission, whether it's a vacuum or an atmosphere. The hatch must be able to withstand the pressure force acting on it from the suit side, have no minimal deflection, under which pressure leaks do not occur. On the most recent space suit design, xEMU, the hatch is a separate assembly of a structural plate, sealing O-rings, pressure bladders, and attachment mechanisms. It mounts to the hard upper torso (HUT) of the spacesuit and opens like a door with hinges on one side. It is then also compressed by the PLSS backpack [87].

With the changes to the backplate design, we decided to update the design of the hatch and incorporate it into the PLSS design, instead of it being a part of xPGS as in xEMU design. Referencing the studies done by NASA on the hatch designs and material options [88], we're using the hatch mass options as baseline for comparison of our hatch mass.

The hatch undergone many iterations in the design from a fully Al-6061 hatch, to a completely made of CFRP with coating, to a mix of AL-6061 and CFRP. The following figure shows the design iterations going from the oldest to the newest from left to right. Top and bottom show the front, facing the PGS and back, facing the backplate, respectively.

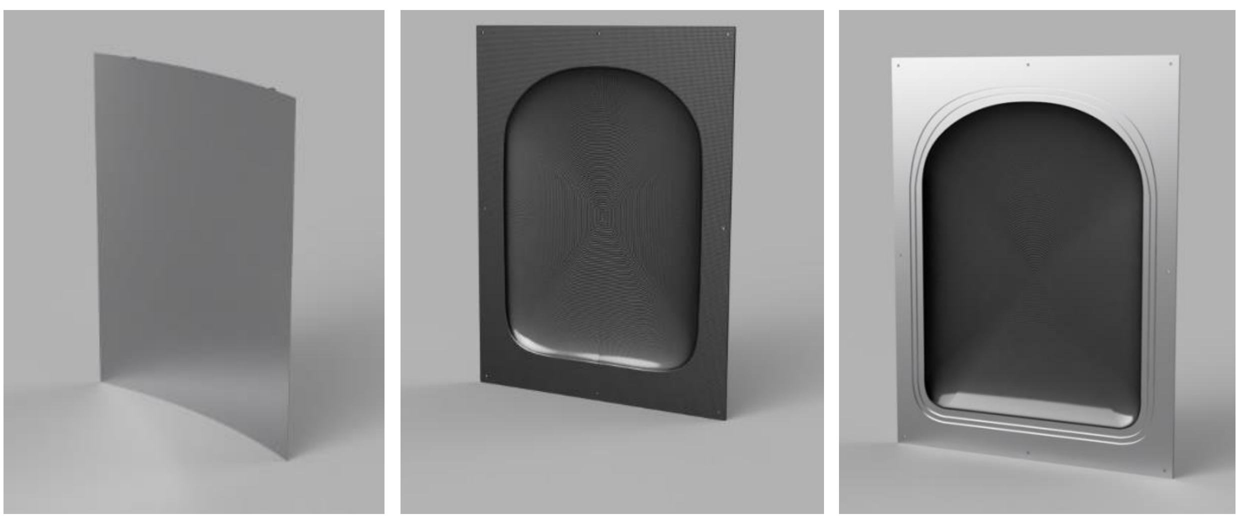

Figure 7.3.1: Evolution of hatch design

To begin estimating dimensions of the HUT, we used the "*Exploration Extravehicular Mobility Unit (xEMU) Hard Upper Torso (HUT) Chamber B thermal vacuum testing results*" paper cited above to estimate the size of the HUT opening and the "*An examination of spacesuit entry types and the effect on suit architecture*" paper on different designs of the back-entry suits to get an idea of dimensions for a realistic HUT opening [89]. We matched the overall height and width of the hatch to that of the isogrid backplate.

The overall dimensions of the hatch are **30.5" (0.7747 m)** height **and 23" (0.5842 m)** width [90]. To simplify the analysis, the hatch was split into a flat sealing face and a domed pressure-facing surface. In earlier versions of the design, sealing O-rings were designed to be on the HUT, with the hatch sealing rim acting on them as a face seal. Upon further consideration, we decided to move the O-rings to the rim of the hatch. This would allow astronauts to get into the PGS easier and follow closer with traditional designs for the hatch. Additionally, for redundancy 2 O-rings are used in this design. The Al-6061 sealing rim would be bonded with CFRP pressure bulkhead. In turn, this assembly is bolted to the backplate.

Looking at the domed pressure-facing surface first, the key design changes were in making it curved as opposed to the flat plate in the xEMU hatch design. This was motivated by the fact that this surface is essentially a pressure bulkhead, and typically any pressure vessel is designed with curved geometry. Key parameters that needed to be estimated to design it were the dimensions of the HUT opening, which as mentioned above were based on dimensions of different HUTs opening found in "*An examination of spacesuit entry types and the effect on suit architecture*" paper. Based on that data, we estimated bulkhead height to be **24" (0.6096 m)** and approximately **18" (0.4572 m)** in width. As shown in the figure below.

Redacted due to Export Control/CUI requirements.

Figure 7.3.2: Hatch pressure bulkhead dimensions

Additional parameters needed to design this part were the rise of the dome, radius of curvature, and thickness. To determine thickness, use thin membrane theory. More specifically stress for a spherical cap under uniform pressure:

$$\sigma = \frac{PR}{2t} \tag{7.1}$$

For simplicity, quasi-isotropic CFRP material with an average yield strength of **356 MPa** [91]. Per NASA safety factor standards, a good SF for composite parts is **2** [92]. This is applied to the yield stress to get maximum allowable stress on the bulkhead. R in equation 7.1 is a radius of curvature, which was calculated via geometric relationships between rise of a dome and its span:

$$R = \frac{b^2}{8h} + \frac{h}{2} \tag{7.2}$$

With h - rise of the dome and b - span of the bulkhead.

Rise of the dome was determined using width (18") as span of the bulkhead and ratio of h/b, which is between 0.02 and 0.1 for a shallow shell. Choosing approximately average value for the ratio 0.055, the rise of the dome was determined to be **1" (0.0254m)**. The resultant radius of curvature is **40.94" (1.04 m)**, and the resulting thickness is **0.097mm**.

Although CFRP is commonly used in pressure vessels for its great performance under tension, its porosity presents a challenge when using it in this application. To compensate for this property of CFRP, the domed surface will be coated.

Turning to the flat rim of the hatch, the main driver for its design is the O-rings and compression forces required for them. We're using Viton O-rings with 0.139" cross-section and shore A hardness (durometer) of 60. Using Parker O-Ring Handbook, designed O-ring grooves according to the standard for face-sealing with 20-30% compression for the chosen O-rings [93]. The figure below outlines in red the groove dimensions we're using for this design. Given that our design includes 2 O-rings for redundancy, as stated above, we decided that 20% compression would be sufficient. With that in mind, gland depth, groove width and groove radius are **0.101", 0.158" and 0.010"**, respectively.

O-Ring Face Seal Glands These dimensions are intended primarily for face type O-ring seals and low temperature applications.

O-Ring Size Parker No. 2	W Cross Section Nominal	W Cross Section Actual	L Gland Depth	Squeeze Actual	Squeeze %	G Groove Width Liquids	G Groove Width Vacuum and Gases	R Groove Radius
004 through 050	1/16	.070 ±.003 (1.78 mm)	.050 to .054	.013 to .023	19 to 32	.101 to .107	.084 to .089	.005 to .015
102 through 178	3/32	.103 ±.003 (2.62 mm)	.074 to .080	.020 to .032	20 to 30	.136 to .142	.120 to .125	.005 to .015
201 through 284	1/8	.139 ±.004 (3.53 mm	.101 to .107	.028 to .042	20 to 30	.177 to .187	.158 to .164	.010 to .025
309 through 395	3/16	.210 ±.005 (5.33 mm)	.152 to .162	.043 to .063	21 to 30	.270 to .290	.239 to .244	.020 to .035
425 through 475	1/4	.275 ±.006 (6.99 mm)	.201 to .211	.058 to .080	21 to 29	.342 to .362	.309 to .314	.020 to .035
Special	3/8	.375 ±.007 (9.52 mm)	.276 to .286	.082 to .106	22 to 28	.475 to .485	.419 to .424	.030 to .045
Special	1/2	.500 ±.008 (12.7 mm)	.370 to .380	.112 to .138	22 to 27	.638 to .645	.560 to .565	.030 to .045

Figure 7.3.3: O-ring groove dimensions

To estimate thickness of the flat rim region, use equation 7.3 for deflection of a thin rectangular plate with clamped edges:

$$\delta = K\frac{qa^4}{D} \tag{7.3}$$

Where, K is the coefficient that depends on boundary conditions, q is the applied pressure, a is unsupported length and D is flexural rigidity:

$$D = \frac{Et^3}{12(1-\nu^2)} \tag{7.4}$$

With E - modulus of elasticity, t – thickness, v – Poisson's ratio.

To maintain the hatch removable and easy to examine, it's mounted to the backplate via 8 M6 bolts. The average distance between bolts is 13" (0.33 m), which is used as a in equation (7.3). Modulus of elasticity and Poisson's ratio for Al-6061 are 68.9 GPa and 0.33, respectively [94]. For simplicity, assuming clamped conditions and using K = 0.002. To get the pressure on the plate, use compression force/unit length for chosen O-rings and approximate sealing width. To accurately estimate the compression force on the O-rings, again referred to Parker handbook and used the figure below.

Figure or Table containing sensitive information, or possible unauthorized copyright information has been removed.

Figure 7.3.4: O-ring compression force chart

This yields a rim thickness of **0.54” (13.7 mm)**. However, that would result in a significantly heavy part (7.1 kg). To help reduce the thickness of the part and provide uniform compression for the O-rings, a latching mechanism has been in development. It is discussed in section 7.6 but suffice to say that introducing such a system provides possibilities to reduce rim thickness and, therefore, to reduce rim mass.

Overall, hatch mass is estimated to be under 5kg. It consists of a CFRP pressure bulkhead, and Al-6061 sealing rim, and these components are bonded together.

7.4 Isogrid Backplate (Emma Perez)

The backplate serves as the structural foundation for the PLSS, providing mounting surface for all the components necessary for Mars mission. It must withstand distributed point load masses from each internal component with minimal deflection, while also interfacing with both the hatch and the outer cover.

In the xEMU PLSS, the backplate was a solid piece of titanium with welded channel designs [90] and weighed about 21.2 kg [8]. To redesign this, we decided to route the tubing directly onto the backplate, which allowed the re-evaluation of the material choice for this component. The new material had to meet several competing requirements: low electrical resistivity and high thermal conductivity to support electronics being directly mounted onto the surface of the backplate, combined with high yield strength and low density to minimize overall system mass.

As seen in the table below, Table 7.4.1, Aluminum 6061 emerged as the clear choice. It offered the strength-to-weight ratio we needed while also being significantly easier to manufacture than titanium and being significantly lighter weight than stainless steel.

Material	Density (kg/m^3)	Yield Strength (MPa)	Thermal Conductivity (W/m-K)	Electrical Resistivity (μΩ-m)	Mass (kg) 24x32x0.3 $inch^3$
Ti-6Al-4V [2B]	4430	~1100	6.70	1.68	21.2
Aluminum 6061-T6 [3B]	2810	~270	167	0.0515	13.4
Stainless Steel 316 [4B]	8000	~310	15.0	0.75	38.2

Table 7.4.1: Trade study table of backplate materials

With the material selected, the next challenge was determining a way to remove unnecessary mass while also providing the most amount of structural support. The solution was found in using an isogrid pattern, whose triangular rib cross sections provide the stiffness and load distribution needed across the surface of the backplate. In order to minimize mass while optimizing strength, the geometry of the isogrid (including skin thickness, rib height, rib width, and triangular cell spacing) had to be carefully calculated. Below is a figure 7.4.1 of the isogrid geometry and the corresponding dimensions.

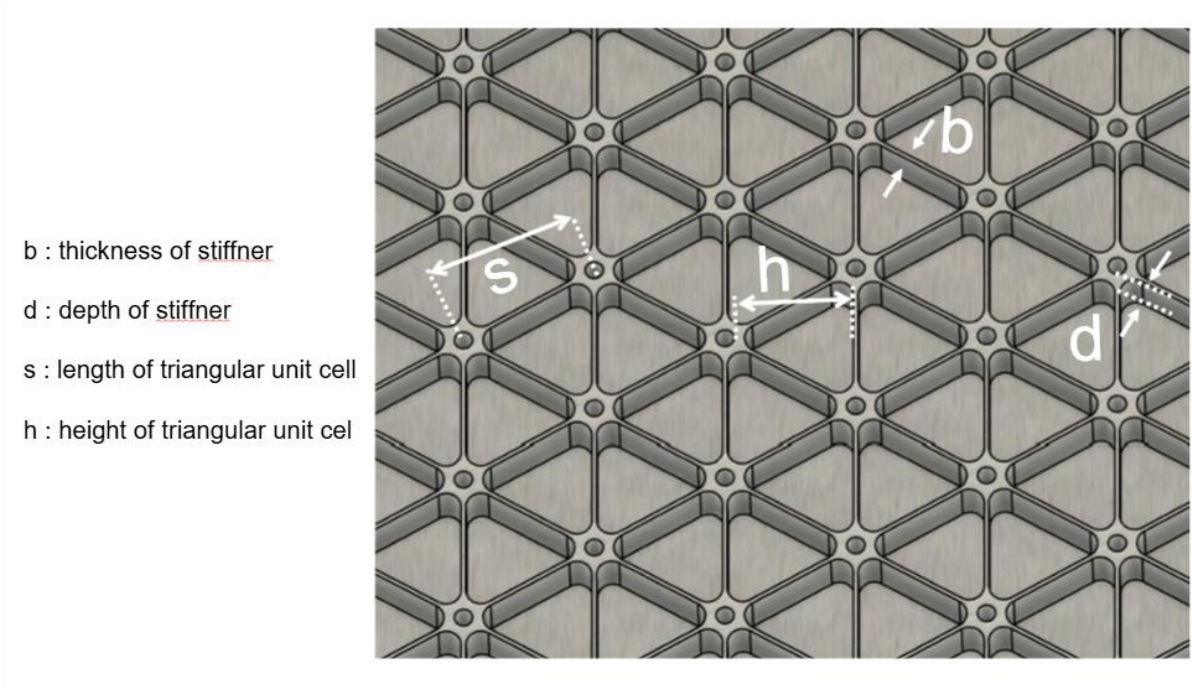

Figure 7.4.1: Isogrid geometry nomenclature

To evaluate the structural performance of candidate geometries, an analytical model based on homogenized plate theory was created referencing JSC-65828B, *Structural Design Requirements and Factors of Safety for Spaceflight Hardware for Human Spaceflight* [98] for factors of safety. The PLSS backplate was modeled as an equivalent homogenized isogrid panel under discrete point loads corresponding to oxygen tanks, avionics boxes, thermal control hardware, battery systems, and life support components. Classical plate theory and Navier-series superposition methods were used to estimate bending stresses and deflections for a clamped rectangular plate. Each subsystem mass was converted into an inertial launch load, where (m_i) is the component mass, (g)is gravitational acceleration, and (n_g) is the Falcon 9 worst-case survivable crash load factor of 9g.

$$F_i = m_i g n_g \tag{7.5}$$

The isogrid structure was homogenized into an equivalent continuous plate using the methodology presented in NASA CR-124075 Isogrid Design Handbook [99]. Homogenization replaces the discrete rib network with an equivalent plate possessing the same overall bending stiffness and structural response, enabling rapid analytical evaluation without detailed finite element modeling.

The rib area parameter, representing the ratio between rib material and skin material within a unit triangular cell, was defined as:

$$\alpha = \frac{b_w d}{th} \tag{7.6}$$

where (b_w) is rib width, (d) is rib depth, (t) is skin thickness, and (h) is the triangular cell height given by:

$$h = \frac{\sqrt{3}}{2} s \tag{7.7}$$

The rib depth ratio was defined as:

$$\delta = \frac{d}{t} \tag{7.8}$$

Using these geometric parameters, the equivalent stiffness parameter was calculated as:

$$\beta^2 = 3\alpha(1+\delta)^2 + (1+\alpha)(1+\alpha\delta^2) \tag{7.8}$$

The equivalent bending stiffness of the homogenized plate was then determined from classical plate theory as:

$$D = \frac{Et^3}{12(1-\nu^2)} \frac{\beta^2}{1+\alpha} \tag{7.9}$$

where (E) is Young's modulus and (ν) is Poisson's ratio.

The equivalent monocoque thickness, representing the thickness of a solid plate with equivalent bending behavior, was calculated as:

$$t^* = \frac{t\beta}{\sqrt{1+\alpha}} \tag{7.10}$$

The equivalent section modulus per unit width was then defined as:

$$S_{eq} = \frac{(t^*)^2}{6} \tag{7.11}$$

The discrete subsystem loads were modeled as concentrated point loads distributed across the backplate at estimated subsystem center of mass locations. Bending moments and deflections were calculated through linear superposition of classical concentrated load solutions for clamped rectangular plates:

$$M(x,y) = \sum_{i=1}^{n} M_i(x,y) \tag{7.12}$$

The resulting bending stress in the homogenized plate was calculated as:

$$\sigma = \frac{M}{S_{eq}} \tag{7.13}$$

Skin buckling was evaluated using classical plate buckling theory with aerospace knockdown factors applied:

$$\sigma_{cr,skin} = K_D \left(\frac{k\pi^2 E}{12(1-\nu^2)}\right)\left(\frac{t}{s}\right)^2 \tag{7.14}$$

where (k) is the plate buckling coefficient and (K_D) is the empirical knockdown factor.

Rib buckling was evaluated using Euler column buckling theory:

$$\sigma_{cr,rib} = K_D \frac{\pi^2 EI}{(KL)^2 A} \tag{7.15}$$

where (I) is rib moment of inertia, (A) is rib cross-sectional area, (L) is unsupported rib length, and (K) is the effective length factor.

Plate deflection was calculated through superposition of concentrated-load plate solutions:

$$\delta(x,y) = \sum_{i=1}^{n} \delta_i(x,y) \tag{7.16}$$

Margins of safety were evaluated for yield, ultimate, buckling, and deflection criteria using:

$$MS = \frac{Allowable}{Actual} - 1 \tag{7.17}$$

The optimization objective was to minimize total backplate mass while satisfying stress, buckling, manufacturability, and deflection constraints:

$$\min(\text{mass}) \tag{7.18}$$

subject to:

$$\sigma \leq \sigma_{allow}$$

$$\sigma \leq \sigma_{cr}$$

$$\delta \leq \delta_{allow}$$

$$\frac{d}{b_w} \leq 20$$

A MATLAB optimization code was developed following these analytical steps, as shown in the accompanying flowchart Figure 7.4.2.

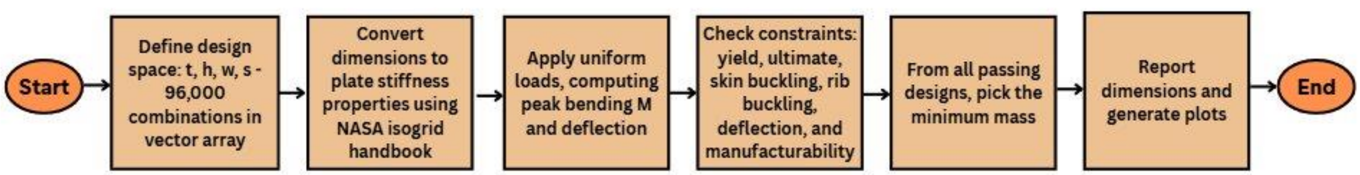

Figure 7.4.2: MATLAB flow chart of isogrid analysis

Essentially, we iterated over arrays of different skin thicknesses, rib heights, rib widths, and cell spacings, converting each combination into equivalent plate stiffness properties using the equations above. Each candidate design was then checked against the stress, buckling, and deflection constraint equations, and only the passing designs were carried forward to evaluate for minimum mass. Following this iteration we see the following solutions:

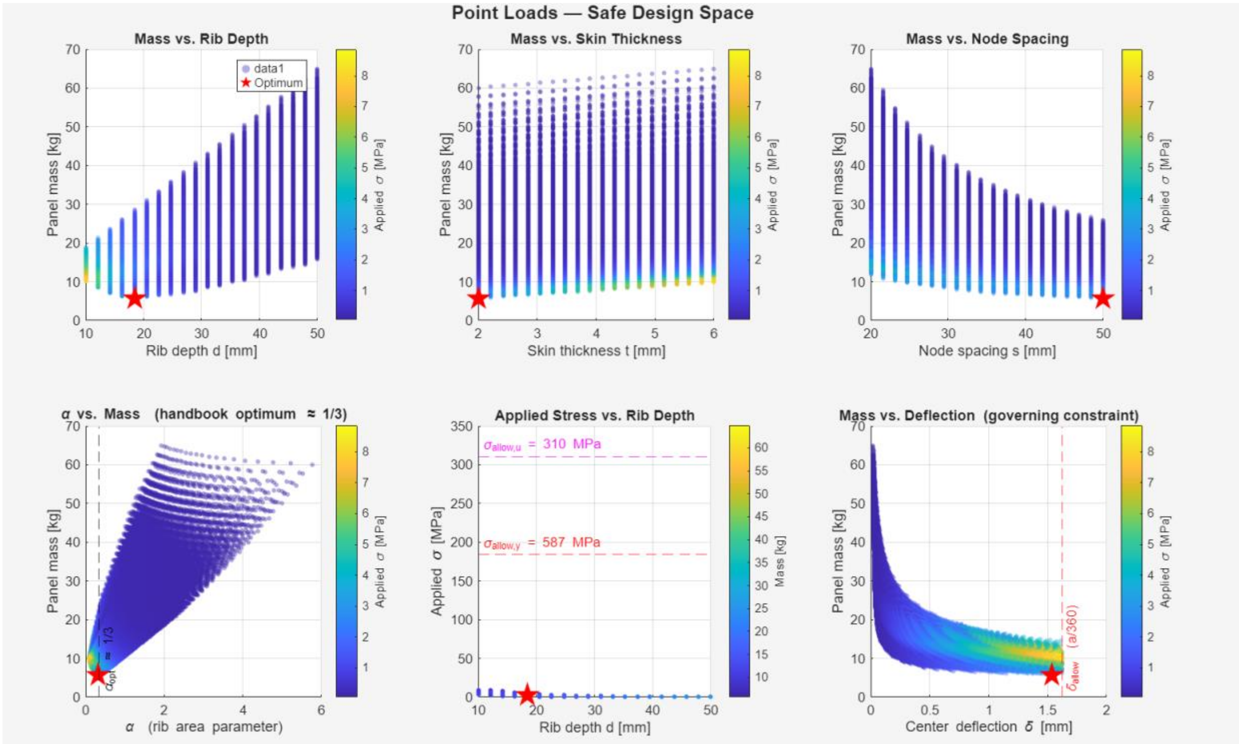

Figure 7.4.4: Full design space analysis, showing every combination of geometry tested and contour plotting by how much stress each design endures.

The figure 7.4.4 above shows the design space rib depth, skin thickness, and node spacing iteration within the defined bounds and structural constraints. The results show across all three geometric parameters, the minimum mass solution (marked by a red star) trended towards shallow ribs, thin skin, and a larger node spacing. It is worth noting that the applied stress across the passing designs remained well below both the yield and ultimate allowable, which is seen in the stress vs. rib depth plot. The governing constraint for the design was deflection, with the minimum mass design reaching a margin of safety of zero.

Figure 7.4.5 shows the design trade space when holding the node spacing, s, held fixed at 50 mm. This confirms the optimization result, showing that the minimum mass geometry identified by the iteration remains within the safe design space at the optimum node spacing. The resulting optimum geometry is summarized in table 7.4.2.

For further view of isogrid calculations and MATLAB script, view appendix 14.1.

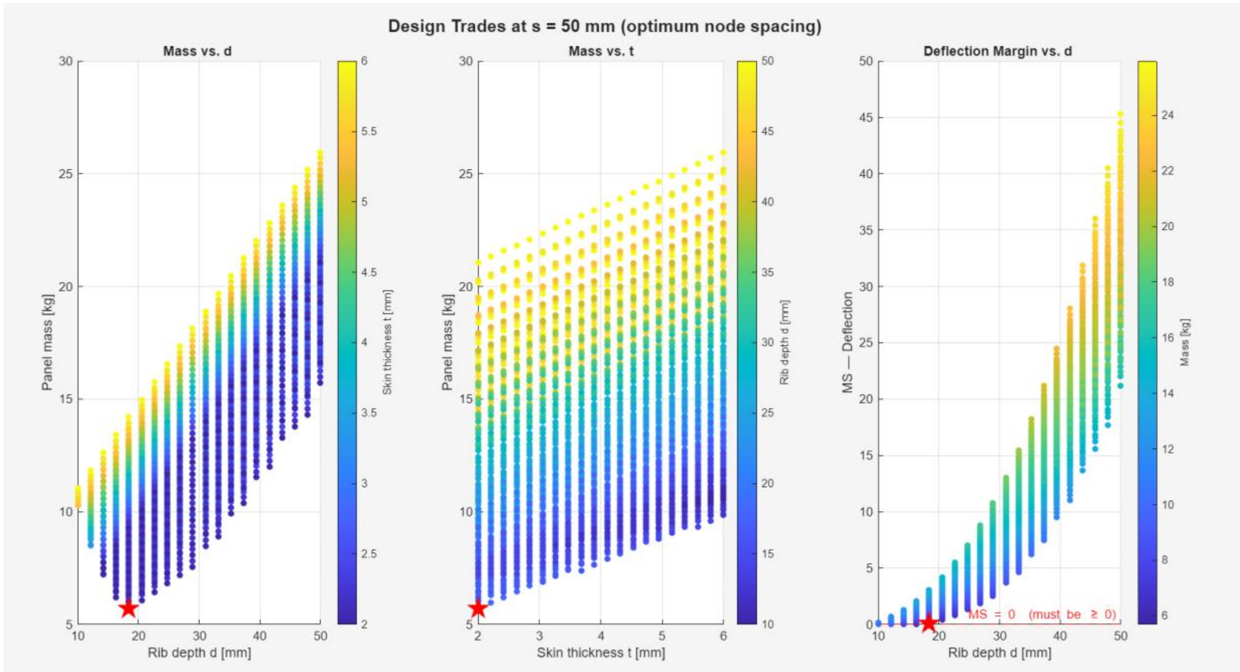

Figure 7.4.5: Design space if node spacing is held constant at 50 mm.

Skin Thickness (mm)	Isogrid Stiffness Depth (mm)	Isogrid Stiffness Width (mm)	Spacing (mm)	Backplate Mass (kg)
2.00	18.42	1.50	50.0	7.84

Table 7.4.2: Optimum geometry result from MATLAB iteration.

To further verify these results, finite element analysis (FEA) was conducted using Autodesk Fusion. An adaptive mesh was applied to the geometry, allowing the solver to automatically refine element density in regions of complex geometry and high stress gradients such as the isogrid ***fins*** and mounting holes.

Boundary conditions were defined by fully constraining all bolt hole faces, simulating a rigid bolted interface with the hatch. These locations and the isogrid fins are recognized as potential stress concentration sites and were therefore the primary regions of interest in this evaluation. Component masses were represented as point masses applied at their respective mounting locations on the backplate, capturing the loading contribution of the assembled hardware.

A load case consisting of a 9g gravitational acceleration. This load factor was selected to simulate crash loading conditions and determine if an adequate margin of safety was met.

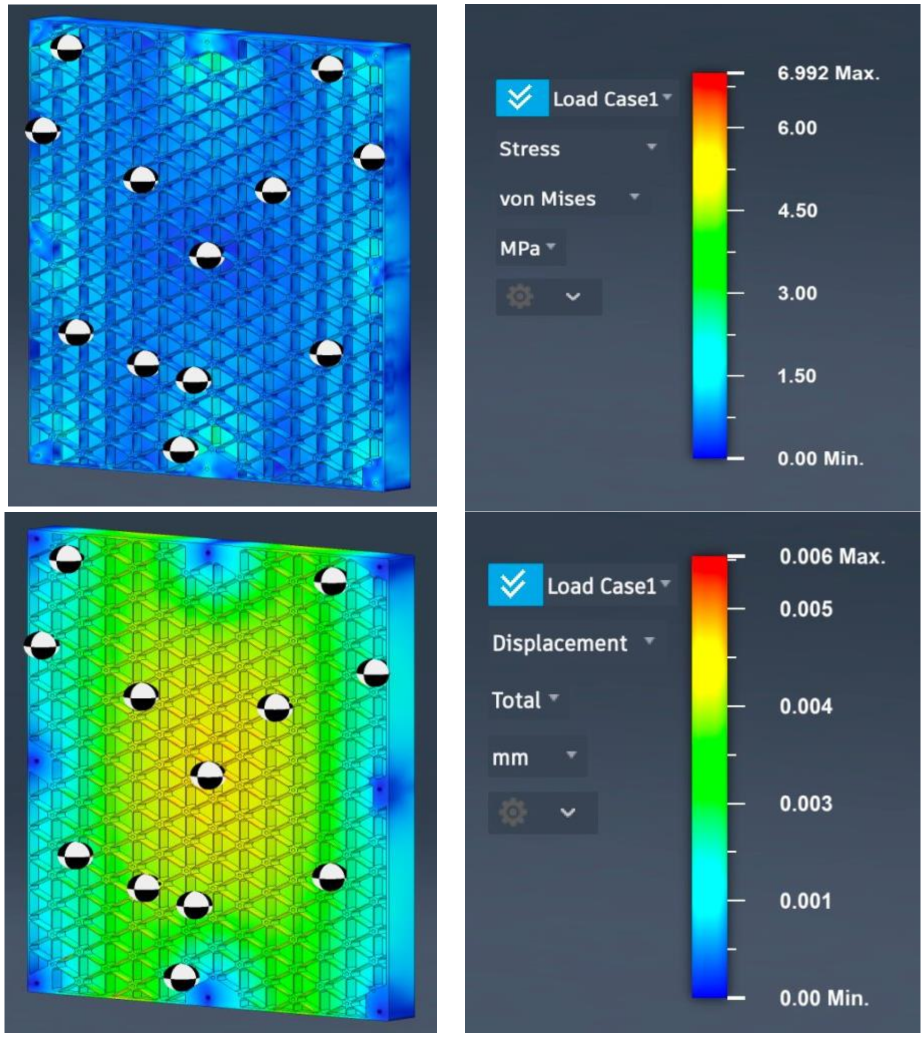

Figure 7.4.6: FEA analysis. Top von Mises stress analysis. Bottom displacement analysis.

The FEA results showed good agreement with the analytical predictions, providing confidence in the final design.

In addition to the isogrid panel, the backplate incorporates a rectangular frame extruding from the rear face, which serves as the attachment interface to the hatch. The dimensions of this frame account for the bolt size requirements as well as the curvature offset distance from the hatch surface.

Initially, it was considered manufacturing the frame as a separate uniform piece, with consistent thickness for bolt and nut plate installation, but this added an additional 3-4 kg estimate to the system. Instead, the frame was integrated directly into the isogrid as a single machined piece (simplifying manufacturing), adding localized reinforcement only at the bolt holt locations to accommodate for the nut plates. This approach allows bolts to be installed and removed from one side without needing to access the nut, which is critical for accessibility and maintenance assembly. The result was a lighter, more integrated solution without sacrificing the structural requirements at the interface.

Redacted due to Export Control/CUI requirements.

Figure 7.4.7: CAD backplate showing isogrid, frame, and reinforced bolt holes.

7.5 Cover (Sid Garg)

The cover is one of the largest components of the PLSS and plays a big role in protecting all the components mounted on the isogrid backplate from the Mars environment and external forces. Material selection and structural design decisions made for the cover had to meet several requirements: mass less than 10.5 kg, structural resistance to impact loads from falling backwards, structural resistance to crash loads, thermal conduction of 150 watts of waste heat away from the PLSS internals, and radiation of that heat into the Martian atmosphere. The Mars environment imposes additional constraints including thermal cycling and Mars regolith.

The old xEMU cover mass is 10.5 kg [8] and used composite materials to protect all sensitive components from external loads and environmental factors.

Mars surface temperatures range from approximately -153°C to +20°C [2C], and over the course of an EVA and across multiple missions, the PLSS cover will be subjected to repeated thermal cycling through this range. Beyond thermal loading, the Martian environment contains regolith that is fine, abrasive, and electrostatically charged, making them prone to damage exposed hardware. The cover serves as the primary mechanical barrier protecting sensitive PLSS components from regolith contact and buildup.

The structural impact loading analysis for PLSS cover panel is where the system is subjected to a backwards fall on the Martian surface. The analysis determines the kinetic energy delivered to the PLSS at the moment of ground contact, which serves as the primary design load for cover regarding material selection, material thicknesses, and isogrid pattern. The fall scenario is modeled as rigid body rotation when the astronaut tips backwards pivoting about the feet, similarly to a falling tree.

The following parameters define the fall scenario:

- Total system mass: m = 230 kg (astronaut + suit + PLSS mass) [101]
- Astronaut height: H = 1.905 m (75 in) [4C]
- Martian gravitational acceleration: g = 3.72 m/s²
- Center of mass height: h_{CoM} = 60%
- Stopping distance: d = 50 mm

The rib depth ratio was defined as:

$$h_{CoM} = 0.60\, H = 1.143\, m \tag{7.19}$$

The suited astronaut and PLSS assembly are treated as a uniform rod rotating about one end. The moment of inertia about the foot contact point is given by:

$$I_{rot} = \frac{1}{3}\, m\, H^2 \tag{7.20}$$

Substituting values:

$$I_{rot} = 278.2\, kg \cdot m^2 \tag{7.21}$$

Conservation of energy is applied to determine the angular velocity at the moment of PLSS ground contact. Gravitational potential energy of the CoM is fully converted to rotational kinetic energy:

$$m\, g\, h_{CoM} = \frac{1}{2} I_{rot} \omega^2 \tag{7.22}$$

Solving for angular velocity ω:

$$\omega^2 = \frac{2\, m\, g\, h_{CoM}}{I_{rot}} \tag{7.23}$$

$$\omega = 2.651\, rad/s \tag{7.24}$$

The linear velocity at the PLSS contact point is obtained from the angular velocity and the contact radius:

$$v_{PLSS} = \omega \times h_{CoM} \tag{7.25}$$

$$v_{PLSS} = 3.031\, m/s \tag{7.26}$$

The total kinetic energy at the moment of PLSS contact is computed from the system rotational inertia and angular velocity:

$$KE = \frac{1}{2} I_{rot} \omega^2 \tag{7.27}$$

$$KE = 978\, J \tag{7.28}$$

The peak impact force is estimated using the energy-displacement method, appropriate when contact duration is unknown but structural stopping distance can be estimated:

$$F = \frac{KE}{d} \tag{7.29}$$

A conservative worst-case check is performed at d = 10 mm, which accounts for sequential deformation of the outer fabric layer and the box beam structure:

$$F_{max} = 97{,}800\ kN \tag{7.30}$$

This section presents the structural load analysis for the Portable Life Support System (PLSS) cover panel under launch vehicle ascent loading. During Falcon 9 potential crash load, the PLSS experiences an acceleration of 9g.

The following parameters define the crash load scenario:

- PLSS mass: m = 60 kg
- Launch vehicle: Falcon 9 (SpaceX)
- Maximum axial acceleration: a = 9g
- Standard gravitational acceleration: $g_0 = 9.81\ m/s^2$

The peak crash acceleration experienced by the PLSS during Falcon 9 is specified as 9g. The equivalent physical acceleration is:

$$a = n \times g_0 \tag{7.31}$$

$$a = 88.29\ m/s^2 \tag{7.32}$$

The inertial force acting on the PLSS assembly is obtained by applying Newton's second law to the assembly mass under the equivalent acceleration. This represents the force that must be transmitted through the cover structure and mounting interfaces:

$$F = m_{PLSS} \times a \tag{7.33}$$

$$F = 5.30\ kN \tag{7.34}$$

Redacted due to Export Control/CUI requirements.

Figure 7.5.1 Cover CAD

Redacted due to Export Control/CUI requirements.

Figure 7.5.2 Labeled diagram of cover components

Label	Component	Description	Mass (kg)
1	Inner Sandwich Beam Layer: Isogrid	11.5 mm thick Al 6061	1.833
2	Middle Sandwich Beam Layer: Foam	30 mm thick Rohacell Hero 110	1.494
3	Outer Sandwich Beam Layer	1.5 mm thick Al 6061	2.256
4	Side Panels	1.5 mm thick Al 6061	2.308
5	Heat Transfer Pins	6 mm diameter Al 6061	0.139
		TOTAL	**8.03**

Table 7.5.1 Cover component breakdown with final mass total

The beam type was selected by comparing four candidate cross-section types: a monolithic CFRP shell, a composite I-beam, a box beam, and a sandwich panel. Each was evaluated against the three requirements: bending stiffness under distributed load, impact energy absorption during a backward fall, and a viable thermal conduction path through the panel thickness.

A monolithic composite shell concentrates all structural material at a single thickness, which is mass-inefficient for bending-dominated loading. More critically, an unreinforced CFRP shell has poor impact toughness. Carbon fiber composite structures are relatively brittle, but they resist deflection well under quasi-static load but fail suddenly under impact without absorbing significant energy. Meeting the fall and crash load cases with this material would require a very heavy laminate.

An I-beam cross-section addresses the bending efficiency problem by placing material in the flanges at maximum distance from the neutral axis. However, adapting it to a cover face would require long flanges which could locally buckle and has an open web geometry that provides no core volume for energy absorption or thermal conduction.

A box beam solves the enclosure problem and adds torsional stiffness that open sections lack. Box sections in aluminum or composite are the standard choice for crash structures because their closed geometry enables controlled progressive crushing. However, a box beam is still a one-dimensional structural member; tiling multiple box beams to form a panel face is structurally inefficient.

A sandwich panel combines the key advantages of each alternative while avoiding their primary limitations. The face sheets are placed at maximum distance from the neutral axis and carry bending-induced normal stresses. The core carries transverse shear and, critically, absorbs impact energy that neither the I-beam nor box beam can replicate over a panel geometry. The enclosed construction provides a continuous surface to prevent regolith from damaging sensitive components.

With the sandwich beam architecture established, there are several foam options available in the Rohacell HERO family. Rohacell HERO-110 has the best properties for our use case even though it has a higher density when compared to HERO-51 and HERO-71.

Grade	Density (kg/m^3)	Comp. Strength (MPa)	Tensile Strength (MPa)	Elongation at Break (%)	Max Shear Strain (%)	Max Autoclave Temp (°C)
HERO-51	52	0.6	2.6	8.0	7.0	180
HERO-71	75	1.1	4.1	9.5	7.2	180
HERO-110	110	2.5	6.3	9.9	7.2	180

Table 7.5.2 Rohacell HERO Family Mechanical Properties [103]

The one property Rohacell HERO-110 does not provide is thermal conductivity. The cover must conduct 150 watts of waste heat from the PLSS internals to the outer radiating surface. Therefore, there is an array of Al 6061 pins is integrated through the core thickness on the back panel to provide the required conduction path. Pin diameter and amount are to be determined by the following analysis that will allow 150 watts of heat to pass through the cover into the Mars atmosphere.

The following parameters define the pin array thermal analysis:

- Governing heat load: Q = 150 W
- Maximum allowable temperature rise across core: ΔT = 15 K (design target)
- Back panel area: A = 30.5 × 23 in = 0.4526 m^2
- Foam core thickness: L = 30 mm = 0.030 m
- HERO-110 thermal conductivity: k_{foam} = 0.0282 W/(m·K) [5C]
- Al 6061-T6 thermal conductivity: k_{Al} = 167 W/(m·K) [6C]
- Al 6061-T6 density: ρ = 2700 kg/m^3 [6C]
- Pin diameter: d = 6 mm = 0.006 m
- Array pattern: square grid

For a square pin array with pin diameter d and center-to-center pitch p, the aluminum area fraction φ is:

$$\varphi = \frac{\pi(d/2)^2}{p^2} \tag{7.35}$$

The effective through-thickness conductivity of the composite panel is:

$$k_{eff} = \varphi \cdot k_{Al} + (1 - \varphi) \cdot k_{foam} \tag{7.36}$$

The temperature rise across the panel under heat load Q is:

$$\Delta T = \frac{Q \cdot L}{A \cdot k_{eff}} \tag{7.37}$$

Rearranging Equation 19 for the minimum effective conductivity required to satisfy the 15 K budget:

$$k_{eff,req} = 0.663\ W/(m \cdot K) \tag{7.38}$$

Solving Equation 18 for the required area fraction:

$$\varphi_{req} = \frac{k_{eff,req} - k_{foam}}{k_{Al} - k_{foam}} \tag{7.39}$$

$$\varphi_{req} = 0.00380 = (0.38\%) \tag{7.40}$$

An aluminum area fraction of 0.38% is sufficient to carry the full 150 W load. This is a direct consequence of the large conductivity ratio between Al 6061-T6 and HERO-110 foam (k_{Al} / k_{foam} ≈ 5,920).

With pin diameter fixed at 6 mm, Equation 7.41 is solved for the required center-to-center pitch:

$$p = \sqrt{\frac{\pi(d/2)^2}{\varphi_{req}}} \tag{7.41}$$

$$p = 0.0863\, m \approx 3.40\, in \tag{7.42}$$

A 3.40-inch pitch on the 30.5 × 23 inch back panel yields a square grid of 9 columns by 7 rows. The total pin count is:

$$N = 63 \;\; pins \tag{7.43}$$

The total aluminum volume required is determined from the minimum area fraction φ_{req}:

$$V_{total} = \varphi_{req} \times A \times L \tag{7.44}$$

$$V_{total} = 5.16 \times 10^{-5}\, m^3 \tag{7.45}$$

The total mass of all pins is:

$$m_{total} = \rho \times V_{total} \tag{7.46}$$

$$m_{total} = 0.139\, kg \tag{7.47}$$

Using this thermal analysis, the aluminum pins will add 0.139 kg to the overall cover mass and span from the isogrid to the thin aluminum plate 30 mm away.

The isogrid structure will be the innermost layer of the three-layered cover design. Following similar calculation and material selection to that of the isogrid backplate analysis, the panel dimensions are 775 by 584 mm (30.5 x 23 in.) and the material is Al 6061-T6. The governing impact load was derived assuming the worst case impact scenario of a fully loaded 230 kg astronaut and suit system from a standing height of 1.1 m on the Martian surface. This yields an impact kinetic energy was calculated as:

$$KE = 0.5m(2gh) \tag{7.48}$$

Yielding a kinetic energy of about 472 J. The outer layer and foam interior absorb a portion of this energy prior to any load impact reaching the isogrid structure. The residual kinetic energy transmitted to the isogrid was calculated as the difference between the total impact energy and the energy absorbed by the initial two layers seen in previous sections. An ultimate safety factor of 2.0 was applied to the resulting peak force.

The isogrid geometry was optimized using the same iterative approach as in the backplate section. It follows a four parameter design space: skin thickness, rib depth, rib width, and rib spacing. Isogrid equivalent stiffness and section modulus were computed following the methodology described in the backplate analysis per the Isogrid Design handbook [99]. The deflection and stress constraints were evaluated against a 20 mm allowable deformation limit and the Al 6061-T6 allowable stress, with the minimum mass design selected from all configurations satisfying both constraints. The optimized isogrid mass and dimensions are seen in the figure below. Full calculation MATLAB code see appendix 14.3.

Skin Thickness (mm)	Isogrid Stiffness Depth (mm)	Isogrid Stiffness Width (mm)	Spacing (mm)	Isogrid Mass (kg)
1.50	10.0	1.50	150.0	2.26

Table 7.5.3 Optimum geometry result from MATLAB iteration isogrid cover design

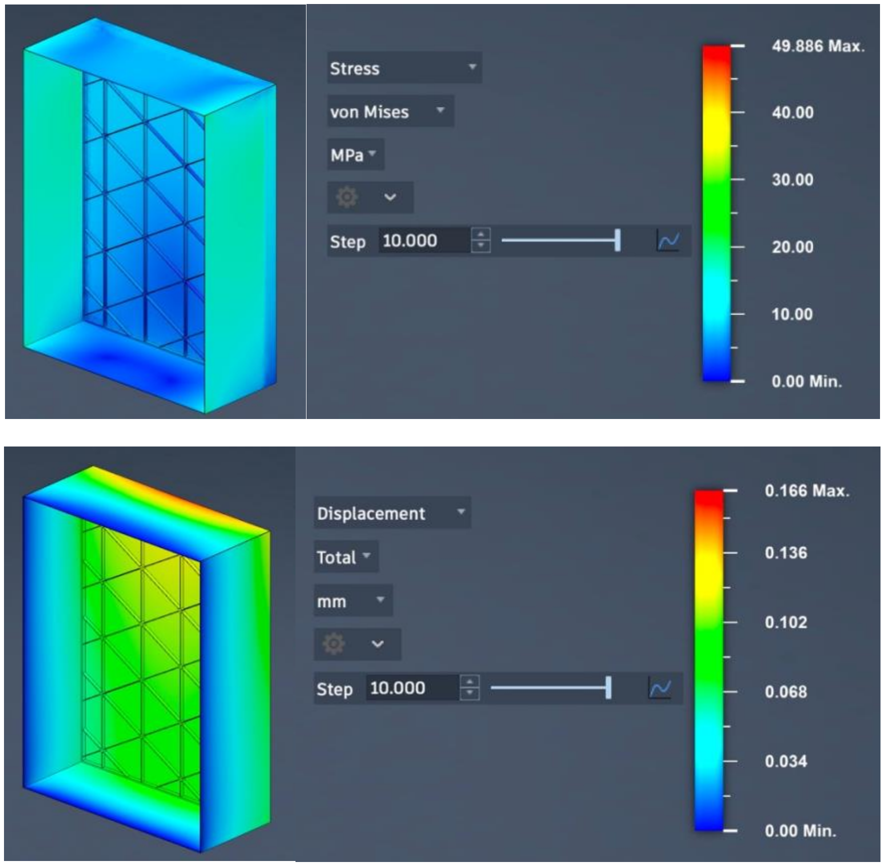

Figure 7.5.3 Impact Loading FEA for Cover

The impact force load was applied on the top edge of the cover. The FEA results show a minimum safety factor of 5.5, which is over the required amount of 2. This validates this cover design for use on Mars.

7.6 Latches (Kateryna Sukhina)

As mentioned before, in the hatch section of the report, a properly designed latching mechanism will supply uniform compression loading on the O-rings, yield in decreasing thickness of the sealing rim, thereby reducing its mass, and simplifying overall usage of the suit for the astronaut.

Key parameters required to design the latching mechanism are as follows: total force required to compress the O-rings, number of latches and spacing between them. Referencing Parker O-ring Handbook, total compression force on an O-ring can be found by multiplying its cord length by compression force per inch of length, defined as a range of force values based on O-ring cross section and durometer [7A].

$$F_{total} = \frac{F_{compression}}{inch} * cord\ length \tag{7.49}$$

For the O-rings used in our design, reference figure 7.2.1.4 to get compression force per unit length. Cord lengths differ slightly between the inner, closer to the pressure bulkhead, and outer O-rings. Smaller being 80" and larger 83". Using average compression force per unit length of 5.5 lbf/in, this results in total compression forces of **440 lbf (1957.2 N)** and **456.6 lbf (2030.6 N),** respectively. So, the total compression force for both O-rings results in **896.5 lbf (~4000 N)**.

To effectively reduce required thickness of the hatch rim, refer to equation (7.50) in section 7.2.1 and unsupported length parameter, a, for latch spacing. Given that this term is raised to the fourth power, decreasing it, will significantly decrease required thickness:

$$t_{rim} = (K\frac{qa^4 12(1-\nu^2)}{E\delta})^{\frac{1}{3}} \tag{7.50}$$

As an example of how much mass optimization this would provide, plugging the same constats as in section 7.2.1, but adjusting a to be 6" instead of 13" reduces required thickness of the rim from 0.54" to 0.2". This results in a 3 times lighter sealing rim. However, trade-offs must be carefully considered in designing the latches. The smaller parameter a becomes, the more latches are required, which can increase overall mass of the latching mechanism. Additionally, total compression force is divided evenly between the latches, therefore the more latches are used, the less compressive force per latch is required. In turn, generally the less compressive force is required per latch, the lighter it is. Hence, additional trade-off between number of latches and their mass is introduced.

Overall, although the general estimation of number of latches and compression force required per latch is fairly straightforward, more considerations need to be accounted for as the design matures.

7.7 Life Support Brackets (Sid Garg)

The life support brackets, or the O2 tank brackets, requires structural analysis to determine the required clamping force per clamp to prevent tank sliding under crash loading with friction, the corresponding bolt preload torque required to generate that clamping force, and the margin of safety for the M6 fastener under the applied preload. The governing load case is the Falcon 9 crash load at 9g axial acceleration. Two tank configurations are evaluated: a primary O2 tank and a secondary O2.

The following parameters define the bracket clamping analysis:

- Governing load: Falcon 9 crash load, $n = 9g_o$
- Standard gravitational acceleration: $g_0 = 9.81\ m/s^2$
- Mass of primary tank with oxygen: $m_1 = 3.9$ kg
- Mass of secondary tank with oxygen: $m_2 = 7.6$ kg
- Number of clamps per tank: 2
- Number of bolts per clamp: 1
- Coefficient of static friction (aluminum on carbon fiber): $\mu = 0.23$ [1F]
- Torque coefficient: $K = 0.18$ [2F]
- Bolt diameter: $d = 6$ mm (M6)
- Factor of Safety required: FS = 2
- M6 Grade 8.8 Bolt Preload: $T_{allow} = 11.8$ Nm [3F]

The tank is retained by two clamps. For two clamps to collectively resist the total inertial force $F_{inertial}$ via friction, the required clamping force per clamp is derived from friction equilibrium:

$$F_{clamp} = \frac{mn}{2\mu} = \frac{9mg_o}{2\mu} \tag{7.51}$$

For the primary tank ($m_1 = 3.9$ kg):

$$F_{clamp,1} = 748.6\ N \tag{7.52}$$

For the secondary tank ($m_2 = 7.6$ kg):

$$F_{clamp,2} = 1{,}458\ N \tag{7.53}$$

The bolt preload required to generate the clamping force is determined using the standard torque-tension relationship per the NASA Preloaded Joint Analysis Methodology for Space Flight Systems [4F]:

$$T = NKd \tag{7.54}$$

where T is the applied torque, N is the required bolt preload (equal to the clamping force F since one bolt per clamp), K is the torque coefficient, and d is the nominal bolt diameter.

For the primary tank:

$$T_1 = 0.808\ N \cdot m \tag{7.55}$$

For the secondary tank:

$$T_2 = 1.575\ N \cdot m \tag{7.56}$$

The margin of safety for each bolt is calculated by comparing the applied bolt preload to the M6 bolt preload specifications:

$$MS = \frac{T_{allow}}{FS\ x\ T_{applied}} - 1 \tag{7.57}$$

For the primary tank bolt:

$$MS_1 = 3.7 \tag{7.58}$$

For the secondary tank bolt:

$$MS_2 = 2.7 \tag{7.59}$$

These results prove that both bolts pass the margin of safety requirement. The primary tank bolt carries a larger margin due to its lower tank mass and correspondingly lower required clamping force relative to the M6 bolt allowable.

7.8 Bolts (Emma Perez)

The attachments for the components and isogrid + hatch assembly require a simplified bolt analysis. The analysis evaluated bolt shear failure and bearing failure within the Al 6061-T6 backplate structure under worst case launch loading conditions. Table 7.8.1 summarized the input parameters and material properties used in the bolt joint verification analysis.

Parameter	Symbol	Value	Units	Notes
PLSS total mass	M	63	Kg	Fully loaded
Launch acceleration	a	88.3	m/s^2	9g
Ultimate safety factor	SF	2.0	-	Per program requirement
Number of attachment bolts	N	8	-	Equal load distribution assumed
Bolt diameter	d	6	mm	M6 fastener
Effective bearing thickness	t	57	mm	Isogrid + frame at joint interface
Al 6061-T6 yield strength [3B]	$\sigma_{y,Al}$	275	MPa	Bearing allowable
Grade 8.8 bolt yield strength [1G]	$F_{tu,bolt}$	830	MPa	ASTM F568M, Class 8.8, full-size
Allowable bolt shear [2G]	$F_{su,bolt}$	479	MPa	0.577 × F_tu,bolt (von Mises)

Table 7.8.1: Input parameters for M6 bolt analysis.

The total inertial launch load was calculated using the fully loaded PLSS mass subjected to a 9g acceleration environment with an ultimate factor of safety of 2.0 [99]:

$$F_{total} = ma \cdot SF \tag{7.60}$$

where (m) is the total PLSS mass (for this analysis we assumed 63 kg [8]), (a) is the applied launch acceleration, and (SF) is the ultimate safety factor. The total load was assumed to be distributed equally across four structural attachment bolts:

$$F_{bolt} = \frac{F_{total}}{N_{bolts}} \tag{7.61}$$

where ($N_{bolts} = 8$).

Bolt shear stress was evaluated assuming single-shear loading on each M6 fastener. The bolt shear area was calculated as:

$$A_{shear} = \frac{\pi d^2}{4} \tag{7.62}$$

where (d) is the bolt diameter. The resulting bolt shear stress was then determined from:

$$\tau_{bolt} = \frac{F_{bolt}}{A_{shear}} \tag{7.63}$$

The allowable bolt shear stress was determined using the von Mises distortion energy criterion applied to the Grade 8.8 minimum ultimate tensile strength per ASTM F568M:

$$F_{su,bolt} = 0.577F_{tu,bolt} \tag{7.64}$$

This approach is consistent with NASA-STD-5020B, which defines the allowable ultimate shear load based on the fastener material ultimate shear strength rather than yield strength.

Bearing stress within the Al 6061-T6 isogrid and frame structure was evaluated using the projected bearing area between the bolt and surrounding material:

$$\sigma_{bearing} = \frac{F_{bolt}}{dt} \tag{7.65}$$

where (t) is the effective structural thickness at the joint interface. A conservative bearing allowable equal to the Al 6061-T6 yield strength was assumed for preliminary sizing purposes.

Margins of safety for both shear and bearing failure modes were calculated using equation 14 in the backplate section. The governing joint failure mode was identified as the minimum margin of safety across all evaluated failure mechanisms. Joint adequacy was verified when all margins of safety exceeded unity.

A MATLAB verification script was developed to automate the bolt shear and bearing calculations, identify the governing failure mode, and verify compliance with structural safety requirements under worst-case launch loading conditions. Full calculation and code can be seen in Appendix 14

Parameter	Value	Units
Total ultimate inertial load, F_{total}	11,124.5	N
Load per bolt, F_{bolt}	1,390.6	N
Applied bolt shear stress, τ_{bolt}	49.18	MPa
Allowable bolt shear stress, $F_{su,bolt}$	461.60	MPa
MS – bolt shear	**8.39**	-

Governing failure mode	Bolt shear	-
Minimum margin of safety	**8.39**	-
Joint status	**PASS**	-

Table 7.8.2: Bolt analysis results table

Both failure modes that were evaluated, bolt shear and bearing, result in margins of safety (MoS) well above the requirement under worst-case ultimate launch loading. The governing failure mode is bolt shear with a MoS of 8.39. Bearing stress within the isogrid and frame structure is less critical as the MoS is 66.63. These results confirm that the eight M6 Grade 8.8 bolts provide adequate structural margin for the isogrid and hatch assembly under the 9g ultimate load environment.

7.9 Structures Conclusion

The structural analysis presented in this section of the report demonstrates that the isogrid geometry design will reduce backplate mass by 55%. This shows significant weight savings for Mars mission and reduces the astronaut workload in this environment. The bolt analysis confirms that M6 bolts will provide substantial structural margin under worst case 9g ultimate launch loading. These results provide adequate analysis to be further verified by fabrication and physical testing.

Hatch designed as part of the PLSS backpack simplifies the system and shows promising results for mass savings as compared to the current xEMU hatch. With careful designing of the latching system, such a configuration would allow the astronaut to open the PLSS backpack autonomously, removing the need to assistance during donning and doffing of the suit.

Cover reduces mass by 2.47 kg while still providing impact resistance if the astronaut falls backwards. This new cover design features a sandwich beam with a Rohacell HERO-110 foam core for impact resistance and an isogrid for reduced deflection. Designed for the worst case scenarios of falling backwards impact load and Falcon 9 crash loads, the cover has a new mass of 8.03 kg with a 23.5% reduction compared to the old xEMU design. In the future, some more work needs to be done including incorporating a small door to allow for ease of maintainability in the event something doesn't work and doing analysis on a curved cover design instead of the current simplified flat cover.

8 Risk Assessment and Mitigation

8.1 Risk Overview (Sara Carter)

Due to the nature of the PLSS, risk analysis and mitigation is incredibly important throughout the design process to ensure that the final product will be safe and prevent the astronaut from getting killed. We have used NASA STD-6105 to properly evaluate the safety of our systems. Throughout this process, a majority of the components that are included in the PLSS are already thoroughly risk mitigated through their intrinsic requirements, as defined by NASA, the team, and the project definition.

8.2 Risk Process (Sara Carter)

The risk process started with us defining the risk assessment through NASA STD-6105. This includes the risk table, the designation of risk within the table, and the designation of ratings of Likelihood and Consequence on a scale of 1 to 5. The table is show in Figure 8.2.1, where green section represents low risk, yellow is medium risk, and red is high risk.

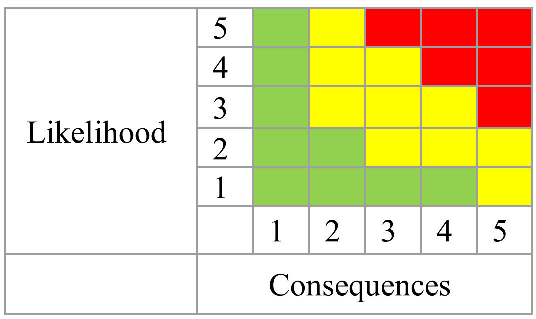

Figure 8.2.1: Risk Analysis Matrix [111]

To determine the placement of each components, a chart corresponding to the 1 to 5 scale were created based on more NASA standards, and is as follows.

5x5 Rating	Qualitative Likelihood	Quantitative Likelihood - Personal Injury/Illness	Qualitative Severity
5	Very high	10% or more (1/10)	Injury or illness resulting in fatality or permanent total disability
4	High	Less than 10% (1/10)	Injury or illness resulting in permanent partial disability
3	Moderate	Less than 1% (1/100)	Injury or illness resulting in days away from work or hospitalization
2	Low	Less than 0.1% (1/1,000)	Short term injury or illness
1	Very low	Less than 0.01% (1/10,000)	Minor injury

Table 8.2.1: Risk Scale Designations

These were then implemented into a sheet to be evaluated through a process of talking to each subteam and collecting all of the components that they had done research on. A baseline risk was evaluated against the discretion of the applicable subteam, the systems subteam, and the defined requirements for the project.

8.3 Risk Sheet (Sara Carter and Chris Witherspoon)

Subteam	Component	Severity	Explanation	Occurrence	Explanation	Mitigations	Risk
CS (C)	Oxygen Tanks		Contains backup systems - 2 hour extra reserve and secondary tank		Very unlikely but contains many different posibilities (suit puncture, tank rupture, tubing material tear, valve failure)	Senors that alert presure and oxygen levels, proper gas dispersion, and structural integrity	Low
CS (C)	CO2 Scrubber (LiOH/TCC/Particulate Filters)		They are able to act as a consumable for excess oxygen (but there isn't too much time ~<30 mins)		If juts one of the 2 components fails in either of the loops the entire loop would fail	Should be able to operate for some time without battery - the 2nd tank pushes oxygen continously if (without fans) if the first tank fails	
CS (C)	Oxygen Tubing		The oxygen tubing is necessary throughout the PLSS to deliver oxygen to the astronaut. This is necessary for both the primary and secondary (backup) tank		Inconel 625 - slide 21		
CS (C)	Temperature Sensor		The PLSS could still operate without the temperature sensor however the mitigations to detect potential failure would be at loss				
CS (C)	Pressure Sensor (100% O2 oxygen sensor not a pressure sensor)		The PLSS could still operate without the pressure sensor however the mitigations to detect potential failure would be at loss				
CS (C)	Gauges		Gauges are essential for proper regulation/dispersion of flow throughout the PLSS system		(valve etc - Monel K-500) - slide 21		

Subteam	Component	Severity	Explanation	Occurrence	Explanation	Mitigations	Risk
PPT (C)	Solid State Battery		There would likely be astronaut fatality if the battery failed		There has been astronomical environmental testing that shows VERY unlikely failure of the battery	Sensors indicating low/critical battery health - adding a secondary smaller battery for redundancy	Very low
PPT (C)	Thermochromic Coating		If the coating is broken the SWME would make it up (the cure time is 7 days)		It can get scratched but it's lowkey invincible		
PPT (C)	Heat Tubing (water cooling for electronics)		There are 4 (2 avionics and 2 crew systems) - if one broke then there is no more heat but the others can still function				
PPT (C)	Sensor		If the sensors fail to detect temperature to properly regulate ventilation, then the SWME can just directly vent out to avoid temperatures from getting too hot				
PPT (C)	SWME		If the main SWME fails then the backup SWME kicks in to ventilate properly		Performance degradation only occurs after about 1200 hours of continuous testing (over 100 missions)	Pressure and temperature sensors to monitor prediction of mechanical failures	
AFSS(S)	Avionics Box	4	The electronics would stop working or malfunction from high heat - this results in failure for the whole system	1	Active cooling for the box exists from power but the material itself might not have proper cooling	Temperature sensors present throughout the avionics box, cooling tubes also remove heat from the system	Low
AFSS(S)	Controllers	3	Controllers dictate the flow of O2 throughout the system, but since Oxygen has emergency flow then low risk of	1	Backup controllers means low likelihood of failure	Backup controllers provide a requirements level mitigation	Low

Subteam	Component	Severity	Explanation	Occurrence	Explanation	Mitigations	Risk
			injury, unless all systems fail				
AFSS(S)	Communication	1	Communications include the radio and Wi-Fi, which would be inconvenient if they stopped working but not catastrophically hazardous.	1	No Backup systems, but technology has been used in past PLSS's, so they are reliable.	No mitigations here due to lowest Risk level, but components will be looked over during maintenance.	Low
LSM (S)	Pressure Plate	5	High potential for fatality if there is a rupture of the pressure plate	1	Pre-loaded bolts, re-enforced hinges, and double O-ring seal have low chance	Leakage should be detected through pressure sensors and potential detection of rupture thru plate deformation	Medium*
LSM (S)	Isogrid	5	Bucking/deformation are low severity but would need to be fixed before a future EVA. Full shearing would result in PLSS disassembly	1	High strength margin which results in low chance of failure	Deformation should be visible and detection thru radiographic testing equipment	Medium*
LSM (S)	Shell	5	High severity if the astronaut falls and crushes components. Lower severity if the cover just falls and exposes components	1	Does not have the highest strength margin, which could result in failure with a backwards fall	Deformation should be visible and inspections would take place after any fall	Medium*
LSM (S)	O-rings	4	High severity if seal gets ruptured due to loss of pressure in suit. Two larger O-ring layers solve for that.	1		Pre-EVA O-ring seals should be checked and in maintenances O-rings should be examined	Low

Table 8.3.1 Risk Sheet (S-Sara, C-Chris)

8.4 Risk Analysis - Challenges (Chris Witherspoon)

8.4.1 Configuration Management and Inter-Subteam Risk Synchronization

The primary operational bottleneck encountered during the risk assessment phase was maintaining a synchronized baseline across multiple engineering domains. Because the risk matrix required simultaneous inputs from specialized subsystems, specifically Power, Propulsion, and Thermal (PPT), Lunar Surface Module (LSM), Autonomous Flight Safety Systems (AFSS), Crew Systems (CS), and Mission Planning Assessment (MPA), the risk analysis was inherently dependent on a rapidly moving technical target.

A compounding challenge arose when individual subteams executed iterative design changes to their components *after* an initial risk assessment and failure mode mitigation strategy had already been established and documented. For example, a modification in material selection by a hardware subteam or a change in software logic by the autonomous flight safety team would instantly invalidate previously calculated severity and occurrence scores.

Because there was no centralized, automated notification system to flag localized component revisions, tracking these updates required continuous manual auditing. Consequently, the risk analysis was subject to frequent retroactive rework, as the systems team had to constantly re-evaluate how a minor, post-analysis change in one subteam's component might cascade into new, unquantified failure modes for the rest of the architecture.

8.4.2 Data Asymmetry and Qualitative Standardization Constraints

Standardizing the qualitative metrics, specifically assigning uniform values for Severity and Occurrence, across four distinct technical domains introduced significant analytical friction. Each subteam naturally viewed risk through the lens of their specific engineering discipline, leading to inherent data asymmetry.

Quantifying the occurrence rate of a mechanical failure (such as a structural material tear or valve rupture in a thermal loop) relies on historical hardware cycle data. Conversely, evaluating risk for an autonomous flight safety system (AFSS) requires analyzing algorithmic failure rates and software edge cases. Aligning these fundamentally different types of failure data into a single, cohesive matrix made it difficult to establish a standardized baseline.

Ensuring that a "High" severity rating in the Mission Planning sector carried the exact same critical weight and operational meaning as a "High" severity rating in the Propulsion or Crew Systems sectors required exhaustive calibration meetings to eliminate subjective bias from individual subteam inputs.

8.4.3 Empirical Research Alignment and Mitigation Verification

A substantial hurdle in completing the risk matrix was the rigorous requirement to justify the proposed mitigations and occurrence rankings with credible, empirical aerospace research. Rather than relying on speculative engineering intuition, every component entry—ranging from life-support scrubbers to complex propulsion manifolds—demanded external verification to ensure the validity of the risk profile.

Finding peer-reviewed literature, historical flight failure databases, and aerospace standards that precisely aligned with our specific design constraints proved to be incredibly time-consuming. Because our analysis covered highly diverse subsystems, the research phase required deep-diving into completely disparate fields of study.

Validating a single mitigation strategy often meant cross-referencing niche technical data, such as material degradation charts for specialized alloys (like Inconel), gas dispersion behavior in low-pressure environments, or the chemical degradation rates of carbon dioxide scrubbers (LiOH). The sheer volume of technical literature required to verify the safety margins for PPT, LSM, AFSS, CS, and MPA components simultaneously created a massive cognitive and administrative load, severely lengthening the timeline required to finalize the risk assessment.

9 Testing and Analysis

9.1 Testing and Analysis Overview (Mahek)

The goal of MPA was to test our design and certain design choices to see the impact on the astronaut. We conducted two tests in total: Center of Gravity and Maintainability. While we did consider other tests, we decided against them for various reasons. We worked with all the sub teams to gather necessary information to conduct these tests as accurately as possible.

9.2 Center of Gravity Testing

9.2.1 Test Reasoning (Vijay Dayal)

Due to the focused nature of the project goal, the Mission Planning team was majorly in charge of testing. Since there was no testable hardware, early brainstorming for testing revolved around defining possible design parameters. The center of gravity (CG) of a system can be a simple parameter to adjust for modular designs. If tests resulted in revealing relevant trends related to CG, the PLSS proposal could maximize benefits from CG placement.

The variables of interest for testing would be CG placement and exertion. Being able to isolate and measure these parameters, their correlation can be analyzed.

9.2.2 Test Precedents (Vijay Dayal)

For work for ENAE100 in the Fall 2025 semester, University of Maryland freshmen worked on PLSS innovation alongside the KOALA team. They performed testing relevant to backpack CG and exertion. Their data used heart rate as a measure of exertion. They used a hiking backpack and placed modules in different locations during different trials. During each trial, a subject would start walking at a set speed on a treadmill. This speed was chosen by each subject. The team measured heart rate for each different configuration at the same speed for each.

NASA also has performed CG testing with regards to exertion [112]. In contrast to the ENAE100 team, they had each participant rank their perceived exertion on a scale from 1 to 10. NASA did not use a modular design to test specific CG locations, but rather they used existing PLSS and “backpack” systems to test their performance.

We decided we could innovate these tests because they both had parts that the others did not. Our version of the test would focus on both perceived and physiological measurements while trying to hold more constant variables. We also decided we could include a control group that would give us a comparison of each subject's physiologic response to the testing methodology.

Testing Preparation

For our tests, we decided to use heart rate as our physiological measurement due to simplicity and availability. Heart rate is considered a typical parameter that can physiologically strain. It also has a positive correlation with other measurements related to perceived exertion [113]. Since resting heart rate varies widely from person to person, heart rate elevation was also logged. This metric is the difference between measured heart rate and resting heart rate. As for perceived exertion, we decided to use the Bedford scale because it is a qualitative scale that allows to see if changes need to be made and how much the subject thought about the exertion.

The ENAE100 team used a backpack with modules placed in different locations to create different configurations for where the weight would be held. We tried to use that backpack at first but realized that the backpack was unable to have the weights adhere in one position without moving and therefore would cause small perturbations in the location of the weights. This seemed like a small issue at first, but it revealed a larger issue of backpack sway and weight migration that would not be present in a PLSS.

The testing location was done in the Neutral Buoyancy Lab since it provided access to a heart rate monitor and treadmill with adjustable speeds. Out of materials that were already available to us, we decided to implement different configurations using a weighted vest. This allowed us to have configurable weight locations, like a backpack, but also fastened the weights to allow for resistance to weight migration.

Within this test, there was originally a distinction between "added" weight and "on your feet" weight. If a participant had a lower natural weight but was told to carry the same weight as a heavier participant, the first participant is technically carrying less weight "on their feet." Due to the diversity in our participants, it was apparent that it would be difficult to have each participant have a controlled "on your feet" weight while still maintaining the integrity of the PLSS simulation.

There was a lot of access to different small masses in the Neutral Buoyancy Lab, but calibration was difficult due to inconsistencies in scales. We ended up relying on specific sets that were marked with their weights to define their individual weight. After the creation of each configuration, we also had each participant stand on a scale and subtracted their weight to validate the measurement matched what was intended.

At first, using the weighted vest constrained us to only use the small weights that could fit within each compartment in the vest. It also required our total weight to be able to be evenly divisible between each compartment. Since we wanted to include more weight, we searched for alternate solutions. We found that we were able to utilize belts on top of the vests. This allowed us to supplement the weight on each section as needed.

In terms of choosing an appropriate weight to hold constant, we had to consider the weight that could feasibly be held by our smallest participant, the weight of the system we were trying to simulate, and which weights were available to use. We ended up deciding that 14.52 kg was the maximum weight our participants were able to withstand and be able to appropriately test in Earth gravity. This was less mass than preferable, but the test would not have been accessible to all our participants with a larger mass.

When considering our measurements, we also realized the spread of natural resting heart rates between participants was scattered. To normalize this measurement for each participant, we decided to use heart rate elevation. This means finding the difference between measured heart rate and resting heart rate. This more clearly shows the effect of the experiment without other environmental variables.

9.2.3 Testing Procedures (Mahek)

Required materials:

- Heart rate monitor
- Stopwatch
- Weighted vest
- Weighted belt
- Adjustable speed treadmill

To set up the backpacks:

- Unloaded: ensure all the weights are out of the vest (Figure 9.2.1)
- Bottom Back Heavy: put roughly 1.81 kg (2 bags) into each of the bottom four pockets in the back and add the 7.26 kg belt for a total of 14.52 kg roughly
- Top Back Heavy: put roughly 1.81 kg (2 bags) into each of the top four pockets in the back and add the 7.26 kg belt for a total of 14.52 kg roughly
- Dispersed: put roughly 1.81 kg (2 bags) into each of the pockets in front and back

Figure 9.2.1: Weighted vest with flap open to show pockets for weights

For the trial run:

1. Select the subject
2. Enter the subject's height and weight at the top of the Excel sheet
3. Instruct the subject to wear the heart rate monitor around their wrist
4. Determine the resting heart rate and enter the value into the required Excel sheet
5. Have the subject wear the configured weighted vest and stand on the treadmill
    a. Four trials in this order: unloaded, bottom back heavy, top back heavy, dispersed
6. Explain to the subject the data collection procedure:
    a. Read off heart rate every one minute for a total of 10 minutes
7. Set the treadmill to 4.83 kilometers per hour
8. Start data collection
9. Record data into an excel sheet
10. After completion of 10 minutes, have subject rate the trial using the Bedford scale (Figure 9.2.2)
11. Have Subject 1 rest while setting up Subject 2 for a trial
12. Repeat steps 1-10 for Subject 2
13. Set up and repeat steps 1-12 with all subjects
14. Make sure heart rate goes back to resting beats per minute to ensure accuracy

Figure or Table containing sensitive information, or possible unauthorized copyright information has been removed.

Figure 9.2.2: NASA Bedford Workload Scale used for Qualitative Data [115]

The four configurations were chosen after deliberation on how to get a unique enough center of gravity (CG) to see a difference in exertion. The unloaded gives us a baseline to verify that the heart rate elevation is aligned correctly. Having a bottom and top-heavy configuration allows for a possible analysis of whether moving against the body COG helps. The dispersed configuration helps see a possible correlation of if COG is in the middle, if it helps compared to an extreme top or bottom. The walking speed of 4.82 kilometers per hour was chosen as it is the average walking speed, according to Cronkleton [116]. The weight was a constraint that was a bit unexpected. When MPA reached the testing site, the total weight possible with the given resources was about 14.52 kg. While this is a low number, it was still well enough to see possible influences of moving the COG. Additionally, due to time constraints, each run was 10 minutes. This timing allowed us to see where the heart rate was leveling off after a peak, a decision made after a discussion with Dr. Akin. Reading the heart rate every minute allowed for enough variability to see the difference in exertion. As for the Bedford rating, one of the goals was to see if perceived exertion was impacted as well, to make sure astronauts are comfortable throughout the test. The Bedford scale allowed us to get an accurate rating for the procedure of the test and keep it objective enough to make sure all the subjects were rating on the same perception. These were how the design choices were made.

9.2.4 Analysis of Center of Gravity Results (Eric)

The results from the center of gravity test can be seen below in Figure 9.2.3, which displays three graphs, time walking with all three center of gravity configuration versus the heart rate elevation. Here, heart rate elevation corresponds to the measured heart rate taken at that time minus the initial heart rate at the start of each trial. Each graph corresponds to each subject we tested, and in this figure, there are three graphs representing the 3 total subjects we tested. Instead of trying to look at these three graphs all at once, we deduced that these overall trends would be better visualized if the average of all three heart rate elevations per configuration were taken for each subject.

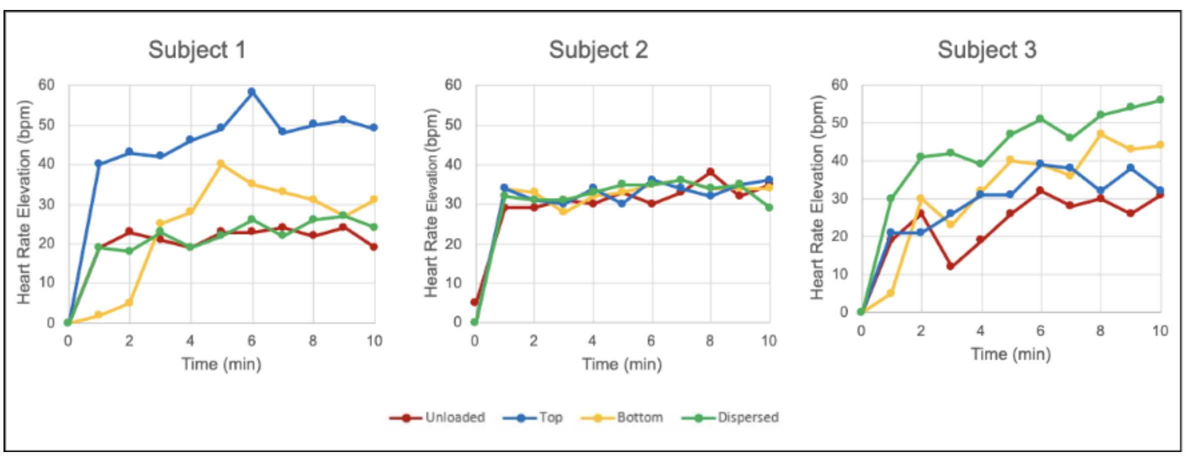

Figure 9.2.3: Time Walking with CG Configurations vs. Heart Rate Elevation for All Three Subjects (Mahek & Vijay)

From our deduction and dedication to communicating our results in a more complete way, we arrived at Figure 9.2.4, which is titled time walking with CG configurations vs average heart rate elevation for all 3 subjects. We figured this was a much easier way to look at the overall trends of the data rather than trying to look at the trends in all three graphs at once.

Figure 9.2.4: Time Walking with CG Configurations vs. Average Heart Rate Elevation for All Three Subjects (Mahek & Vijay)

Right off the bat upon first examination, all configurations exhibit a sharp rise in average heart rate during the first minute, with increases of approximately 20 to 30 beats per minute as the subject adjusts to the treadmill speed. After minute one, the curves begin to separate by configuration with the corresponding colors; unloaded = red, top = blue, bottom = yellow, and dispersed = green. The unloaded curve stabilizes between roughly 21-30 bpm from minutes 2-10 showing the lowest sustained average heart rate elevation. The top and bottom configurations show very similar heart rate elevation trends, remaining within approximately 1–5 bpm of each other from minutes 4 through 10. For example, at minute 5 the top configuration is 32.7 bpm while the bottom is 37.7 bpm, a difference of about 5 bpm. By minute 8, the values are 36.7 bpm (top) and 34.3 bpm (bottom), reducing the difference to about 2.4 bpm. At minute 10, the two are nearly identical at 35.0 bpm and 36.3 bpm, with only a 1.3 bpm difference. Overall, this indicates that both configurations produce nearly equivalent physiological responses over time. If we look at the dispersed configuration curve, it remains the highest after minute 2 and continues to increase throughout the later minutes. By minute 10, it reaches approximately 40.7 bpm, which is about 12 bpm higher than the unloaded condition. This sustained elevation indicates that the dispersed configuration produces the greatest cardiovascular demand over the walking period.

	Subject 1	**Subject 2**	**Subject 3**	**Average**
Unloaded	1	1	1	1
Top	3	2	3	2.67
Bottom	2	2	5	3
Dispersed	1	2	2	1.67

Table 9.2.1: Bedford Scale Data from Our Center of Gravity Test (Vijay)

At the conclusion of each test, we employed a dual-pronged approach to evaluate the results, incorporating both quantitative and qualitative data. The quantitative results are shown above, while the qualitative assessment was conducted using the NASA Bedford Workload Scale, where each subject completed the evaluation following the trial, as shown in Table 9.2.1. This approach allowed for a direct comparison between measured physiological response and perceived effort across different configurations. The NASA Bedford ratings show a clear difference between perceived difficulty and measured physiological response. The bottom configuration is rated as the most difficult, with an average score of 3.00, even though it does not produce the highest heart rate. In contrast, the dispersed configuration has a lower perceived workload rating of 1.67, despite consistently producing the highest heart rate elevation across the trials. This highlights that subjective effort does not directly align with cardiovascular demand in this dataset. Looking at the heart rate trends, the dispersed configuration remains the highest after minute 2 and continues increasing through the later minutes. By minute 10, it reaches approximately 40.7 bpm, which is about 12 bpm higher than the unloaded condition. It also stays above the other configurations from minutes 2 through 10, indicating a sustained increase in physiological demand during steady walking. From a design perspective, these results suggest that distributed mass increases cardiovascular strain even if it feels easier for the user. While the dispersed configuration may be perceived as more comfortable, it places a greater sustained load on the body. As a result, it appears to be a less favorable center of gravity strategy for the PLSS design compared to more concentrated mass configurations. It is important to note that the discrepancy between qualitative and quantitative data will be explored much more in depth in the next section.

9.2.5 Retesting Dispersed (Mahek)

The major mismatch between the quantitative and qualitative data for dispersed raised concerns about the validity of the data. With the dispersed configuration, Bedford rating being low and the quantitative being very high, this needed to be redone. By isolating the dispersed, we are trying to get a match between the qualitative low rating on the Bedford scale and the quantitative high average. For the retesting, we called back the same subjects and had the same configuration for dispersed weight vests. After their resting heart rate was recorded, the subjects took turns walking for 10 minutes, while reading out their heartbeat from the monitor every minute. This was compared to the past results again (shown below in Figure 9.2.5 and 9.2.6).

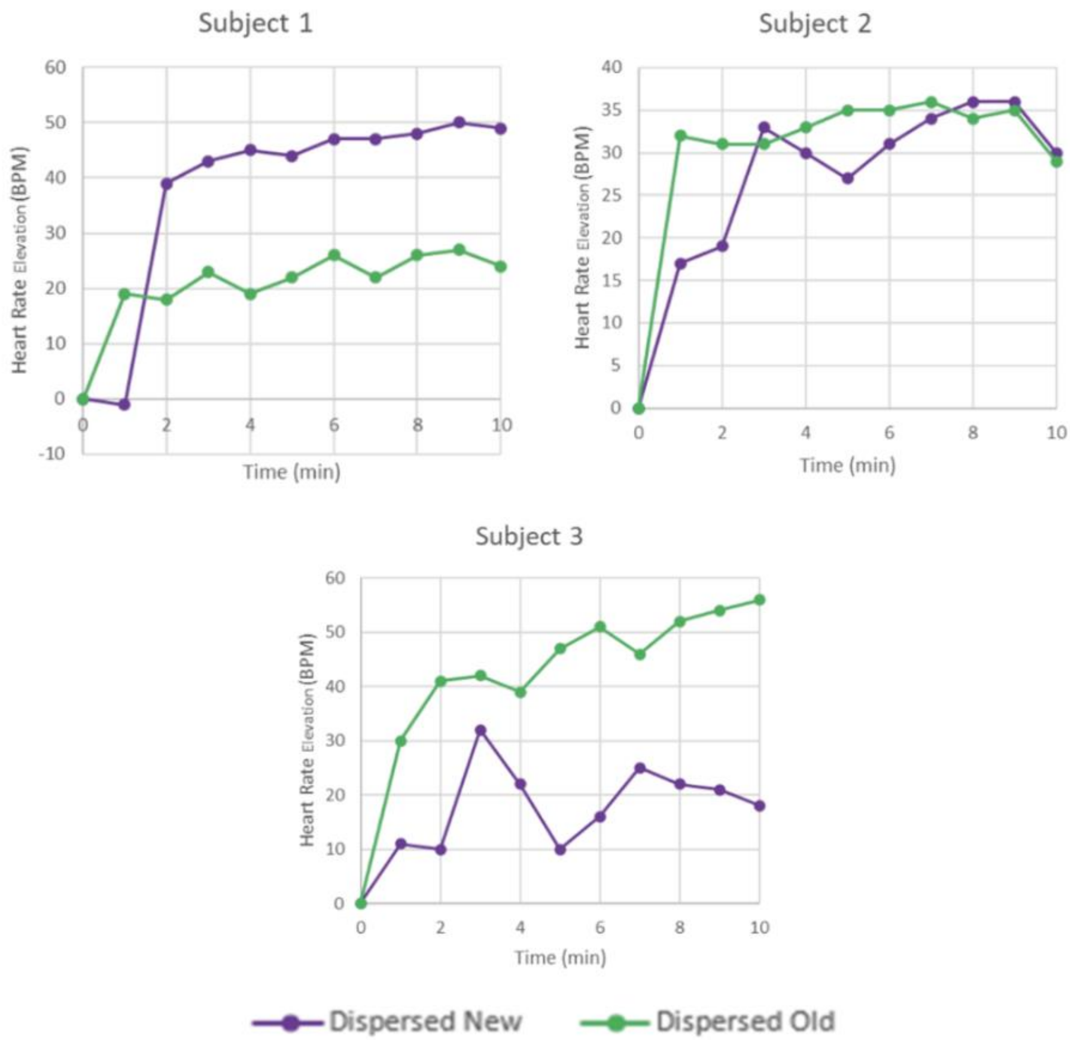

Figure 9.2.5: Resting Individual Data Compared (Mahek & Vijay)

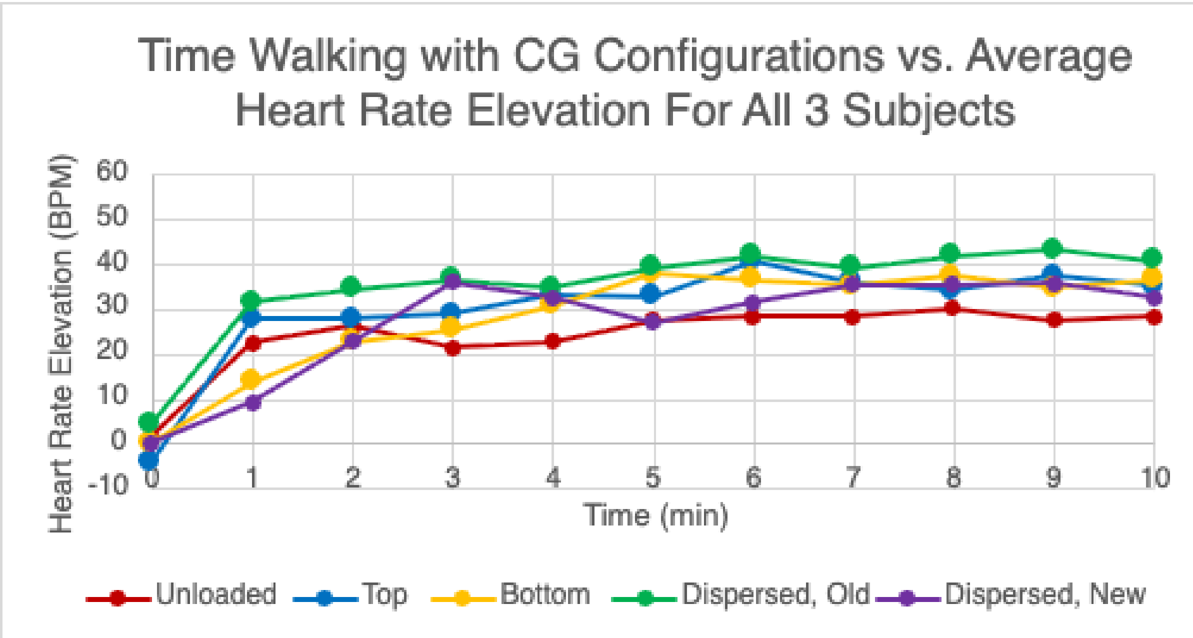

Figure 9.2.6: Retested Dispersed Weight Added to Past Tests (Mahek & Vijay)

The results of the center of gravity test are inconclusive. For Subject 1, the heart rate elevation increased, while Subject 3 decreased. Subject 2 was relatively similar to their previous test run. When compared to the average, the new run was in the middle of all the other configurations. There are many reasons that this could be, but the most reasonable is fatigue. Despite our confidence in our visual analysis, we also decided it was important to implement an actual statistical analysis test to further validate this data.

9.2.6 Scrapped Statistical Analysis (Vijay Dayal)

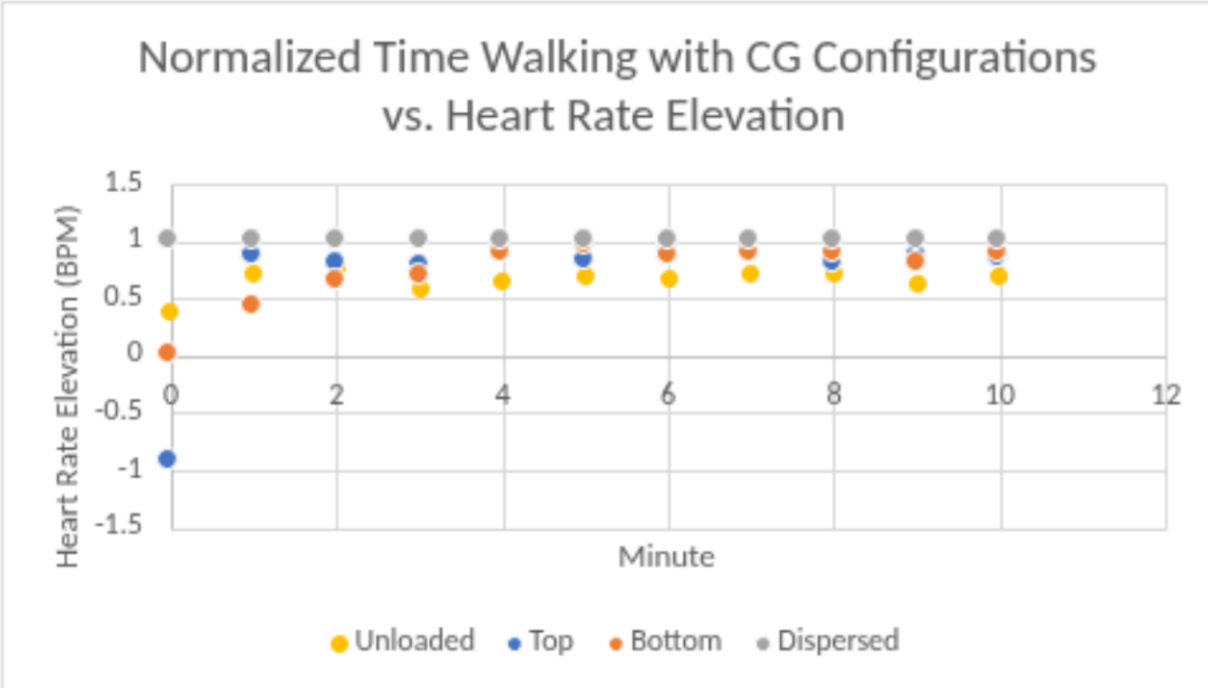

Figure 9.2.7: Scatter plot of normalized heart rate elevations of each subject (Mahek & Vijay)

The above graph (Figure 9.2.7) was created to more clearly describe the difference between each configuration. It displays the normalized values for each averaged data set. This means the highest and "worst" performing data point is equal to 1. And anything that performed better is displayed as a ratio out of the highest data point. Since the dispersed data set had the highest heart rate elevation average during every minute, it maintains a constant value of 1 through graph. We decided not to display this graph because it can be misleading as compared to the raw average values. This makes it seem that the dispersed configuration performed considerably worse than reality. It also makes the top configuration seem significantly better.

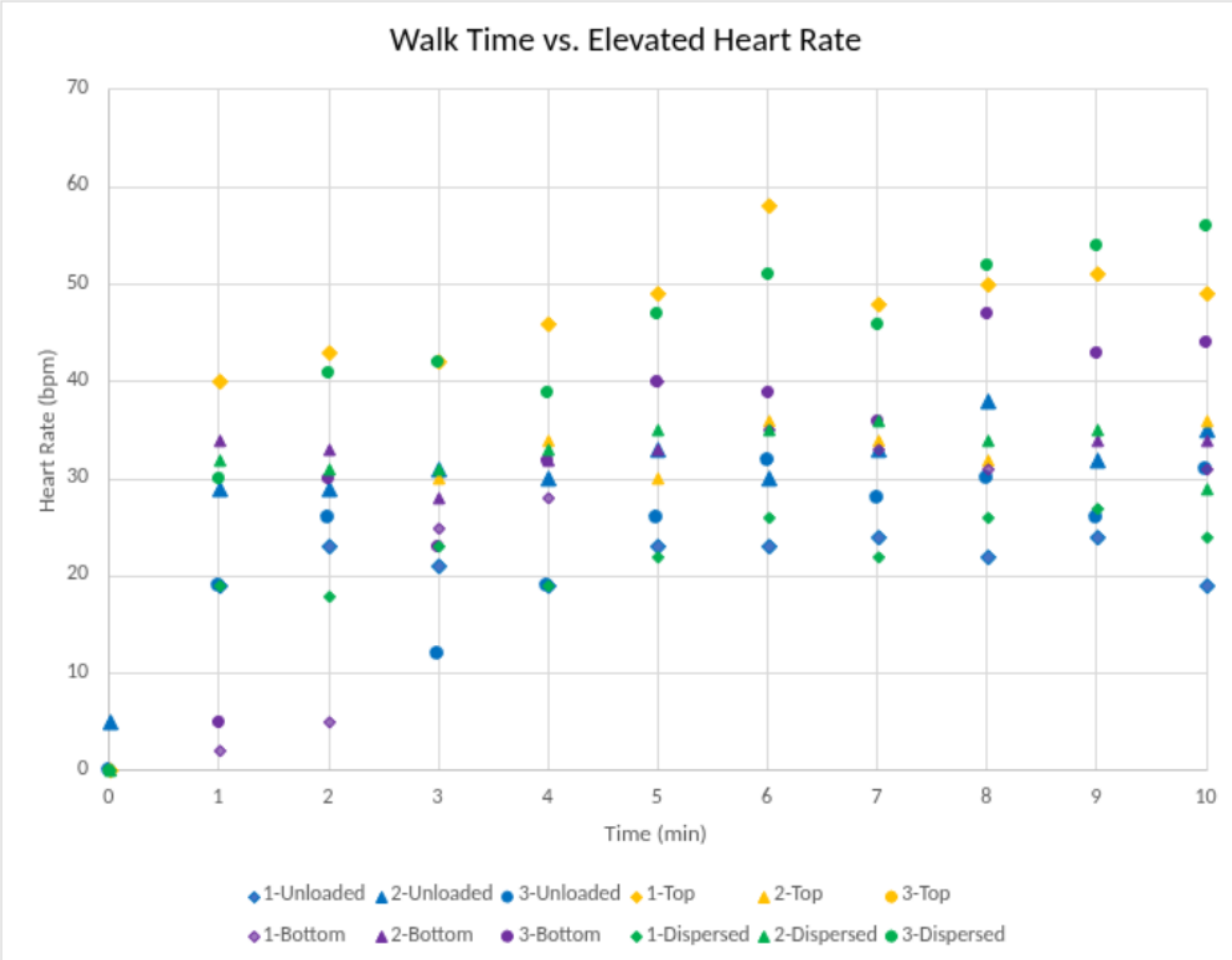

Figure 9.2.8: Raw data scatter plot of all tests and subjects

The above graph (Figure 9.2.8) displays all of our raw data. The same configurations are displayed using color while the same participant is displayed using the shape. We decided not to include this graph because it is overwhelming and not easy to decipher what the graph conveys. Due to the overwhelming amount of symbols, it is hard to focus on one to see the trends. It can still be helpful to show overall ranges of heart rate elevation ranges and timing, but it was scrapped in favor of showing each subject's averaged data sets.

9.2.7 Further Validation: T-Test (Vijay Dayal)

Since our data was based on a low sample size and our data was very spread, it was hard to decide on a test that would best describe our results. Our final decision was to perform a t-test to compare the average heart rates in the old and new trials. The results from this test would determine if the averages between the two sets of data were significantly statistically different.

The t-test resulted in a p-value of 0.001271. This represents the likelihood this data set exits assuming the null hypothesis. In the case of this t-test, the null hypothesis is that the two compared data sets are not significantly statistically different. This would also imply that the two underlying populations are comparable. Since the likelihood of this data spread assuming the null hypothesis is so low, it is acceptable to reject it.

We also performed the t-test on each individual subject. These p-values performed similarly. One of the values went as low as p = 10^-13.

This is a very low result which implies that the two data sets are significantly different. This confirmed our hypothesis that there were confounding factors not controlled in our tests. These variables must include things other than fatigue because none of our participants did tests beforehand. This could also be a failure of our measuring methods with qualitative physiology. There are most likely better methods of measuring exertion that are not heart rate.

9.2.8 Center of Gravity Takeaways and Future (Mahek Shah)

There were several takeaways we had from this test. One big takeaway was that human testing has too many factors to fully account for. A big factor was fatigue from either the previous activities or previous trials. Fatigue is known to increase exertion, which would increase the elevation of the heart rate. Additionally, we had not accounted for Mar's environment fully: a lighter body weight should be carrying more weight, and a heavier body weight should be carrying less weight because of Mars gravity effect. With this knowledge, having a consistent weight for this test is not a good idea. Subject 1, who was our heaviest, had an advantage and would experience a smaller elevation in heart rate than Subject 3, who was the lightest, having a disadvantage. This would affect heart rate elevation because of these advantages.

In the future, MPA has a few suggestions. The first suggestion is to control the weight to account for Mars' gravity. Additionally, we think using an 80/20 modular back vest will have repeatability of the COG. If given more time, MPA was thinking about using a dumbbell sort of geometry to help with adding and removing weight, while knowing easily where the COG is (Appendix F for more information). Furthermore, as this is a test with humans, we would like to control more variables, especially fatigue. A good way to combat it is to only run one configuration at a time, with a significant break before the trial to allow recovery from previous activities, such as walking to the test site. This would allow for the resting heart rate to drop to everyday levels and the exertion to hopefully go down too. This is why we initially did the retest of the dispersed weight; however, we did not account for previous activity, which could have accounted for the variation per subject. Finally, this test was only done with 3 subjects due to time constraints. In the future, having more subjects, at least ten to fifteen, would help get a better correlation between exertion and COG.

Overall, with more time this test could be repeated for better results.

9.2.9 Scrapped Tests (Mahek Shah)

FMEA:

When we first started this project, we had a bunch of tests we wanted to do, since we are ambitious. However, due to time and material constraints, we decided against it, and one test was reassigned to the LSM sub-team. The reassigned test was the FMEA analysis. The LSM sub-team's role is to check the design for failure modes and make sure the design can complete the task. Since MPA wanted to help, we figured we would do the test through computer software analysis and hand calculations. However, due to the complexity of the design, we decided to only do the computer analysis. Furthermore, MPA decided that this additional help was not beneficial to the LSM, as LSM needed to trade studies on their decisions and could not wait for our analysis.

Mobility:

A test that was scrapped is our mobility test. The objective of this test was to ensure that the astronauts are able to complete all necessary tasks with the weight of the PLSS. To do this test, we would need a PLSS mock-up of the exterior with the proper COG. The tasks the subject would have had to do were (but not limited to):

- Climbing up stairs
- Shoveling sand
- Picking up heavy objects
- Walking around obstacles

However, there is a standard we got from NASA and other studies, making these results extraneous. Our thought was to validate our design, but, again, we had a standard to be able to follow. Furthermore, going lighter should help improve mobility, as there is no added restraint.

Stress on Isogrid:

The goal was to have an Isogrid to test how much stress and strain it can take. This was going to be done using the Tinius Obsen 25st Tensile Testing Machine. However, this was not done for 3 reasons. The information we would have gained can be obtained from a theoretical analysis and FMEA. Secondly, we would have had to make several mockups to test this. There is no iterative way to test, as it would be tested till failure. Lastly, time and money constraints: to make and test all these models would take time and resources. Therefore, this test was also scrapped.

9.3 Maintainability Test

9.3.1 Test overview (Eric Sibanda)

Maintainability refers to ease with which maintenance activities can be performed on an asset or piece of equipment [117]. This perfectly sums up the main goal of the maintainability test we are going to propose. More specially, our goal here is to use a full-scale volumetric PLSS mockup and evaluate how easy it is to access components and perform replacements under realistic conditions. These realistic conditions would allow us to determine if the configuration is a viable option since after all it should take forever to replace the necessary parts. This full scale volumetric PLSS mockup represents the final optimized weight configuration after multiple design iterations and the integration of parts ordered through the systems sub team. We would like to thank the other sub teams for identifying the required components and providing the dimensions needed to support this final design. We will have participants complete specific tasks using a reference guide, all under time constraints to simulate real operational pressure. For this test, we are measuring both qualitative and quantitative data as well as completion time and feedback from the participants. For the qualitative data, we are proposing the use of the NASA Modified System Usability Scale or the NMSUS Scale (see figure 9.3.1 for more details).

NASA Modified System Usability Scale (SUS) - NMSUS

	Strongly Disagree 1	2	3	4	Strongly Agree 5
1. I thought the system was easy to use.	O	O	O	O	O
2. I think that I would need technical support to be able to use this system.	O	O	O	O	O
3. I found the various functions in this system were well integrated.	O	O	O	O	O
4. I thought there was too much inconsistency in this system.	O	O	O	O	O
5. I imagine that most trained crewmembers would learn to use this system very quickly.	O	O	O	O	O
6. I found the system very cumbersome to use.	O	O	O	O	O
7. I felt very confident using the system.	O	O	O	O	O
8. I needed a lot of training on this system in order to get going.	O	O	O	O	O

Scoring
The NMSUS is scored using the following equation, which is based on SUS (see Lewis & Sauro, The Factor Structure of the System Usability Scale):
*NMSUS = 3.125 * ((Q1-1)+(5-Q2)+(Q3-1)+(5-Q4)+(Q5-1)+(5-Q6)+(Q7-1)+(5-Q8))*

Figure 9.3.1: NASA Modified Usability Scale (SUS)- NMSUS [118]

For the test itself, we defined a set of representative maintenance tasks that cover both simple and more complex operations. Some of these are straightforward, such as replacing random nuts or bolts or replacing the lithium hydroxide batteries. Other tasks are paired systems that need to be handled together, for ex, the RCA+TCC. So instead of treating those as separate tasks, we evaluate them as a single replacement process, since that better reflects how they would actually be serviced. See Table 9.3.1 for a look at the full list of tasks and how we plan to collect our data.

Name of Participant:							
Parts To Be Replaced	Nuts and Bolts	Lithium Hydroxide Batteries	Rapid Cycle Amine and Trace Contaminant Control	Mounts, Welding, Fastners	Lithium Hydroxide Panels	Purging and Recharging Cooling Water	Recharge Oxygen
Completion Time (sec)							
NMSUS Score							
Participant Feedback							

Table 9.3.1: Maintainability Data Collection

9.3.2 Simulation (Mahek)

We realized after the printing of the parts, we need to be able to simulate the steps with our resources, following the User Manual (Appendix B). This is the breakdown of how each step was simulated.

Battery:

1. The test subject was told to find both the batteries = Time 1.
2. Inspect the mounts by shaking the batteries' Velcro = Time 2.
3. Take the batteries out = Time 3
4. Walk and place the batteries on one of the Team Members' hands = Time 4
5. Go back after a couple of seconds = Time 5
6. Replace the batteries within the PLSS = Time 6

Oxygen Loop;

1. Find all the parts based on the diagram & Open an app on the iPad for Oxygen Flow Rate check = Time 1
2. Using their hands, skim over the parts to simulate Visual check for leaks = Time 2

Avionics box:

1. Identify all parts = Time 1
2. Check the screws visually = Time 2
3. Shake the part to make sure it is secured on the mount = Time 3
4. Open an app on the iPad to "Check system status" = Time 4
5. Wait for team member to say something is wrong = Time 5
6. Take out the box with the screws and remove all the screws = Time 6
7. Take out one of the panels and walk to a team member = Time 7
8. Walk back from the team member to the PLSS = Time 8
9. Put in panel and screw on the lid = Time 9

10. Put the box in if removed = Time 10
11. Reopen the same app on iPad = Time 11

LiOH Canister & TCC:

1. Time 1
    1.1. Open app 1 to simulate "Flow Rate Check"
    1.2. Open app 2 for "pressure sensor check"
    1.3. Open app 3 for "carbon dioxide level check"
    1.4. Touch canister and wait for team member to call out if it is warm
2. Time 2
    2.1. Assuming there is a problem, open up two water bottles to simulate the isolation of the ventilation loop as there would be valves
    2.2. Remove the part
    2.3. Walk to a team member to "dispose"
    2.4. Look at the part to "inspect"
3. Time 3
    3.1. Put back the part to "reinstall"
    3.2. Close the two water bottle lids to reopen the valves
    3.3. Feel around part to check for "leaks" and wait for team member to call out for time
    3.4. Open app 3 again to "check CO_2 level"
4. Time 4
    4.1. Open up 4 screws of the avionics box
    4.2. Remove Thermal Filter part and walk to team member
    4.3. Inspect the part and walk back
    4.4. Put back the filter

SWME:

*This was not fully simulated because of our restriction in testing space and SWME not printed yet, but how we would do it is mentioned below:

1. Find both batteries instead of SWME because it would be in a close spot = Time 1
2. Locate the water bottle being the feedwater tank = Time 2
3. Fill up water bottle = Time 3
4. Find and open App 1 on iPad to simulate heat input test = Time 4
5. Find and open App 2 on iPad to simulate checking outlet temperatures = Time 5
6. Write down these temperatures and cross-reference them = Time 6
7. Visually check the oxygen loop instead of the SWME (as not printed fully) for leaks = Time 7
8. Find and open App 3 on iPad for "checking silicone level" = Time 8
9. Find and open App 4 on iPad for "checking total organic carbon" = Time 9

10. Write down these values and cross-reference with team member = Time 10
11. Find and open App 5 on iPad for “BPV” = Time 11
12. Check the time on the analog clock for checking the potentiometer voltage check = Time 12
13. Find and open App 6 on iPad for “temperature sensor drift” = Time 13
14. Turn off and on the iPad to simulate the restarting the software = Time 14
15. Open up 2 water bottle lids to close the valves = Time 15
16. Take out both batteries because the SWME would be in a close spot = Time 16
17. Empty 2 water bottles to simulate pressure and water draining = Time 17
18. Remove 6 screws of the avionics box and check the screws for color inspection = Time 18
19. Take a little bottle cap and fill it with water to simulate sample testing= Time 19
20. Put the water from the cap into the water bottle for simulating the biocide injection = Time 20
21. Put back the screws and batteries = Time 21
22. Fill up the 2 water bottles and close the lids = Time 22
23. Visual check oxygen loop again = Time 23

** While these steps seem like they might take a while, we are assuming it would be close to the time as the avionics boxes, if not a little more. However, the total times have been only several minutes, so even if it is a little longer, this should not be an issue.

9.3.3 Maintainability Test Assembly and Findings (Vijay, Eric, Mahek)

We were unable to completely get all our intended mounts printed. Our main brackets for attaching the oxygen tanks to the isogrid were properly implemented using hammernuts and M4 screws. For many of the other components, we ended up needing to go to Home Depot and purchase Velcro for the remaining components.

The total data for both the times and the NMSUS usability scores are below (see Table 9.3.1):

Total Time for Each Task (s)

Task	Subject 1	Subject 2	Subject 3	Average
Battery	99.9	107.38	96.29	101.19
Oxygen Loop	42	34.46	31.62	36.02666667
LiOH & TCC	251.23	307.1	205.01	254.4466667
Avionics	833.76	632.67	764.32	743.5833333
Usability Score for Each Task (NMSUS)				
Task	Subject 1	Subject 2	Subject 3	Average
Battery	87.5	75	68.75	77.08333333
Oxygen Loop	78.125	68.75	87.5	78.125
LiOH & TCC	53.125	50	59.375	54.16666667
Avionics	84.375	56.25	56.25	65.625

Table 9.3.2: Total Times and Usability Scores for Maintainability Tasks

The distribution of times and usability scores is much less spread compared to CG testing. The requirement for NMUS scores to be counted as a success is 85, which none of our subjects gave for any tests. However, we believe this is due to the fact that the subjects are not well educated on how to use the scale, and therefore, leading to the low scores. All subjects commented that the design was easy to use and well laid out, other than the comments mentioned later. These tests are also much more repeatable, which implies these findings were much more accurate as a test of system maintainability.

Raw data can be found below in Appendix E.

The averages for the timing and NMSUS score of each of our tasks are shown below:

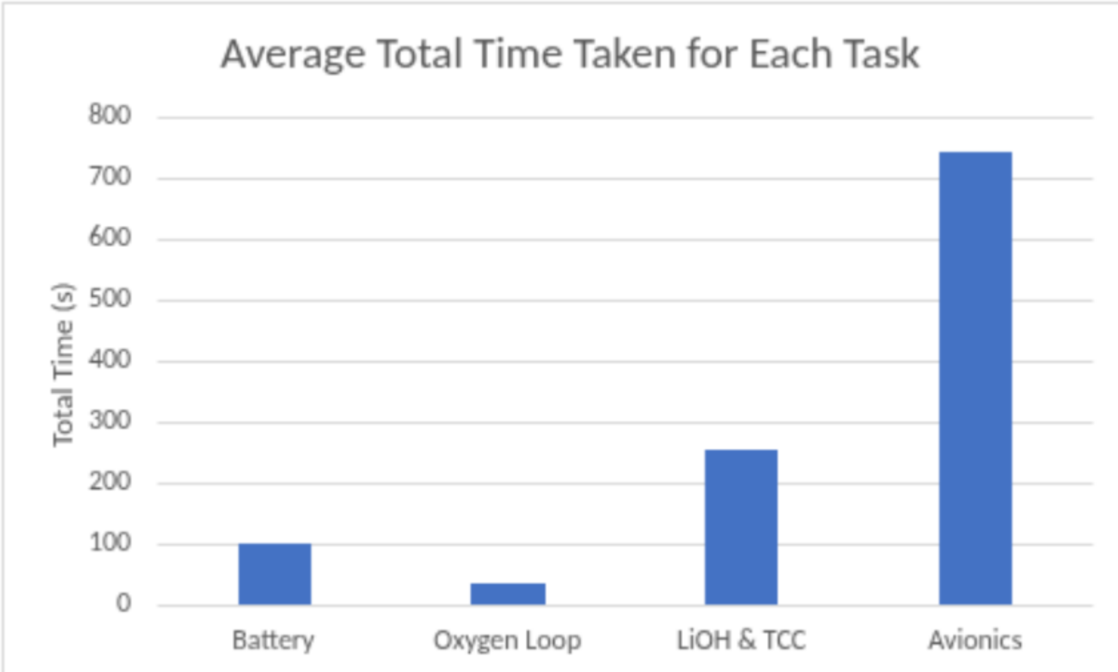

Figure 9.3.2: Averages for Task Time During Maintainability Testing

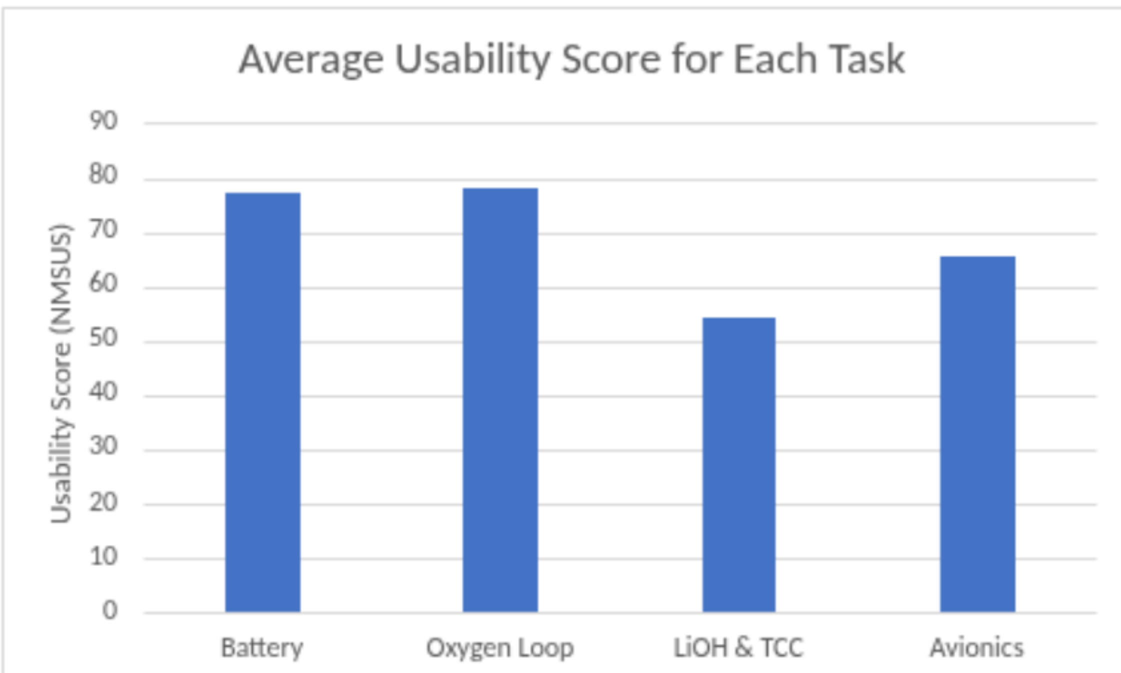

Figure 9.3.3: Averages for Usability Score During Maintainability Testing

During testing, we had a few comments from participants about two tasks:

Avionics:

- Subject 1 Comment: back nut was very hard to access
- Subject 2 Comment: The screws are close to the oxygen loop, they might be damaged during avionics box maintenance

LiOh and TCC:

- Subject 2 Comment: LiOh removal hard due to O2 tank nearby

Our implementation that we used for our final mock-up design utilized M4 bolts rather than M6 bolts as intended by the LSM team. Using smaller bolts allows them to fall easily into the isogrid insets. This caused the average times for the Avionics task to be inflated. Using the larger, intended bolts most likely would allow for a more compatible sizing that would lessen maintenance time.

Another notable takeaway is that while one component is being worked, the others would get hit or moved around. Unless the operator or participant are very careful, they run the risk of damaging other systems. This means components that need to be maintained often should not be placed near sensitive components.

Total Time for Each Task (s)				
Task	Subject 1	Subject 2	Subject 3	Average
Battery	99.9	107.38	96.29	101.19
Oxygen Loop	42	34.46	31.62	36.02666667
LiOH & TCC	251.23	307.1	205.01	254.4466667
Avionics	833.76	632.67	764.32	743.5833333
Usability Score for Each Task (NMSUS)				
Task	Subject 1	Subject 2	Subject 3	Average
Battery	87.5	75	68.75	77.08333333
Oxygen Loop	78.125	68.75	87.5	78.125
LiOH & TCC	53.125	50	59.375	54.16666667
Avionics	84.375	56.25	56.25	65.625

Table 9.3.3: Total Times and Usability Scores for Maintainability Tasks

10 Conclusion and Future Ideas

There are various avenues we recommend future researchers to explore in order to reduce PLSS mass even further. Starting with the oxygen subsystem, one limitation of the current oxygen consumables and tank sizing model is that the astronaut's metabolic rate is assumed to be constant throughout the EVA, except for peak metabolic activity. Because oxygen consumption is directly proportional to metabolic demand, this assumption causes the total oxygen mass to scale approximately linearly with EVA duration.

In reality, we know this relationship would likely become nonlinear as EVA duration increases. Longer EVAs require more oxygen storage and larger tanks, which would increase the total mass that has to be carried by the astronaut. This additional mass would raise the astronaut’s physical workload, leading to a higher metabolic rate, and therefore more oxygen consumption than what we modeled.

Due to limited available data, this relationship was not incorporated into the present model. Future work could focus on integrating human metabolic performance models and variable workload profiles to better understand the nonlinear relationship between EVA duration and oxygen consumption.

One major avenue for future work is testing various configurations of layer thickness for radiation shielding. Public research into layered shielding demonstrates the potential of generic layered radiation shielding, but it is possible that even more mass could be saved by tailoring the shielding of each avionics housing to the specific needs of the components inside, minimizing the amount of heavy tungsten needed and thus reducing mass. Additionally, as explained earlier in this report, the development of dedicated space-rated software defined radios for use on the PLSS could potentially reduce the mass of the radio subsystem, but specific design of such a system is outside of the scope of this project.

The overall design of avionics boxes also would need to be tailored to the needs of each specific controller. Housing optimizations based on component size and shape could potentially lead to further mass improvements in the avionics boxes. By optimizing component placement and cooling configuration based on specific avionics component geometry, it is possible that the surface area required to contain the controllers could be reduced, thus reducing required housing mass.

Given more time and resources, the structures sub-team would have explored hinge design and analysis for the hatch assembly by looking into material selection and load impact cases. Although these components are small, they may provide some mass reduction to the overall PLSS weight. Additionally, the sub-team would have coordinated with mission planning team to identify opportunities to optimize bolt or mounting configurations for improved accessibility and maintainability. Finally, the isogrid backplate design should by physically fabricated and tested for structural integrity to validate the analytical calculations presented in this report. Testing would confirm the simplified assumptions made in this analysis, particularly in regard to the load distribution and bearing behavior at the joint interfaces.

Additionally, latching mechanism for the interface between PLSS hatch and the HUT can become a source of significant mass optimization. As discussed before, properly designed latches can impact sealing rim thickness, thereby reducing mass of the hatch. With more time available, the LSM team would've dived into different latching mechanism and developed an appropriate cam latch ring system with a mechanism that actuates and releases the latches simultaneously via a lever easily accessible to the astronaut.

Another part of the hatch that could be revisited is the pressure bulkhead. In the analysis LSM team assumed quasi-isotropic, however considering different weave patterns may be beneficial to improve performance of the components.

Finally for the hatch, thermal analysis hasn't been conducted to assess if bonding CFRP pressure bulkhead to the Al-6061 would be problematic for long-term use in Mars environment. Additionally, with the latest recommendations on hatch design arriving so close to the end of the project term, the model presented in section 7.2.1 would still need to be analyzed using FEA tools to ensure that it maintains a positive safety margin.

11 Appendix A. References

[1] NASA, *Moon to Mars eXploration Habitat (M2M X-Hab) Challenge Solicitation 2026*, National Aeronautics and Space Administration, Washington, DC, 2025. M2M X-Hab Challenge Solicitation 2026

[2] NASA, *NASA Space System Protection Standard Handbook*, NASA-HDBK-1002, Draft Version, National Aeronautics and Space Administration, Washington, DC, n.d. NASA-HDBK-1002 Draft

[3] NASA, *NASA Space Flight Human-System Standard, Volume 1: Crew Health*, NASA-STD-3001, Vol. 1, Rev. C, National Aeronautics and Space Administration, Washington, DC, 2022. NASA STD-3001 Volume 1

[4] NASA, *NASA Space Flight Human-System Standard, Volume 2: Human Factors, Habitability, and Environmental Health*, NASA-STD-3001, Vol. 2, Rev. E, National Aeronautics and Space Administration, Washington, DC, 2023. NASA STD-3001 Volume 2

[5] Space Exploration Technologies Corp. (SpaceX), *Falcon User's Guide*, Version dated May 9, 2025, Hawthorne, CA, 2025. SpaceX Falcon User's Guide

[6] Mavridis, C., Concept of Operations for the xEMU Project Delta Preliminary Design Review, NASA Johnson Space Center, Houston, TX, Sept. 2020.

[7] Howard, R. L., and Gernhardt, M. L., *NASA EVA Architecture Study*, NASA Technical Report NASA/TM-2012-217353, National Aeronautics and Space Administration, Houston, TX, 2012. NASA EVA Architecture Study

[8] Ogilvie, R., Miller, S., and Hetherington, R., "Advanced Material Options for the Portable Life Support System," *53rd International Conference on Environmental Systems*, ICES-2024-127, Louisville, KY, 21–25 July 2024.

[9] Chullen, C., *Sensors and Systems for Spacesuits: Advanced Spacesuit Development*, NASA Small Business Innovation Research (SBIR) and Small Business Technology Transfer (STTR) Program Presentation, National Aeronautics and Space Administration, Houston, TX, June 26, 2017.NASA NTRS Spacesuit Development Presentation

[10] Hirschorn, S., *NASA Systems Engineering Handbook*, NASA/SP-2016-6105 Rev. 2, National Aeronautics and Space Administration, Washington, DC, 2016. NASA Systems Engineering Handbook

[11] Lobmeyer, D. M., Oliver, M., Quick, E. J., Lawson, O. J., Barrett, L. W., Conger, B. C., Chullen, C., and Campbell, C., "Martian Exploration Portable Life Support System Schematic Study," ICES-2025-90, 54th International Conference on Environmental Systems, 2025.

[12] Journal of the International Society of Sports Nutrition, “Misconceptions about Aerobic and Anaerobic Energy Expenditure,” Vol. 2, No. 2, 2005, pp. 32–37.

[13] Ogilvie, R., Campbell, C., Hatziprokopiou, I., Walz, R., and Rogers, J., “Oxygen Regulator History, Development, & Testing Results,” ICES-2023-027, 52nd International Conference on Environmental Systems, 2023.

[14] Watts, C., Campbell, C., Vogel, M., and Conger, B., “Space Suit Portable Life Support System Test Bed (PLSS 1.0) Development and Testing,” NASA Technical Report 20120007410, 2012.

[15] Paul, H. L., Jennings, M. A., and Waguespack, G., “Requirements and Sizing Investigation for Constellation Space Suit Portable Life Support System Trace Contaminant Control,” NASA Technical Report 20100018504, 2010.

[16] Luxfer Gas Cylinders, “L6X® – Carbon Composite Type 3 Cylinders,” n.d., URL: https://www.luxfercylinders.com/product/l6x-composite-cylinder/, retrieved 16 May 2026.

[17] Baker, A., Miller, S., and Hargrove, S., “xPLSS Structural Backplate Design, Manufacture, and Test Overview,” 52nd International Conference on Environmental Systems, 2023.

[18] Junaedi, C., Hawley, K., Loebick, C., and Cameron, N., "Regenerable Trace Contaminant Control for Advanced Portable Life Support System," *54th International Conference on Environmental Systems*, Prague, Czech Republic, 2025, ICES-2025-231.

[19] Wójtowicz, M. A., Cosgrove, J. E., Serio, M. A., Nalette, T., Guerrero, S. V., Papale, W., and Wilburn, M. S., "Development of Trace Contaminant Control Prototypes for the Primary Life Support System (PLSS)," *47th International Conference on Environmental Systems*, Charleston, SC, 2017, ICES-2017-270.

[20] Francisco, D. R. (2025). NASA-STD-3001 Volume 2, Revision E, NASA Spaceflight Human-System Standard Volume 2: Human Factors, Habitability, and Environmental Health. *N/A*, (A).

[21] DELGADO-ALONSO, J. E. S. U. S., & Chambers, A. (2013). Miniature Sensor Probe for O2, CO2, and H2O Monitoring in Portable Life Support Systems. In *43rd International Conference on Environmental Systems* (p. 3365).

[22] *Hypercapnia*. Cleveland Clinic. (2026, April 17). https://my.clevelandclinic.org/health/diseases/24808-hypercapnia

[23] Anchondo, I., & Campbell, C. (2017). *Development Specification for the Portable Life Support System (PLSS) Thermal Loop Pump* (No. JSC-CN-39975).

[24] Makel, J., Wangberg, F., Martin, R., & Ogilvie, R. (2025, July). Continued Development of Multi-Gas Microsensor Array for the Exploration Portable Life Support System. In *54th International Conference on Environmental Systems (ICES)* (No. ICES-2025-222).

[25] DeHennis, A., & Chae, J. (2007). Pressure sensors. In *Comprehensive microsystems* (pp. 101-133). Elsevier.

[26] *Humidity sensor types*. Atlas Scientific. (2025, July 30). https://atlas-scientific.com/blog/humidity-sensor-types/

[27] Watts, C. A., & Vogel, M. (2012, March). Spacesuit Portable Life Support System Breadboard (PLSS 1.0) Development and Test Results. In *42nd International Conference on Environmental Systems* (No. JSC-CN-26043).

[28] Quinn, G., Carra, M., Converse, D., & Chullen, C. (2016, July). Portable Life Support System 2.5 Fan Design and Development. In *International Conference on Environmental Systems* (No. JSC-CN-35597).

[29] *4 types of temperature sensors*. Atlas Scientific. (2025a, July 30). https://atlas-scientific.com/blog/types-of-temperature-sensors/

[30] *4 wire PT1000 (platinum 1000 ohm) RTD surface temperature sensor with self adhesive patch and 40 inches (1 meter) of lead wire*. Evolution Sensors and Controls. (n.d.). https://evosensors.com/products/4-wire-pt1000-platinum-1000-ohm-rtd-surface-temperature-sensor-with-self-adhesive-patch-and-40-inches-1-meter-of-lead-wire?variant=36847694971048&country=US&currency=USD&utm_medium=product_sync&utm_source=google&utm_content=sag_organic&utm_campaign=sag_organic

[31] *Flexible FEP sealed RTD sensor PT100 3 wire design with 10 to 100ft long lead wire lengths for chemical and wet applications*. Evolution Sensors and Controls. (n.d.-b). https://evosensors.com/products/flexible-fep-sealed-rtd-sensor-pt100-3-wire-design-for-chemical-and-wet-applications-10ft-of-pfa-insulated-lead-wire?_pos=1&_sid=a5f4f8dfe&_ss=r

[32] Filburn, T., Dolder, C., Tufano, B., & Paul, H. L. (2007, July). A New Method for Breath Capture Inside a Space Suit Helmet. In *International Conference On Environmental Systems*. SAE Technical Paper.

[33] *CO2 sensors: Which type should you be looking for?*. Kaiterra. (n.d.). https://learn.kaiterra.com/en/air-academy/carbon-dioxide-sensors

[34] Hodgson, E., Dionne, S., Gervais, E., & Anchondo, I. (2012, January). Maturing Pump Technology for EVA Applications in a Collaborative Environment. In *International Conference on Environmental Systems* (No. JSC-CN-26074).

[35] Sladek C., Andersen, N., Goodman, E., Lewandowski, M., and Westheimer, D., “Comparison of Exploration Portable Life Support Subsystem (xPLSS) Thermal Modeling to Thermal Vacuum Testing,” *53rd International Conference on Environmental Systems*, 2024. https://hdl.handle.net/2346/98792

[36] “NASA Extravehicular Mobility Unit (EMU) LSS/SSA Data Book", NASA JSC-E-DAA-TN55224, September 2017. lpi.usra.edu/lunar/artemis/NASA-EMU-Data-Book-JSC-E-DAA-TN55224.pdf

[37] Bakula C. J., Theofylaktos O., “Antenna Design Considerations for the Advanced Extravehicular Mobility Unit”, NASA/TM—2015-218730, April 2015. ntrs.nasa.gov/api/citations/20150008350/downloads/20150008350.pdf

[38] “Understanding Bluetooth Range,” Bluetooth, bluetooth.com/learn-about-bluetooth/key-attributes/range/.
[39] “Bluetooth technology overview,” Bluetooth, bluetooth.com/learn-about-bluetooth/tech-overview/
[40] “FL BT EPA 2 - Wireless module”, Phoenix Contact, phoenixcontact.com/en-us/products/wireless-module-fl-bt-epa-2-1005869?type=pdf
[41] “What is Bluetooth Class?” Ezurio, www.ezurio.com/support/faqs/what-bluetooth-class
[42] “Yaesu VX-3R", Yaesu, yaesu.com/product-detail.aspx?Model=VX-3R&CatName=Legacy
[43] “Replacement for YAESU VX-3 VX-2 VX-2R VR-160 VX-1 VX-2E FNB-82LI Battery”, Amazon, amazon.com/Replacement-Battery-YAESU-VR-160-FNB-82LI/dp /B07T15FLSK
[44] “Understanding Bluetooth Range: How Far Does Bluetooth Reach?”, Bose, bose.com/stories/bluetooth-range-how-far-does-bluetooth-reach
[45] Hwu S., Upanavage M., Sham C., "Lunar Surface Propagation Modeling and Effects on Communications," 26th International Communications Satellite Systems Conference (ICSSC). June 2008. doi.org/10.2514/6.2008-5495
[46] “WiFi 6E Wireless Card Intel AX210”, Amazon, amazon.com/Wireless-Bluetooth-Tri-Band-5400Mbps-Network/dp/B09WQSNMCT?th=1
[47] Smiths Metal Centres, “6061 Aluminum Technical Datasheet,” 2023. https://www.smithmetal.com/pdf/aluminium/6xxx/6061.pdf
[48] Technical Products, Inc., “PEEK 30% Glass Filled Material Specifications.” https://www.technicalproductsinc.com/pdf/Specs/PEEK%20GF30%20Specs.pdf
[49] Ensinger Plastics, “TECAPEEK CF30 Black - Stock Shapes (rods, plates, tubes),” 2015. https://www.ensingerplastics.com/en-us/shapes/peek-tecapeek-cf30-black#/product-technical-detail-collapse-item-1-lvl-1
[50] Technical Products, Inc., “Ultem 1000 Material Specifications.” https://www.technicalproductsinc.com/pdf/Specs/Ultem%20Specs.pdf
[51] Toray Composite Materials America, Inc., “TORAYCA T300 Standard Modulus Carbon Fiber Data Sheet,” 2025. https://www.toraycma.com/wp-content/uploads/T300-Data-Sheet.pdf
[52] Zhai, Z., Feng, L., Liu, Z., and Li, G., “Water Absorption Test for Carbon Fiber Epoxy Resin Composite Based on Electrical Resistance,” *Polymer Testing*, Vol. 56, Dec. 2016, pp 394-397. https://doi.org/10.1016/j.polymertesting.2016.10.020
[53] Kang, J. H., Gordon, K. L., Ward, D., Belancik, G., Jagtap, P., and Sauti, G., “Highly Thermally Conductive Hybrid Carbon Fiber Polymer Composite for Radiator Application,” *52nd International Conference on Environmental Systems*, 2023. https://hdl.handle.net/2346/94578

[54] Li, H., Guo, H., Tu, H., Chen, X., Zeng, X., "Research on B4C/PEEK Composite Material Radiation Shielding". Polymers (Basel). 2024 Oct 15;16(20):2902. doi: 10.3390/polym16202902. PMID: 39458730; PMCID: PMC11510741.

[55] Cao, Y., Yang, H., Wan, K., Li, D., He, Q., Wu, H., "High-performance PEEK composite materials research on 3D printing for neutron and photon radiation shielding", Composites Part A: Applied Science and Manufacturing, Volume 185, 2024, 108352, ISSN 1359-835X,https://doi.org/10.1016/j.compositesa.2024.108352.

[56] W. C. Fan, C. R. Drumm, S. B. Roeske and G. J. Scrivner, "Shielding considerations for satellite microelectronics," IEEE Transactions on Nuclear Science, vol. 43, no. 6, pp. 2790-2796, Dec. 1996, doi: 10.1109/23.556868.

[57] Wrobel, J., Hoyt, R., Cushing, J., Jaster, M., Voronka, N., Slostad, J., & Paritsky, L., "Versatile Structural Radiation Shielding and Thermal Insulation through Additive Manufacturing," Small Satellite Conference, 2013. https://digitalcommons.usu.edu/smallsat/2013/all2013/61/

[58] Thomas, G., "Packaging Factors for Portable Life Support Subsystems Based on Apollo and Shuttle Systems," *23rd International Conference on Environmental Systems*, 1993. https://doi.org/10.4271/932182

[59] Fenske, M. T., Barth, J. L., Didion, J. R., and Mule, P., "The Development of Lightweight Electronics Enclosures for Space Applications," *S.A.M.P.E. Journal*, 1999. https://ntrs.nasa.gov/api/citations/19990025337/downloads/19990025337.pdf

[60] Khan, M. A., Lipscomb, G., Lin, A., Baldridge, K. C., Petersen, E. M., Steele, J., Abney, M. B., and Bhattacharyya, D. "Performance Evaluation and Model of Spacesuit Cooling by Hydrophobic Hollow Fiber-Membrane Based Water Evaporation through Pores." *Journal of Membrane Science*, Vol. 673, 2023, p. 121497. https://doi.org/10.1016/j.memsci.2023.121497.

[61] [Strock, N. C., Frisco, D., Dillon, E. L., Estep, P. N., Norcross, J., Prejean, B. J., Fincke, R. S., and K. Marshall-Goebel. Evaluation of Aerobic Standards for Lunar Surface Extravehicular Activities. *Nasa.gov*. https://ntrs.nasa.gov/citations/20220014309. Accessed May 17, 2026.

[62] Tachikawa, S., Nagano, H., Ohnishi, A., and Nagasaka, Y. "Advanced Passive Thermal Control Materials and Devices for Spacecraft: A Review." *International Journal of Thermophysics*, Vol. 43, No. 6, 2022. https://doi.org/10.1007/s10765-022-03010-3.

[63] Editor Engineeringtoolbox. Ethylene Glycol Heat-Transfer Fluid Properties: Density, Data & Charts. *Engineeringtoolbox.com*. https://www.engineeringtoolbox.com/ethylene-glycol-d_146.html. Accessed May 17, 2026.

[64] Editor Engineeringtoolbox. Propylene Glycol Based Heat-Transfer Fluids. *Engineeringtoolbox.com*. https://www.engineeringtoolbox.com/propylene-glycol-d_363.html. Accessed May 17, 2026.

[65] NuTherm® HC-40 High Performance, Potassium Formate/Water-Based Closed System Heat Transfer Fluid Ideal for Low Temperature Applications. *NUGENTEC*. https://nugentec.com/nutherm-hc-40-high-performance-potassium-formate-water-based-closed-system-heat-transfer-fluid-ideal-for-low-temperature-applications/?srsltid=AfmBOor4BU0Ez5wdBYVR_1IxEsFwzfCFYL3ARVJFTPnzOSCU82Qh77eX. Accessed May 17, 2026.

[66] Santos, A. C., Guimarães, L. N. F., and Leite, V. S. F. O. "Copper Water Heat Pipe Applied for Stirling Engine." *Brazilian Journal of Radiation Sciences*, Vol. 10, No. 3A, 2022. https://doi.org/10.15392/2319-0612.2022.1876.

[67] *Tgard™ 500 Thermally Conductive Insulators*.

[68] Heat Pipe Performance Calculator. *Boyd | Trusted Innovation*. https://www.boydcorp.com/about-boyd/resources/calculators-selector-tools/heat-pipe-performance-calculator.html. Accessed May 17, 2026.

[69] Video on Master Bond EP48TC | Low Thermal Resistant Epoxy Paste | MasterBond.com. *Masterbond.com*. https://www.masterbond.com/de/video/breaking-through-walls-thermal-management. Accessed May 17, 2026.

[70] Supmea Auto. What's the Relationship between Pipe Diameter, Pressure, and Flow? *Supmea Automation Co.,Ltd*. https://www.supmeaauto.com/training/flow-rate-and-pressure. Accessed May 17, 2026.

[71] Braided PTFE Lined Flex Hose. *Vibrant Performance*. https://vibrantperformance.com/braided-ptfe-lined-flex-hose-v1016/. Accessed May 17, 2026.

[72] *Construction Applications Benefits Medium Pressure Smooth Bore Hose of PTFE SB Series • SB-SERIES*.

[73] Ulrich, D. Tube Bending Formulas | Ultimate Tube Bender Parts. *Bender parts | Ultimate bender tube bender parts plus Inc*. https://www.benderparts.com/tube-bending-formulas/. Accessed May 18, 2026.

[74] QD, Dry Break -4 an JIC Aluminum, ETP, Brakes. *Racetronix.biz*. https://www.racetronix.biz/p/qd-dry-break-4-an-jic-aluminum-etp-brakes/qds-b0304ae. Accessed May 17, 2026.

[75] Hengeveld, D. W., Foster, I. J., Bird, T. J., Lockwood, D., and Allison, J. "Thermochromic Variable Emissivity Material Thermal Modeling and Test Correlation." *54th International Conference on Environmental Systems*, 2025. https://doi.org/10.32865/2346/102604.

[76] Variable Emittance Materials: Adaptive Thermal Control for Spacecraft - Surface Optics Corporation. *Surface Optics Corporation*. https://surfaceoptics.com/variable-emittance-materials-spacecraft-thermal-control/. Accessed May 17, 2026.

[77] Xu, Q., Ji, H., Ren, Y., Ou, Y., Liu, B., Wang, Y., Chen, Y., Long, P., Deng, C., and Wang, J. "VO2-Based Spacecraft Smart Radiator with High Emissivity Tunability and Protective Layer." *Nanomaterials*, Vol. 14, No. 16, 2024, p. 1348. https://doi.org/10.3390/nano14161348.

[78] AZ Technology, Inc. *Aztechnology.com*. https://www.aztechnology.com/. Accessed May 17, 2026.

[79] San Diego State University. *Wien's Law*.

[80] Dai, Y., et al., "Thermal Runaway Process in Lithium-Ion Batteries: A Review," *Next Energy*, Vol. 6, 2025, p. 100186. https://doi.org/10.1016/j.nxener.2024.100186

[81] "Advancements in Sodium-Ion Batteries Technology: A Comprehensive Review of Recent Development on Materials, Mechanisms, Applications, and Prospects for Energy Storage," *Journal of Energy Storage*, 2025. ScienceDirect Article

[82] "Solid-State Architecture Batteries for Enhanced Rechargeability and Safety (SABERS) for Extended Deep Space Applications," *NASA Technical Reports Server (NTRS)*, NASA, 2020. NASA NTRS Citation

[83] Miyazawa, Y., Shimada, T., Fuse, T., Shimada, S., Nishiura, S., Okamoto, H., Okawa, T., Hoshino, T., Kawasaki, O., and Naito, H., "Space Demonstration of All-Solid-State Lithium-Ion Batteries Aboard the International Space Station," *Aerospace*, Vol. 12, No. 6, 2025, pp. 514–514. https://doi.org/10.3390/aerospace12060514

[84] Stanford University Cui Group, "Research on Advanced Battery Technologies," Stanford University. Stanford Cui Group PDF

[85] Ozkan, M., Ozkan, M., Abaoag, B., Antony, H., and Nelson, C., "A Comprehensive Review of Solid-State Lithium Batteries: Fast Charging Characteristics and In-Operando Diagnostics," *Nano Energy*, Vol. 142, Part B, 2025, p. 111232. https://doi.org/10.1016/j.nanoen.2025.111232

[86] "Lithium-Ion Battery Demonstration for the 2007 NASA Desert Research and Technology Studies (Desert RATS) Program," *NASA Technical Reports Server (NTRS)*, NASA, 2008. NASA NTRS PDF

[87] Swartout, B., Meginnis, I., and Westheimer, D., "Exploration Extravehicular Mobility Unit (xEMU) Hard Upper Torso (HUT) Chamber B Thermal Vacuum Testing Results," 53rd International Conference on Environmental Systems, ICES-2024-215, 2024.

[88] Meginnis, I. M., Rhodes, R. A., and Kim, D. J., "NASA Advanced Space Suit xEMU Development Report – Hard Upper Torso Assembly," 51st International Conference on Environmental Systems, ICES-2022-258, 2022.

[89] Graziosi, D., Ferl, J., & Splawn, K. "An examination of spacesuit entry types and the effect on suit architecture". In Space 2004 Conference and Exhibit. American Institute of Aeronautics and Astronautics. https://doi.org/10.2514/6.2004-5969

[90] Baker, A. (2023, July). "xPLSS structural backplate design, manufacture, and test overview". Presented at the International Conference on Environmental Systems (ICES 2023). NASA Johnson Space Center. NASA Technical Reports Server PDF (ntrs.nasa.gov)

[91] Fonseca, G. (n.d.). "Epoxy/HS carbon fiber, UD composite, quasi-isotropic laminate" [PDF]. Scribd. Scribd document

[92] National Aeronautics and Space Administration, Office of the Chief Engineer. (2022). "NASA-STD-5001B w/Change 3: Structural design and test factors of safety for spaceflight hardware" (NASA Technical Standard No. NASA-STD-5001B). NASA Technical Standards System (standards.nasa.gov)

[93] Parker Hannifin Corporation, O-Ring Division. (n.d.). "Parker O-ring handbook" (ORD 5700). Parker Hannifin Corporation. https://www.parker.com/content/dam/Parker-com/Literature/O-Ring-Division-Literature/ORD-5700.pdf (parker.com)

[94] ZoM. (2012, July 11). "Aluminium / aluminum 6061 alloy (UNS A96061)". AZoM – The A to Z of Materials. AZoM article

[95] Aerospace Metals, "Titanium Ti-6Al-4V (Grade 5), STA Data Sheet," Aerospace Metals, Online, URL: https://www.aerospacemetals.com/wp-content/uploads/2023/07/Titanium-Ti-6Al-4V-Grade-5-STA-Data-Sheet.pdf

[96] Eco Aluminum, "Aluminum Alloy 6061-T6/T651 Data Sheet," Eco Aluminum, Online, URL: https://eco-alum.com/wp-content/uploads/6061-T6_T651-Aluminum-Alloy-Data-Sheet.pdf

[97] United Performance Metals, "316/316L Stainless Steel Data Sheet," United Performance Metals, Online, URL: https://www.upmet.com/sites/default/files/products/datasheet/316316l-datasheet.pdf

[98] Bernstein, K. S., "Structural Design Requirements and Factors of Safety for Spaceflight Hardware for Human Spaceflight," JSC-65828, Rev. B, Change 1, NASA Johnson Space Center, Houston, TX, July 2014.

[99] McDonnell Douglas Astronautics Company, "Isogrid Design Handbook," NASA CR-124075, Rev. A, NASA Marshall Space Flight Center, Huntington Beach, CA, February 1973.

[100] "Mars Facts," NASA Science, NASA, https://science.nasa.gov/mars/facts/ (retrieved 18 May 2026).

[101] Cheuvront, S. N., "Body Size and Its Implications upon Resource Utilization during Human Space Exploration Missions," *Scientific Reports*, Vol. 10, No. 1, Aug. 2020, p. 13836. https://doi.org/10.1038/s41598-020-70054-6

[102] "Astronaut Selection and Training," NASA FS-2011-11-057-JSC, NASA Johnson Space Center, Houston, TX, 2011. https://www.nasa.gov/wp-content/uploads/2017/05/606877main_fs-2011-11-057-jsc-astro_trng.pdf
[103] "ROHACELL® HERO – Thermal Insulator," Technical Information, Evonik Operations GmbH, June 2022. https://products.evonik.com/assets/34/34/ROHACELL_HERO_Thermal_Insulator_Rev_06_22_EN_243434.pdf
[104] "Aluminum 6061-T6," ASM Material Data Sheet, MatWeb, https://asm.matweb.com/search/SpecificMaterial.asp?bassnum=MA6061T6 (retrieved 18 May 2026).
[105] Schön, J., "Coefficient of Friction for Aluminum in Contact with a Carbon Fiber Epoxy Composite," *Tribology International*, Vol. 37, No. 5, 2004, pp. 395–404. https://doi.org/10.1016/j.triboint.2003.11.008
[106] "Mechanical Fastener Torque Guidelines," Directive No. 540-PG-8072.1.2B, NASA Goddard Space Flight Center, Greenbelt, MD, July 2020. https://www.csbf.nasa.gov/documents/540-PG-8072.1.2B%20Signed%20and%20released.pdf
[107] "Metric Bolts – Maximum Torque," Engineering Toolbox, https://www.engineeringtoolbox.com/metric-bolts-maximum-torque-d_2054.html (retrieved 18 May 2026).
[108] Chambers, J. A., "Preloaded Joint Analysis Methodology for Space Flight Systems," NASA TM-106943, NASA Lewis Research Center, Cleveland, OH, Dec. 1995. https://ntrs.nasa.gov/api/citations/19960012183/downloads/19960012183.pdf
[109] Boltport Fasteners, "ASTM F568M Specification," Boltport Fasteners, Online, URL: https://boltport.com/specifications/astm-f568m/
[110] Roe, R. R., "Requirements for Threaded Fastening Systems in Spaceflight Hardware," NASA-STD-5020B, NASA, Washington, DC, August 2021.
[111] Hirschorn, S., *NASA Systems Engineering Handbook*, NASA/SP-2016-6105 Rev. 2, National Aeronautics and Space Administration, Washington, DC, 2016. NASA Systems Engineering Handbook
[112] Watts, C., Campbell, C., Vogel, M., and Conger, B., "Space Suit Portable Life Support System Test Bed (PLSS 1.0) Development and Testing," 2012. https://doi.org/https://ntrs.nasa.gov/citations/20120007410
[113] Zinoubi, B., Zbidi, S., Vandewalle, H., Chamari, K., and Driss, T., "Relationships Between Rating of Perceived Exertion, Heart Rate and Blood Lactate During Continuous and Alternated-Intensity Cycling
[114] Exercises," *Biology of sport*, Vol. 35, No. 1, 2017, pp. 29–37. https://doi.org/10.5114/biolsport.2018.70749
[115] Berik, M., "The Usefulness of Subjective Task Load Assessment Methods for Predicting Pilot Task Load in General Aviation Organizations," *Scientific Papers of*

Silesian University of Technology Organization and Management Series, Vol. 19, No. 32, 2024. https://doi.org/10.29119/1641-3466.2024.200.2.

[116] Cronkleton, E., "What Is the Average Walking Speed of an Adult?," Healthline Media, Mar 14 2019. Retrieved 14 May 2026. https://www.healthline.com/health/exercise-fitness/average-walking-speed#takeaway

[117] "Maintainability Vs. Reliability," Onupkeep. Retrieved 14 May 2026. https://upkeep.com/learning/maintainability/

[118] Anderson, K., and Robertson, I., "Development and Validation of the NASA Modified System Usability Scale (NMSUS): A Brief Summary," NASA Technical Reports Server (NTRS), Nov 28 2022. Retrieved 5 May 2026. https://ntrs.nasa.gov/citations/20220017395

[119] NASA, "5.0 Human Performance and Error," NASA, Feb 18 2025. Retrieved 14 May 2026. https://www.nasa.gov/reference/5-0-human-performance-anderror-vol-2/

[120] DiSabito, J., Graziosi, J., Muller, D., Szrama, G., Valis, L., Buffa, E., and Probst, M., "The Competitive Standing of State-of-the-Art PLSS Technologies Given Prospective EVA Cadence," *54th International Conference on Environmental Systems*, 2025. Retrieved 18 May 2026. https://ntrs.nasa.gov/api/citations/20250003716/downloads/ICES-2025-mxPLSS%20Paper_FinalDraft_footer_04232025.pdf

[121] Chullen, C., Campbell, C., Papale, W., Hawes, K., and Wichowski, R., "Rapid Cycle Amine 3.0 System Development," *45th International Conference on Environmental Systems*, 2015. Retrieved 18 May 2026. https://ntrs.nasa.gov/citations/20160005888

[122] Jagtap, P., Belancik, G., Jan, D., Chen, W., and Hall, S., "Power Optimization of Cryogenic CO_2 Deposition Capture in Deep Space," *50th International Conference on Environmental Systems*, 2020. Retrieved 18 May 2026. https://ntrs.nasa.gov/api/citations/20205004234/downloads/ICES-2020-405.pdf

[123] Peters, B., and Westheimer, D., "EMU Metox Performance Testing," *48th International Conference on Environmental Systems*, 2018. Retrieved 18 May 2026. https://ttu-ir.tdl.org/items/08ca10db-71a3-430e-8c8d-893d2b96ae82

[124] Varian, Inc., "Dry Scroll Pumps Technical Specifications," *Vacuum Technologies Catalog*. Retrieved 18 May 2026. https://photos.labwrench.com/equipmentManuals/6234-2121.pdf

12 Appendix B. User Manual

12.1 Charging the Solid State Battery

12.1.1 Objective

Figure 12.1.1: Solid State Battery Location

Recharge the primary and backup solid state battery units and return them to their original mounting location.

12.1.2 Handling Considerations

- Handle all components carefully to prevent damage to the volumetric mockup
- Do not apply excessive force when removing Velcro-mounted components
- Ensure adjacent wiring and nearby components are not disturbed during handling

12.1.3 Required Tools / Equipment

- Simulation timing device (e.g., phone or stopwatch)
- Mock charging cable (if applicable)

12.1.4 Component Location

The solid-state battery assembly is located next to the lithium hydroxide canister. The backup battery is stacked on top of the primary battery.

12.1.5 Procedure

Step 1: Locate the battery assembly
Identify the primary battery and backup battery next to the lithium hydroxide canister.

Step 2: Inspect the mounting method
Confirm that both batteries are secured together with Velcro and that the battery assembly is also attached to the board using Velcro.

Step 3: Remove the batteries
Carefully detach both the backup battery and primary battery from the board. Keep the batteries together unless they need to be separated for charging.

Step 4: Connect the charging cables
Attach the required charging cable to each battery. If both batteries cannot be charged at the same time, charge them one at a time.

Step 5: Simulate charging time
Place your phone over each battery for one minute to represent the charging period.

Step 6: Reinstall the batteries
After charging is complete, return the primary battery and backup battery to their original position next to the lithium hydroxide canister. Make sure the batteries are securely attached with Velcro.

12.1.6 Verification/Completion Criteria

- Both batteries are returned to their original stacked configuration
- Velcro attachments are secure between the batteries and the board
- No surrounding components or wiring have been disturbed
- Charging simulation has been completed for each batter

12.1.7 Assumptions

- Batteries are represented by 3D printed blocks for volumetric and accessibility testing
- Velcro attachment is used to simulate a simplified quick-access fastening method within the mockup
- Charging is simulated using a timed placeholder method rather than an active electrical charging system
- In an operational PLSS system, the solid-state battery would likely function as a sealed, non-serviceable unit during EVA operations
- Battery maintenance during a mission would primarily involve charging through an external interface and monitoring battery health parameters

- Removal or replacement of the battery assembly would most likely occur during ground servicing, refurbishment, or major maintenance operations rather than during astronaut EVA activities
- The servicing procedure described in this mockup is intended for maintainability and accessibility testing purposes only

12.2 Inspecting The Oxygen Loop

12.2.1 Objective

Figure 12.2.1: Oxygen Loop Location

Components of the oxygen loop system highlighted in red. The highlighted region includes the oxygen storage tanks, regulator assembly, pump stack with an integrated fan beneath it, and the multi parameter life support sensor used for system monitoring.

12.2.2 Handling Considerations

- Ensure all oxygen loop connections remain secure during inspection
- Do not loosen, disconnect, or remove any tubing or component connections unless directed
- Do not remove the oxygen tanks from their fasteners
- Note that each component is connected as part of the full loop, so removing one component may require partial or full deconstruction of the loop

12.2.3 Component Location

There are multiple components that make up the oxygen loop:

- Fans
- Regulators
- Pump
- Tanks

The small oxygen tank is located on the bottom left side of the isogrid, while the large oxygen tank is located on the bottom right side. The remaining oxygen loop components are arranged around the pill-shaped tanks.

12.2.4 Procedure

Step 1: Verify required components
Confirm that all required oxygen loop components are present and undamaged. The required components are:

- 3 fans
- 2 pumps
- 2 tanks
- 2 regulators
- 2 multi-parameter astronaut life support sensors (MPALSS)

Step 2: Check Oxygen Flow Rate
Using the display panel on both MPALSS's, check the oxygen flow rate reading associated with the regulator. The expected range should be between **3 and 8 actual cubic feet per minute (acfm)** [115]**.**

Step 3: Inspect for connection leaks
Check near the connection point between the regulator and oxygen tank for any noticeable draft. If a draft is detected, the oxygen loop should be considered faulty.

Step 4: Report failure if needed
If a leak, draft, missing component, damaged component, or abnormal flow rate is identified, report the issue to mission control.

12.2.5 Verification/Completion Criteria

- All required oxygen loop components are present and properly connected
- Oxygen flow rate is within the expected range of 3 to 8 acfm
- No draft or leak is detected near the regulator and tank connection
- Astronaut is assumed to be properly supplied with oxygen based on the inspection results

12.2.6 Assumptions

- Oxygen loop components are represented by mock components for volumetric and accessibility testing
- The oxygen loop is assumed to operate automatically during the procedure
- The current mockup lacks a secondary pump because it was not manufactured with the system
- Leak detection is simulated through a draft check at the regulator and oxygen tank connection
- The procedure is intended to verify layout, accessibility, and inspection workflow rather than actual oxygen delivery performance

12.3 Avionics Boxes

Figure 12.3.1: Avionics Box Locations

12.3.1 Objective

Inspect the avionics boxes to ensure structural integrity, verify system status, and perform corrective maintenance if a failure is identified.

12.3.2 Handling Considerations

- Handle all avionics boxes carefully to avoid damaging the mockup structure or internal components
- Do not apply excessive force when testing box stability
- Maintain control of all hardware (screws and nuts) during removal to prevent loss

- Ensure surrounding components and wiring are not disturbed during inspection or maintenance

Component Location
There are three avionics boxes located within the system:

- Top right position
- Top left position
- Center position, beneath the lithium hydroxide canister and solid state batteries

Each avionics box is secured with **eight M4 screws and corresponding nuts located on the underside of the mounting surface**

12.3.3 Procedure

Step 1: Locate avionics boxes
Identify all three avionics boxes in their designated positions.

Step 2: Inspect structural fastening
Verify that all eight screws on each avionics box are present and tightened. Ensure the top cover is fully secured.

Step 3: Verify mounting stability
Gently jostle each avionics box to confirm it is securely attached to the isogrid structure. No significant movement should be observed.

Step 4: Check system status
Observe the external status monitoring device to confirm that all avionics and battery systems are functioning properly. After properly completing the previous steps, mission control will provide information about system status.

Step 5: Identify failure (if applicable)
If mission control indicates a malfunction, determine which avionics box is associated with the issue.

Step 6: Remove faulty avionics box
Using the 3 mm hex key, begin loosening the eight M4 screws securing the avionics box.
Use needle-nose pliers to hold the nuts on the underside during removal.
Carefully remove all screws and retain the nuts to prevent loss.

Step 7: Access internal circuitry
Remove the top cover of the avionics box to expose the internal circuitry.

Step 8: Replace circuitry
Remove the faulty circuitry and install the replacement mock component in the same configuration.

Step 9: Reassemble the avionics box
Reattach the top cover and align all mounting holes.
Insert all eight screws and secure them with the corresponding nuts using the hex key and pliers.
Tighten all fasteners evenly to ensure proper seating.

Step 10: Reinstall and secure
Ensure the avionics box is firmly reattached to the isogrid structure and properly aligned.

Step 11: Recheck system status
Use the external status monitoring device to verify that the system is functioning correctly after reinstallation.

12.3.4 Verification/Completion Criteria

- All eight screws and nuts per avionics box are installed and securely fastened
- Each avionics box is firmly attached to the isogrid with no excessive movement
- External status monitoring device indicates all systems are functioning properly
- Any faulty circuitry has been successfully replaced and the enclosure properly reassembled

12.3.5 Assumptions

- Avionics boxes and internal circuitry are represented by mock components for volumetric and accessibility testing
- M4 screws and nuts simulate realistic mechanical fastening methods
- External status device represents system health monitoring
- All components are assumed to be removable and serviceable for the purpose of this test

12.4 LiOH Canister & TCC

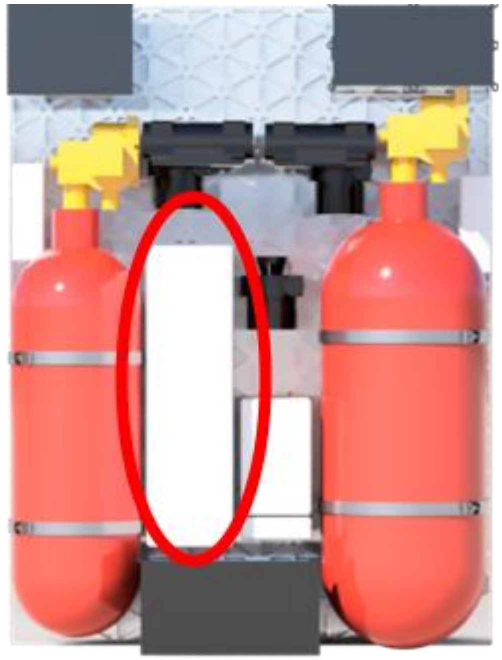

Figure 12.4.1: Lithium Hydroxide Canister Location

12.4.1 Objective

Inspect the lithium hydroxide canister and Thermal Control Component system to verify ventilation flow, carbon dioxide removal, pressure behavior, and component accessibility within the volumetric mockup.

12.4.2 Handling Considerations

- Handle all components carefully to prevent damage to the volumetric mockup
- Do not apply excessive force when removing Velcro-mounted components
- Ensure adjacent wiring, tubing, and nearby components are not disturbed during handling
- Use caution when handling the LiOH canister, since an operational canister may become warm during use

12.4.3 Mock Tools / Equipment

- Display panel (if applicable)
- Suit display panel
- Mock LiOH canister
- Mock thermal filter cartridge

12.4.4 Component Location

The LiOH canister and TCC components are located near the central region of the mockup, close to the solid-state batteries and oxygen loop components.

12.4.5 Procedure

LiOH Canister Inspection
Step 1: Ventilation flow rate check
On the display panel, locate **"FLOW RATE CHECK."** Verify that the displayed flow rate is between **85 and 227 Lpm.**

If the flow rate is below the acceptable range, record that the canister may be saturated or clogged in an operational system. For this mockup test, proceed with the simulated replacement sequence.

Step 2: Pressure sensor check
Review the pressure sensor readings across the LiOH canister. A specific nominal value is not currently available, but readings should remain within approximately **20%** of the expected operating value. If the pressure reading falls outside this range, record the issue and proceed with the simulated replacement sequence.

Step 3: Carbon dioxide level check
On the suit display panel, verify the carbon dioxide level. The CO_2 level should remain below **2.5 mmHg**. If the CO_2 level exceeds this limit, record the issue and proceed with the simulated replacement sequence.

Step 4: Moisture and temperature condition check
Carefully inspect the canister by touch. In an operational system, the canister should not feel warm or hot, and there should be no visible water vapor or moisture accumulation.

LiOH Canister Replacement
Step 1: Isolating the ventilation loop
Simulate turning off the appropriate valves to represent isolating the ventilation loop. This action does not control an active ventilation system in the mockup.
Step 2: Removing the canister
Simulate removing the screws securing the canister or detach the Velcro-mounted canister if Velcro is being used. Carefully remove the mock canister from the system.

Step 3: Disposal of the used canister
Place the removed mock canister aside to represent disposal according to hazardous waste protocol. No actual hazardous material is present in the mockup.

Step 4: Inspect the mock replacement canister
Use the same mock LiOH canister to represent the replacement unit. Inspect the seals and outer surfaces for visible damage before reinstalling it.

Step 5: Reinstall the mock canister
Insert the same mock canister back into the system in the same orientation as before. Simulate securing it with screws or reattach it using Velcro, depending on the mockup configuration.

Step 6: Reopening the ventilation loop
Simulate opening the valves to represent restoring flow through the ventilation loop.

Step 7: Check for leaks
Inspect the ventilation loop connection points for signs of improper sealing. In an operational system, bubbles or escaping air would indicate a leak. For the mockup, visually confirm that all tubing and connection points remain properly seated.

Step 8: Recheck CO_2 levels
After five minutes, recheck the CO_2 level on the suit display panel to confirm that the simulated replacement procedure has been completed successfully.

Thermal Filter Replacement
Step 1: Removing pressure cap
Unscrewing the pressure cap from the thermal filter housing.
Step 2: Remove mock cartridge
Carefully extract the existing mock thermal filter cartridge.

Step 3: Inspect and reinstall cartridge
Inspect the same mock cartridge for damage, then reinsert it into the housing in the correct orientation to simulate installing a replacement cartridge.

Step 4: Reinstalling pressure cap
Screw the pressure cap back onto the housing and confirm that it is properly seated.

Verification / Completion Criteria

- Ventilation flow rate is between 85 and 227 Lpm
- CO_2 level is below 2.5 mmHg

- Pressure sensor readings remain within the acceptable range
- LiOH canister is secure and properly oriented
- Tubing and connection points remain properly seated
- Simulated valve operation has been completed
- Mock thermal filter cartridge has been removed, inspected, and reinstalled
- No adjacent wiring, tubing, or nearby components have been disturbed

Assumptions

- The LiOH canister and TCC components are represented by mock components for volumetric and accessibility testing
- Velcro may be used in the mockup to represent simplified component attachment methods
- Screw removal and reinstallation are simulated for maintainability testing purposes
- Valve opening and closing procedures are simulated and do not control an active ventilation system
- The replacement LiOH canister procedure uses the same mock canister rather than a physically different replacement unit
- The thermal filter replacement procedure reuses the same mock cartridge to simulate the replacement process
- The 20% pressure sensor limit is used as a placeholder because a nominal operational pressure value was not available
- Hazardous waste disposal steps are included to represent realistic operational procedures for a flight-rated LiOH canister
- The procedure is intended to evaluate accessibility, maintainability, crew interaction, and inspection workflow rather than actual chemical filtration or ventilation performance

12.5 Servicing The SWME

Figure 12.5.1: SWME Location

12.5.1 Objective

Inspect and service the Spacesuit Water Membrane Evaporator (SWME) system to verify water level, heat rejection performance, leakage condition, water quality, and sensor response within the volumetric mockup.

12.5.2 Handling Considerations

- Keep the SWME wet at all times during handling and servicing
- If the SWME is removed, place it in iodinated water storage to prevent drying
- Do not disconnect water lines unless the SWME has been isolated from the loop
- Ensure surrounding tubing, wiring, and nearby components are not disturbed during handling
- Do not attempt to pressurize the SWME without ground support equipment

Mock Tools / Equipment

- Display panel or simulated display interface
- Mock iodinated water supply
- Feedwater tank marker or fill-level indicator
- Mock water collection container
- Mock 500 mL sample container
- Mock biocide injection tool, if applicable
- Fastening tool, if simulated fasteners are used
- Visual inspection checklist
- Replacement SWME representation, if available

12.5.3 Component Location

The SWME is stacked together with the battery assembly near the lower central region of the isogrid structure, directly beneath the lithium hydroxide canister. The SWME is connected to the thermal control and water loop system through nearby water lines, valves, sensors, and the feedwater tank.

12.5.4 Procedures

Simulated Feedwater Tank Replenishment

Step 1: Simulate locating iodinated water supply
Identify the mock iodinated water storage location onboard the system.

Step 2: Simulate locating the feedwater tank
Identify the feedwater tank connected to the SWME loop.

Step 3: Simulate refilling the feedwater tank
Represent adding iodinated water to the feedwater tank until it reaches the marked fill level.

Simulated Heat Rejection Test

Step 1: Simulate heat input test
Using the display panel, select the **600 W heat input** test to represent SWME heat rejection operation.

Step 2: Simulate outlet temperature check
Read the SWME outlet temperature from the display or sensor location. The expected outlet temperature is **11°C to 13°C**.

Step 3: Record test result
If the outlet temperature is within range, record the SWME as passing the simulated heat rejection test.

Step 4: Simulate corrective action if failed
If the outlet temperature is outside the expected range, record that water flow would be increased in an operational system. If the issue remains unresolved, the SWME would be replaced.

Simulated Leakage Test

Step 1: Simulate visual leak inspection
Inspect the SWME, water lines, and connection points for visible signs of leakage.

Step 2: Record leakage condition
If visible leakage is observed, record the SWME as failed. Since the mockup cannot be pressurized without ground support equipment, replacement would be required in an operational system.

Simulated Water Quality Check

Step 1: Simulate silicon level check
Using the display panel or sensor reading, verify that the silicon level in the loop water is below **5.8 ppm**.

Step 2: Simulate total organic carbon check
Using the display panel or sensor reading, verify that total organic carbon is below **13 ppm**.

Step 3: Record water quality result
If either reading exceeds the acceptable limit, record the issue for follow-up maintenance.

Simulated Sensor Check

Step 1: Simulate BPV display check
Cycle through the BPV readings on the display panel.

Step 2: Simulate potentiometer voltage check
Monitor the potentiometer voltage and confirm that it remains within **0 to 4400 mV**.

Step 3: Simulate temperature sensor drift check
Compare the SWME inlet and outlet calibrated temperature references. The exact calibrated reference values are currently unknown, but the drift should not exceed **2°C**.

Step 4: Simulate corrective action if drift is high
If the drift is **greater than 2°C**, record that a software offset would be applied from the display panel. If the offset does not resolve the issue, the controller would be replaced.

Simulated SWME Replacement

Step 1: Simulate isolating the SWME
Close the mock valves to represent isolating the SWME from the water loop.

Step 2: Maintain wet condition
Keep the SWME wet at all times. If removed, place the SWME in iodinated water storage.

Step 3: Simulate pressure release
Confirm that the display indicates **0 psig** before continuing.

Step 4: Simulate water drainage and sampling
Represent draining water from the SWME and collecting a minimum **500 mL sample**.

Step 5: Simulate water line disconnection
Carefully disconnect or represent disconnecting the water lines from the SWME.

Step 6: Simulate fastener removal
Remove or represent removing the screws securing the SWME to the mockup.

Step 7: Simulate SWME color inspection
Inspect the SWME for color condition. Yellow or purple coloration is acceptable if present.

Step 8: Simulate sample testing
Represent testing the collected sample for microbial concentration. The acceptable result should be below **1×10^6 CFU/mL.**

Step 9: Simulate biocide injection
Represent injecting biocide into the water loop.

Step 10: Simulate replacement installation
Use the same SWME to represent a replacement unit. Reinstall it by reversing the removal steps.

Step 11: Simulate water line reconnection
Reconnect or represent reconnecting all water lines and confirm that each connection is secure.

Step 12: Simulate refilling with iodinated water
Represent filling the SWME loop with iodinated water.

Step 13: Simulate potentiometer recheck
Use the display panel to confirm that the potentiometer reading remains within the expected range.

Step 14: Simulate final leak check
Inspect the SWME and water line connections for visible leaks after reinstallation.

12.5.5 Verification / Completion Criteria

- SWME remains wet or is represented as being kept wet throughout the procedure
- Feedwater tank is filled or simulated as filled to the marked level
- Simulated SWME outlet temperature is within the expected range of **11°C to 13°C**
- No visible leaks are observed at the SWME or water line connection points
- Simulated silicon level is below **5.8 ppm**
- Simulated total organic carbon is below **13 ppm**
- Simulated potentiometer voltage remains between **0 and 4400 mV**
- Simulated temperature sensor drift does not exceed **2°C**
- Mock water sample collection is completed
- SWME is reinstalled or represented as reinstalled and refilled with iodinated water

12.5.6 Assumptions

- The SWME and related water loop components are represented by mock components for volumetric and accessibility testing
- All SWME inspection, servicing, valve operation, pressure release, water sampling, biocide injection, and replacement actions are simulated
- The same SWME component may be reused to represent a replacement unit during the test
- The system cannot be pressurized without ground support equipment
- Iodinated water storage is represented to show that the SWME should remain wet during servicing
- The procedure evaluates accessibility, maintainability, crew interaction, and inspection workflow rather than actual thermal control or water processing performance

13 Appendix C. Design Iterations

13.1 Thermal - Lithium Chloride and Metal Organic Frameworks

Lithium Chloride Absorber Radiators (LCARs) were one of the first thermal control concepts investigated for this design because NASA had already demonstrated they could function in Mars-like environments. Instead of venting water directly to the atmosphere like a standard SWME, the LCAR chemically absorbs the evaporated water vapor using lithium chloride while also rejecting heat through radiator panels mounted on the PLSS shell, depicted in Figure 13.1.1.

Figure or Table containing sensitive information, or possible unauthorized copyright information has been removed.

Figure 13.1.1: Lithium chloride absorber radiator design (Izenson et al., 2017)

This creates a partially closed-loop system capable of preserving most of the water normally lost during EVA operations. Early in the project, before the full 500 W thermal requirement was established, the concept was evaluated assuming an average 300 W heat load over a 10-hour EVA.

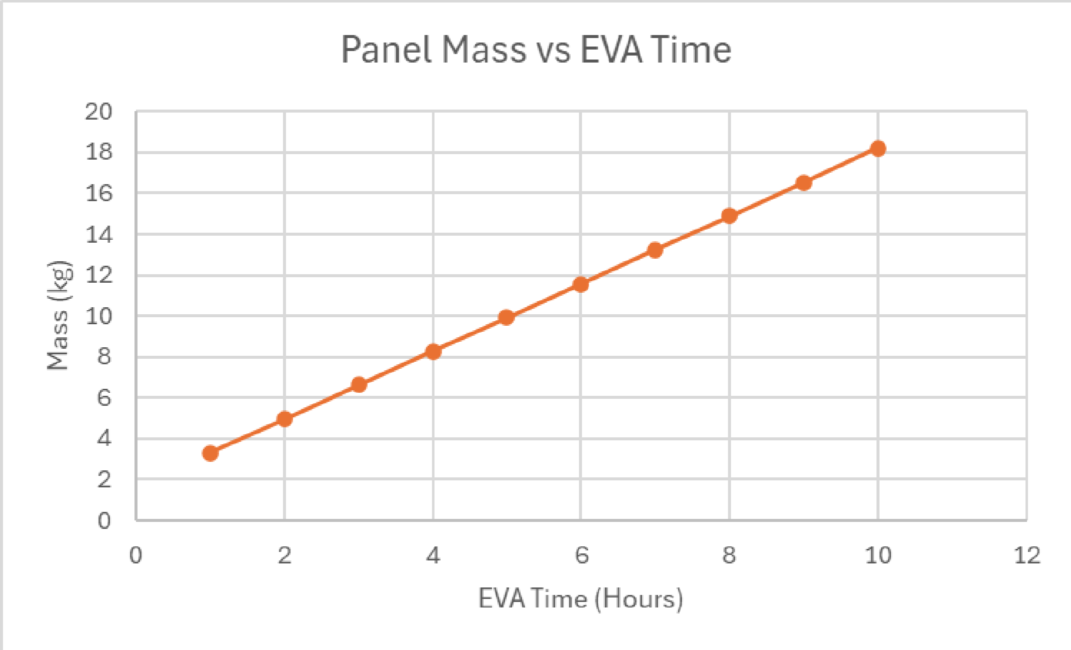

Figure 13.1.2: Panel mass vs EVA time for lithium chloride absorber radiator design

The overall thermal architecture of the PLSS would remain mostly unchanged with an LCAR system. The LCVG loop, pumps, and dehumidification process still function the same way, but instead of the SWME acting as the primary heat sink, the evaporated water vapor is routed into absorber panels integrated into the backpack shell. Lithium chloride was selected because of its strong water absorption capability, high latent heat storage, and relatively good thermal conductivity. NASA testing showed that during a 10-hour test, water entered the evaporator near 30°C and exited the absorber near 19°C while roughly 2 kg of water was absorbed over the test duration. These results showed that the concept could significantly reduce consumable water losses compared to direct SWME venting.

However, several major drawbacks became apparent during analysis. The lithium chloride solution is highly corrosive and extremely sensitive to CO_2 contamination, meaning the system requires nearly perfect seals and a heavy containment structure. This added significant structural mass, reducing the benefit from preserving water. Another limitation is that the absorber has a fixed sorbent capacity, meaning it can only absorb a limited amount of water before regeneration is required. Extending EVA duration would therefore require additional absorber mass.

Because of these issues, Metal-Organic Frameworks (MOFs), specifically IRMOF-10, were investigated as a lighter alternative to lithium chloride absorbers. MOFs initially appeared promising because of their much lower density and lower regeneration temperatures. IRMOF-10 has a density of roughly 0.304 g/cm³ compared to about 2.07 g/cm³ for the SEAR LiCl absorber sponge, suggesting large mass reductions could be possible. Regeneration temperatures were also lower, around 55–85°C instead of roughly 100°C for LiCl systems.

Properties	**SEAR Absorber Sponge** (LiCl + absorbed solution ~45% LiCl by mass) (Izenson et al., 2017)	**IRMOF-10** (Wieme et al., 2019)
Density	**2.07 g/cm^3**	**0.304 g/cm^3**
Cp (J/kg K)	**2600**	**860**
Water uptake per gram	**1.24 g/g**	**0.6-1 g/g**
Dry Mass (structural)	**1045 g (per 190g LiCl)**	**Significantly lighter ***
Regeneration Temperature	**100 C**	**55–85 C**
Thermal Conductivity	**0.6 W/mK**	**0.09 W/m·K**

Table 13.1.1: Lithium Chloride vs IRMOF-10 thermal and intensive properties

Despite these advantages, the MOF concept introduced thermal limitations. The largest issue was thermal conductivity. IRMOF-10 has a thermal conductivity of only about 0.09 W/m·K compared to roughly 0.6 W/m·K for the LiCl absorber radiator. This made it difficult to transfer heat from the absorber material to the radiator surface efficiently. To compensate, the design would require many conductive pins to spread heat, increasing mass and complexity. Our analysis also suggested that a small compressor would likely be required to improve SWME vapor flow through the MOF structure, introducing additional power and hardware requirements, while also canceling the benefit of the higher pressure difference that makes the panels a better surface to convect into than directly to Mars .

Surface area constraints on the PLSS also limited the practicality of the design. Early calculations estimated that supporting a 300 W average heat load for a 10-hour EVA would require approximately 18 kg of MOF-based absorber panels covering about 1.01 m² of surface area. Although MOFs had potential for water preservation, the overall system mass increase outweighed the benefit within the available PLSS volume and area constraints. In addition, unlike the LiCl systems already tested by NASA in Mars-relevant environments, the MOF systems considered had not yet been tested under realistic Mars conditions.

Overall, both the LCAR and MOF concepts demonstrated that reducing SWME water loss is possible, but at significant mass and integration costs. The LiCl absorber, despite NASA testing, strong water uptake, and good thermal performance, ultimately required heavy containment hardware and introduced corrosion and contamination concerns, making it unrealistic. MOFs offered lower density and lower regeneration temperatures, but their poor thermal conductivity and large structural requirements largely offset the theoretical advantage. These early studies ultimately led to the final hybrid radiator-SWME design.

13.2 Thermal - Thermochromic and Electrochromic Coatings (Ayush)

Electrochromic surfaces are coatings that change their emissivity state based upon an electrical stimulus. This emissivity change is accomplished through either a voltage-driven ion exchange or electrochemical reaction, which would change the optical properties of the thin film that is used as the variable emittance material. The main advantage that comes from this type of system is the tunability it offers. While thermochromic coatings offer only two states of emissivity, which will be touched upon later, an electrochromic coating offers much more. An electrochromic coating can change its emissivity depending on how many volts (typically 1-3 V) are sent to it, with very minimal switching power. Depending on the voltage sent to the coating, the emissivity can reach a specific value depending on the needs of the system. This offers a very tuned and versatile solution to heat rejection. Additionally, once an emissivity is set, most electrochromic coatings can hold their emissivity without the need for additional power input, meaning that very little power draw would be required from the PLSS battery. The switching time can take between seconds and minutes, but this is not much of an issue considering there is no reason to expect a sudden unexpected jump or drop in the amount of heat that needs to be rejected. However, there were a few detriments that came from this design, which led to it not being chosen as our coating for the radiator. First is the poor UV durability for polymer-based electrochromic materials. There are a variety of polymer-based materials that are necessary for the design, which raises concerns from long term exposure. There is reason to be concerned about the degradation that may occur over long term missions. This concern regarding long term usability is the second cause of not moving forward with this coating. The cycling stability issues that arise from concern over durability of materials means that over hundreds of EVAs, it is not certain that the radiator will perform as well at the end of a long term stay on Mars or the moon as it did at the beginning of that stay. Additionally, while there has been some testing done of electrochromic materials in low orbit and on the ISS, we believe that our other options have gone through more rigorous testing and have been proven more capable than this one.

Thermochromic coatings, on the other hand, are a passive system, with the stimulus that determines the change in emissivity being based off the surface temperature of the coating. This type of coating has two emissivity states, a “hot” state and a “cold” state. The hot state would exhibit a high emissivity, making it much more capable of rejecting excess heat from the PLSS, while the cold state would do the opposite, exhibit a lower emissivity when the PLSS was cooler, allowing it to conserve heat in case the interior got too cold. This type of coating is an attractive option for a few reasons. It has been shown to survive millions of switching cycles beyond what competing phase change materials have delivered, and does not require any sort of electronics, electrical input, or mechanical parts to function, making it a simple, reliable, and lightweight coating. In addition, it has been used in satellites as well as other space vehicles, so we are confident in its capabilities in PLSS applications. Thermochromic coatings come with some stipulations in order to effectively use them as a radiator coating, but these are easily met and come with very little cost or risk. One weakness is that the existence of only two emissivity states means that the emissivity cannot be tuned and meet the needs of the system as specifically as an electrochromic coating can. However, the dynamics of heat rejection should not be so extreme as to require an extremely tuned solution, and thermochromic coating would automatically switch to meet the needs of the system. Additionally, the lack of tunability would mean that the temperature around which the switching would occur would be determined by the active material in the coating, rather than what the radiator would need the switching point to be. However, a process called doping would be used to solve this, which will be described in greater detail further. Lastly, protection from atomic oxygen would need to be implemented into the coating, which is typically incorporated into the material stack that the coating is made up of.

The type of thermochromic coating that we investigated as our most promising option, a type that is a very commonly used coating type for spacecraft applications, was a Vanadium Dioxide (VO_2) coating. This coating would operate by transitioning between its cold state, a semiconductor phase with low infrared emissivity, and its hot state, a metallic phase with much higher emissivity. This transition would occur at 68 °C (154 °F), its “switching point.” This is not the temperature we would want the radiator to switch emissivity at, but doping could be used to move the switching point down to meet the requirements of the PLSS.

A typical vanadium dioxide coating consists of four layers: a base, spacer, active, and a protective layer (TiO_2). The base, which would be aluminum for our radiator, is a highly reflective metal substrate that prevents transmission and forces infrared radiation to interact with the layers above it. This base would act as the radiator’s surface and would include tubing and be bonded to outside of PLSS. The spacer layer, which is typically Barium Fluoride, is meant to serve as a dielectric spacer. The thickness of this layer is tuned to best create Fabry–Perot resonance and modulate emissivity. If properly sized, it can strengthen the emissions of the coating. Lastly, the protective layer is typically Titanium Oxide, and works as a thin, durable outer layer that protects against oxidation, dust, and UV without significantly degrading IR performance. This is the measure that protects the coating from oxygen to preserve functionality. Depicted below is a visualization of how these layers would be stacked and interact with each other.

Doping, as mentioned before, is the method through which the switching point of the coating can be changed to fit the needs of the radiator. To investigate the capabilities of doping to change the switching point, we referenced a study conducted in the Air Force Research Laboratory that investigated thermal capabilities of variable emittance materials, which also touched on the capabilities of doping. In this study, doping is employed as a method to lower the phase transition temperature of vanadium dioxide. For a pure VO_2 layer, not the multilayer stack depicted and discussed previously, it was found that the transition temperature can be reduced by approximately 22 K for every one percent of vanadium atoms replaced by tungsten. In the present experiment, the phase transition temperature was lowered by about 40 K. This approach has successfully pushed the transition below 273 K (0 °C). As a result, the switching temperature of thermochromic coating panels—around 298 K—corresponds to an emissivity of 0.55. The high emissivity state for this new layer was about .65, with a low state of about .3.

Figure or Table containing sensitive information, or possible unauthorized copyright information has been removed.

Figure 13.2.1: Emissivity vs Temperature for a doped VO2 stack [75]

13.3 Structures - CFRP Hatch Design (Kateryna Sukhina)

Bulk of the project period, post PDR, was spent designing a fully CFRP hatch. For simplicity of preliminary estimations, the hatch was split into 2 components: pressure bulkhead and sealing rim. While the pressure bulkhead calculations remain the same as those in the Hatch section of this paper, the sealing rim was analyzed slightly differently.

The main distinction between this design and the final version described in the hatch section is the definition of the interface between HUT and PLSS backpack. Initially, with a fully CFRP hatch, O-ring grooves would have to be on the HUT, with the CFRP rim of the hatch acting as a face seal on the O-rings. To estimate required thickness of the rim, we used the same thin rectangular plate deflection formula, equations 2 and 3 in the Hatch section of the report. Assuming quasi-isentropic CFRP, the required thickness to resist deflection under the same bolting configuration ended up being approximately **0.6” (15.24 mm)**. However, this would result in a significantly heavy rim, around 8kg. Therefore, the next optimization of this design was introducing a reinforcing rim around the sealing region, while maintaining thinner overall rim. This configuration is shown in the figure below, red arrows pointing to the reinforcement.

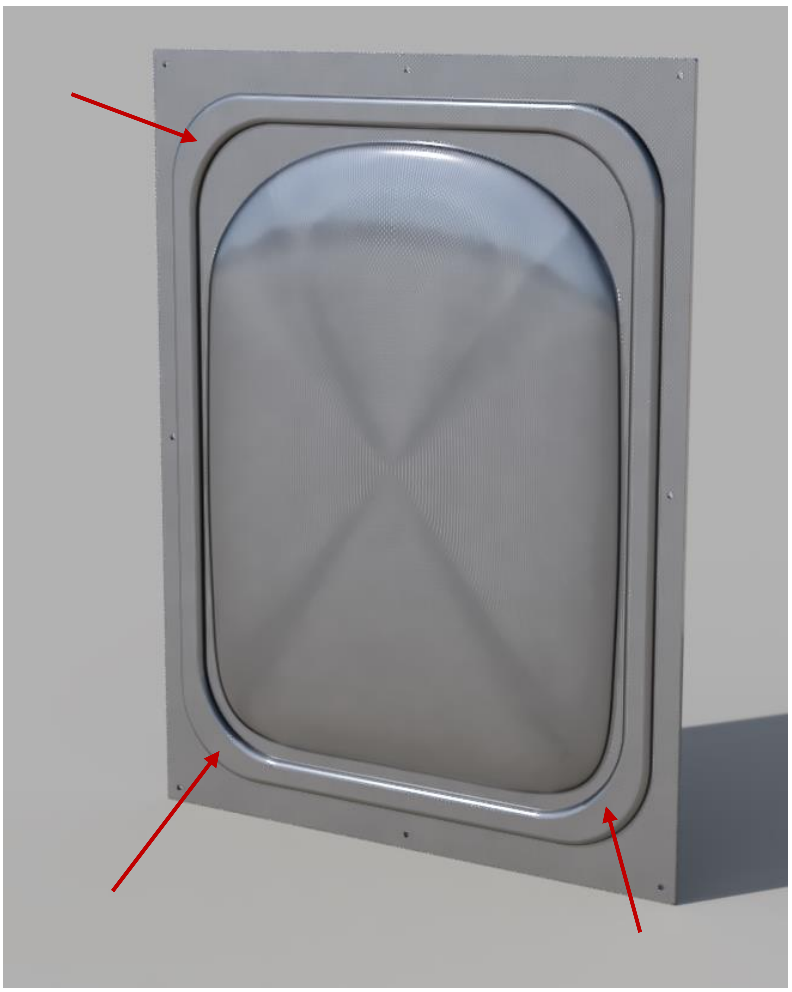

Figure 13.3.1: CFRP hatch back side (facing PLSS)

In the early stages of this design, before mounting mechanism via M6 bolts was designed, in thickness of the rim a simplifying assumption was made. We assumed clamped boundary condition which resulted in a rim with thickness of 0.2” **(5.08 mm)**. Using this as the baseline for overall rim thickness, we reinforced approximate O-ring sealing surface to 0.6” and verified validity of this design with FEA, which will be discussed in more detail further in this section.

Additionally, to allow for bolting through the carbon fiber, AL-6061 threaded inserts would need to be inserted into the part during the layup stage.

There are a few complications introduced when using CFRP for sealing.

Firstly, carbon fiber is a porous, rough material. O-rings generally require a smooth surface to be sealed effectively, and especially face seals. Some ways of dealing with this issue include coating the sealing surface to provide a smoother finish and/or choose larger cross-section, larger durometer O-rings that are more forgiving to imperfections in the sealing surface. For this reason, despite initially choosing 0.07” cross-section O-rings with durometer 70, we decided to size up to 0.21” cross-section O-rings with durometer 50. This was further adjusted for the most recent design described in section 7.2.1.

Secondly, latching mechanisms are much harder to develop on CFRP given its brittleness. However, latching mechanisms are required for the hatch, to provide uniform compression on the O-rings.

Hence, updating the design to the one described in section 7.2.1 (Hatch) aids in both issues presented above. It also simplifies operations for the astronaut by not requiring them to climb into the back of the HUT through the O-rings. Instead, the whole PLSS assembly opens, allowing for clean entry to the PGS.

To touch on the FEA conducted for the CFRP hatch, it was tested under static conditions, with the following set-up:

1. Forces:
    - Pressure force distributed over bulkhead area, F = 16000 N
    - Compression force for both O-rings, F = 10820 N
    - Crash load of 9Gs
2. Constraints: Fixed edges
3. Factor of safety: 2

The results were promising, despite a low, but positive, margin of safety of 0.055. The figures below show FEA results for Von Mises stress (A) and displacement (B).

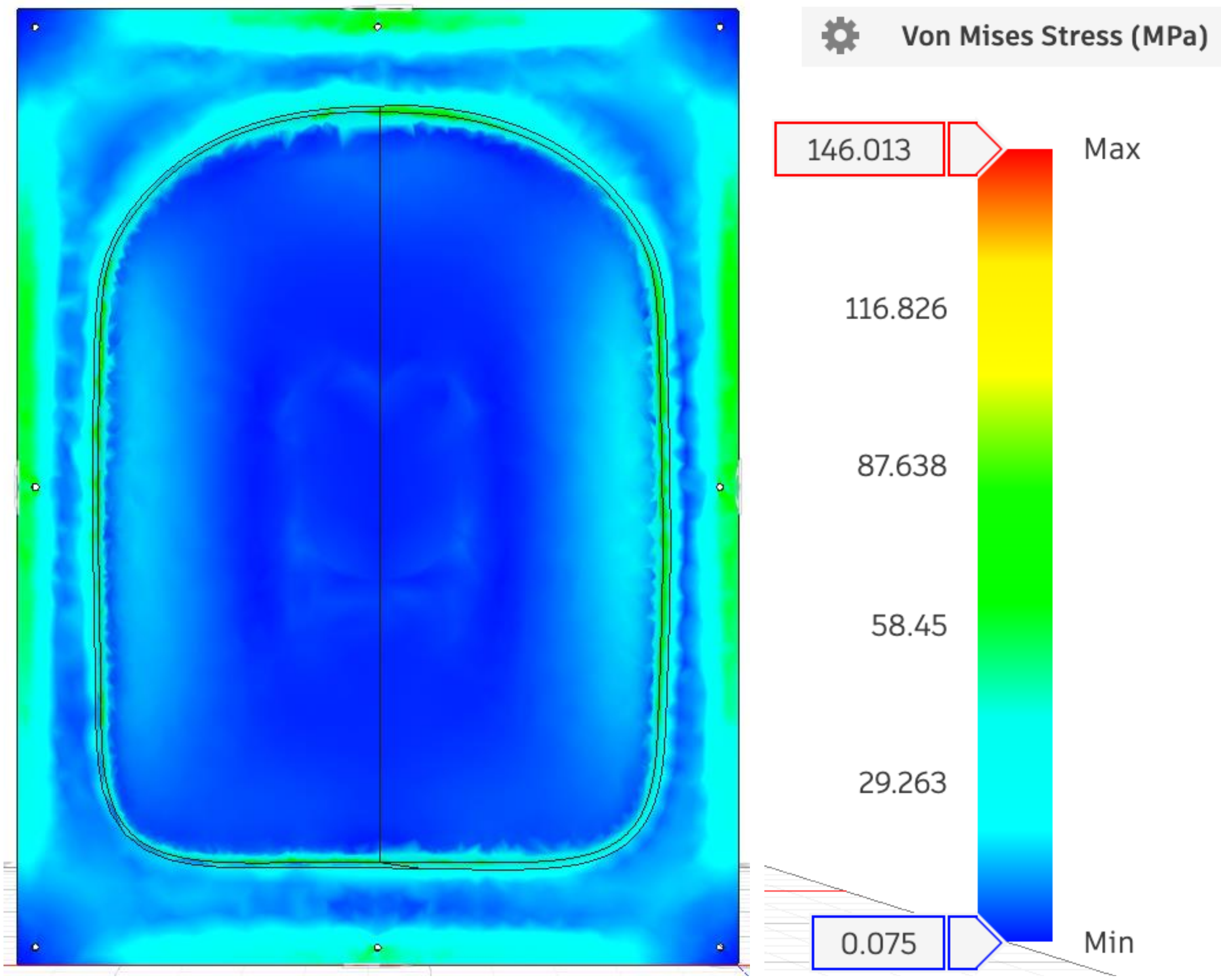

Von Mises Stress (MPa)
146.013
Max
116.826
87.638
58.45
29.263
0.075
Min

(A)

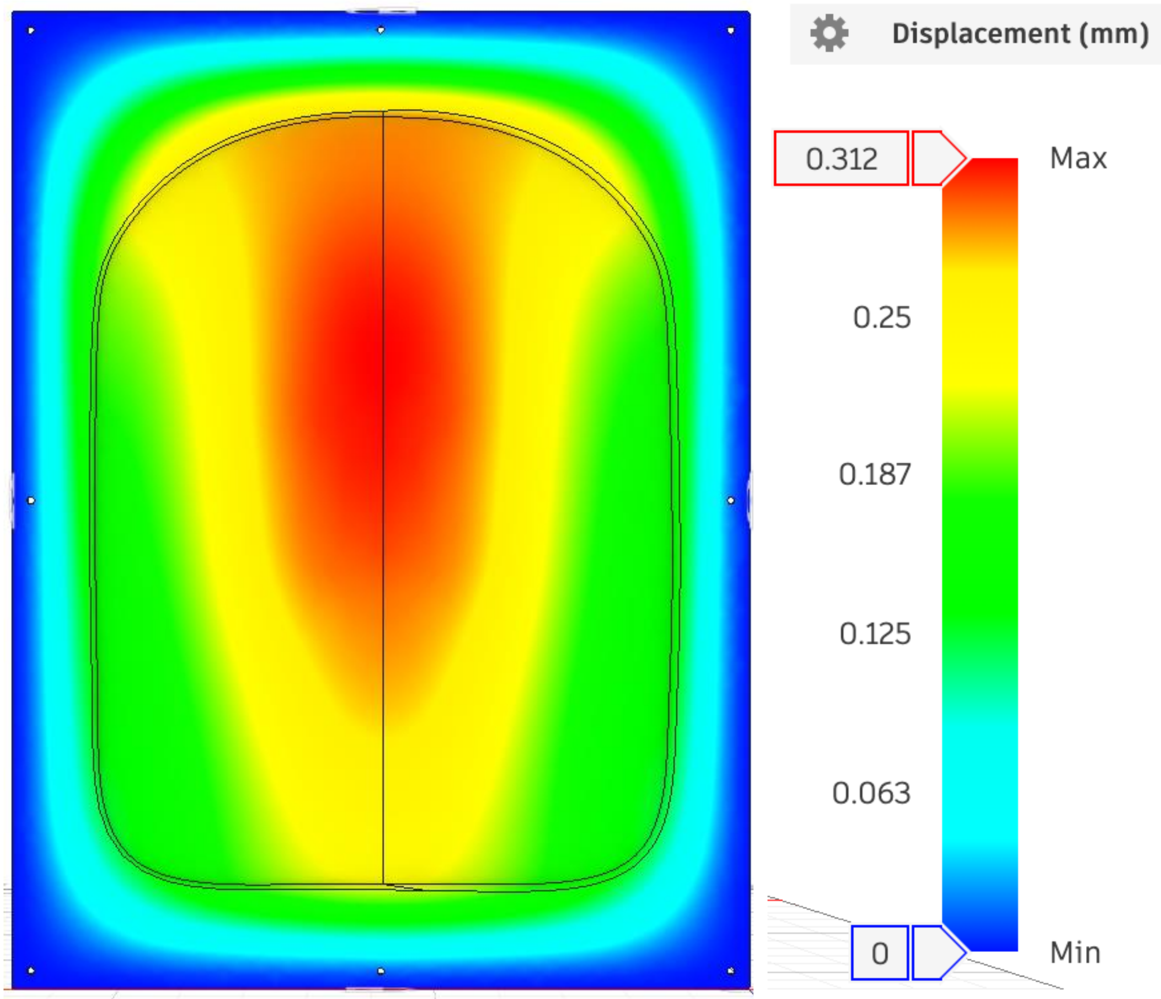

(B)

Figure 13.3.2: FEA results for CFRP hatch

13.4 Avionics – First Iteration Avionics Box (Chase Latyak)

The design for the consolidated avionics boxes went through two major iterations, with the first being detailed in this section. Conceptually, both designs set out to accomplish the same goal: reduce mass via overall material changes while incorporating innovative technologies like lightweight shielding and aluminum components for radiation shielding and thermal conduction respectively. Whereas the current design incorporates a maximum of two controllers per box, the first iteration contained three controllers per box, organized as shown in figure 13.4.1, for a total of three avionics boxes. The idea of separating primary and backup controllers was still used in this first iteration as well.

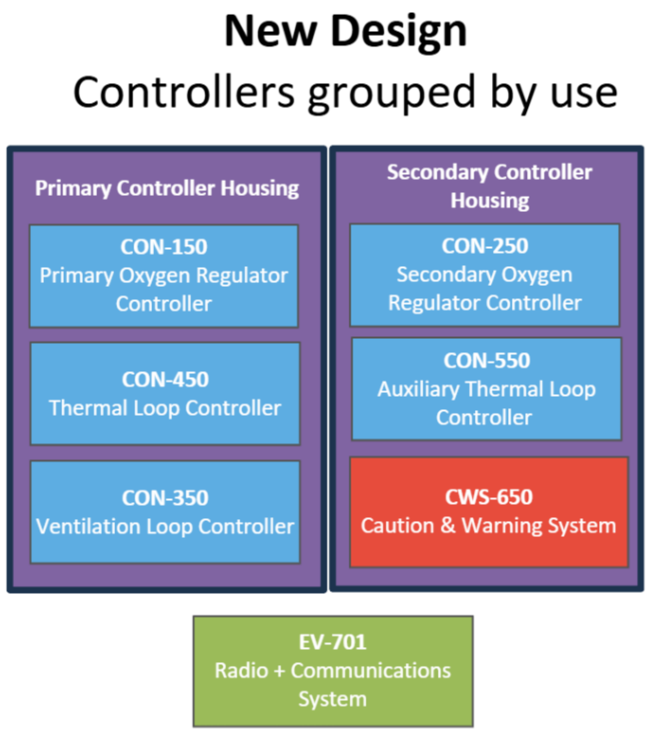

Figure 13.4.1: First iteration avionics box configuration.

The key difference in how these boxes were designed was that the first iteration featured a design with shelves for each controller and cold plate to be mounted, with all three being stacked vertically within the box. The idea would be to have each controller directly on an associated cold plate, though these aluminum plates would be much thinner at just 1.27 mm than the current 4 mm design. The plates would have one thicker section through the middle, where a singular embedded heat pipe would go straight through the plate, for a total of three straight heat pipes. Originally, these heat pipes were copper, which is why the CAD assembly contains copper-colored pipes, but the issues of galvanic corrosion between aluminum and copper led to the switch to aluminum for both the plates and pipes in the current design. The exterior of the box featured holes for these heat pipes to pass through, as well as arbitrarily sized holes for wiring, just like the current design. Instead of being separated in halves, the majority of the box was one solid piece that would connect to the isogrid backplate with some bracket mechanism similar to the current design, though the brackets were not yet included on this first iteration in the CAD models or drawings. The side of the box directly opposite the backplate would be a removable lid, which featured eight M4 bolt holes to connect to the main structure of the box and keep the shelves in place. Figure 13.4.2 shows the exterior of the box, figures 13.4.3 and 13.4.4 show the interior design of the assembly, figure 13.4.5 contains the aluminum shelf CAD model, and figures 13.4.6 and 13.4.7 are the engineering drawings for the PEEK box and the aluminum shelf respectively.

Redacted due to Export Control/CUI requirements.

Figure 13.4.2: First iteration avionics box exterior CAD model.

Redacted due to Export Control/CUI requirements.

Figure 13.4.3: First iteration avionics box assembly, side view.

Redacted due to Export Control/CUI requirements.

Figure 13.4.4: First iteration avionics box assembly, isometric view.

Redacted due to Export Control/CUI requirements.

Figure 13.4.5: First iteration aluminum shelf CAD model, bottom isometric view.

Redacted due to Export Control/CUI requirements.

Figure 13.4.6: First iteration avionics box engineering drawing, all dimensions in mm.

Redacted due to Export Control/CUI requirements.

Figure 13.4.7: First iteration aluminum shelf engineering drawing, all dimensions in mm.

While this design incorporated the general improvements we wanted to make as methods of saving mass in the avionics system, there were a few major flaws that led to the next iteration's design. Firstly, the box itself would be impossible to remove or disassemble in its current configuration, because there is no way to disconnect the heat pipes. Since these pipes run directly through the solid side of the box, this essentially would need to not only be manufactured in a way to combine these pieces but also would not allow the shelves to actually slide in and out as intended for potential maintenance or replacement. This is why the current design features two distinct halves that essentially clamp around the heat pipe, allowing for the box to be disassembled and electronics to be accessed while maintaining the thermal loop. The other major error is the cold plates being on the opposite side of the electronics, as the heat would need to flow through the bottom circuit board instead of the hot components directly making contact with the cold plate in the updated design. For these reasons, the shelf design was updated to maintain the benefits of consolidating electronics into fewer boxes while accounting for these problems.

Although mass of the current design is actually 0.22 kg lighter than this first iteration, it should be noted that the mass of the copper heat pipes was considered part of the avionics box mass in the first iteration. While the length of pipe that runs through the boxes was not very long, typically about 18 cm, copper is quite dense and thus the heat pipes contributed 0.45 kg to the total mass of all three boxes combined. This means that going from three boxes to four did slightly increase the overall mass since the heat pipes were not considered part of the avionics box mass in the current design, but the switch from copper should help offset the change somewhat. Overall, the core ideas between both the current design and first iteration were the same, and highlight the viability of decreasing avionics mass in the PLSS through new materials and box design.

14 Appendix D. Code

14.1 Isogrid MATLAB Code (Emma Perez)

Figure or Table containing sensitive information, or possible unauthorized copyright information has been removed.

Figure or Table containing sensitive information, or possible unauthorized copyright information has been removed.

Figure or Table containing sensitive information, or possible unauthorized copyright information has been removed.

Figure or Table containing sensitive information, or possible unauthorized copyright information has been removed.

Figure or Table containing sensitive information, or possible unauthorized copyright information has been removed.

Figure or Table containing sensitive information, or possible unauthorized copyright information has been removed.

Figure or Table containing sensitive information, or possible unauthorized copyright information has been removed.

Figure or Table containing sensitive information, or possible unauthorized copyright information has been removed.

14.2 Bolt Analysis MATLAB Code (Emma Perez)

Figure or Table containing sensitive information, or possible unauthorized copyright information has been removed.

Figure or Table containing sensitive information, or possible unauthorized copyright information has been removed.

14.3 Cover Isogrid Analysis MATLAB Code (Emma Perez)

Figure or Table containing sensitive information, or possible unauthorized copyright information has been removed.

Figure or Table containing sensitive information, or possible unauthorized copyright information has been removed.

Figure or Table containing sensitive information, or possible unauthorized copyright information has been removed.

Figure or Table containing sensitive information, or possible unauthorized copyright information has been removed.

15 Appendix E: Testing and Analysis Raw Data (MPA Team)

15.1 Center Of Gravity Raw Data (MPA Team)

Document Link: cog results.xlsx

Data was collected on two different heart rate monitors. Empty cells correspond to a heart rate monitor not being used.

Subject Number	Resting Heart Rate (BPM) - Samsung	Resting Heart Rate (BPM) - Akin's
Day 1		
1	85	80
2	70	
3	97	95
Day 2		
1		83
2		80
3		89

Unloaded Configuration

Subject Number:	Time (minute)	Heart Rate (BPM)- Samsung	Heart Rate (BPM)- Akins
1	0		85
	1		104
	2		108
	3		106
	4		104

Overall Bedford Workload Rating Scale
1

	5		108
	6		108
	7		109
	8		107
	9		109
	10		104

Subject Number:	**Time (minute)**	**Heart Rate (BPM)- Samsung**	**Heart Rate (BPM)- Akins**
2	0	75	
	1	99	
	2	99	
	3	101	
	4	100	
	5	103	
	6	100	
	7	103	
	8	108	
	9	102	
	10	105	

Overall Bedford Workload Rating Scale
1

Subject Number:	**Time (seconds)**	**Heart Rate (BPM)- Samsung**	**Heart Rate (BPM) - Akin**
3	0	97	95
	1	116	116
	2	123	120

Overall Bedford Workload Rating Scale
1

	3	109	109
	4	116	125
	5	123	120
	6	129	129
	7	125	116
	8	127	127
	9	123	125
	10	128	127

Top Configuration

Subject Number:	Time (minute)	Heart Rate (BPM)- Samsung	Heart Rate (BPM)- Akins
1	0	70	
	1	110	
	2	113	
	3	112	
	4	116	
	5	119	
	6	128	
	7	118	
	8	120	
	9	121	
	10	119	

Overall Bedford Workload Rating Scale
3

Subject Number:	Time (minute)	Heart Rate (BPM)- Samsung	Heart Rate (BPM)- Akins
2	0	69	
	1	103	
	2	100	
	3	99	
	4	103	
	5	99	
	6	105	
	7	103	
	8	101	
	9	104	
	10	105	

Overall Bedford Workload Rating Scale
2

Subject Number:	Time (seconds)	Heart Rate (BPM)- Samsung	Heart Rate (BPM) - Akin
3	0	101	101
	1	122	126
	2	122	120
	3	127	128
	4	132	131
	5	132	131
	6	140	141
	7	139	138
	8	133	129
	9	139	139

Overall Bedford Workload Rating Scale
3

	10	133	136

Bottom Configuration

Subject Number:	Time (minute)	Heart Rate (BPM)- Samsung	Heart Rate (BPM)- Akins
1	0	85	
	1	87	
	2	90	
	3	110	
	4	113	
	5	125	
	6	120	
	7	118	
	8	116	
	9	112	
	10	116	

Overall Bedford Workload Rating Scale
2

Subject Number:	Time (minute)	Heart Rate (BPM)- Samsung	Heart Rate (BPM)- Akins
2	0	70	
	1	104	
	2	103	
	3	98	
	4	102	
	5	103	
	6	105	

Overall Bedford Workload Rating Scale
2

	7	106	
	8	104	
	9	104	
	10	104	

Subject Number:	Time (seconds)	Heart Rate (BPM)- Samsung	Heart Rate (BPM) - Akin
3	0	97	97
	1	102	113
	2	127	121
	3	120	116
	4	129	125
	5	137	137
	6	136	131
	7	133	134
	8	144	144
	9	140	138
	10	141	141

Overall Bedford Workload Rating Scale
5

Dispersed Configuration, Day 1

Subject Number:	Time (minute)	Heart Rate (BPM)- Samsung Galaxy Watch 6	
1	0	97	
	1	116	
	2	115	
	3	120	

Overall Bedford Workload Rating Scale
1

	4	116			
	5	119			
	6	123			
	7	119			
	8	123			
	9	124			
	10	121			
Subject Number:	**Time (minute)**	**Heart Rate (BPM)- Samsung Galaxy Watch 6**			**Overall Bedford Workload Rating Scale**
2	0	74			2
	1	106			
	2	105			
	3	105			
	4	107			
	5	109			
	6	109			
	7	110			
	8	108			
	9	109			
	10	103			
Subject Number:	**Time (seconds)**	**Heart Rate (BPM)- Samsung**	**Heart Rate (BPM) - Akin**		**Overall Bedford Workload Rating Scale**
3	0	94	99		2
	1	124	113		
	2	135	135		

	3	136	136
	4	133	133
	5	141	141
	6	145	145
	7	140	140
	8	146	145
	9	148	148
	10	150	149

Dispersed Configuration, Day 2

Subject Number:	**Time (minutes)**	**Heart Rate (BPM)**
1	0	83
Bedford: 1	1	82
	2	122
	3	126
	4	128
	5	127
	6	130
	7	130
	8	131
	9	133
	10	132
Subject Number:	**Time (seconds)**	**Heart Rate (BPM)**
2	0	80
Bedford: 2	1	97
	2	99
	3	113

	4	110
	5	107
	6	111
	7	114
	8	116
	9	116
	10	110
Subject Number:	**Time (seconds)**	**Heart Rate (BPM)**
3	0	89
Bedford: 1	1	100
	2	99
	3	121
	4	111
	5	99
	6	105
	7	114
	8	111
	9	110
	10	107

16.2 Maintainability Raw Data (MPA Team)

Document link: Maintainability Findings.xlsx

Time per step (s) for the Battery

Step	Subject 1	Subject 2	Subject 3
1	7	9.58	5.04
2	6.37	5.5	6.42
3	16.89	10.42	7.77

	4	6.62	4.84	6.32
	5	60	64.92	60
	6	3.02	12.12	10.74
Total		99.9	107.38	96.29

NMSUS Question	Subject 1	Subject 2	Subject 3	
	1	5	4	5
	2	2	1	2
	3	4	3	3
	4	1	2	1
	5	5	4	1
	6	1	2	1
	7	3	4	2
	8	1	2	1
Usability Score		87.5	75	68.75

Time per step (s) for the Oxygen
Loop

Step	Subject 1	Subject 2	Subject 3	
	1	19	17.3	22.38
	2	23	17.16	9.24
Total		42	34.46	31.62

NMSUS Question	Subject 1	Subject 2	Subject 3	
	1	5	4	5
	2	2	2	1
	3	3	3	4
	4	1	2	1
	5	5	4	3
	6	3	2	1
	7	3	4	5
	8	1	3	2
Usability Score		78.125	68.75	87.5

Time per step (s) for the LiOh/TCC

Step	Subject 1	Subject 2	Subject 3

	1	26.67	20.8	21.92
	2	36.22	42.6	22.52
	3	72.34	76.7	65.94
	4	116	167	94.63
Total		251.23	307.1	205.01

NMSUS Question	Subject 1	Subject 2	Subject 3
1	3	2	3
2	4	2	4
3	4	3	3
4	2	3	2
5	3	4	5
6	3	3	2
7	3	3	4
8	3	4	4
Usability Score	53.125	50	59.375

Time per step (s) for the Avionics Box

Step	Subject 1	Subject 2	Subject 3
1	3.63	12.08	11.44
2	15.99	14.91	19.96
3	15.96	13.15	13.26
4	18.15	9.93	7.83
5	17.46	17.6	13.59
6	278.3	257	314.86
7	5	2	5
8	29.27	2.93	46.6
9	420	280	299.09
10	15.2	14.41	25.97
11	14.8	8.66	6.72
Total	833.76	632.67	764.32

NMSUS Question	Subject 1	Subject 2	Subject 3
1	4	4	1
2	1	3	2
3	5	4	3
4	1	2	2
5	5	4	1
6	5	4	1
7	5	3	5
8	1	4	3
			56.25
Usability Score	84.375	56.25	

16 Appendix F: Scrapped Modular Test Ideas (MPA Team)

16.1 Scrapped Modular Test Ideas Breakdown (MPA Team)

Linear rail systems with a platform for z-axis movement

Figure or Table containing sensitive information, or possible unauthorized copyright information has been removed.

- Get like 2 or 3 of these
- Attach to the horizontal bars
  - Will add weight but not too much hopefully but can be adjusted with the weight we can control

v-line rails

Figure or Table containing sensitive information, or possible unauthorized copyright information has been removed.

- Might be less mass
- Might not be good for heavy weight (haven't done the full research yet)
- Similar use as above

After talking to Dr. Akin:

- Don't do z-axis too much --> look at 80/20 catalogue on official website to see the little one that let us move
- Figure out a **locking system** for horizontal movement and vertical movement
    - Horizontal we might need to add holes in original COG vest (shoutout Meredith Embrey, graduate student at SSL) for underwater
    - But vertical there are already holes in original COG vest for underwater
- We need to look at making new modules because current ones don't let us figure out COG perfectly but if we make a bar or something to that affect **(like a barbell)** we can locate COG more easily as we would know where it is on the bar (**final design to look at)**
- Figure out test a bit more to which configurations we want to run now based on available movement
    - Make a procedure document